

AFIT/GE/ENG/93D-23

AD-A274 078



S DTIC
ELECTE
DEC 27 1993
A

Multiple Model Adaptive Estimation
Applied to the LAMBDA URV
for Failure Detection and Identification.

THESIS
David W. Lane
Captain, U.S. Air Force

AFIT/GE/ENG/93D-23

This document has been approved
for public release and sale; its
distribution is unlimited.

December 2, 1993

93 12 22 141

023788

93-31028



**Best
Available
Copy**

AFIT/GE/ENG/93D-23

**Multiple Model Adaptive Estimation Applied to the LAMBDA URV
for Failure Detection and Identification.**

THESIS

**Presented to the Faculty of the Graduate School of Engineering
of the Air Force Institute of Technology
Air University
In Partial Fulfillment of the
Requirements for the Degree of
Master of Science (Electrical Engineering)**

**David W. Lane, B.E.
Captain, U.S. Air Force**

December 1993

December 2, 1993

Accession For	
NTIS	CRA&I <input checked="" type="checkbox"/>
DTIC	IAS <input type="checkbox"/>
Unannounced	<input type="checkbox"/>
Justification	
By	
Distribution/	
Availability Codes	
Dist	Avail and/or Special
A-1	

DTIC QUALITY INSPECTED 5

Table of Contents

	Page
List of Figures	v
List of Tables	x
Abstract	xii
 I. Introduction	 1-1
1.1 Problem Statement	1-2
1.2 Continuation of AFIT Research	1-3
1.2.1 Updated LAMBDA state space model from Wright Laboratories	1-4
1.2.2 Closed Loop Controller	1-4
1.2.3 Dither Technique	1-4
1.2.4 Dual Failure Detection and Identification	1-4
1.3 MMAE Background	1-5
1.3.1 Kalman Filter Equations	1-5
1.3.2 Development of the Multiple Model Adaptive Estimation Algorithm	1-7
1.3.3 Beta Dominance	1-9
1.3.4 Scalar Residual Monitoring	1-10
1.3.5 Filter Tuning	1-12
1.4 Hierarchical Modeling Structure	1-12
1.5 Research Objectives	1-14
1.5.1 Develop Best Dither	1-14
1.5.2 Proof of Hierarchical Concept	1-16
1.6 Scope of Research	1-16
1.7 Limitations	1-17
1.8 Summary of Following Chapters	1-18

	Page
II. Literature Review	2-1
2.1 Early Research	2-1
2.2 MMAE at the Air Force Institute of Technology	2-3
2.3 Chapter Summary	2-4
III. Methodology	3-1
3.1 Software Tools	3-1
3.2 LAMBDA Model	3-2
3.2.1 Truth Model	3-3
3.2.2 Flight Control System Design	3-7
3.2.3 Dryden Wind Gust Model	3-9
3.3 MMAE Design	3-13
3.3.1 Structure of MMAE	3-13
3.3.2 Kalman Filter Design	3-15
3.4 Test Runs	3-21
3.4.1 Monte Carlo Runs	3-21
3.4.2 Input Dithers	3-21
3.4.3 Single Failure Verification	3-23
3.4.4 Dual Failure Performance Evaluation	3-23
3.4.5 Output Format	3-24
3.5 Chapter Summary	3-26
IV. Results and Primary Analyses	4-1
4.1 Tuning the Kalman Filters	4-1
4.2 Investigation of Dithers	4-4
4.2.1 Analysis of MMAE Performance Against Varying Dither Fre- quency	4-35
4.2.2 Optimal Dither	4-42

	Page
4.3 Pilot Command Inputs	4-44
4.4 Dual Failure Performance	4-49
4.5 Chapter Summary	4-58
V. Secondary Analyses	5-1
5.1 Failure of Yaw Rate Sensor	5-1
5.2 Failure of Feedback Sensors	5-3
5.3 Dithering at the Phugoid Frequency and Low Magnitude	5-14
5.4 Chapter Summary	5-18
VI. Conclusions and Recommendations	6-1
6.1 Summary of Findings	6-1
6.2 Suggestions for Implementing an Effective MMAE on LAMBDA . . .	6-5
6.3 Recommended Topics for Further Research	6-5
6.4 Report Summary	6-8
Appendix A. Dimensional Stability Derivatives	A-1
Appendix B. Bode Plots of Actuator Transfer Functions	B-1
Appendix C. Difference Equations for QFT Prefilters and Compensators	C-1
Appendix D. Failure ID Time vs <i>g</i>-forces as Dither Magnitude Changes	D-1
Appendix E. Single Failure Probability Plots	E-1
Appendix F. Dual Failure Probability Plots	F-1
Bibliography	BIB-1
Vita	VITA-1

List of Figures

Figure	Page
1.1. Multiple Model Filtering Algorithm	1-2
1.2. Hierarchical Multiple Model Filtering Structure.	1-14
3.1. QFT Flight Control System	3-8
3.2. First and Second-Order Elevator Actuator Bode Plots.	3-18
3.3. First and Second-Order Aileron Actuator Bode Plots.	3-19
3.4. Sample of MMAE Probability Histories.	3-25
4.1. <i>g</i> -forces vs ID time for Right Elevator Actuator failure as frequency changes. . .	4-8
4.2. <i>g</i> -forces vs ID time for Left Elevator Actuator failure as frequency changes. . .	4-10
4.3. <i>g</i> -forces vs ID time for Forward Velocity Sensor failure as frequency changes. . .	4-12
4.4. <i>g</i> -forces vs ID time for Angle of Attack Sensor failure as frequency changes. . .	4-14
4.5. <i>g</i> -forces vs ID time for Pitch Rate Sensor failure as frequency changes.	4-16
4.6. <i>g</i> -forces vs ID time for Pitch Angle Sensor failure as frequency changes.	4-18
4.7. <i>g</i> -forces vs ID time for Right Aileron Actuator failure as frequency changes. . .	4-20
4.8. <i>g</i> -forces vs ID time for Left Aileron Actuator failure as frequency changes. . . .	4-22
4.9. <i>g</i> -forces vs ID time for Right Rudder Actuator failure as frequency changes. . .	4-24
4.10. <i>g</i> -forces vs ID time for Left Rudder Actuator failure as frequency changes. . . .	4-26
4.11. <i>g</i> -forces vs ID time for Sideslip Angle Sensor failure as frequency changes. . . .	4-28
4.12. <i>g</i> -forces vs ID time for Roll Rate Sensor failure as frequency changes.	4-30
4.13. <i>g</i> -forces vs ID time for Roll Angle Sensor failure as frequency changes.	4-32
4.14. <i>g</i> -forces vs ID time for Yaw Rate Sensor failure as frequency changes.	4-34
4.15. MMAE Filter Probability Plots with the Optimal Dither Technique.	4-43
4.16. Pilot Command Inputs.	4-46
4.17. MMAE Filter Probabilities with Pilot Command Inputs.	4-47
4.18. MMAE Filter Probability with Pilot Command Inputs and Rudder Failure. . .	4-48

Figure	Page
4.19. Dual Failure MMAE filter Probability Plots with the Right Elevator Actuator Failing at 4.00 sec. and Each Actuator Failing at 5.00 sec.	4-51
4.20. Dual Failure MMAE filter Probability Plots with the Right Elevator Actuator Failing at 4.00 sec. and Each Sensor Failing at 5.00 sec.	4-52
4.21. MMAE Recovery from False First Detection.	4-57
5.1. Yaw Rate Sensor MMAE Probabilities.	5-2
5.2. Residuals of FF Filter on FF Aircraft	5-4
5.3. Residuals of FF Filter on S4 Failure	5-5
5.4. Residuals of S4 Filter on S4 Failure	5-6
5.5. Pitch Command Dither with Amplitude ± 4 deg/sec and Frequency 6.6611 rad/sec.	5-7
5.6. Flight Data Sensors Tracking S4 Failure	5-9
5.7. Residuals of FF Filter on S3 Failure	5-10
5.8. Residuals of S3 Filter on S3 Failure	5-11
5.9. Residuals of S4 Filter on S3 Failure	5-12
5.10. Flight Data Sensors Tracking S3 Failure	5-13
5.11. Pitch Rate State with Failed Pitch Rate Sensor	5-13
5.12. Filter Probability Histories at Phugoid Frequency	5-15
5.13. Command Inputs at Phugoid Frequency.	5-17
B.1. Log Magnitude Response of Forward Velocity to Left Elevator.	B-1
B.2. Log Magnitude Response of Angle of attack to Left Elevator.	B-2
B.3. Log Magnitude Response of Pitch Rate to Left Elevator.	B-2
B.4. Log Magnitude Response of Pitch Angle to Left Elevator.	B-3
B.5. Log Magnitude Response of Sideslip Angle to Left Aileron.	B-3
B.6. Log Magnitude Response of Roll Rate to Left Aileron.	B-4
B.7. Log Magnitude Response of Roll Angle to Left Aileron.	B-4
B.8. Log Magnitude Response of Yaw Rate to Left Aileron.	B-5
B.9. Log Magnitude Response of Sideslip Angle to Left Rudder.	B-5

Figure	Page
B.10. Log Magnitude Response of Roll Rate to Left Rudder.	B-6
B.11. Log Magnitude Response of Roll Angle to Left Rudder.	B-6
B.12. Log Magnitude Response of Yaw Rate to Left Rudder.	B-7
D.1. <i>g</i> -forces vs ID time for Right Elevator Actuator failure as magnitude changes. .	D-3
D.2. <i>g</i> -forces vs ID time for Left Elevator Actuator failure as magnitude changes. . .	D-5
D.3. <i>g</i> -forces vs ID time for Forward Velocity Sensor failure as magnitude changes. .	D-7
D.4. <i>g</i> -forces vs ID time for Angle of Attack Sensor failure as magnitude changes. . .	D-9
D.5. <i>g</i> -forces vs ID time for Pitch Rate Sensor failure as magnitude changes.	D-11
D.6. <i>g</i> -forces vs ID time for Pitch Angle Sensor failure as magnitude changes.	D-13
D.7. <i>g</i> -forces vs ID time for Right Aileron Actuator failure as magnitude changes. . .	D-15
D.8. <i>g</i> -forces vs ID time for Left Aileron Actuator failure as magnitude changes. . . .	D-17
D.9. <i>g</i> -forces vs ID time for Right Rudder Actuator failure as magnitude changes. . .	D-19
D.10. <i>g</i> -forces vs ID time for Left Rudder Actuator failure as magnitude changes. . . .	D-21
D.11. <i>g</i> -forces vs ID time for Sideslip Angle Sensor failure as magnitude changes. . . .	D-23
D.12. <i>g</i> -forces vs ID time for Roll Rate Sensor failure as magnitude changes.	D-25
D.13. <i>g</i> -forces vs ID time for Roll Angle Sensor failure as magnitude changes.	D-27
D.14. <i>g</i> -forces vs ID time for Yaw Rate Sensor failure as magnitude changes.	D-29
E.1. MMAE Performance With Fully Functional Aircraft Failure Using Optimal Dither.	E-2
E.2. MMAE Performance With Right Elevator Actuator Failure Using Optimal Dither.	E-3
E.3. MMAE Performance With Left Elevator Actuator Failure Using Optimal Dither.	E-4
E.4. MMAE Performance With Right Aileron Actuator Failure Using Optimal Dither.	E-5
E.5. MMAE Performance With Left Aileron Actuator Failure Using Optimal Dither.	E-6
E.6. MMAE Performance With Right Rudder Actuator Failure Using Optimal Dither.	E-7
E.7. MMAE Performance With Left Rudder Actuator Failure Using Optimal Dither.	E-8
E.8. MMAE Performance With Forward Velocity Sensor Failure Using Optimal Dither.	E-9
E.9. MMAE Performance With Angle of Attack Sensor Failure Using Optimal Dither.	E-10

Figure	Page
E.10. MMAE Performance With Pitch Rate Sensor Failure Using Optimal Dither. . .	E-11
E.11. MMAE Performance With Pitch Angle Sensor Failure Using Optimal Dither. .	E-12
E.12. MMAE Performance With Sideslip Angle Sensor Failure Using Optimal Dither.	E-13
E.13. MMAE Performance With Roll Rate Sensor Failure Using Optimal Dither. . . .	E-14
E.14. MMAE Performance With Roll Angle Sensor Failure Using Optimal Dither. . .	E-15
E.15. MMAE Performance With Yaw Rate Sensor Failure Using Optimal Dither. . .	E-16
F.1. Dual Failures with Left Elevator Actuator as First Failure.	F-2
F.2. Dual Failures with Left Elevator Actuator as First Failure.	F-3
F.3. Dual Failures with Right Aileron Actuator as First Failure.	F-4
F.4. Dual Failures with Right Aileron Actuator as First Failure.	F-5
F.5. Dual Failures with Left Aileron Actuator as First Failure.	F-6
F.6. Dual Failures with Left Aileron Actuator as First Failure.	F-7
F.7. Dual Failures with Right Rudder Actuator as First Failure.	F-8
F.8. Dual Failures with Right Aileron Actuator as First Failure.	F-9
F.9. Dual Failures with Left Rudder Actuator as First Failure.	F-10
F.10. Dual Failures with Right Aileron Actuator as First Failure.	F-11
F.11. Dual Failures with Forward Velocity Sensor as First Failure.	F-12
F.12. Dual Failures with Forward Velocity Sensor as First Failure.	F-13
F.13. Dual Failures with Angle of Attack Sensor as First Failure.	F-14
F.14. Dual Failures with Angle of Attack Sensor as First Failure.	F-15
F.15. Dual Failures with Pitch Rate Sensor as First Failure.	F-16
F.16. Dual Failures with Pitch Rate Sensor as First Failure.	F-17
F.17. Dual Failures with Pitch Angle Sensor as First Failure.	F-18
F.18. Dual Failures with Pitch Angle Sensor as First Failure.	F-19
F.19. Dual Failures with Sideslip Angle Sensor as First Failure.	F-20
F.20. Dual Failures with Sideslip Angle Sensor as First Failure.	F-21
F.21. Dual Failures with Roll Rate Sensor as First Failure.	F-22

Figure	Page
F.22. Dual Failures with Roll Rate Sensor as First Failure.	F-23
F.23. Dual Failures with Roll Angle Sensor as First Failure.	F-24
F.24. Dual Failures with Roll Angle Sensor as First Failure.	F-25
F.25. Dual Failures with Yaw Rate Sensor as First Failure.	F-26
F.26. Dual Failures with Yaw Rate Sensor as First Failure.	F-27

List of Tables

Table	Page
1.1. Nominal Flight Conditions.	1-17
3.1. Nominal Flight Conditions.	3-4
3.2. Range Limits on Control Surface Movement.	3-5
3.3. Sensor Noise Variances.	3-7
3.4. MMAE Kalman Filter Codes.	3-24
4.1. <i>g</i> -forces vs ID time: Right Elevator Actuator , varying frequency	4-7
4.2. <i>g</i> -forces vs ID time: Left Elevator Actuator , varying frequency	4-9
4.3. <i>g</i> -forces vs ID time: Forward Velocity Sensor , varying frequency	4-11
4.4. <i>g</i> -forces vs ID time: Angle of Attack Sensor , varying frequency	4-13
4.5. <i>g</i> -forces vs ID time: Pitch Rate Sensor , varying frequency	4-15
4.6. <i>g</i> -forces vs ID time: Pitch Angle Sensor , varying frequency	4-17
4.7. <i>g</i> -forces vs ID time: Right Aileron Actuator , varying frequency	4-19
4.8. <i>g</i> -forces vs ID time: Left Aileron Actuator , varying frequency	4-21
4.9. <i>g</i> -forces vs ID time: Right Rudder Actuator , varying frequency	4-23
4.10. <i>g</i> -forces vs ID time: Left Rudder Actuator , varying frequency	4-25
4.11. <i>g</i> -forces vs ID time: Sideslip Angle Sensor , varying frequency	4-27
4.12. <i>g</i> -forces vs ID time: Roll Rate Sensor , varying frequency	4-29
4.13. <i>g</i> -forces vs ID time: Roll Angle Sensor , varying frequency	4-31
4.14. <i>g</i> -forces vs ID time: Yaw Rate Sensor , varying frequency	4-33
4.15. Reducing Magnitude vs Increasing Frequency of Dither	4-38
4.16. Reducing Magnitude vs Increasing Frequency of Dither	4-41
5.1. Lateral and Vertical Acceleration Statistics Resulting from One Complete Cycle of Phugoid Frequency Dither.	5-14

Table	Page
A.1. LAMBDA longitudinal primed dimensional stability derivatives.	A-1
A.2. LAMBDA lateral primed dimensional stability derivatives.	A-2
D.1. <i>g</i> -forces vs ID time: Right Elevator Actuator , varying magnitude	D-2
D.2. <i>g</i> -forces vs ID time: Left Elevator Actuator , varying magnitude	D-4
D.3. <i>g</i> -forces vs ID time: Forward Velocity Sensor , varying magnitude	D-6
D.4. <i>g</i> -forces vs ID time: Angle of Attack Sensor , varying magnitude	D-8
D.5. <i>g</i> -forces vs ID time: Pitch Rate Sensor , varying magnitude	D-10
D.6. <i>g</i> -forces vs ID time: Pitch Angle Sensor , varying magnitude	D-12
D.7. <i>g</i> -forces vs ID time: Right Aileron Actuator , varying magnitude	D-14
D.8. <i>g</i> -forces vs ID time: Left Aileron Actuator , varying magnitude	D-16
D.9. <i>g</i> -forces vs ID time: Right Rudder Actuator , varying magnitude	D-18
D.10. <i>g</i> -forces vs ID time: Left Rudder Actuator , varying magnitude	D-20
D.11. <i>g</i> -forces vs ID time: Sideslip Angle Sensor , varying magnitude	D-22
D.12. <i>g</i> -forces vs ID time: Roll Rate Sensor , varying magnitude	D-24
D.13. <i>g</i> -forces vs ID time: Roll Angle Sensor , varying magnitude	D-26
D.14. <i>g</i> -forces vs ID time: Yaw Rate Sensor , varying magnitude	D-28
E.1. MMAE Kalman Filter Codes.	E-1
F.1. MMAE Kalman Filter Codes.	F-1

Abstract

Multiple Model Adaptive Estimation (MMAE) is a method of estimating unknown system parameters by modeling all possible parameter configurations in several models. The parameters for this research are failure status conditions associated with flight control actuators and sensors on the LAMBDA Unmanned Research Vehicle, an experimental aircraft operated by Wright Laboratory Flight Controls Division, Flight Controls Techniques Branch at Wright-Patterson Air Force Base, Ohio. Six actuator failures and eight sensor failures are modeled, along with the fully functional aircraft, in fifteen elemental Kalman filters. These filters propagate and update their own aircraft state estimates in real time. A probability computation representing the likelihood of each elemental filter's match to the true condition of the aircraft is used to generate relative probabilities for each filter's hypothesis. In this research, the MMAE algorithm is extended for the identification of dual failures through the use of a hierarchical structure of filter banks. The ability of the MMAE to identify dual failures in the face of wind gust uncertainty and sensor noise is investigated. Aircraft state excitation is required for effective MMAE performance. Therefore, the form of an optimal input dither signal is derived through extensive experimentation. Dither signals are applied to the command inputs of a Quantitative Feedback Theory (QFT) flight control system which controls pitch rate, roll rate, and sideslip angle. In particular, the MMAE performance is studied as sinusoidal dither inputs are varied in frequency and magnitude. An analysis of tuning techniques for the elemental filters within the MMAE is presented. The monitoring of scalar residuals associated with controlled aircraft states is presented with respect to its effect on MMAE performance.

Multiple Model Adaptive Estimation Applied to the LAMBDA URV for Failure Detection and Identification.

I. Introduction

The problem of fault detection and isolation in aircraft control systems has been and will continue to be a major engineering challenge. The engineer is faced with a delicate balancing act. He is constantly trading effectiveness for simplicity and exchanging redundancy for weight savings. The subject of this thesis will, when developed, become a key tool in the design of aircraft that will push performance beyond what is conceived as possible today. The multiple model adaptive estimation algorithm has the potential to replace many redundant aircraft components that require space and consume energy. It would be highly desirable to exchange those components for a small portion of computer resources allocated to running a fault detection algorithm.

In this thesis, Multiple Model Adaptive Estimation (MMAE) is being applied to failure detection and isolation in sensors and flight control actuators. Specifically, a multiple model adaptive estimation algorithm is employed to detect these failures on the LAMBDA URV (Unmanned Research Vehicle) as simulated in a computer model. The MMAE algorithmic structure is shown in Figure 1.1. The measurement, z , and knowledge of the control input are presented to each Kalman filter in the active bank of Kalman filters which, in turn, produce their own unique state estimates, \hat{x}_k , and residuals, r_k . The residuals are combined to form probabilities of correctness, p_k , associated with each filter. These probabilities weight the individual state estimates appropriately and their sum is the probability-weighted average MMAE state estimate.

Several failures will be synthesized in a truth model to produce a database of control inputs and sensor measurements. The MMAE algorithm will employ a bank of Kalman filters, each driven by a model which simulates one of the possible failed conditions. Expected measurements from each Kalman filter will be compared with the database of true measurements. Then the filter with the best match between expected and true measurements is declared to correspond to the model that mirrors the truth model.

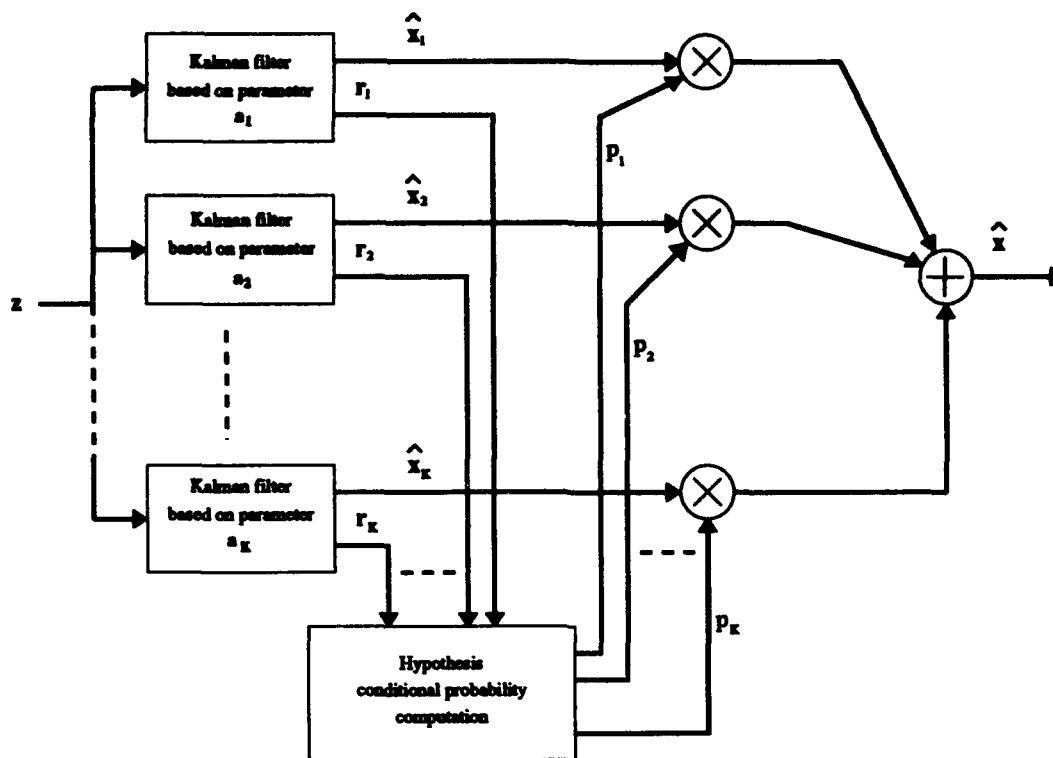


Figure 1.1 Multiple Model Filtering Algorithm. Reproduced from [11:p.132].

Our first objective is to build on the work of Capt Peter Hanlon [3] by extending the single failure isolation that he accomplished to dual failure isolation. The second objective of equal importance is to find and develop optimum test inputs known as dithers. Dithering is required to excite the dynamic responses of the aircraft system so that the measurements of these responses may be analyzed by the MMAE algorithm. Thus, an optimum dither pattern will enhance the detection and isolation performance of the MMAE algorithm.

1.1 Problem Statement

The problem at hand centers on the automatic detection of and compensation for failed control surface authority and flight data sensor degradation. The situation arises as a result of aircraft battle damage or in-flight equipment malfunction. Although the results of such failures will often be catastrophic with high performance aircraft, there are some configurations of failures that would allow the aircraft to continue flying if only a controller designed for that specific situation

were put on-line. A solution to this problem will automatically and correctly identify the failed component(s) and select the proper controller. In this thesis we will apply the Multiple Model Adaptive Estimation algorithm to the problem of failure detection and isolation.

Multiple Model Adaptive Estimation is an algorithm used to estimate states and parameters in a dynamic system [11]. Parameters are quantities that describe the constrained physical characteristics of the system and are usually constant over a short range of time. The dynamic states which do vary appreciably over this short time are estimated using a Kalman filter designed around a mathematical model which holds the parameters as true constants. In the real world, parameters themselves have dynamic properties. However, they vary so slowly that their values are taken to be constant when discussing the behavior of the dynamic states. While Kalman filtering estimates the values of dynamic states assuming known parameter values, MMAE seeks to identify the changes in parameters as well. Numerous techniques have been developed to identify parameters in dynamic systems of all types. Many of these rely on schemes to converge upon a parameter value by seeking out the true value whatever it may be. The computational cost of these methods is high. On the other hand, MMAE presents a refined set of hypothesized parameter possibilities and attempts to match measurements taken from the true system to measurements predicted by one of these possibilities.

1.2 Continuation of AFIT Research

In 1992, Capt Hanlon completed his thesis on the application of MMAE to the LAMBDA URV [3]. He established the validity of previously established MMAE characteristics for single failures [15, 19, 21, 22] and improved the algorithm for quicker and more decisive convergence. A major obstacle for Hanlon was that the LAMBDA model he used did not have a closed loop controller (see Appendix A for a description of the LAMBDA URV). Therefore, the automatic feedback that would normally provide continuous correction inputs did not exist. Since the open-loop system is unstable, this made the failure identification problem much more challenging.

Our work in this thesis, the second application of MMAE to the LAMBDA, differs from Hanlon's in a few significant areas. The first two concern the LAMBDA model. The remaining differences are in research objectives which, of course, aim to build on the previous work.

1.2.1 Updated LAMBDA state space model from Wright Laboratories. Data collected from recent flight tests has led to the development of a more accurate state space representation of the LAMBDA URV [26]. Stability derivatives used in the LAMBDA model for this research are closer representations of its true dynamic behavior than those used in Hanlon's work and are listed in Tables A.1 and A.2. A new state space LAMBDA model [26] representing both longitudinal and lateral dynamics was obtained from Capt S. Sheldon of the Wright Laboratory Flight Controls Division, Flight Controls Techniques Branch. This model is discussed in Subsection 3.2.1.

1.2.2 Closed Loop Controller. A robust closed loop controller has been obtained from Wright Laboratories. This controller is the result of a Quantitative Feedback Theory (QFT) design [26] and is implemented in low order difference equations found in Appendix C. The command inputs are pitch rate, roll rate, and sideslip angle. Prefilters, rate feedback, and cascade compensators are used in each of the control loops. A washout filter is included in the yaw rate feedback loop. A more thorough presentation and diagram are found in Subsection 3.2.2.

1.2.3 Dither Technique. In order for an MMAE algorithm to identify failures in a dynamic system, the modes of that system must be excited. Only when known inputs are allowed to provoke a response is the algorithm able to determine if a degradation in control authority or sensing capability has occurred. This known input is called a dither input.

A primary goal of this research is to find an optimal input dither technique. Optimal is defined in this case to be a balance between system identification and subliminality. The latter quality refers to our desire to keep the magnitude of the dither's dynamic response so low that the pilot is unaware that his aircraft is undergoing an automatic test.

Hanlon found that the best dither had frequency characteristics in consonance with the natural modes of the aircraft. He studied the eigenvalues of the continuous time model to arrive at an effective oscillation frequency [3:p.36]. The present research will build on his work by testing other dither formats. These will include sine waves, doublets, and triangle waves. Concentration will be on defining the optimal magnitude and frequency of sine wave dithers.

1.2.4 Dual Failure Detection and Identification. Previous work with the LAMBDA model concluded that MMAE was effective at isolating single failures. The present research aims to prove

that a hierarchical MMAE structure [14, 15, 16, 17, 21, 22] is effective in identifying dual failures. The machinations of MMAE are the same, the real difference lies in the initial failure hypothesis. With single failure detection, the initial hypothesis is always a fully functional system. The MMAE filter bank consists of filters which hypothesize either a fully functional system or only one failure. The dual failure hierarchy will start the same way. In addition, once a single failure is identified, the system re-initializes with the single failure hypothesis filter as the initial hypothesis. The bank of on-line filters changes to those that hypothesize either only that single failure or two failures, one of which is the first failure that has already been detected. In addition, a fully functional filter is kept on-line in case of a mis-identification of the first declared failure. This allows the algorithm to revert to the condition in which the initial hypothesis is a fully functional system. Such a case is described more fully in Subsection 5.3. Research will demonstrate the MMAE algorithm is convergent to the correct dual failure status and will portray the time required to make the correct failure declaration.

1.3 MMAE Background

In the introduction, the reader was given a general description of what Multiple Model Adaptive Estimation is and how it is applied to our problem. Here we will establish the mathematical basis for a multiple model algorithm. However, the research of this thesis is not limited to the mathematical development. Important terms and concepts are defined presently so that the reader may have a more thorough understanding of why they are altered to suit our research.

1.3.1 Kalman Filter Equations. A thorough understanding of the Kalman filter update and propagation equations is an essential background for the reader. For reference, the equations are restated here. Consider the continuous linear system represented by the linear stochastic difference equation with state vector x and control input vector u .

$$x(t_{i+1}) = \Phi(t_{i+1}, t_i)x(t_i) + B_d(t_i)u(t_i) + G_d(t_i)w_d(t_i) \quad (1.1)$$

and the discrete time measurements modeled by

$$z(t_i) = H(t_i)x(t_i) + v(t_i) \quad (1.2)$$

Sans serif font is used for \mathbf{x} , \mathbf{w}_d , \mathbf{z} , and \mathbf{v} to denote the fact that these are random processes as opposed to real-valued variables, which are expressed in Times Roman font. $\mathbf{w}_d(t_i)$ and $\mathbf{v}(t_i)$ are zero-mean white Gaussian noise processes that are independent of each other and that have covariance kernels given by

$$E\{\mathbf{w}_d(t_i)\mathbf{w}_d^T(t_j)\} = \mathbf{Q}_d(t_i)\delta_{ij} \quad (1.3)$$

$$E\{\mathbf{v}(t_i)\mathbf{v}^T(t_j)\} = \mathbf{R}(t_i)\delta_{ij} \quad (1.4)$$

where δ_{ij} is the Kronecker delta, defined to be one if its subscripts are the same and zero otherwise. $\mathbf{R}(t_i)$ is positive definite for all t_i . $\mathbf{Q}_d(t_i)$ is positive semidefinite and related to \mathbf{Q} and \mathbf{G} of the continuous-time model by [10:p.171]:

$$\mathbf{Q}_d(t_i) = \int_{t_i}^{t_{i+1}} \Phi(t_{i+1}, \tau) \mathbf{G}(\tau) \mathbf{Q}(\tau) \mathbf{G}^T(\tau) \Phi^T(t_{i+1}, \tau) d\tau \quad (1.5)$$

This underlying continuous-time model for which Equation (1.1) is an equivalent discrete-time model is given by

$$\dot{\mathbf{x}}(t) = \mathbf{F}(t)\mathbf{x}(t) + \mathbf{B}(t)\mathbf{u}(t) + \mathbf{G}(t)\mathbf{w}(t) \quad (1.6)$$

where $\mathbf{w}(t)$ is zero-mean white Gaussian noise with covariance kernel:

$$E\{\mathbf{w}(t)\mathbf{w}^T(t+\tau)\} = \mathbf{Q}(t)\delta(\tau) \quad (1.7)$$

where $\delta(\tau)$ is the Dirac delta function. The state transition matrix $\Phi(t_{i+1}, t_i)$ in Equations (1.1) and (1.5) is the solution to

$$\dot{\Phi}(t, t_i) = \mathbf{F}(t)\Phi(t, t_i) \quad (1.8)$$

$$\Phi(t_i, t_i) = \mathbf{I} \quad (1.9)$$

The optimal state estimate at time t_i before incorporating the measurement at that time is denoted by $\hat{\mathbf{x}}(t_i^-)$, while the corresponding estimate after the measurement update is denoted by $\hat{\mathbf{x}}(t_i^+)$. The state estimate and its covariance matrix, $\mathbf{P}(t_i^-)$, have initial conditions $\hat{\mathbf{x}}_0$ and \mathbf{P}_0 at time t_0 and are propagated forward from time t_{i-1} to time t_i by the discrete time *propagation*

equations [10:pp.171-172]:

$$\hat{\mathbf{x}}(t_i^-) = \Phi(t_i, t_{i-1})\hat{\mathbf{x}}(t_{i-1}^+) + \mathbf{B}_d(t_{i-1})\mathbf{u}(t_{i-1}) \quad (1.10)$$

$$\mathbf{P}(t_i^-) = \Phi(t_i, t_{i-1})\mathbf{P}(t_{i-1}^+)\Phi^T(t_i, t_{i-1}) + \mathbf{G}_d(t_{i-1})\mathbf{Q}_d(t_{i-1})\mathbf{G}_d^T(t_{i-1}) \quad (1.11)$$

where \mathbf{B}_d is related to the input transformation matrix \mathbf{B} of the continuous-time model, Equation (1.6), by [10:p.171]:

$$\mathbf{B}_d(t_i) = \int_{t_i}^{t_{i+1}} \Phi(t_{i+1}, \tau)\mathbf{B}(\tau)d\tau \quad (1.12)$$

Finally, because the discrete time model of Equation (1.1) is derived from a continuous-time model [10:p.175]

$$\mathbf{G}_d(t_i) = \mathbf{I} \quad (1.13)$$

The propagated optimal state estimate and its covariance matrix are then updated with information from the current measurement \mathbf{z}_i weighted according to a Kalman filter gain $\mathbf{K}(t_i)$. The *update equations* are [10:p.217]:

$$\mathbf{K}(t_i) = \mathbf{P}(t_i^-)\mathbf{H}^T(t_i) [\mathbf{H}(t_i)\mathbf{P}(t_i^-)\mathbf{H}^T(t_i) + \mathbf{R}(t_i)]^{-1} \quad (1.14)$$

$$\hat{\mathbf{x}}(t_i^+) = \hat{\mathbf{x}}(t_i^-) + \mathbf{K}(t_i) [\mathbf{z}_i - \mathbf{H}(t_i)\hat{\mathbf{x}}(t_i^-)] \quad (1.15)$$

$$\mathbf{P}(t_i^+) = \mathbf{P}(t_i^-) - \mathbf{K}(t_i)\mathbf{H}(t_i)\mathbf{P}(t_i^-) \quad (1.16)$$

1.3.2 Development of the Multiple Model Adaptive Estimation Algorithm. The problem addressed by multiple model filtering model is that of developing a state estimate and parameter estimate, given a time history of measurements and applied control inputs. The system dynamics are modeled by a linear stochastic difference equation as in Equation (1.1) and the available measurements are modeled as in Equation (1.2). A vector, \mathbf{a} , of uncertain parameters in the model may have an impact on any or all of Φ , \mathbf{B}_d , \mathbf{H} , \mathbf{Q}_d , and \mathbf{R} . In this research, \mathbf{a} is a scalar and its discrete point values are associated with the specific failure status of the vehicle.

Our objective is to find a hypothesis conditional probability $p_k(t_i)$ that will give an indication of how well a model based on parameter vector value \mathbf{a}_k matches the measurements produced by a

system based on parameter vector a_j . If $k = j$, the probability should ideally be 1. More generally, we want to know the probability that the uncertain parameter a assumes the value a_k , given a measurement history up to the current time t_i :

$$p_k(t_i) \equiv \text{prob}\{a = a_k | Z(t_i) = Z_i\} \quad (1.17)$$

where $Z(t_i)$ is the history of measurements of the form given by Equation (1.2) up to time t_i :

$$Z(t_i) = \begin{bmatrix} z(t_1) \\ z(t_2) \\ \vdots \\ z(t_i) \end{bmatrix} \quad (1.18)$$

When the measurement random process takes on a realized value, the time history of measurements becomes known implicitly and is represented by

$$Z_i = \begin{bmatrix} z_1 \\ z_2 \\ \vdots \\ z_i \end{bmatrix} \quad (1.19)$$

Since we are going to define an on-line algorithm, we would like the expression for $p_k(t_i)$ to be recursive: the current calculation is based only on the results of the prior sample time and the new inputs at the current time. A development given in [11:pp.129-132] results in

$$p_k(t_i) = \frac{f_{Z(t_i)|a, Z(t_{i-1})}(z_i | a_k, Z_{i-1}) p_k(t_{i-1})}{\sum_{j=1}^K f_{Z(t_i)|a, Z(t_{i-1})}(z_i | a_j, Z_{i-1}) p_j(t_{i-1})} \quad (1.20)$$

where z_i is the actual realization of measurements at time t_i . Equation (1.20) is a recursive expression. We need only to resolve expressions for the probability densities. The probability of realizing measurement z_i at time t_i , given that we already have a history of measurements through

time t_{i-1} , Z_{i-1} , and we are considering only one assumed value of the vector of parameters, a_k :

$$f_{Z(t_i)|a, Z(t_{i-1})}(z_i|a_k, Z_{i-1}) = \frac{1}{(2\pi)^{m/2} |A_k(t_i)|^{1/2}} \exp \{ \cdot \} \quad (1.21)$$

$$\{ \cdot \} = \left\{ -\frac{1}{2} r_k^T(t_i) A_k^{-1}(t_i) r_k(t_i) \right\} \quad (1.22)$$

The residuals, r_k , are the differences between actual measurements and predicted measurements in a Kalman filter based on the assumed parameter value a_k :

$$r_k(t_i) = z(t_i) - H_k(t_i) \hat{x}_k(t_i^-) \quad (1.23)$$

where the superscript '-' on t_i^- denotes the instant in time before the Kalman filter update occurs. The residuals are easily computed from the incoming measurements, $z(t_i)$, and the state estimate which is produced by that Kalman filter. The residual is anticipated to have covariance A_k which is calculated as in Equation (1.24):

$$A_k = H_k P_k^- H_k^T + R_k \quad (1.24)$$

where P_k^- is the steady state value of $P_k(t_i^-)$.

1.3.3 Beta Dominance. The leading coefficient of the probability density function given by Equation (1.21) is a scaling term. Known as the β term, its function is to make the area under the density function equal to unity. Note in particular that the one-half power of the determinant of the residual covariance matrix, $|A_k|^{1/2}$, is a multiplier on the probability. The probability associated with elemental filter k depends on the magnitude of $|A_k|$ for that elemental filter. The problem is that $|A_k|$ tends to be small for filters based on the assumption of a sensor failure because a total sensor failure manifests itself as a row of zeros in the H matrix. Since A_k is given by Equation (1.24), this would result in a smaller than usual residual covariance associated with that failed sensor filter. If the terms given by Equation (1.22) were the same for all elemental filters in the MMAE (i.e., for all k), one would desire all a_k values to be declared equally likely. However, under these conditions, the β term will cause higher p_k values to be associated with those hypotheses that correspond to

lower $|A_k|$ values. Thus, false alarms on sensor failures are more likely to result. This effect is called β dominance.

In fact, it has been proven that false alarms on sensor failures do result when a probability density of the form given by Equation (1.21) is used [3, 12, 14, 15, 16, 17, 21]. Therefore, in our research, β dominance will be avoided from the onset by eliminating altogether the leading coefficient in Equation (1.21), as suggested and evaluated by [3, 12, 14, 15, 16, 17, 21].

1.3.4 Scalar Residual Monitoring. Probabilities generated by the MMAE algorithm give a sense of relative "correctness" associated with each elemental filter. Very often the situation will arise in which two filters may have probabilities that are nearly equal, even though only one is the correct filter. This confounds the identification process and unless more information is obtained, two filters will improperly share recognition as the correct filter.

Each probability is developed from the sum of products of scalar residuals. The term $r_k^T(t_i)A_k^{-1}(t_i)r_k(t_i)$ in Equation (1.22) may be broken down into its scalar components to gain more insight into exactly which scalar measurement does not agree with a filter-predicted measurement. This can be used to enhance isolation of individual *sensor* failures. Consider the following example system resulting from a three element residual:

$$r = \begin{bmatrix} r_1 \\ r_2 \\ r_3 \end{bmatrix} \quad (1.25)$$

An expansion in scalar components yields

$$r_k^T(t_i)A_k^{-1}(t_i)r_k(t_i) = \begin{bmatrix} r_1 & r_2 & r_3 \end{bmatrix} \begin{bmatrix} A_{11}^{-1} & A_{12}^{-1} & A_{13}^{-1} \\ A_{12}^{-1} & A_{22}^{-1} & A_{23}^{-1} \\ A_{13}^{-1} & A_{23}^{-1} & A_{33}^{-1} \end{bmatrix} \begin{bmatrix} r_1 \\ r_2 \\ r_3 \end{bmatrix} \quad (1.26)$$

$$= r_1^2 A_{11}^{-1} + r_2^2 A_{22}^{-1} + r_3^2 A_{33}^{-1} + 2r_1 r_2 A_{12}^{-1} + 2r_1 r_3 A_{13}^{-1} + 2r_2 r_3 A_{23}^{-1} \quad (1.27)$$

Note that a large single element of r has the same effect on probability as moderate magnitudes of all elements of r (see Equations (1.22), (1.21), and (1.20)). Also, recall that $r_k^T(t_i)A_k^{-1}(t_i)r_k(t_i)$ is simply scaled to generate $\{\cdot\}$ in Equation (1.22).

Residual monitoring is a means of capitalizing on the large quick changes in a single scalar element of r_k while the remaining elements exhibit their previous average characteristics. This technique is most effective in identifying sensor failures. A functional sensor's measurement is characterized by a non-zero dynamic mean (due to the useful signal) with sensor noise added. Upon failure, the mean will go to zero or some constant bias. At that time the Kalman filter continues to estimate the sensor state based upon its internal model and prior measurements. This estimate will vary significantly from the current measurement which is based on nothing but noise. Hence, a large step change will be seen in the residual (if the prior measurements were not near zero). The Kalman filter will continue to present state estimates based in part on the internal model which is responding to the applied dither. As time goes on, predicted measurements from the Kalman filter are being subtracted from zero-mean noise to form the scalar residual which, in turn, oscillates according to this dither.

Scalar residual monitoring is useful in the following situation. Assume that there is some ambiguity about whether sensor j has failed. There are two techniques available to resolve this ambiguity. (1) Look at the scalar residual for sensor j in any elemental filter *except* that which assumes a failed sensor j . If that scalar residual is bigger than anticipated, we have corroborating evidence that sensor j has failed. (2) If the scalar residual for sensor j in the filter that does assume sensor j has failed is bigger than anticipated, we have a corroborating vote that sensor j has not failed. Additionally, keep in mind that if the hypothesis of an elemental filter is correct, all scalar residuals in that filter should be white and zero-mean. However, if the hypothesis is wrong, the dither applied to the system will appear in the residuals because of the effect on the true measurements. These residuals are not properly compensated by the estimated measurement, $H_k(t_i)\hat{x}_k(t_i^-)$, in Equation (1.23), as noted before. Such signals are readily detected and useful for hypothesis testing decisions.

Thus, the behavior of a single scalar element of r provides insight beyond the information found in the scalar quantity $r_k^T(t_i)A_k^{-1}(t_i)r_k(t_i)$ alone. If the behavior of scalar residuals were

studied, insight such as this could help to design an algorithm that converges quickly to a correct failure identification while the MMAE algorithm is only able to resolve the failure to two possible failures.

1.3.5 Filter Tuning. There are two opposing forces in the design of the Kalman filters used in the MMAE scheme. The first is that, as engineers, we want to limit the number of failure status possibilities. This means that we want a coarsely discretized parameter space. The other force is our desire to estimate the *degree* to which a failure has occurred. A finely discretized parameter space would serve our purposes here. The link between a modeled point in parameter space and an unmodeled point in parameter space is made by tuning the Kalman filter associated with the modeled point.

We would like to have the MMAE algorithm declare an elevator actuator failure (or, even better, a *partial* failure) even if it is still 10, 50, or even 75 percent effective. On the other hand, we don't want the algorithm to identify a pitch rate sensor failure falsely when the true failure is on an elevator actuator. The balance is struck by carefully tuning each Kalman filter with respect to all others.

Another feature of the MMAE algorithm is the ability to *blend* failure hypotheses by weighting individual filter states according to their respective MMAE filter probabilities. Rather than finely discretizing the parameter space to allow a range of partial failures to be hypothesized in various elemental filters as described above, partial failures may be detected with a coarsely defined parameter space coupled with this blending action. For instance, the MMAE might model only the fully functional aircraft and *fully* failed sensors or actuators, and by placing substantial probability weight on the fully functional aircraft filter and the fully failed elevator filter, it could correctly indicate a certain percentage loss of that actuator. With this approach, both advantages of finding the degree of failure and of employing the least number of filters are realized.

1.4 Hierarchical Modeling Structure

The MMAE is capable of identifying only a limited number of failures. This limit is tied directly to the number of on-line filters. If a failure occurs which is not modeled in an on-line filter, the MMAE algorithm will not identify it, though it may indicate that *some* failure did occur.

We wish to identify the failure status of $K = 14$ individual components in our research. If we sought to identify single failures, only $K + 1$ or 15 filters would be required to remain on-line. That is, we would run one filter for each hypothesized failure plus one filter for the fully functional aircraft hypothesis. Identification of multiple failures requires individual Kalman filters for each combination of possible failures. Our research is limited to dual failures, which would require the generation of $1 + K + K!/((K - 2)!2!)$ or 106 filters representing no failure, single failures, and dual failures.

Even though 106 possibilities exist, we must limit the number of filters kept on-line at any given time. The overriding factor is that 106 Kalman filters running simultaneously will require computational power beyond conceivable capacity. A second factor is that probabilities generated by MMAE are shared between the on-line filters. The more filters there are on-line, the more the probabilities are "watered down". This makes convergence to one filter hypothesis less likely. The solution is to utilize a hierarchical structure of filter banks.

The hierarchical bank structure features one bank of active filters and several banks on standby, ready to be loaded into the processor and brought on-line at any time. See Figure 1.2. The initial on-line bank at Level 0 includes the fully functional filter and all single failure filters. Filters at Level 0 remain active as long as the MMAE-generated probability remains with the fully functional filter. Upon detection of a single failure, the MMAE probability shifts to the single failure filter corresponding to that failure. All other single failure filters are removed and a new bank of double failure filters is loaded and activated. The new bank includes only those dual failure filters that represent the failure already detected plus one more failure. The fully functional filter remains on-line as a back-tracking path in case of a false initial failure identification. The single failure filter for the initial failure also remains on-line and carries the highest probability until a second failure occurs. At this point, the probability shifts to the corresponding dual failure filter. For our purposes of detecting and identifying only two failures, no new bank is loaded to look for a third failure.

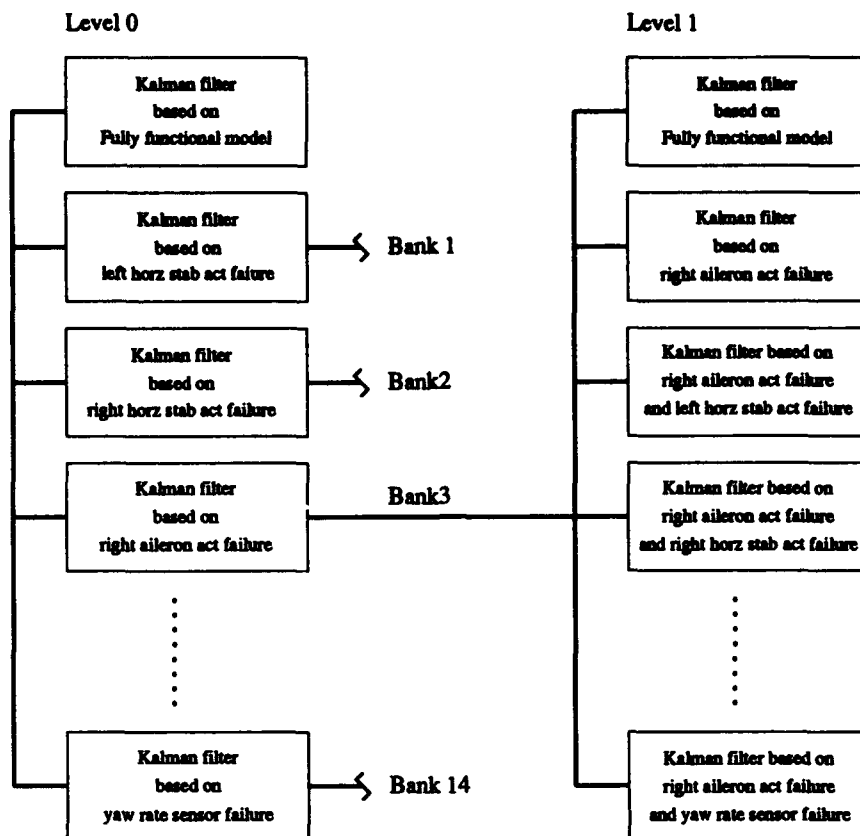


Figure 1.2 Hierarchical Multiple Model Filtering Structure.

1.5 Research Objectives

There are two primary objectives to this research. One is to develop a dithering technique that satisfies specifications of subliminality and of sufficient system excitation for failure identification. The other is to prove that a hierarchical structure is capable of isolating at least two failures correctly, without false alarms, and in minimal time. Before pressing on to these objectives, we must re-verify the results of Hanlon's work [3] in light of the differences discussed in Sections 1.2.1 and 1.2.2 concerning the updated LAMBDA model and the addition of a closed loop controller.

Specific research questions are posed in italics.

1.5.1 Develop Best Dither. As mentioned in Section 1.2.3, the ability of the MMAE algorithm to identify specific failures is directly related to the method used to excite the dynamic modes of the aircraft.

What is the form of the dither input that causes the quickest convergence of the MMAE algorithm to a correct failure hypothesis?

The speed of detection is emphasized here but a correct failure hypothesis must be reached without false alarms or missed alarms, if possible.

What magnitude of lateral and vertical g-forces would be considered to be "subliminal" to the aircrew?

The subliminality of g-forces is a subjective issue. A real answer to this question is found through physiological research to determine a human's sensitivity to g-forces. This thesis does not intend to address such questions as, "What magnitude of g-forces are noticeable?", or "What magnitude of g-forces are annoying?" Therefore, the subliminality question has been addressed strictly through library research [1, 15, 20].

What is the best balance between subliminality and failure identification time?

The magnitude of dither inputs is bounded on the low side by failure identification time constraints and on the high side by subliminality constraints. Hopefully, we will find that the low bound is lower than the high bound. If not, an intelligent trade-off must be made.

What format of dither input will provide the best overall performance in terms of failure protection, aircrew convenience, and comfort?

Three formats are suggested: (1) Automatically induced dither input. This is the ideal format. There is no aircrew awareness or intervention and continuous failure protection is provided. (2) Pilot turn-on and turn-off of automatic dithering system. Continuous protection is not provided, but this may be a valid alternative if we find that the minimum dither required for failure identification is much greater than the maximum subliminal dither. Under such conditions, a pilot would want the option of being able to turn the dither off for certain periods of time. (3) Pilot-induced routine. Engineering studies produce an input signal that is generated in flight by the pilot moving the stick and rudder peddles. The advantage here is that the pilot always has complete control of his aircraft, without the "disturbance" of an externally generated dither. The disadvantage is that continuous failure protection is not provided.

1.5.2 Proof of Hierarchical Concept. In Section 1.4, the hierarchical concept was developed as a strategy of detecting and isolating up to two failures. Our goal is to prove that this concept is valid and that it works under conditions of noisy measurement signals and wind gust turbulence.

Does the MMAE hierarchical-structured failure detection algorithm converge to the correct dual failure hypothesis?

Does the algorithm converge to the correct dual failure hypothesis quickly enough to prevent incorrect failure hypotheses declarations or severely degraded control of the aircraft?

It is desired that the algorithm converge to some dual failure hypothesis under all dual failure conditions. Moreover, it should converge to the correct dual failure hypothesis to be of any value. Our research is intended to show that, regardless of type or order of two failure occurrences, the algorithm is able to identify those failures without false alarms.

Is the algorithm's performance path-dependent for the identification of simultaneous dual failures?

It is true that some specific types of failures are more readily identified than others [3, 15, 19, 21]. In the case of simultaneous or near simultaneous failures, the hierarchical structure will force the algorithm to identify a single failure first, then identify the second failure. We will find out if this logical structure degrades the algorithm's performance in the face of many combinations of dual failures.

1.6 Scope of Research

All research will be done through computer simulation. This is valid since the MMAE algorithm will be implemented in a digital processor once fielded. Also, the updated LAMBDA model will give excellent representation of the aircraft's dynamics in a digital simulation.

The software tool for this research is an amalgamation of Menke's software and Hanlon's software used in their theses, [15] and [3], respectively. Menke's hierarchically structured software will be used to implement the dual failure scheme. Hanlon's MMAE software will implement the MMAE algorithm inside of the hierarchical structure.

The aircraft dynamics will be simulated in a state space format in MATLAB [8] to generate truth model simulation data. This will generate a measurement time history vector and a control input time history vector. These vectors will be sent to the MMAE software system, which is implemented in FORTRAN. The Kalman filters of the MMAE system will have discrete-time, somewhat reduced-order versions of the LAMBDA model embedded within their structure in order to propagate estimates from one sample time to the next.

The aircraft equations of motion are linearized about a nominal flight conditions given in Table 1.1. These conditions represent the LAMBDA in level cruise, a condition where dither inputs would be required to excite the aircraft dynamics for good MMAE performance. Second

Table 1.1 Nominal Flight Conditions.

Parameter	Symbol	Value	Units
Trim Velocity	U_0	169	feet/second
Weight	mg	200	pounds
Center of Gravity	X_{cg}	46.8	inches
Pitch Angle	θ_0	0	degrees
Dynamic Pressure	Q	30.43	pounds/feet ²

order actuator dynamics will be included in the state space model. Sensor dynamics, however, are neglected. That is, the dynamic states of the state space model are used as vehicle perturbation velocity, angular rates, and angle sensor readings directly. The flight control system is implemented in difference equations and provides stable closed loop control of pitch rate, roll rate, and sideslip angle. The flight control system is described fully in Subsection 3.2.2.

Failures for the following set of fourteen aircraft flight control system components will be studied. The six actuators of interest are: right elevator actuator, left elevator actuator, right aileron actuator, left aileron actuator, right rudder actuator, left rudder actuator. In addition, there are eight flight data sensors: velocity sensor, angle of attack sensor, pitch rate sensor, pitch angle sensor, sideslip sensor, roll rate sensor, roll angle sensor, and yaw rate sensor.

1.7 Limitations

Even though our research concerns the in-flight characteristics of a real aircraft, our research will be limited to digital computer simulation only. Since no real human pilot will be flying this

aircraft, we won't be able to test the proposed dithers for pilot comfort. In the case of the LAMBDA remotely piloted vehicle, pilot comfort may be defined as the lack of annoyance due to dithers while operating the joystick for remote control. As stated before, the subliminality limits on g -forces have been determined through library research. We must depend on the findings of others for our definition of "subliminal".

The hierarchical concept is designed to handle multiple failures. Conceivably, a hierarchical structure could handle the one-by-one failure of all modeled components. Our efforts are aimed at proving the legitimacy of the hierarchical concept. To do this, we are employing only the minimum structure required for this proof – two failures. This should be sufficient since the MMAE algorithm is intended to work the same regardless of where in the hierarchical structure it is being employed: an initial condition is hypothesized and all other possible conditions are continuously checked for validity. Research done in this thesis will demonstrate that this is the case.

1.8 Summary of Following Chapters

This introduction chapter provided a statement of the problem, background, and some specific questions which will be the focus of our research. A historical background will be provided in the next chapter. The reader will note that a thorough literature review has been undertaken and that the current research effort falls in a logical succession to those preceding it.

Chapter III gives a specific road map on how our research will be conducted. Software tools will be described. Our implementation of the LAMBDA dynamics along with its controller and wind gust model will be presented as well. A presentation on the MMAE design specifics and Kalman filter designs will give the reader detailed insight into the machinations of our complete system. Finally, Chapter III concludes with an output format description which will be useful in analysis.

Chapter IV will be a detailed presentation of the results of our research. An analysis will be presented in Chapter V. Here, answers to the research questions posed in Section 1.5 will be found. Finally, a conclusion will wrap up the significant findings of our work and present ideas for future research.

II. Literature Review

Through recent years, several research efforts have sought to prove the earlier claims that Multiple Model Adaptive Estimation (MMAE) can be used as an effective algorithm to identify parameters (particularly sensor and/or actuator failure status) in a flight control environment. Mathematical development was followed by computer simulation. Computer simulation has revealed many difficulties in realizing the anticipated potential of MMAE. Though many problems have been solved, more research is required to affirm controlled and stable operation in actual flight. With the LAMBDA Unmanned Research Vehicle (URV), the in-flight data needed as proof of concept may be obtained with minimal cost and essentially no threat to human life. Actual flight testing is on the horizon.

2.1 Early Research

In 1965, D. T. Magill established the mathematical framework for MMAE [6]. He proposed a set of Kalman filters, each based on a different system model based upon a distinct value of a parameter vector. In a Kalman filter, the difference between the measurements from the true plant and the predicted measurements from the estimated states are known as residuals, r :

$$r = z - H\hat{x}^- \quad (2.1)$$

If the model in the Kalman filter is not an accurate portrayal of the actual system, the predicted measurements, $H\hat{x}^-$, will not match the actual measurements, z . The residual gives information about this mismatch. Magill used these residuals to produce a weighted sum of the state estimates that would be theoretically better than a state estimate produced by a single Kalman filter based on a single presumed value for the parameter vector.

An excellent paper on the broader topic of failure detection is by Willsky [25]. In 1976, he gave an overview of many methods used in determining changes in plant parameters. Noteworthy is his anticipation of the growth in computer power that would facilitate implementation of several of the techniques he reviews. He states that accurate and reliable algorithms will be complex and require modern parallel processing computer structures. As the complexity of algorithms increases,

though, the need for redundant hardware may decrease. Thus, Willsky has unveiled the secret for perfecting a failure detection algorithm.

Willsky points out that an improvement in failure detection could be obtained by studying the characteristics of several failure modes. This would limit the possibilities of parameters to estimate and give up-front information about failures one would anticipate. One of the promising techniques he mentions makes use of a bank of filters, each designed for a specific failure. Probabilities indicating a level of truth for each filter's hypothesis are formed from their respective residuals.

The advent of the F-8C Digital Fly By Wire (DFBW) research aircraft presented the opportunity to test computer-driven flight control algorithms on an airborne aircraft. Athans *et. al.* [1] attempted to implement Multiple Model Adaptive Control (MMAC) on the F-8C for the purpose of estimating flight conditions. The structure of an MMAC algorithm is similar to that of Figure 1.1, except that each elemental filter is cascaded with a deterministic optimal controller that accepts \hat{x}_k as input and produces u_k as an output, and then u_{MMAC} is generated as a probability-weighted average of the u_k 's. The authors were, in effect, estimating dynamic pressure through an MMAC algorithm that did not make use of air data sensors which normally provide dynamic pressure information. Thus, this MMAC adapted to a different uncertain parameter than the failure status parameters of the current research. A bank of Linear Quadratic Gaussian (LQG) compensators was set up to cover the range of possible flight conditions for the F-8C. Each compensator had coupled to it a filter that used rate and acceleration information to develop a residual and a state estimate. Each LQG compensator produced a control input based on the state vector presented by its respective filter. All residuals were compiled in a probability evaluator, which in turn assigned a probability weighting to each control input from all LQG compensators. Finally, a composite control input was computed from the weighted sum of all control inputs and sent to the aircraft controls. An important finding from this work is the negative effect of β dominance (see Subsection 1.3.3) which is treated in AFIT theses to be discussed.

Dunn and Montgomery [2] also made use of the F-8C program, but the results of their efforts were limited to computer simulation in anticipation of better results before attempting in-flight tests. Their work is related to the current study of failure detection in that their system attempted to estimate aerodynamic stability derivatives. The first point of interest to us deals with the dither

signals Dunn and Montgomery used to stimulate the dynamic modes of the aircraft. They found that identifiability of parameters is enhanced when the amplitude of the test control input, or dither, is increased. The dither must have a large enough signal to noise ratio (SNR) so that its effect is distinct from the disturbances caused by the atmosphere. On the other hand, one would like this automatic test signal to be subliminal to the pilot. Hence, a balance between identifiability and subliminally must be struck. Secondly, we are interested to learn that the estimation process may go unstable if the dither frequency is too low. Also, if the dither frequency is much above those of the aircraft's dynamics, the sensor data will provide no useful information for parameter estimation.

2.2 MMAE at the Air Force Institute of Technology

Thesis work at AFIT has spanned a few years, and the current research will build directly upon those efforts. Donald Pogoda [13, 19] and Richard Stevens [14, 21] both applied Multiple Model Adaptive Control algorithms to the STOL (short takeoff/landing) F-15. Stevens installed a Command Generator Tracker / Proportional plus Integral / Kalman Filter (CGT/PI/KF) controller in each elemental controller to form a bank of controllers that would identify actuator and sensor failures on the STOL F-15 and reconfigured the commanded control of the aircraft accordingly. He contributed knowledge on the tuning of the Kalman filters in this structure. Each filter representing a certain failure must have a unique domain in parameter space. This means that the characteristics of residuals for a given filter must be unique to that failure, yet be responsive to partial failures of that type as well. Furthermore, he identified the effect of β dominance in his results, showing that the leading coefficient of the probability density function given by Equation (1.21) caused false alarms biased toward sensor failures. This is due to the scaling of probabilities by the inverse of the determinant of the covariance of residuals. Each residual has a different covariance, especially those associated with failures of sensors, which tend to be small, as explained in Section 1.3.3. The inverse of this covariance determinant is a multiplier on the probability. So, one can see how sensor failures are pre-disposed to having a failure probability that is higher than fully functional aircraft or failed actuator conditions.

Later on, Menke [15] and Stratton [22] developed MMAE-based controllers for the VISTA F-16. In contrast with an MMAC, an MMAE-based controller uses the structure of Figure 1.1

directly, and then the \hat{x} produced by the MMAE in that figure is passed to a *single* controller to produce the control u . This single controller may be informed of the best estimate of the uncertain parameter, \hat{a} , and adapt to that estimate, or it may simply be a single pre-existing control law (as for Menke's and Stratton's research) or an enhanced-robustness controller designed specifically to provide good control despite parameter variations. Menke [17] again demonstrated the importance of Kalman filter tuning for each elemental filter representing one type of sensor or actuator failure. The state estimates from each filter are weighted by a probability computation which utilizes residuals from each elemental filter to develop a composite state *estimate* vector. The MMAE composite state estimate vector is sent to a single controller, the VISTA F-16 flight control system, which produces a single control input vector.

The importance of Menke's work to the current work is that he studied a hierarchical structure of failure detection which was able to detect up to two sequential or simultaneous faults. Furthermore, he performed an analysis of dither inputs. The qualities of these input signals are directly related to the failure identification ability of the MMAE algorithm [17].

Finally, the first application of MMAE to the LAMBDA URV was made by Hanlon [3]. He studied single actuator and sensor failures and established that the algorithm does in fact converge to a single failure hypothesis. Again, he noted the effect of β dominance, as did his predecessors. Also, dither inputs were found to be most effective when they carry the natural frequencies of the aircraft dynamics. Finally, Hanlon experimented with changes to the $-\frac{1}{2}$ coefficient of Equation (1.22).

The focus of the current work is, of course, to build on the findings of Hanlon and Menke by setting up a hierarchical structure of failure detection for the LAMBDA URV and to provide further refinement of the dither techniques required for effective failure identification.

2.3 Chapter Summary

A review of important literature on the topic of Multiple Model Adaptive Estimation has been accomplished. The basis for MMAE was established in 1965 by D. T. Magill when he proposed that estimated states from several Kalman filters could be combined to form a better estimate of the true states than state estimates from only one Kalman filter, when faced with parameter

uncertainty in the model upon which the filters are based. The F-8C digital fly-by-wire aircraft presented the opportunity to test MMAE on an airborne aircraft. As a result, several important conclusions were published, including the effect of β dominance.

Research at the Air Force Institute of Technology in recent years has established several concepts that improve the performance of the MMAE algorithm. Extensions to Multiple Model Adaptive Control have demonstrated that this algorithm can be used effectively in flight control systems. Finally, a great deal of work has been accomplished to identify characteristics of MMAE performance when minor modifications to the algorithm are installed in an attempt to enhance failure identification.

III. Methodology

In this chapter, we establish the specific details of how our investigation is to be carried out. The research is confined to a study using software tools to simulate the aerodynamic states, flight control system states, and flight sensor measurements of the LAMBDA URV during flight through moderate wind conditions. The flight information generated by the software simulation will be referred to as the *truth data*. This truth data is used by the MMAE algorithm implemented in FORTRAN, which develops failure detection and identification decisions based upon the performance of its bank of Kalman filters.

The design of the MMAE algorithm is well established and the code for this thesis will be a modified version of Capt Hanlon's FORTRAN MMAE program [3] which was generated from Menke's code [15]. One important change to Hanlon's code will be the addition of a hierarchical structure, similar to that of Stevens [21] and Menke [15], to detect dual failures rather than just single failures. Since the aircraft truth model is augmented with a wind simulation model, the Kalman filters will have to be tuned to account for this injection of uncertainty. The standard procedure for tuning Kalman filters in an MMAE system is to compare residual tracking against the standard deviation statistic computed by the filter for that residual. An alternate procedure for Kalman filter tuning is investigated in this thesis.

The test procedure will feature various input dithers for enhancing failure identification, which will be applied to the truth model simulation to generate truth data. The truth data will then serve as the input to the MMAE algorithm. Results of the MMAE will be displayed in graphical format as well as tabular data formatted for easy analysis. The goal is to match changes in dither characteristics to variations in MMAE performance, with the overall objective being to demonstrate as many correct identifications with as little delay and as few false alarms and/or ambiguous declarations as possible.

3.1 Software Tools

All tools used in this study will be either FORTRAN programs [23] or MATLAB programs [8]. MATLAB is favored where manipulation of matrices and other standard mathematical functions are prevalent. Furthermore, a distinct advantage is gained by using the graphical model building

capabilities found in the Simulink tool [9] of MATLAB. FORTRAN is employed for three reasons. First, the MMAE code currently exists in FORTRAN. Second, an MMAE algorithm written in FORTRAN is easily and efficiently transferred to the machine language used by LAMBDA's on-board computer. Finally, the MMAE algorithm will be run literally thousands of times, and efficiently coded FORTRAN will generate object code capable of much faster execution than MATLAB m-files which are re-compiled each time they are run. Therefore, a great deal of time will be saved in awaiting test results by using compiled FORTRAN code.

3.2 LAMBDA Model

LAMBDA is an unmanned research vehicle (URV). It resembles a large radio controlled airplane with a wingspan of 14 feet. It is equipped with the flight data sensors which we are studying as potentially failed components. The primary flight control surfaces include left and right elevators, left and right ailerons, and left and right rudders. These, too, are to be viewed as potentially failed components. In addition, four flap surfaces and a throttle control are featured on the real LAMBDA but not included in our model. The throttle is not included because, though it is a primary means of flight control, it is not part of the flight control system. Rather, the LAMBDA typically is flown at full throttle. Therefore a failed condition is engine cutoff which is immediately followed by emergency landing procedures, conditions obvious to any pilot without the help of an MMAE algorithm. The flaps are not included in the model of our study because they are not primary flight control surfaces. Failure of a flap would not cause a reconfiguration of the flight control system, but its obvious effects would cause a pilot to reverse his conscious command to deploy them. In summation, we will be studying the effects of the failure of each of eight flight data sensors and six primary flight control actuators.

The LAMBDA is a stable system in the short period, phugoid, roll subsidence, and Dutch roll modes. Its spiral divergence mode is unstable with a long time constant. So, although its modes are faster, this aircraft resembles a typical manned aircraft in performance.

Previous MMAE work using the LAMBDA assumed no flight control system [3]. Command inputs went directly to the actuators without being modified by a flight control system. Capt S. Rasmussen, WL/FIG, has designed a Quantitative Feedback Theory (QFT) controller which will be

implemented in our truth model [26]. The addition of a feedback controller should aid the MMAE algorithm in correctly identifying failures because the additional commands to the actuators should provide natural dithering while rejecting the effects of wind gusts. Moreover, the difficulties in the design of the MMAE elemental filters in the previous research [3] due to diverse eigenvalues of the open loop system (particularly the unstable mode's eigenvalue) should be remedied by the feedback control system.

3.2.1 Truth Model. The aerodynamic portion of the LAMBDA is represented by aerodynamic dimensional derivatives which were generated from test data of actual LAMBDA flights. This information was obtained from Capt S. Sheldon, WL/FIGS [26] and numerical values and definitions may be found in Appendix A. Dimensional derivatives are determined by experiment and they describe the change in one aircraft state variable due to a change in some other aircraft state variable. The primed symbols distinguish dimensional derivatives from non-dimensional derivatives which are related to the former by a factor indicating the nominal flight condition. Aircraft state variables are perturbations from nominal conditions and, since all nominal angles and rates except velocity are zero, the state variables are defined as follows: u - forward velocity perturbation, α - angle of attack, q - pitch rate, θ - pitch angle, β - sideslip angle, p - roll rate, ϕ - roll angle, r - yaw rate. The control variables are: δ_{e_l} - left elevator angle, δ_{e_r} - right elevator angle, δ_{a_l} - left aileron angle, δ_{a_r} - right aileron angle, δ_{r_l} - left rudder angle, and δ_{r_r} - right rudder angle.

The eight-state model of the form $\dot{\mathbf{x}} = \mathbf{F}\mathbf{x} + \mathbf{B}\mathbf{u}$ in terms of the dimensional derivatives is shown in Equation (3.1). The values assumed by the dimensional derivatives depend on the equilibrium flight condition about which the model is linearized. We will work with the flight conditions in Table 1.1, which is repeated below as Table 3.1. These particular conditions are chosen because they represent the aircraft in level cruise, the condition of predominant concern for

this vehicle.

$$\begin{bmatrix} \dot{u} \\ \dot{\alpha} \\ \dot{q} \\ \dot{\theta} \\ \dot{\beta} \\ \dot{p} \\ \dot{\phi} \\ \dot{r} \end{bmatrix} = \begin{bmatrix} X'_u & X'_\alpha & X'_q & X'_\theta & 0 & 0 & 0 & 0 \\ Z'_u & Z'_\alpha & Z'_q & Z'_\theta & 0 & 0 & 0 & 0 \\ M'_u & M'_\alpha & M'_q & M'_\theta & 0 & 0 & 0 & 0 \\ 0 & 0 & 1 & 0 & 0 & 0 & 0 & 0 \\ 0 & 0 & 0 & 0 & Y'_\beta & Y'_p & Y'_\phi & Y'_r \\ 0 & 0 & 0 & 0 & L'_\beta & L'_p & 0 & L'_r \\ 0 & 0 & 0 & 0 & 0 & 1 & 0 & 0 \\ 0 & 0 & 0 & 0 & N'_\beta & N'_p & 0 & N'_r \end{bmatrix} \begin{bmatrix} u \\ \alpha \\ q \\ \theta \\ \beta \\ p \\ \phi \\ r \end{bmatrix} \quad (3.1)$$

$$+ \begin{bmatrix} X'_{\delta_{a,l}} & X'_{\delta_{a,r}} & X'_{\delta_{e,l}} & X'_{\delta_{e,r}} & 0 & 0 \\ Z'_{\delta_{a,l}} & Z'_{\delta_{a,r}} & Z'_{\delta_{e,l}} & Z'_{\delta_{e,r}} & 0 & 0 \\ M'_{\delta_{a,l}} & M'_{\delta_{a,r}} & M'_{\delta_{e,l}} & M'_{\delta_{e,r}} & 0 & 0 \\ 0 & 0 & 0 & 0 & 0 & 0 \\ Y'_{\delta_{a,l}} & Y'_{\delta_{a,r}} & Y'_{\delta_{e,l}} & Y'_{\delta_{e,r}} & Y'_{\delta_{r,l}} & Y'_{\delta_{r,r}} \\ L'_{\delta_{a,l}} & L'_{\delta_{a,r}} & L'_{\delta_{e,l}} & L'_{\delta_{e,r}} & L'_{\delta_{r,l}} & L'_{\delta_{r,r}} \\ 0 & 0 & 0 & 0 & 0 & 0 \\ N'_{\delta_{a,l}} & N'_{\delta_{a,r}} & N'_{\delta_{e,l}} & N'_{\delta_{e,r}} & N'_{\delta_{r,l}} & N'_{\delta_{r,r}} \end{bmatrix} \begin{bmatrix} \delta_{a,l} \\ \delta_{a,r} \\ \delta_{e,l} \\ \delta_{e,r} \\ \delta_{r,l} \\ \delta_{r,r} \end{bmatrix}$$

Note that the input matrix of Equation (3.1) has left and right inputs for each type of control surface. This will allow us to apply independent dither inputs to a control surface on one side of the vehicle in order to distinguish its effects from the surface on the other side. Cross coupling terms also help distinguish right from left elevator and right from left aileron. These terms appear in the input transformation matrix of Equation (3.1) as the Y' , L' , and N' terms in columns 1 and 2 for

Table 3.1 Nominal Flight Conditions.

Parameter	Symbol	Value	Units
Trim Velocity	U_0	169	feet/second
Weight	mg	200	pounds
Center of Gravity	X_{cg}	46.8	inches
Pitch Angle	θ_0	0	degrees
Dynamic Pressure	Q	30.43	pounds/feet ²

the elevator and as X' , Z' , and M' terms in columns 3 and 4 for the ailerons. No cross coupling into the longitudinal channel exists for the rudders. The lack of such terms reasonably represents the behavior of the real LAMBDA since the center of the rudder surfaces lies near the horizontal reference line drawn from the aircraft center of mass. Therefore, negligible pitching moments due to rudder drag are induced with rudder deflection.

The inputs into Equation (3.1) are control surface angles. The control surfaces are driven by actuators which have their own dynamic characteristics. The transfer functions relating actuator command to actuator position are shown in Equations (3.2), (3.3), and (3.4) [26]:

Elevator Actuator:

$$\frac{\delta_e(s)}{\delta_{e_c}(s)} = \frac{136.20}{s^2 + 21.628s + 176.63} \quad (3.2)$$

Aileron Actuator:

$$\frac{\delta_a(s)}{\delta_{a_c}(s)} = \frac{216.84}{s^2 + 22.147s + 224.42} \quad (3.3)$$

Rudder Actuator:

$$\frac{\delta_r(s)}{\delta_{r_c}(s)} = \frac{39060}{s + 4.4372} \quad (3.4)$$

See Appendix B for Bode plots of aircraft response and Subsection 3.3.2.1 for Bode plots of actuator responses. The real control surfaces on LAMBDA are limited in their range of movement according to the limits in Table 3.2.

Table 3.2 Range Limits on Control Surface Movement.

Control Surface	Limits [degrees]
elevator	$\pm 15^\circ$
aileron	$\pm 15^\circ$
rudder	$\pm 20^\circ$

In addition to the aircraft equations of motion, it will be necessary to study vertical and lateral g -forces experienced by a would-be pilot. The following equations are implemented in the state space form of the truth model:

Lateral Acceleration:

$$A_y = U_0\dot{\beta} - g\phi + U_0r + l_z\dot{r} - l_z\dot{p} \quad (3.5)$$

Vertical Acceleration:

$$A_z = U_0 \dot{\alpha} - U_0 q + l_z \dot{q} \quad (3.6)$$

U_0 is the trim velocity from Table 3.1. The values for l_z and l_x represent the coordinate position of a pilot relative to the center of gravity of the aircraft. Since LAMBDA has no pilot on-board, l_z and l_x were chosen to correspond to the location of the on-board accelerometer [24:p. 2.9] and have the values given by

$$\begin{aligned} l_z &= 0.3279 \text{ ft} \\ l_x &= 0.2903 \text{ ft} \end{aligned} \quad (3.7)$$

Thus, in the event that data from this thesis is correlated to in-flight tests, no coordinate conversion would be necessary to compare g -forces.

The LAMBDA has eight flight data sensors which correspond to the eight state variables of Equation (3.1). The outputs of the sensors are noisy representations of the state variables. The model for each sensor in our truth model is simply the state variable plus zero-mean white Gaussian noise of variance (or mean squared value) $R_{i,i}$ which is the corresponding i -th diagonal element of the 8-by-8 measurement noise covariance matrix, R :

$$R = \begin{bmatrix} R_\alpha & 0 & 0 & 0 & 0 & 0 & 0 & 0 \\ 0 & R_\alpha & 0 & 0 & 0 & 0 & 0 & 0 \\ 0 & 0 & R_q & 0 & 0 & 0 & 0 & 0 \\ 0 & 0 & 0 & R_\theta & 0 & 0 & 0 & 0 \\ 0 & 0 & 0 & 0 & R_\phi & 0 & 0 & 0 \\ 0 & 0 & 0 & 0 & 0 & R_p & 0 & 0 \\ 0 & 0 & 0 & 0 & 0 & 0 & R_\psi & 0 \\ 0 & 0 & 0 & 0 & 0 & 0 & 0 & R_r \end{bmatrix} \quad (3.8)$$

The values used in Equation (3.8) are those used by Capt Hanlon [3] and are given in Table 3.3. They are the result of analysis of in-flight measurement data.

Table 3.3 Sensor Noise Variances.

Sensor	Symbol	Variance	Units
Forward Velocity	R_u	1.6×10^{-2}	(feet/second) ²
Angle of Attack	R_α	1.15×10^{-5}	radians ²
Pitch Rate	R_q	1.194×10^{-3}	(radians/second) ²
Pitch Angle	R_θ	6.98×10^{-6}	radians ²
Sideslip Angle	R_β	8.7264×10^{-5}	radians ²
Roll Rate	R_r	1.122×10^{-3}	(radians/second) ²
Roll Angle	R_ϕ	1.45×10^{-5}	radians ²
Yaw Rate	R_r	9.801×10^{-3}	(radians/second) ²

3.2.2 Flight Control System Design. A flight control system (FCS) based on a Quantitative Feedback Theory (QFT) design by Capt S. Rasmussen [26] augments the flight characteristics of our aircraft truth model. The FCS enables the pilot to provide pitch rate commands, roll rate commands, and sideslip angle commands. In order to command left and right control surfaces, the QFT FCS was duplicated in left and right channels for each control axis, thereby enabling independent control of individual surfaces. This configuration is realizable since the controller is implemented in the form of difference equations in the on-board computer and each control surface receives its commands from an individual output port of the computer. The controller makes use of feedback from the aircraft's pitch rate, roll rate, yaw rate, and sideslip angle sensors, which provide noisy measurements of the corresponding aircraft states. Our truth model incorporates the appropriate noise into the sensor measurements. Therefore, the QFT FCS will receive the same noisy measurements that are fed to our MMAE algorithm. Eventually, it would be desirable to replace the noisy measurements with MMAE-provided estimates of these aircraft states.

A block diagram of the QFT FCS is shown in Figure 3.1. The blocks designated by F11_L, F22_L, etc., are the prefilter blocks of the QFT design. Likewise, the G11_L, G22_L, etc., blocks denote feed-forward compensators. Difference equations based on a sampling period of $T = 0.02$ second are provided to implement the prefilters, compensators, and washout filter (see Appendix C). It is important to note that the specific controller design used in this thesis failed its flight test on the LAMBDA in August 1993. Oscillations were induced in the longitudinal channel due to a structural bending mode which resided within the controller's response envelope. The design was successfully corrected but, due to the amount of work that would have to be re-accomplished, the

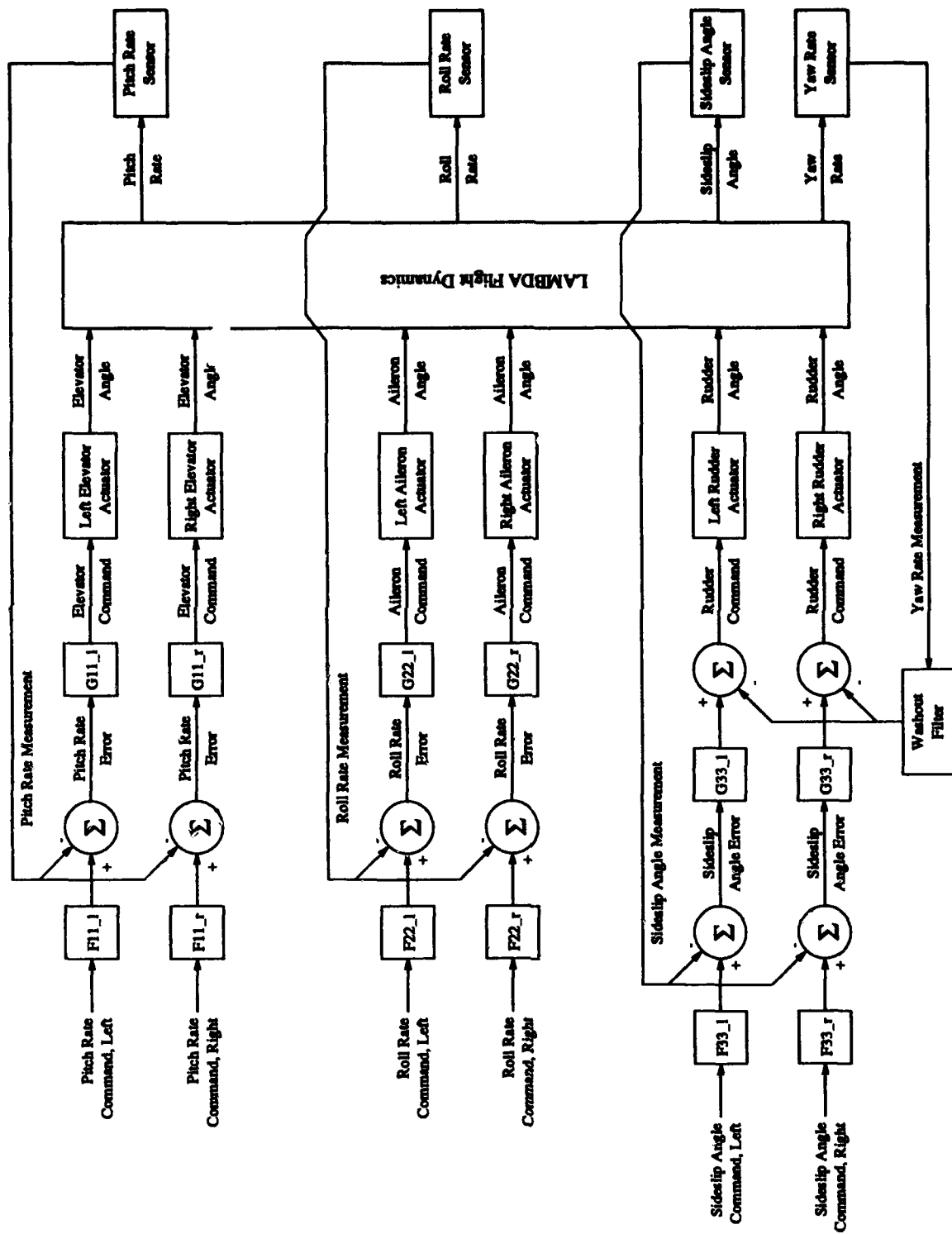


Figure 3.1 QFT Flight Control System Augmenting the LAMBDA Aircraft Model.

previous design is used consistently throughout this thesis. The structural modes of the LAMBDA are not modeled; therefore, controller performance in our truth model should not be unlike the performance of the corrected controller.

At the bottom of Figure 3.1, the reader will see a washout filter block through which yaw rate feedback must pass before being summed with sideslip angle error. The function of this high pass filter is to block the low frequency yaw rates commanded by the pilot in his/her effort to change the sideslip angle. However, high frequency disturbances are passed and subsequently nulled by the controller. In Subsection 5.1, the impact of a failed yaw rate sensor which disables the washout filter will be discussed.

3.2.3 Dryden Wind Gust Model. Our purpose in this thesis is to show that the MMAE algorithm is capable of performing well when the LAMBDA is in atmospheric flight. Wind disturbances are an unavoidable reality in this environment, so we would like to simulate wind in the computer model. The choice of wind gust model is the Dryden wind gust model for two reasons. First, it is the traditional model used in other MMAE theses [3, 19, 21]; and second, it is one of two models specified by MIL-STD-1797 [18]. There are excellent developments of the Dryden wind gust model in Capt Martin's thesis [7] and Capt Pogoda's thesis [19]. The essential aspects of the Dryden model will be explained here.

Wind disturbance of an aircraft is a random process. In the following development, inputs of white Gaussian noise, Equation (3.9), will be "shaped" in the wind gust model then transformed into disturbance terms to be added to the state equations of the aircraft state space model. The input white noises have Gaussian distribution with zero mean and unit strength. This is represented by the continuous time Q matrix in Equation (3.10), where $E\{w(t)w^T(t+\tau)\} = Q(t)\delta(\tau)$:

$$w = \begin{bmatrix} w_u \\ w_w \\ w_p \\ w_r \end{bmatrix} \quad (3.9)$$

$$\mathbf{Q} = \begin{bmatrix} 1 & 0 & 0 & 0 \\ 0 & 1 & 0 & 0 \\ 0 & 0 & 1 & 0 \\ 0 & 0 & 0 & 1 \end{bmatrix} \quad (3.10)$$

The shaping is accomplished by passing the white noises through filters having random process outputs which fit the power spectral densities of the Dryden model specified by MIL-STD-1797, as given in Equations (3.11) through (3.16). Φ represents a power spectral density function. Subscripts correspond to the aircraft state variable subjected to that disturbance, e.g., Φ_{u_g} is the power spectral density of wind gust disturbance associated with forward velocity perturbations. Subscript g denotes a wind gust model power spectral density rather than the PSD of the aircraft state itself.

$$\Phi_{u_g}(\omega) = \sigma_u^2 \frac{2V_T}{L_u} \frac{1}{\omega^2 + \frac{V_T^2}{L_u^2}} \quad (3.11)$$

$$\Phi_{\alpha_g}(\omega) = \sigma_\alpha^2 \frac{3}{2L_w V_T} \frac{\omega^2 + \frac{V_T^2}{12L_u^2}}{\left(\omega^2 + \frac{V_T^2}{4L_u^2}\right)^2} \quad (3.12)$$

$$\Phi_{\dot{\alpha}_g}(\omega) = \frac{\pi^2 V_T^2}{16b^2} \frac{\omega^2}{\omega^2 + \frac{\pi^2 V_T^2}{16b^2}} \Phi_{\alpha_g}(\omega) \quad (3.13)$$

$$\Phi_{p_g}(\omega) = \sigma_p^2 V_T \left(\frac{\pi^{10}}{128,000b^7 L_u^2} \right)^{\frac{1}{2}} \frac{1}{\omega^2 + \frac{\pi^2 V_T^2}{16b^2}} \quad (3.14)$$

$$\Phi_{\beta_g}(\omega) = \sigma_\beta^2 \frac{3}{2L_w V_T} \frac{\omega^2 + \frac{V_T^2}{12L_u^2}}{\left(\omega^2 + \frac{V_T^2}{4L_u^2}\right)^2} \quad (3.15)$$

$$\Phi_{r_g}(\omega) = \frac{\pi^2 V_T^2}{9b^2} \frac{\omega^2}{\omega^2 + \frac{\pi^2 V_T^2}{9b^2}} \Phi_{\beta_g}(\omega) \quad (3.16)$$

V_T is the nominal aircraft velocity and b is the aircraft wingspan. The variables $L_u = 505.2$, $L_w = 252.6$, and $L_w = 50$ are turbulence scale lengths in feet/second and are determined from Figure 266 of MIL-STD-1797 [18] for an altitude of 100 feet above the ground. $\sigma_u = 0.1u_{20} = 5.063$ where $u_{20} = 50.63$ feet/second is the wind speed measured 20 feet above the ground [18:p.653]. $\sigma_\alpha = 8.688$ and $\sigma_\beta = 8.688$ are related to $\sigma_u = 5.063$ as shown in Figure 267 of [18].

The transfer functions of the shaping filters required to produce outputs with the power spectral densities of Equations (3.11) through (3.16) are given respectively by:

$$G_{u_g}(s) = \frac{u_g(s)}{w_u(s)} = \sigma_u \sqrt{\frac{2V_T}{L_u}} \frac{1}{s + \frac{V_T}{L_u}} \quad (3.17)$$

$$G_{\alpha_g}(s) = \frac{\alpha_g(s)}{w_w(s)} = \sigma_w \sqrt{\frac{3}{2L_w V_T}} \frac{s + \frac{\sqrt{3}V_T}{6L_w}}{\left(s + \frac{V_T}{L_w}\right)^2} \quad (3.18)$$

$$G_{q_g}(s) = \frac{q_g(s)}{w_w(s)} = \frac{\pi V_T}{4b} \frac{s}{s + \frac{\pi V_T}{4b}} G_{\alpha_g}(s) \quad (3.19)$$

$$G_{p_g}(s) = \frac{p_g(s)}{w_p(s)} = \sigma_w \left(\frac{\pi^{10} V_T^3}{128,000 b^7 L_w^2} \right)^{1/6} \frac{1}{s + \frac{\pi V_T}{4b}} \quad (3.20)$$

$$G_{\beta_g}(s) = \frac{\beta_g(s)}{w_v(s)} = \sigma_v \sqrt{\frac{3}{2L_v V_T}} \frac{s + \frac{\sqrt{3}V_T}{6L_v}}{\left(s + \frac{V_T}{L_v}\right)^2} \quad (3.21)$$

$$G_{r_g}(s) = \frac{r_g(s)}{w_v(s)} = \frac{-\pi V_T}{3b} \frac{s}{s + \frac{\pi V_T}{3b}} G_{\beta_g}(s) \quad (3.22)$$

The transfer functions are implemented in the state space form $\dot{\mathbf{x}} = \mathbf{F}\mathbf{x} + \mathbf{G}\mathbf{w}$, which incorporates the four independent white noise inputs (w_u , w_w , w_p , and w_v) and eight wind gust states (u_g , α'_g , α_g , q_g , p_g , β'_g , β_g , and r_g). The subscript g denotes that these are perturbations to the respective aircraft states due to wind gusting. The prime on α'_g and β'_g simply means that these are internal states to the second-order α_g and β_g processes, respectively.

$$\begin{bmatrix} \dot{u}_g \\ \dot{\alpha}'_g \\ \dot{\alpha}_g \\ \dot{q}_g \\ \dot{p}_g \\ \dot{\beta}'_g \\ \dot{\beta}_g \\ \dot{r}_g \end{bmatrix} = \begin{bmatrix} \frac{-V_T}{L_u} & 0 & 0 & 0 & \dots \\ 0 & \frac{-V_T}{2L_w} & 0 & 0 & \dots \\ 0 & \sigma_w(1 - \sqrt{3})\sqrt{\frac{V_T}{8L_w^2}} & \frac{V_T}{2L_w} & 0 & \dots \\ 0 & \frac{\pi V_T}{4b}\sigma_w(1 - \sqrt{3})\sqrt{\frac{V_T}{8L_w^2}} & \frac{\pi V_T}{4b}\frac{V_T}{2L_w} & \frac{-\pi V_T}{4b} & \dots \\ 0 & 0 & 0 & 0 & \dots \\ 0 & 0 & 0 & 0 & \dots \\ 0 & 0 & 0 & 0 & \dots \\ 0 & 0 & 0 & 0 & \dots \end{bmatrix}$$

$$\begin{aligned}
& \begin{bmatrix} \dots & 0 & 0 & 0 & 0 \\ \dots & 0 & 0 & 0 & 0 \\ \dots & 0 & 0 & 0 & 0 \\ \dots & 0 & 0 & 0 & 0 \\ \dots & \frac{\pi V_T}{4b} & 0 & 0 & 0 \\ \dots & 0 & \frac{-V_T}{2L_v} & 0 & 0 \\ \dots & 0 & \sigma_v(1-\sqrt{3})\sqrt{\frac{V_T}{8L_v^3}} & -\frac{V_T}{2L_v} & 0 \\ \dots & 0 & -\frac{\pi V_T}{3b}\sigma_v(1-\sqrt{3})\sqrt{\frac{V_T}{8L_v^3}} & \frac{\pi V_T}{3b}\frac{V_T}{2L_v} & -\frac{\pi V_T}{3b} \end{bmatrix} \begin{bmatrix} u_g \\ \alpha'_g \\ \alpha_g \\ q_g \\ p_g \\ \beta'_g \\ \beta_g \\ r_g \end{bmatrix} + \\
& \begin{bmatrix} \sigma_w\sqrt{\frac{3V_T}{L_v}} & 0 & 0 & 0 \\ 0 & 1 & 0 & 0 \\ 0 & \sigma_w\sqrt{\frac{3}{2L_vV_T}} & 0 & 0 \\ 0 & 0 & 0 & 0 \\ 0 & 0 & \sigma_w\left(\frac{\pi^{10}V_T^2}{128,000b^7L_v^2}\right)^{1/6} & 0 \\ 0 & 0 & 0 & 1 \\ 0 & 0 & 0 & \sigma_w\sqrt{\frac{3}{2L_vV_T}} \\ 0 & 0 & 0 & 0 \end{bmatrix} \begin{bmatrix} w_u \\ w_w \\ w_p \\ w_r \end{bmatrix} \quad (3.23)
\end{aligned}$$

Finally, a transformation matrix, T_{wind} as given in Equation (3.24), adds combinations of the unprimed wind states to the aircraft dynamic states as shown in Equation (3.25). Note that the symbols in T_{wind} share the identical values to the corresponding symbols in Equation (3.1).

$$T_{wind} = \begin{bmatrix} -X'_u & 0 & -X'_\alpha & -X'_q & 0 & 0 & 0 & 0 \\ -Z'_u & 0 & -Z'_\alpha & -Z'_q & 0 & 0 & 0 & 0 \\ -M'_u & 0 & -M'_\alpha & -M'_q & 0 & 0 & 0 & 0 \\ 0 & 0 & 0 & 0 & 0 & 0 & 0 & 0 \\ 0 & 0 & 0 & 0 & -Y'_p & 0 & -Y'_\rho & -Y'_r \\ 0 & 0 & 0 & 0 & -L'_p & 0 & -L'_\rho & -L'_r \\ 0 & 0 & 0 & 0 & 0 & 0 & 0 & 0 \\ 0 & 0 & 0 & 0 & -N'_p & 0 & -N'_\rho & -N'_r \end{bmatrix} \quad (3.24)$$

$$\dot{x}_{acft} = Fx_{acft} + Bu + T_{wind}x_{wind} \quad (3.25)$$

The added realism of a wind gust model will cause the QFT flight control system (FCS) to provide actuator commands independent of pilot inputs in an attempt to reject wind disturbances. This effect may be an aid or a hindrance as we search for the best dither input to command in order to enhance failure identification. Nevertheless, wind disturbance is a reality that we should not neglect.

3.3 MMAE Design

The theory behind MMAE was established in Section 1.3. In the present section, the algorithm is presented which is implemented in FORTRAN code. Rather than printing all of the FORTRAN source code with all of the input and output routines, a more simplified digestion of the routines is presented. Only those statements required to get from the algorithm inputs of command inputs and sensor measurements to the algorithm outputs of failure probability and fault declaration are presented.

The FORTRAN code for this thesis is identical to that of Capt Hanlon's thesis [3] with a few modifications. The major difference is that Hanlon's code is designed for single failure identification whereas our code is designed for single *and* dual fault detection. Other changes include a re-formatting of the input and output files so that MATLAB [8] instead of Matrix_x [4] can be used to prepare the input files and process the output. The reason for converting to MATLAB is because it is more widely available at AFIT, numerical problems have been detected in Matrix_x, and because MATLAB's graphics capabilities seem to be more flexible.

3.3.1 Structure of MMAE. The FORTRAN software program used to implement the MMAE algorithm is based on the equations presented in Section 1.3. There are a few subtle points concerning the algorithm's software implementation that bear discussion.

The MMAE program operates on a sample period of $T_s = 0.02$ seconds. This is identical to that of the QFT flight control system on-board the LAMBDA. The impact is that, for each measurement provided at T_s intervals, the MMAE propagates the Kalman filter states and updates them only once. Also, a probability-weighted state estimate, \hat{x}_{MMAE} , is updated once every T_s seconds and failure status inquiries are made on that schedule as well.

Initial probabilities on filters are determined by a lower limit, p_{MIN} , which prevents any probabilities from going to zero:

$$p_{MIN} = 0.001 \quad (3.26)$$

If any probabilities were to go to zero, the recursive nature of filter probability calculation would prohibit subsequent non-zero probabilities. Refer to Equation (1.20). The initial probability on the filter holding the correct hypothesis, p_{MAX} , is pre-calculated according to the total number of filters, $NF = 15$, so that the probability sum of all elemental filters is 1.000.

$$p_{MAX} = [1.000 - p_{MIN}(NF - 1)] = 0.986 \quad (3.27)$$

When a simulation commences, the fully functional filter assumes the maximum probability $p_{MAX} = 0.986$. Similarly, when a new filter is declared to have the correct hypothesis (and that new bank of filters is to be brought on-line), it is reassigned the probability p_{MAX} immediately, and all other filters in the new bank are initialized with probability p_{MIN} .

The $r_k^T(t_i)A^{-1}(t_i)r_k(t_i)$ term of Equation (1.22) is multiplied by -1 rather than the $-\frac{1}{2}$. Hanlon's work established that -1 produced the fastest MMAE probability convergence times while minimizing false alarms [3:p.55]. Furthermore, to prevent numerical difficulties, the $-r_k^T(t_i)A^{-1}(t_i)r_k(t_i)$ is limited to a minimum value of -50 . Also, the β term of Subsection 1.3.3 has been stripped. Superior performance (that is, removing the proneness to false alarms on sensor failures) without this leading coefficient has been established [3, 19, 21].

A probability history window is used for each filter to average the past ten probabilities resulting from calculations suggested by Equation (1.20) before being used to declare that a particular elemental filter has the correct failure status hypothesis, i.e., that its averaged probability exceeds some value, here selected to be 0.5. Hanlon noted that volatility is introduced into the MMAE failure declaration process with shorter window sizes [3]. Conversely, longer windows yield sluggish performance. With a probability window of 10 and a failure declaration trigger of 0.5, the theoretical minimum failure identification time would be nT_s seconds where n is the minimum number of sample periods between actual failure and MMAE identification, and $T_s = 0.02$ second. We can solve for n given the constraints that the filter hypothesizing the failure has the minimum limit on probability, $p_{MIN} = 0.001$, before the failure and the maximum probability, $p_{MAX} = 0.986$, after

the failure as calculated by Equation (1.20).

$$0.5 = 0.986n + 0.001(10 - n)10 \quad (3.28)$$

$$n = 5.066 \quad (3.29)$$

Equations (3.28) and (3.29) tell us that the absolutely fastest failure identification time with our design is $5 \times 0.02 = 0.10$ seconds, under the constraints listed above.

The minimum window-averaged probability required to declare a failure is $p_{TRIG} = 0.5$. The trigger is set at this level because we want only one filter to be declared as holding the correct hypothesis. When all filter probabilities must sum to 1.0, it is possible for only one filter to have a probability of 0.5 or higher.

The items discussed above are steps taken to translate the MMAE theory presented in Chapter I into a practical implementable algorithm which has the structure and performance characteristics required for real world application. The program code used in testing is therefore easily translatable to languages other than FORTRAN.

3.3.2 Kalman Filter Design. The Kalman filters used in the multiple model scheme are organized into banks. Each bank has a primary filter and fourteen secondary filters. These cover all failures possible with the premise that the primary filter reflects the current failure status and that any possibility of one additional failure will be covered by a secondary filter. In the level-zero bank, the primary filter is the fully functional filter, as shown in Figure 1.2. A secondary filter of level-zero becomes a primary filter once the MMAE declares the corresponding failure and moves to a level-one bank. Banks in level-one also include a fully-functional-aircraft filter to provide an escape route back to level-zero in the case of a false failure declaration.

The Kalman filters will operate in the steady-state-gain condition. That is, the MMAE algorithm will use pre-computed constant Kalman filter gain matrices, K_k , and pre-computed constant inverse residual covariance matrices, A_k^{-1} . This leaves the on-line work of the MMAE algorithm limited to the propagation of filter states and residual computation. Discrete time state transition matrices, Φ_k , discrete time input matrices, $B_{d,k}$, and output matrices, H_k , are the only additional data required to accomplish this. Therefore, a MATLAB routine was developed to

create these matrices and store them ahead of time in data files for the MMAE algorithm to use later. Similarly, these pre-computed matrices will lessen the computational load when the MMAE algorithm is implemented on the real LAMBDA.

The truth model consists of the aircraft dynamics model, the wind gust model, second-order actuator models, and a discrete-time flight control system. Since the flight control system (FCS) states are known implicitly at any time, there is no need to model them in the Kalman filters. The actuators may be reduced to first-order models to eliminate computation of four Kalman filter states (see Equations (3.2) and (3.3)). The wind gust states are reducible to scaled additive white noise rather than shaped noise. The resulting Kalman filter model is left to represent only the aircraft dynamics model, single-order actuators, and uncertainty due to wind (without explicit states devoted to estimating the wind).

To accommodate this reduction in complexity from the truth model, the following consideration with respect to inputs must be made. The truth model will have *command inputs* which represent the deflections applied to the aircraft control stick. These command inputs are processed by the FCS and end up as the *actuator command inputs* which are applied to the inputs of the actuators. With the elimination of the FCS from the Kalman filter models, the inputs to the Kalman filter are the actuator command inputs rather than the command inputs.

3.3.2.1 Actuator Order Reduction. Equations (3.2) and (3.3) are second-order transfer functions representing the dynamics of the actuators on-board the LAMBDA. In the interest of saving on-line computational time for our MMAE algorithm, it is desirable to reduce these transfer functions to first-order, thus reducing our Kalman filter model by four states. A study of the second-order transfer functions of Equations (3.2) and (3.3) by referring to the Bode plots of Figures 3.2 and 3.3 shows that the damping ratio is very high and that we can expect good approximations from first-order transfer functions.

A first-order approximation may be obtained by matching its bandwidth and steady state gain to that of the second-order system. The bandwidth is obtained by choosing the frequency at which the gain crosses the half power point. For the elevator, the steady state gain is

$$K_{..} = \frac{136.2}{176.63} = 0.7711 \quad (3.30)$$

At half power, the gain is $0.7711 \times \sqrt{\frac{1}{2}} = 0.5453$. To find the bandwidth, we set $s = j\omega$ and take the square of the transfer function magnitude by squaring the real and imaginary parts and setting this equal to 0.5453^2 .

$$\frac{136.2^2}{(176.63 - \omega^2)^2 + (-j21.6280\omega)^2} = \frac{(\sqrt{\frac{1}{2}})^2(136.2)^2}{176.63^2} \quad (3.31)$$

Algebraic manipulation leaves us with a fourth order polynomial in ω .

$$\omega^4 + [(21.6280)^2 - 2(176.63)]\omega^2 + (176.63)^2 - 2(176.63)^2 = 0 \quad (3.32)$$

which has roots $\omega = \pm j15.5863$ and $\omega = \pm 11.3324$. We desire a real, positive frequency to represent the bandwidth, so we are left with an elevator bandwidth of $BW_e = 11.3324$ rad/sec. Similar calculations reveal that the second-order aileron transfer function has steady state gain, $K_{aa} = 0.9662$ and $BW_a = 14.3024$ rad/sec. First-order transfer functions with these characteristics have the form

$$\frac{K_{ss} \times BW}{(s + BW)} \quad (3.33)$$

Finally, the reduced-order transfer functions for the elevator and aileron actuators used in the Kalman filters are given in Equations (3.34) and (3.35), respectively. The frequency responses of these transfer functions are plotted with the second-order responses in Figures 3.2 and 3.3.

$$\frac{\delta_e(s)}{\delta_{e_c}(s)} = \frac{8.7384}{(s + 11.3324)} \quad (3.34)$$

$$\frac{\delta_a(s)}{\delta_{a_c}(s)} = \frac{13.8193}{(s + 14.3024)} \quad (3.35)$$

Other techniques are available for first-order representation of second-order systems. However, the technique presented above does a good job of matching Bode amplitude ratio plot characteristics over a wider band of frequencies than may other methods.

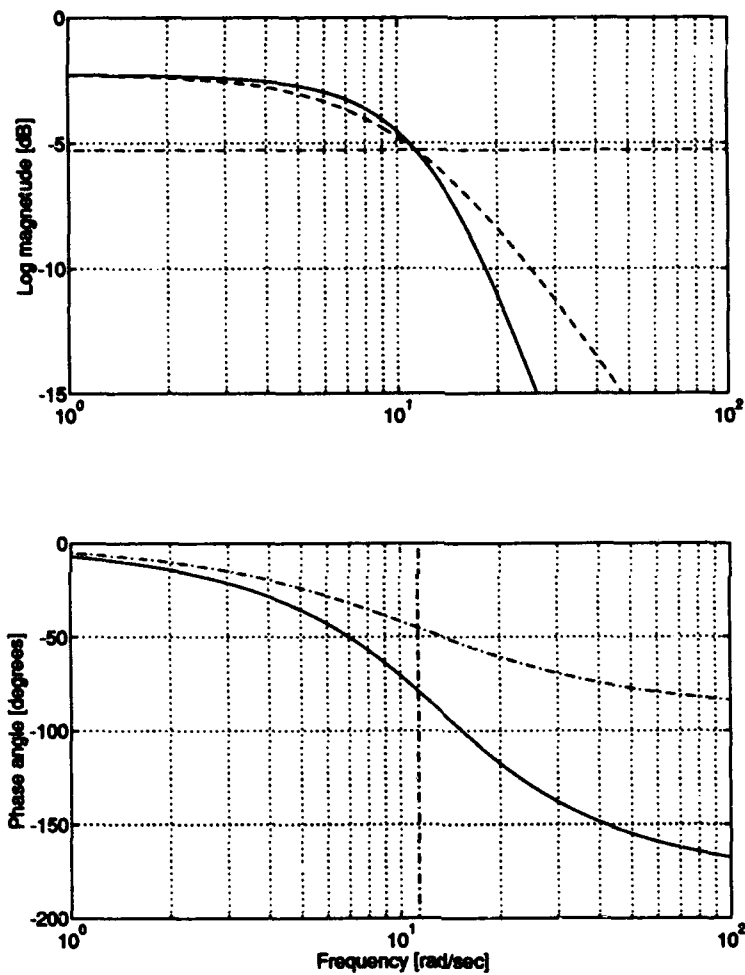


Figure 3.2 First-Order (dashed) and Second-Order (solid) Elevator Actuator Bode Plots. Half Power Magnitude is -5.3 dB. Bandwidth is 11.3 rad/sec.

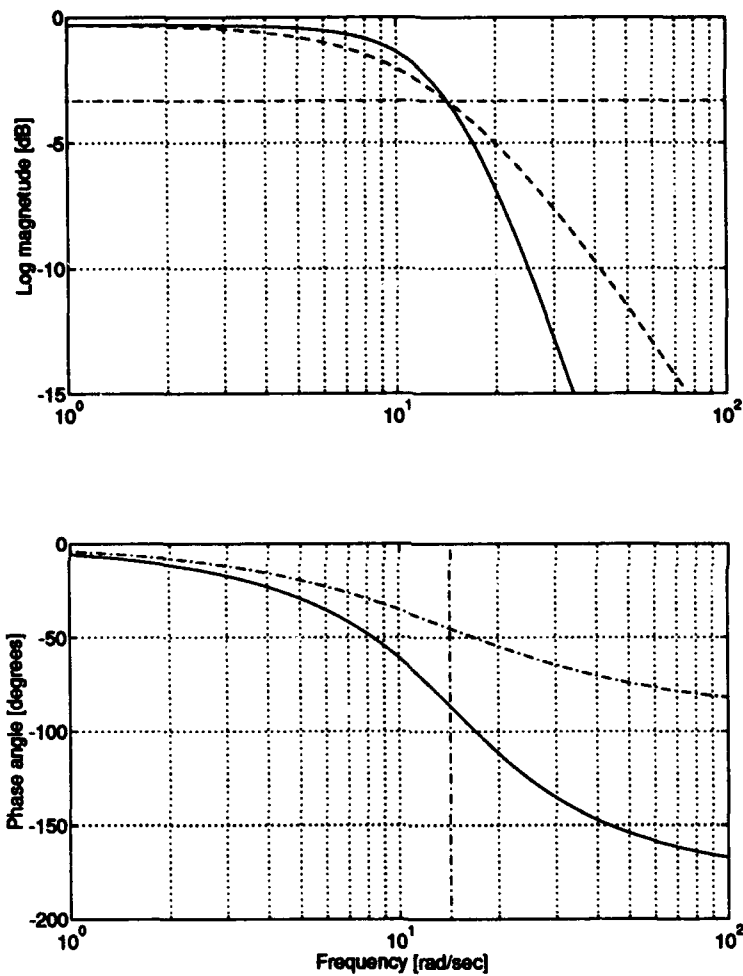


Figure 3.3 First-Order (dashed) and Second-Order (solid) Aileron Actuator Bode Plots. Half Power Magnitude is -3.3 dB. Bandwidth is 14.3 rad/sec.

3.3.2.2 Wind Representation. The wind gust model of Equation (3.23) has eight states, six of which are added in some proportion to the aircraft states as determined by T_{wind} of Equation (3.24). Again, in the interest of saving on-line computational time, the eight-state wind gust model of Equation (3.23) will be replaced in the Kalman filter model by combinations of six scaled white Gaussian noises represented by w_{filter} with strengths determined by

$$Q_{filter} = \begin{bmatrix} Q_u & 0 & 0 & 0 & 0 & 0 \\ 0 & Q_a & Q_{a,q} & 0 & 0 & 0 \\ 0 & Q_{a,q} & Q_q & 0 & 0 & 0 \\ 0 & 0 & 0 & Q_p & 0 & 0 \\ 0 & 0 & 0 & 0 & Q_\beta & Q_{\beta,r} \\ 0 & 0 & 0 & 0 & Q_{\beta,r} & Q_r \end{bmatrix} \quad (3.36)$$

where the subscripts correspond to the subscripts of the wind states in Equation (3.23). The off-diagonal terms represent the cross correlation indicated in the spectral densities of Equations (3.13) and (3.16). In this section, we will show how the elements of Q_{filter} are determined.

Our strategy is to obtain values for Q_{filter} which have the same average power spectral density function magnitude as the wind gust power spectral densities across an appropriate bandwidth. The appropriate bandwidth is that of the corresponding aircraft state variable. Logarithmic magnitude Bode plots of the LAMBDA's dynamic responses are shown in Appendix B. The bandwidth for each aircraft state variable is taken from each plot by subtracting 20 dB from the peak logarithmic magnitude and noting the highest frequency at which the response drops below this line.

The next step is to integrate the power spectral densities from Equations (3.11) through (3.16) from $\omega = 0$ to $\omega = \omega_{BW}$, where ω_{BW} is the bandwidth frequency of the aircraft state that corresponds to the power spectral density in question. The result of the integration is divided by the bandwidth to obtain an average. The average is then placed in the Q_{filter} matrix.

Finally, the transformation matrix, T_{wind} , is used to add the constant strength wind components into the aircraft states. So, for the Kalman filter model, Equation (3.25) becomes

$$\dot{x}_{acft} = Fx_{acft} + Bu + T_{wind}w_{filter} \quad (3.37)$$

T_{wind} is represented by $G(\tau)$ in the Kalman filter state covariance propagation equations, (1.5) and (1.11), and likewise, Q_{filter} is represented by $Q(\tau)$.

The above procedures will produce a Kalman filter model with zero-order wind representation and a good Q with which to begin the tuning process. More detail on these procedures is found in Martin [7].

3.4 Test Runs

3.4.1 Monte Carlo Runs. Due to the large amount of uncertainty generated by the wind gust model, there will be a variance in performance from simulation to simulation even though all parameters remain the same. In order to provide representative performance, ten Monte Carlo runs will be averaged for each set of test conditions. The only variable to change will be the seed that starts the random number generator which produces normally distributed values for the truth model's four inputs to the wind gust model and additive white noises for the sensor measurements. The number ten is chosen out of tradition [3] and because experience with the MMAE algorithm demonstrates that an average of ten runs gives a very good prediction of what happens over a larger sample of runs.

3.4.2 Input Dithers. The input dithers will be applied to the command inputs of the flight control system. In Figure 3.1 these inputs are denoted: left pitch rate command, right pitch rate command, left roll rate command, right roll rate command, left sideslip angle command, and right sideslip angle command. Since these are rate and angle commands, each respective control surface will not necessarily be just a scalar multiple of the magnitude or phase of the applied command signal. It will be important to ensure that the limits of control surface deflection (see Table 3.2) are not violated as the characteristics of the applied dither give no indication of the travel commanded to the surfaces.

Primarily, sinusoidal signals will be used to dither the aircraft. Magnitude, frequency, and phase will be variable parameters. We are particularly interested in the effects of various dither frequencies on failure identification times. The magnitude of dither command also affects failure identification times but this effect is more predictable. In general, larger magnitude dithers shorten identification time. This is known from using the MMAE program in practice runs and from

prior research [3:p.36]. The phase relationship between left and right dithers disambiguates the identification of left from right failed actuators [3:p.37]. A phase relationship between left and right dithers will be established by informal experiment to determine if left failed actuators are continually and easily distinguished from right failed actuators. Once the value for phasing is established, it will not be altered throughout our formal experiments.

The input dither will be used to control the magnitude of g -forces applied to the aircraft. Limits on g -force magnitude are established at $\pm 0.10 g$ for vertical acceleration and $0.20 g$ for the horizontal acceleration. These limits are suggested by Menke [15:p.50] as a result of his "intuitive reasoning and previous handling qualities experience." Athans and his co-authors used a maximum limit of $0.25 g$ in the lateral direction to define their quadratic performance criterion in the design of their Linear Quadratic Gaussian (LQG) compensator for the F-8C aircraft [1:p.771]. Their horizontal limit was established with the understanding that any horizontal acceleration experienced in maneuvering is undesirable and that this limit is used as an LQG weighting factor. Furthermore, discussions with researchers at Armstrong Laboratories Combined Stress Branch reveal that "subliminal" acceleration is indeed an extremely subjective quantity. The human is able to perceive extremely low levels of angular acceleration and linear acceleration on the order of $10^{-2} g$. He or she is able to *endure* several g 's, but, the acceleration range to be described as "not annoying" or "not noticeable" is not in the realm of research conducted by the Combined Stress Branch.

Information from Dr. R. E. Van Patten, Ph.D., P.E., retired from Armstrong Laboratories, points out that the human body is able to detect angular acceleration rates of 0.1 to 0.5 degrees/second/second. Vibration perception of the body is complex and differs from part to part. In the frequency band of 1-10 Hz, the hand is able to sense accelerations as small as $0.010 g$. The visceral cavity has a natural frequency of about 4.5 Hz, so dither frequencies of around $\omega = 28$ rad/sec should be avoided.

A book by Schaefer which compiles the results of many studies on the stress of vibrations and g -loading on human physiology provides insight into the subjectivity of "subliminal" [20:pp.55,57]. In Figure 15 of Schaefer's book, g -forces are plotted against frequency for several curves. The *perception* curve corresponds to the lowest g -forces perceivable by human test subjects. *Voluntary tolerance* describes the level of g -forces which unprotected test subjects refuse to tolerate for ex-

posure durations of over 5 to 20 minutes. This frequency curve peaks at about 3 g 's at the 4 Hz frequency. Test subjects report *unpleasantness* for g -forces of 0.08 g at about 2 Hz and even less acceleration for other frequencies between 1 and 10 Hz. However, Schaefer points out that pilots of military aircraft endure vibrations with g -forces less than 0.08 g for long durations of up to eight hours "without observable detrimental effects on performance or health" [20:p.57]. This research does not define but supports our decision to limit vertical g -forces imposed by our dither routine to 0.10 g .

Finally, a March 1993 interview [5] with an Air Force pilot, Capt Jim Wicker, a C-141 pilot of the 3950th Test Wing, reveals that "subliminal" acceleration might have the quality of unpredictability. Pilots routinely endure acceleration due to wind turbulence without annoyance or degradation of duty performance. Though gusts may be noticeable at times, they cannot be anticipated and this quality may allow higher g -levels to be tolerated than if a constant and predictable sinusoidal application of g -forces were applied.

3.4.3 Single Failure Verification. Tuning the elemental Kalman filters and verifying single failure performance go hand-in-hand. Tuning will only involve changes to Q (since R is assumed to be well known) and verified by achieving consistent MMAE performance in identifying single failures. Criteria for successful single failure performance are: no false alarms in any of ten 12-second Monte Carlo runs for each of fifteen failure configurations; no missed alarms over the same test range; and identification of the correct failure in minimum time, not to exceed 8 seconds. Furthermore, experimentation to find the optimal dither routine will produce improved MMAE performance in identifying single failures.

3.4.4 Dual Failure Performance Evaluation. Using the optimal dither technique developed by our research, the performance of the MMAE algorithm will be tested against dual failures. All possible combinations of two failures will be tested. The first failure induced will precede the second failure by one second. This time lapse should allow the MMAE to identify the first failure and stabilize its probabilities before being subjected to a second failure.

The most important criterion for successful performance is that a majority of MMAE probability must lie with the filter holding the hypothesis of both induced failures. In situations where

Table 3.4 MMAE Kalman Filter Codes.

Code	Filter Model Represents:
FF	fully functional aircraft
A1	right elevator actuator failure
A2	left elevator actuator failure
A3	right aileron actuator failure
A4	left aileron actuator failure
A5	right rudder actuator failure
A6	left rudder actuator failure
S1	forward velocity sensor failure
S2	angle of attack sensor failure
S3	pitch rate sensor failure
S4	pitch angle sensor failure
S5	sideslip angle sensor failure
S6	roll rate sensor failure
S7	roll angle sensor failure
S8	yaw rate sensor failure

the MMAE does not identify the first failure before the second failure is induced, the MMAE is forced to choose a filter hypothesizing only one failure in the face of two failures. The second failure induced may be the first identified and subsequently, the first induced failure may be identified by the MMAE's selection of a level-1 filter that hypothesizes both failures. The *order* of identification is not so important as the fact that both failures have indeed been identified. Nevertheless, order of identification not matching the order of failure onset will be noted in the analysis.

3.4.5 Output Format. MMAE performance will be represented by time histories of the elemental Kalman filter probabilities. The probability traces of the fifteen Kalman filters run simultaneously during an MMAE simulation and the results of ten Monte Carlo runs must be presented in a convenient and easy-to-understand format. Such a one-page compilation of data is shown in Figure 3.4. Codes enumerated in Table 3.4 are used to denote the hypothesis held by each filter. Note that the time axes runs from 2 to 12 seconds. The first two seconds of simulation are eliminated to allow transients to settle out. Failures are introduced four seconds into the simulation. Shown in Figure 3.4 is the MMAE performance against a right elevator actuator failure. The probability at each sample time is the average probability of one filter from ten Monte Carlo runs. The time listed next to the vertical line inside the plot for A1 is the average time

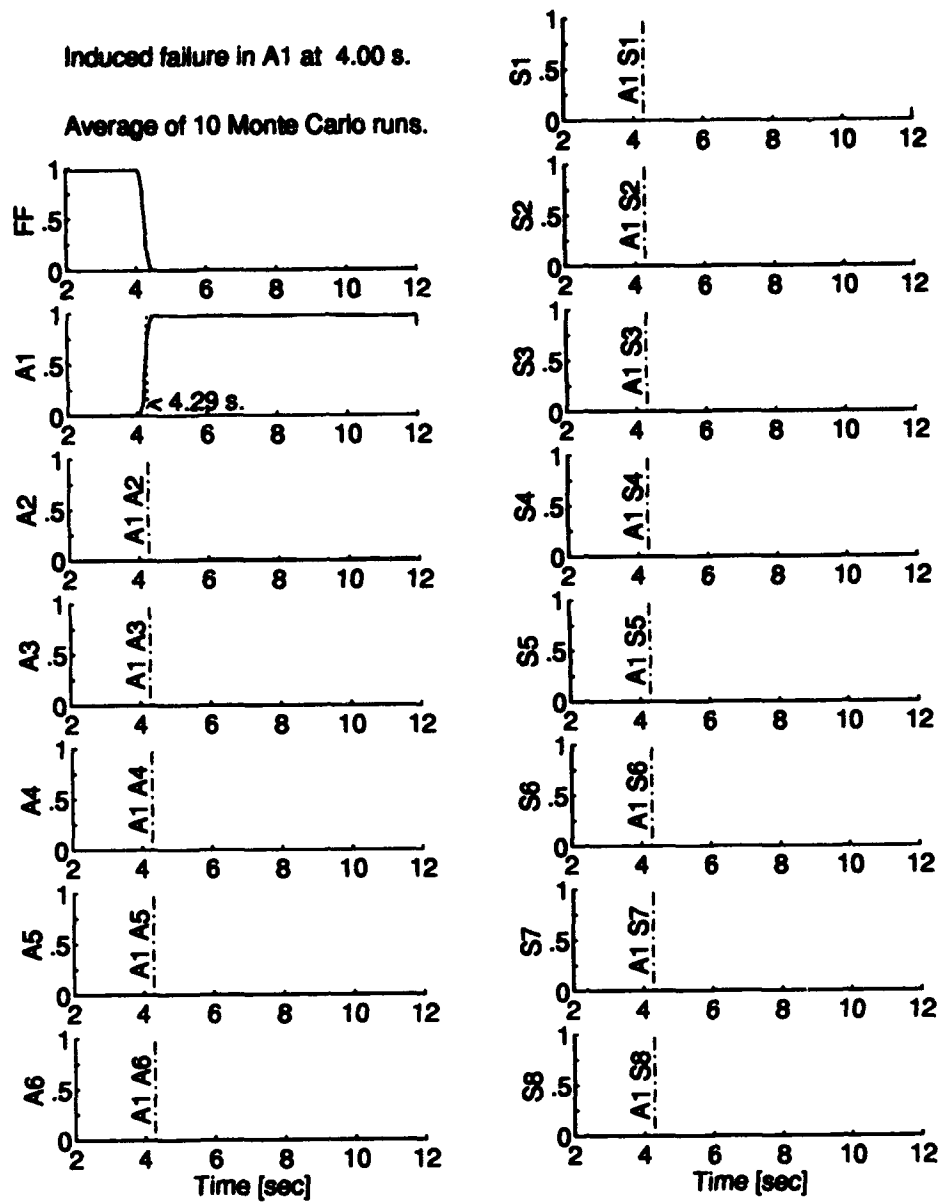


Figure 3.4 Sample of MMAE Probability Histories. Right Elevator Actuator Failure is Induced at 4.00 sec on Each of Ten Monte Carlo Runs.

that the MMAE took to identify the A1 filter as having the correct hypothesis. At this time, the MMAE switches to the filter bank holding the right elevator actuator failure as the primary hypothesis. The probabilities for this new bank of filters are plotted to the right of the vertical dash-dot lines in filters A2 through S8. The double codes on the left of these vertical lines denote the dual failure hypothesis held by the new filters just brought on-line. Recall that fully functional and A1 hypotheses are *also* in the new bank, so the first two plots in the left column are meaningful from the time the new bank is brought on to the 12 second point.

Another presentation format to be used is the compilation of a series of all possible failures induced against the MMAE algorithm. See Figure 4.15. In this case, only the filters with the hypothesized failures are shown. Since fourteen different failures are induced in fifteen different ten-run simulations (including the fully functional condition), fifteen probability traces are shown as in the single simulation case. However, here it is important to remember that each trace is from a simulation with different failure condition than the others.

Each Monte Carlo run will have its own characteristics in terms of time to identify the failure and false and missed alarms. The formats given here only represent the mean probability time histories and not the mean $\pm 1\sigma$ performance boundaries because the we are interested in MMAE failure identification decision times. Knowing the mean $\pm 1\sigma$ statistical boundaries will provide little information that is of use to us in a pictorial representation that already makes a big reduction of the experimental results.

3.5 Chapter Summary

A thorough explanation of the tools and techniques to be used in our experiments has been given in this chapter. Although a detailed code listing of the MATLAB and FORTRAN programs developed for this thesis is not provided in this text, the reader should have an idea of their structure and function when he/she considers the detailed presentation of the LAMBDA model, specifics of the MMAE design, and the desired format of the test results given in this chapter. The Results and Analysis to follow are based on the foundations built here.

IV. Results and Primary Analyses

This chapter presents the data resulting from the performance of tasks described in Chapter III. First, the process of tuning the Kalman filters for the MMAE filter banks is discussed. A new technique for tuning is compared to the analytic method described in the Kalman filter design section of the previous chapter. Secondly, the specifics of a plan to find the optimal dither are presented. The results of executing this plan are discussed in detail, along with an analysis that leads to the conclusion of an optimal dither routine. MMAE performance while using real pilot stick commands for aircraft stimulation are evaluated as an alternate form of dither. Finally, the MMAE performance against dual failures is evaluated.

4.1 Tuning the Kalman Filters

Since the wind gust model is reduced to additive white Gaussian noise in the Kalman filter models as described in Subsection 3.3.2.2, a relatively poor tracking of wind dynamics is expected from the Kalman filters. The power spectral density analysis procedure of Subsection 3.3.2.2 provided a starting Q_{filter} , shown in Equation (4.1):

$$Q_{filter} = \begin{bmatrix} 343 & 0 & 0 & 0 & 0 & 0 \\ 0 & 2.10 \times 10^{-4} & 6.67 \times 10^{-4} & 0 & 0 & 0 \\ 0 & 6.67 \times 10^{-4} & 2.12 \times 10^{-3} & 0 & 0 & 0 \\ 0 & 0 & 0 & 5.87 \times 10^{-3} & 0 & 0 \\ 0 & 0 & 0 & 0 & 1.49 \times 10^{-3} & 1.78 \times 10^{-3} \\ 0 & 0 & 0 & 0 & 1.78 \times 10^{-3} & 2.14 \times 10^{-3} \end{bmatrix} \quad (4.1)$$

Informal experimentation showed that this analytic estimate of Q_{filter} must be adjusted to minimize false alarm declarations by the MMAE. However, the adjustment must be made with the following in mind. Tight tuning in the face of unmodeled dynamics will enhance random filter probability shifts while loose tuning causes sluggish MMAE performance and even missed identifications.

The difficulty in tuning the particular design of filter model represented by Equation (3.37) is that each element of Q_{filter} from Equation (3.36) is not transformed by T_{wind} of Equation (3.25) to affect only one aircraft state variable. Rather, a change in Q_u , for instance, will affect the

covariance of *all* longitudinal aircraft state estimates simultaneously. The same is true for Q_{α} and $Q_{\dot{q}}$. Similarly, the lateral elements of Q_{filter} each have an effect on all of the lateral states. Moreover, the impact of $Q_{\dot{u}}$ may *not* have the majority of influence over the addition of white noise to the aircraft state indicated by its subscript, u , forward velocity perturbation. The white noise added to form \dot{u} is dictated by the constants C_1 through C_4 in Equation (4.2):

$$\dot{u} = X'_u u + X'_\alpha \alpha + X'_q q + X'_\theta \theta + C_1 w_u + C_2 w_{\alpha} + C_3 w_{\dot{q}} + C_4 w_{\alpha, \dot{q}} \quad (4.2)$$

The numerical values of C_1 through C_4 are determined by the multiplication of $T_{wind} \times Q_{filter}$. Even if these constants were easily obtained, it is no trivial exercise to adjust the individual Q 's so that the residuals for each of the four longitudinal aircraft state variables have the desired covariance.

To save time in tuning and to assure that the tuned filter is not prone to false alarms yet able to respond quickly, a tuning algorithm is implemented in MATLAB. The strategy is to use various values for Q_{filter} , form the Kalman filters for the level-0 bank (see Figure 1.2), then run MMAE simulations against fully-functional-aircraft truth data. The diagonal elements of Q_{filter} are incrementally reduced one after the other until five Monte Carlo simulations are run without the MMAE probability of the fully functional filter dropping below 2% of its maximum value, $p_{FF_MAX} = 0.9860$, to $p_{FF} = 0.9663$. The algorithm proceeds as follows: a Q_{filter} is chosen, MMAE simulations are run until $p_{FF} < 0.9663$. If all five Monte Carlo runs result in $p_{FF} \geq 0.9663$ for all time samples, then Q_{filter} is decremented again until a p_{FF} is detected below the limit.

The strategy for decrementing Q_{filter} is to decrement $Q_{\dot{u}}$ by one increment, run one MMAE simulation of five Monte Carlo runs, then decrement Q_{α} by one increment, run one MMAE simulation of five Monte Carlo runs, *etc.*, so that the diagonal elements are reduced in a level manner. Intuitively, this level reduction approach makes sense, because of the relatively equivalent effects imposed by each element of Q_{filter} on the filter's state estimates. Cross correlation terms maintained a cross correlation coefficient of 0.91 so that $Q_{\alpha, \dot{q}} = 0.91\sqrt{Q_{\alpha}}\sqrt{Q_{\dot{q}}}$ and $Q_{\beta, \dot{r}} = 0.91\sqrt{Q_{\beta}}\sqrt{Q_{\dot{r}}}$. The cross correlation coefficient had to be set manually for two reasons. Q_{filter} needs to have positive eigenvalues. Also, too much correlation makes the MMAE algorithm prone to false alarms and too little makes it sluggish. A balance was struck in informal experiment to arrive at the value of 0.91.

The final \mathbf{Q}_{filter} resulting from this algorithm is shown below. Note the severe reduction in $Q_{u,u}$, the (1,1) element. A possible explanation for this is that the five Monte Carlo runs added up to a total of 60.10 seconds, a short time compared to the magnitude of the time constant found in the power spectral density of $\Phi_{u,u}(\omega)$ of Equation (3.11). The differences between Equation (4.1) and Equation (4.3) give some indication of the validity of the noise model reduction procedure presented in Subsection 3.3.2.2.

$$\mathbf{Q}_{filter} = \begin{bmatrix} 3.09 & 0 & 0 & 0 & 0 & 0 \\ 0 & 2.10 \times 10^{-5} & 8.28 \times 10^{-5} & 0 & 0 & 0 \\ 0 & 8.28 \times 10^{-5} & 3.94 \times 10^{-4} & 0 & 0 & 0 \\ 0 & 0 & 0 & 1.06 \times 10^{-3} & 0 & 0 \\ 0 & 0 & 0 & 0 & 9.79 \times 10^{-4} & 1.33 \times 10^{-3} \\ 0 & 0 & 0 & 0 & 1.33 \times 10^{-3} & 2.18 \times 10^{-3} \end{bmatrix} \quad (4.3)$$

The \mathbf{Q}_{filter} of Equation (4.1) was derived from power spectral density analysis. The \mathbf{Q}_{filter} of Equation (4.3) was derived from MMAE algorithm performance analysis.

The MMAE algorithm performs its Kalman filter propagations and updates in the discrete-time equations of (1.10) and (1.15). Maximum use of on-line processing time is gained by pre-computing the constant steady state Kalman filter gain of Equation (1.14). Steady state Kalman filter gains and residual covariance matrices for each elemental filter are pre-computed in MATLAB [8] using the function `dlqe` (discrete linear quadratic estimator). Inputs to `dlqe` are: Φ discretized with a sample period of $T_s = 0.02$ second; \mathbf{G}_d , an identity matrix (see Equation (1.13)); \mathbf{H} of Equation (1.2); \mathbf{R} from Equation (1.4); and a second order approximation of \mathbf{Q}_d from Equation (1.5) as shown below in Equation (4.4).

$$\mathbf{Q}_d \approx (\Phi \mathbf{G} \mathbf{Q} \mathbf{G}^T \Phi^T + \mathbf{G} \mathbf{Q} \mathbf{G}^T) \times \frac{T_s}{2} \quad (4.4)$$

The steady-state state estimation covariance matrix resulting from `dlqe`, \mathbf{P}^- , is used to calculate \mathbf{A}_k as in Equation (1.24). \mathbf{A}_k is inverted and the result is stored in the filter data file along with \mathbf{K} (produced directly by `dlqe`), $\Phi(t_i, t_{i+1})$, \mathbf{H} , and \mathbf{B}_d for real-time use by the MMAE algorithm.

4.2 Investigation of Dithers

The objective of finding an optimal dither is accomplished in this section. The strategy is to determine each failure condition's sensitivity to the frequency of the dither, and then to do an analysis to pick a promising frequency, and finally to adjust the magnitude to improve failure identification time further.

The dithers used are sinusoidal. Each control surface is controlled by a command input dither which has the form $A\sin(\omega t + \phi)$ where A , ω , and ϕ are held constant throughout each simulation. The phase angle, ϕ , is held constant for all simulations. The effects of varying ϕ are not presented in a formal study. However, Hanlon [3] stated that a phase difference between similar control surfaces is essential for MMAE to distinguish right from left failures [3]. The ϕ used here is a 15° offset between right and left sides for all three sets of control surfaces. In addition, the effects of control surfaces on dynamic movement of the aircraft may be reduced by phasing right surface movement 180° out of cycle from the left surface. In selecting a phase offset, the desired effect is a balance of aircraft state excitation and control surface movement. With no phase offset, little surface movements cause moderate changes in aircraft states. With considerable phase offset, the control surfaces end up moving quite a bit because they are fighting each other in the flight control system's attempt to reach the level of aircraft state excitation required by the left and right command inputs. This effect is presented in detail on page 4-35 when elevator actuator failures are discussed. A balance of aircraft state excitation and control surface movement is achieved by using the following phase relationships determined in preliminary experimentation.

$$\begin{aligned}\phi_{er} &= 0^\circ \\ \phi_{el} &= 195^\circ \\ \phi_{ar} &= 30^\circ \\ \phi_{al} &= 225^\circ \\ \phi_{rr} &= 60^\circ \\ \phi_{rl} &= 255^\circ\end{aligned}\tag{4.5}$$

Variations in phase would add another dimension to our research. So, in the interest of time savings, the relationships of Equation (4.5) are held constant throughout all testing done to develop the optimal dither.

Increasing dither magnitude has the effect of decreasing failure identification time for all types of failures, with few exceptions (roll rate sensor and roll angle sensor). This is known both intuitively and by exercising the MMAE system. This inverse relationship will be used after adjusting frequency simply because magnitude adjustment has a known effect. The dither magnitudes are varied in discrete intervals across a range. Thus, our dither magnitude space is discretized to these values: 2, 3, 4, 5, 6, 7, and 8. No finer discretization will be used due to length of time it takes to run each simulation. The frequency study is accomplished with a base magnitude of 6 degrees/second for both the pitch rate and roll rate command inputs, and the sideslip angle command base magnitude will be 6 degrees for the rudder input commands. These magnitudes have the quality of providing great enough state excitation to allow the MMAE to consistently identify failures over the band of test frequencies.

The effects of varying the frequency component, ω , are studied first. There are base frequencies which are multiplied by a frequency factor to get the range of test frequencies in a discretized space. The factors are: 1/16, 1/8, 1/4, 1/2, 1, 1.9, 2, 2.5, 3, and 4. The base frequencies are 6.6611 rad/sec for the elevators (near the short period natural frequency) and 3.6193 rad/sec for the ailerons and rudders (near the Dutch roll natural frequency). However, the selection of the base frequencies should be considered somewhat arbitrary, as they will be multiplied by the stated factors to arrive at various test frequencies.

The presentation of data is in table and companion figure format. Table 4.1 and Figure 4.1 will be used in the following explanation. Remember that dither frequency is the test variable. We are looking for its effects on "Failure ID Time" and "Vertical Acceleration" as labeled in the left-most column of Table 4.1. Trial numbers at the top of each column are numbered with ascending dither frequency, not necessarily in the order that they were performed, for the ease of the reader. An exhaustive array of statistics for vertical g -forces is given for each trial, so that a rough but accurate distribution curve may be visualized to gain a feel for the acceleration environment on board the aircraft. The top plot of Figure 4.1 gives a graphical representation of this statistical

distribution. The $\pm 2\sigma$ statistics are what will be compared against the g -limits in both the vertical and horizontal directions. Now, refer to the bottom plot of Figure 4.1. Here, only the $\pm 2\sigma$ statistics are plotted against vertical acceleration and failure identification time. Each trial is represented by an X. The connecting lines are straight from point to point (no best-fit lines). For clarity, trial numbers are not placed next to the X's although they could easily be correlated to trial numbers by matching "Failure ID Time" from Table 4.1 to the "Time to identify failure" on the abscissa of Figure 4.1.

An interesting feature of these plots is that, for higher frequencies, the $\pm 2\sigma$ bounds are fairly linear and symmetric about the acceleration = 0 g line. As the frequencies go lower, the failure identification times hit a "brick wall" and the accelerations are no longer symmetric but tend to drift in one direction together. This is due to the short time of simulation as compared to the time period of the low frequency dither cycle. Since the dither cycle was not completely finished by the end of the simulation, the acceleration samples cannot be evenly distributed about a mean of zero. If the tests are re-run, the simulation duration should last for an integer number of dither cycles so that an even distribution of acceleration statistics may be obtained. However, these lower frequencies will have other reasons for being undesirable candidates for the optimal dither. Generally, the low frequency dithers caused high g -loading as compared to dithers of higher frequency and identical magnitude. This is because the aircraft's Bode responses have a much higher gain at the low phugoid frequency ($\omega_{ph} = 0.2484$ rad/sec) and low spiral divergence frequency ($\omega_{spiral} = 0.0231$ rad/sec). See Appendix B. Even though the lowest frequency tested in our research is higher than those of the phugoid and spiral modes, the trend toward higher gain with lower frequency does have its effects in our results.

The next 25 pages contain the companion plots and tables for, first the longitudinal channel actuators and sensors, and then the lateral channel actuators and sensors. The order of presentation is different from that of Table 3.4 because it is more convenient to group the actuators with the sensors they influence for purposes of analysis. The reader is encouraged to browse through these pages at leisure before a detailed analysis of these results is presented beginning on page 4-35.

Table 4.1 Results of varying dither frequency to alter Right Elevator Actuator failure identification time and vertical g -forces.

	Trial									
Failure ID time [sec]	1	2	3	4	5	6	7	8	9	10
	0.24	0.24	0.24	0.22	0.23	0.39	0.33	0.42	0.47	0.68
Elevator Dither										
Magnitude [deg/sec]	6.00	6.00	6.00	6.00	6.00	6.00	6.00	6.00	6.00	6.00
Frequency [rad/sec]	0.4163	0.8326	1.6653	3.3306	6.6611	12.6561	13.3222	16.6528	19.9833	26.6444
Vertical Acceleration [g 's]										
maximum occurrence	0.1698	0.2871	0.2510	0.2399	0.2286	0.2435	0.2466	0.2132	0.2432	0.2296
+2 σ	0.0425	0.1272	0.1053	0.0878	0.0767	0.0624	0.0572	0.0561	0.0519	0.0495
+1 σ	-0.0537	0.0415	0.0412	0.0394	0.0355	0.0294	0.0266	0.0267	0.0245	0.0239
mean	-0.1499	-0.0441	-0.0230	-0.0090	-0.0058	-0.0037	-0.0040	-0.0026	-0.0030	-0.0018
-1 σ	-0.2460	-0.1298	-0.0871	-0.0574	-0.0470	-0.0368	-0.0346	-0.0320	-0.0304	-0.0275
-2 σ	-0.3422	-0.2154	-0.1512	-0.1058	-0.0882	-0.0698	-0.0652	-0.0614	-0.0579	-0.0531
minimum occurrence	-0.4597	-0.3919	-0.3444	-0.2648	-0.2883	-0.2747	-0.2625	-0.2447	-0.2366	-0.2447

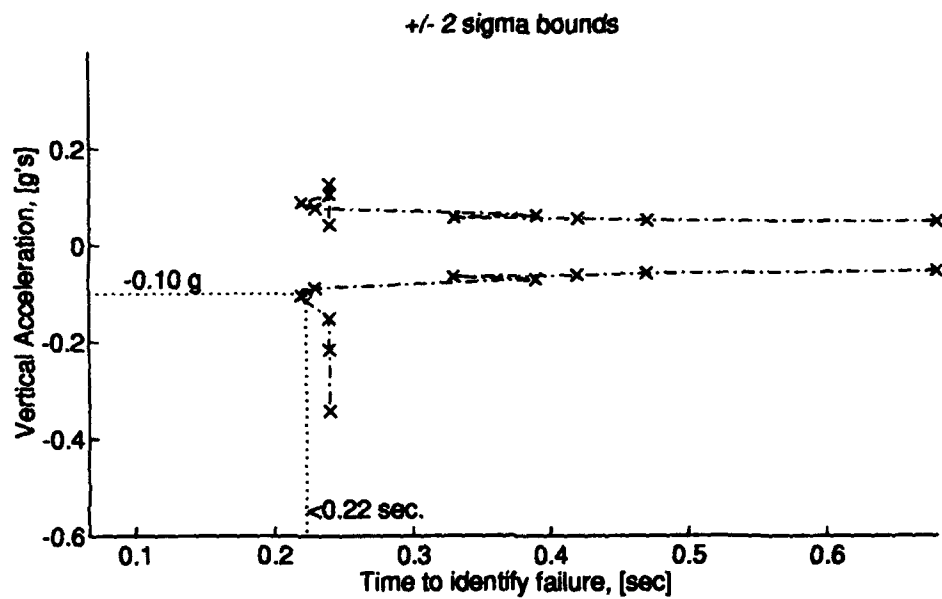
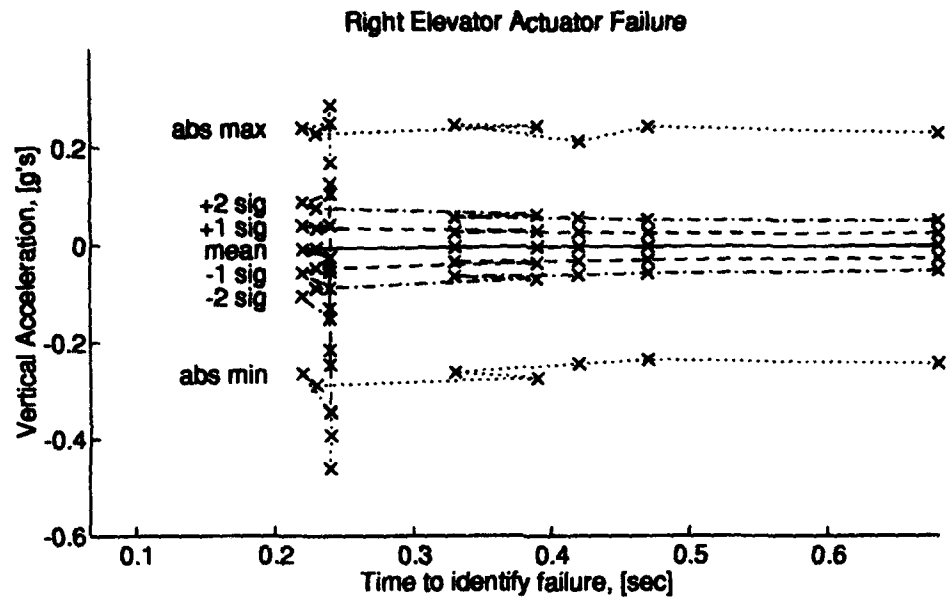


Figure 4.1 *g-forces vs ID time for Right Elevator Actuator failure as frequency changes.*

Table 4.2 Results of varying dither frequency to alter Left Elevator Actuator failure identification time and vertical g -forces.

Trial	1	2	3	4	5	6	7	8	9	10
Failure ID time [sec]	0.24	0.24	0.23	0.20	0.20	0.33	0.25	0.32	0.38	0.53
Elevator Dither										
Magnitude [deg/sec]	6.00	6.00	6.00	6.00	6.00	6.00	6.00	6.00	6.00	6.00
Frequency [rad/sec]	0.4163	0.8326	1.6653	3.3306	6.6611	12.6561	13.3222	16.6528	19.9833	26.6444
Vertical Acceleration [g 's]										
maximum occurrence	0.1698	0.2871	0.2510	0.2399	0.2286	0.2435	0.2466	0.2132	0.2432	0.2296
+2 σ	0.0425	0.1272	0.1053	0.0878	0.0767	0.0624	0.0572	0.0561	0.0519	0.0495
+1 σ	-0.0537	0.0415	0.0412	0.0394	0.0355	0.0294	0.0266	0.0267	0.0245	0.0239
mean	-0.1499	-0.0441	-0.0230	-0.0090	-0.0058	-0.0037	-0.0040	-0.0026	-0.0030	-0.0018
-1 σ	-0.2460	-0.1298	-0.0871	-0.0574	-0.0470	-0.0368	-0.0346	-0.0320	-0.0304	-0.0275
-2 σ	-0.3422	-0.2154	-0.1512	-0.1058	-0.0882	-0.0698	-0.0652	-0.0614	-0.0579	-0.0531
minimum occurrence	-0.4597	-0.3919	-0.3444	-0.2648	-0.2883	-0.2747	-0.2625	-0.2447	-0.2366	-0.2447

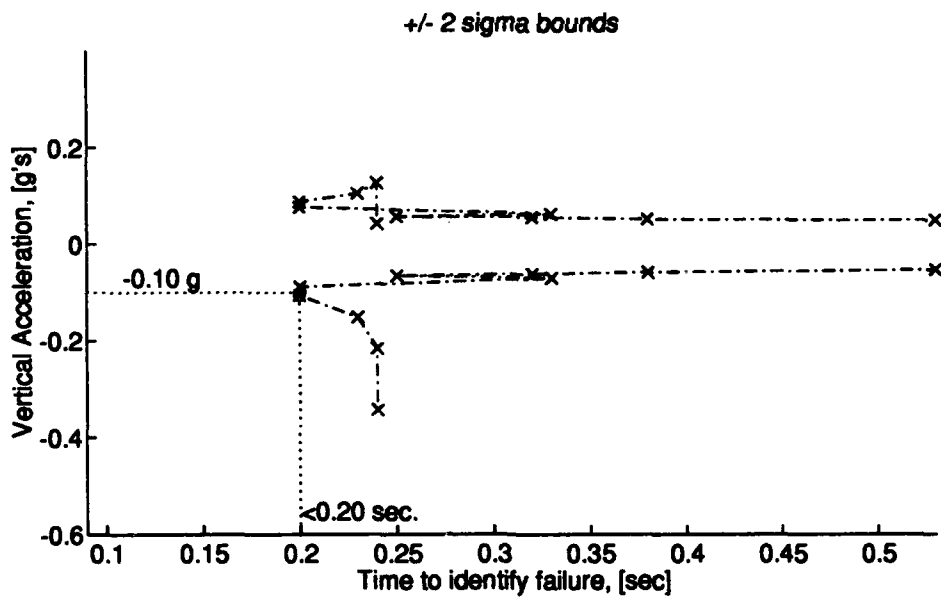
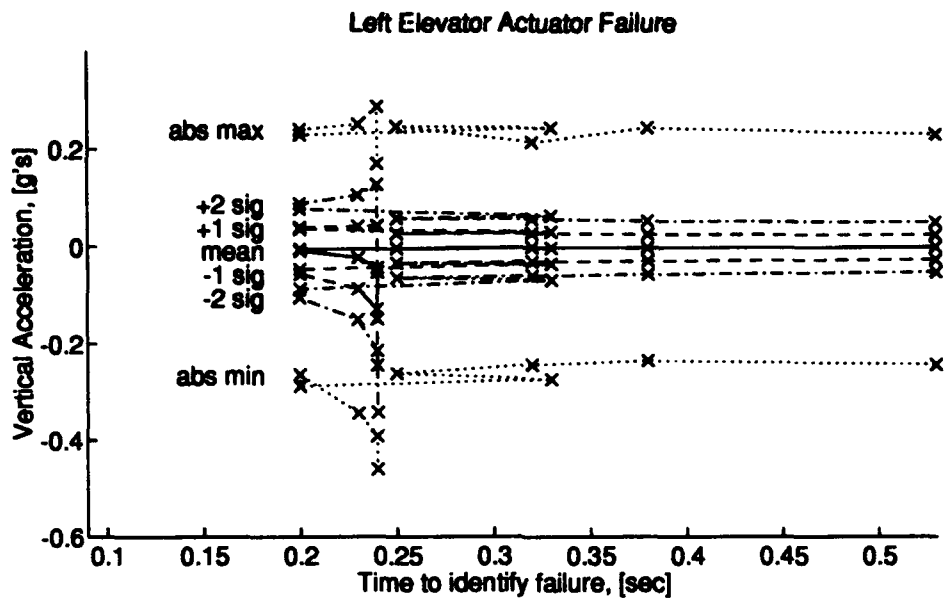


Figure 4.2 *g*-forces vs ID time for Left Elevator Actuator failure as frequency changes.

Table 4.3 Results of varying dither frequency to alter Forward Velocity Sensor failure identification time and vertical g -forces.

Trial	1	2	3	4	5	6	7	8	9	10
Failure ID time [sec]	0.10	0.10	0.58	1.17	1.03	1.19	0.78	0.77	0.84	1.13
Elevator Dither										
Magnitude [deg/sec]	6.00	6.00	6.00	6.00	6.00	6.00	6.00	6.00	6.00	6.00
Frequency [rad/sec]	0.4163	0.8326	1.6653	3.3306	6.6611	12.6561	13.3222	16.6526	19.9833	26.6444
Vertical Acceleration [g 's]										
maximum occurrence	0.1698	0.2871	0.2510	0.2399	0.2286	0.2435	0.2466	0.2132	0.2432	0.2296
+2 σ	0.0425	0.1272	0.1053	0.0878	0.0767	0.0624	0.0572	0.0561	0.0519	0.0495
+1 σ	-0.0537	0.0415	0.0412	0.0394	0.0355	0.0294	0.0266	0.0267	0.0245	0.0239
mean	-0.1499	-0.0441	-0.0230	-0.0090	-0.0058	-0.0037	-0.0040	-0.0026	-0.0030	-0.0018
-1 σ	-0.2460	-0.1298	-0.0871	-0.0574	-0.0470	-0.0368	-0.0346	-0.0320	-0.0304	-0.0275
-2 σ	-0.3422	-0.2154	-0.1512	-0.1058	-0.0882	-0.0698	-0.0652	-0.0614	-0.0579	-0.0531
minimum occurrence	-0.4597	-0.3919	-0.3444	-0.2648	-0.2883	-0.2747	-0.2625	-0.2447	-0.2366	-0.2447

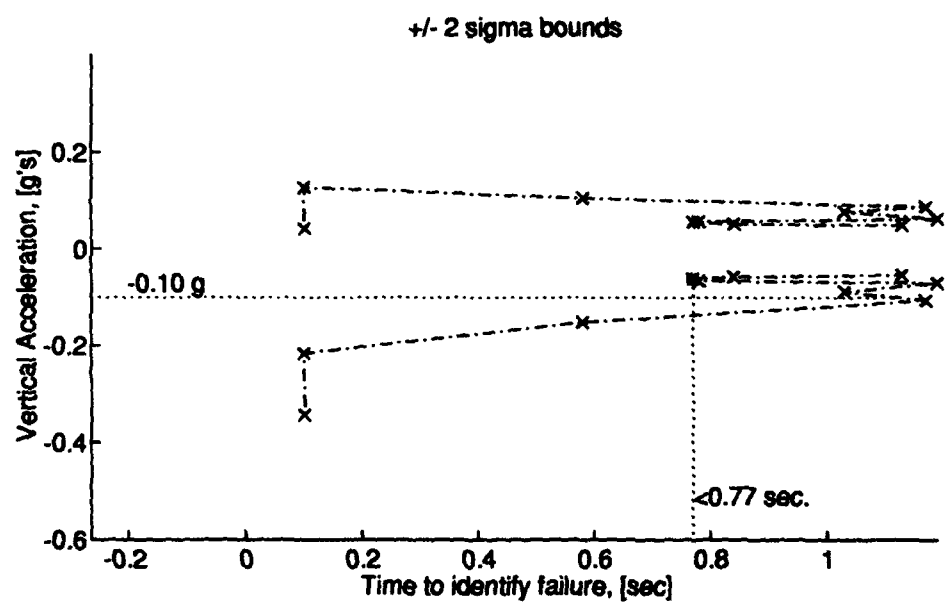
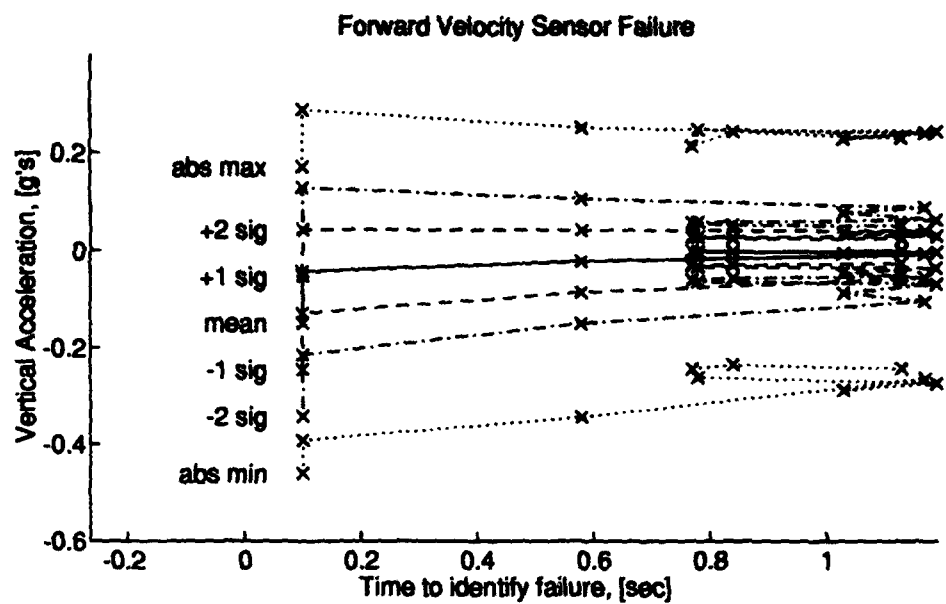


Figure 4.3 *g*-forces vs ID time for Forward Velocity Sensor failure as frequency changes.

Table 4.4 Results of varying dither frequency to alter Angle of Attack Sensor failure identification time and vertical g -forces.

Trial	1	2	3	4	5	6	7	8	9	10
Failure ID time [sec]	0.10	0.10	0.10	0.68	1.96	3.13	3.87	4.55	4.45	5.12
Elevator Dither										
Magnitude [deg/sec]	6.00	6.00	6.00	6.00	6.00	6.00	6.00	6.00	6.00	6.00
Frequency [rad/sec]	0.4163	0.8326	1.6653	3.3306	6.6611	12.6561	13.3222	16.6528	19.9833	26.6444
Vertical Acceleration [g 's]										
maximum occurrence	0.1698	0.2871	0.2510	0.2399	0.2286	0.2435	0.2466	0.2132	0.2432	0.2296
+2 σ	0.0425	0.1272	0.1053	0.0878	0.0767	0.0624	0.0572	0.0561	0.0519	0.0495
+1 σ	-0.0537	0.0415	0.0412	0.0394	0.0355	0.0294	0.0266	0.0267	0.0245	0.0239
mean	-0.1499	-0.0441	-0.0230	-0.0090	-0.0058	-0.0037	-0.0040	-0.0026	-0.0030	-0.0018
-1 σ	-0.2460	-0.1298	-0.0871	-0.0574	-0.0470	-0.0368	-0.0346	-0.0320	-0.0304	-0.0275
-2 σ	-0.3422	-0.2154	-0.1512	-0.1058	-0.0882	-0.0698	-0.0652	-0.0614	-0.0579	-0.0531
minimum occurrence	-0.4597	-0.3919	-0.3444	-0.2648	-0.2883	-0.2747	-0.2625	-0.2447	-0.2366	-0.2447

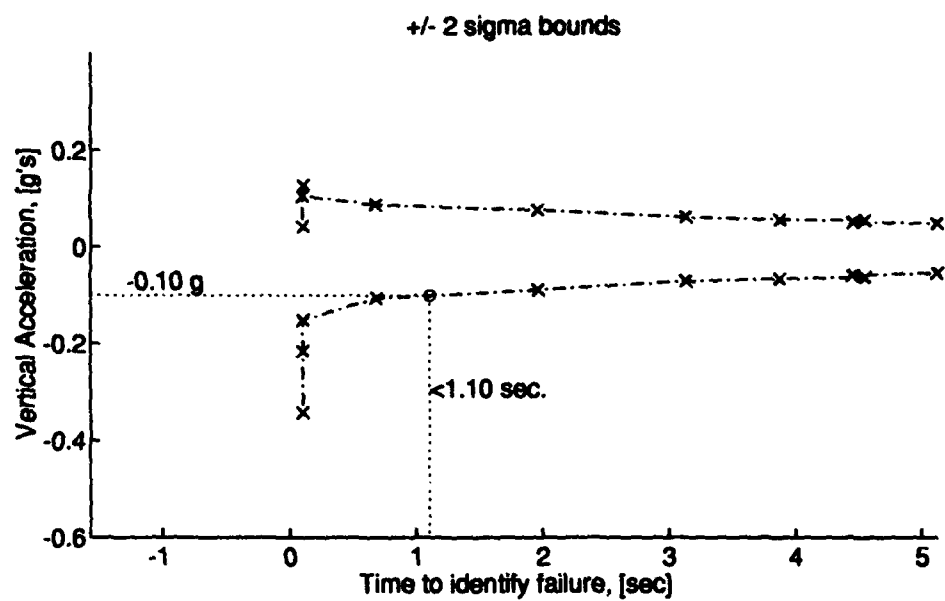
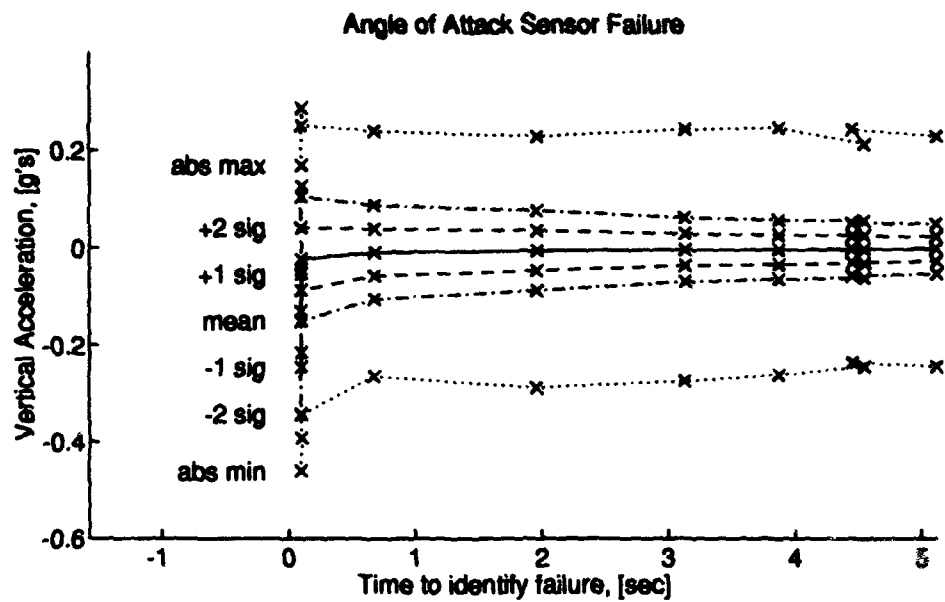


Figure 4.4 *g*-forces vs ID time for Angle of Attack Sensor failure as frequency changes.

Table 4.5 Results of varying dither frequency to alter Pitch Rate Sensor failure identification time and vertical g -forces.

Trial	1	2	3	4	5	6	7	8	9	10
Failure ID time [sec]	0.63	0.36	0.33	0.37	0.52	0.60	0.60	0.62	0.60	0.61
Elevator Dither										
Magnitude [deg/sec]	6.00	6.00	6.00	6.00	6.00	6.00	6.00	6.00	6.00	6.00
Frequency [rad/sec]	0.4163	0.8326	1.6653	3.3306	6.6611	12.6561	13.3222	16.6528	19.9833	26.6444
Vertical Acceleration [g 's]										
maximum occurrence	0.1698	0.2871	0.2510	0.2399	0.2286	0.2435	0.2466	0.2132	0.2432	0.2296
+2 σ	0.0425	0.1272	0.1053	0.0878	0.0767	0.0624	0.0572	0.0561	0.0519	0.0495
+1 σ	-0.0537	0.0415	0.0412	0.0394	0.0355	0.0294	0.0266	0.0267	0.0245	0.0239
mean	-0.1499	-0.0441	-0.0230	-0.0090	-0.0058	-0.0037	-0.0040	-0.0026	-0.0030	-0.0018
-1 σ	-0.2460	-0.1298	-0.0871	-0.0574	-0.0470	-0.0368	-0.0346	-0.0320	-0.0304	-0.0275
-2 σ	-0.3422	-0.2154	-0.1512	-0.1058	-0.0882	-0.0698	-0.0652	-0.0614	-0.0579	-0.0531
minimum occurrence	-0.4597	-0.3919	-0.3444	-0.2648	-0.2883	-0.2747	-0.2625	-0.2447	-0.2366	-0.2447

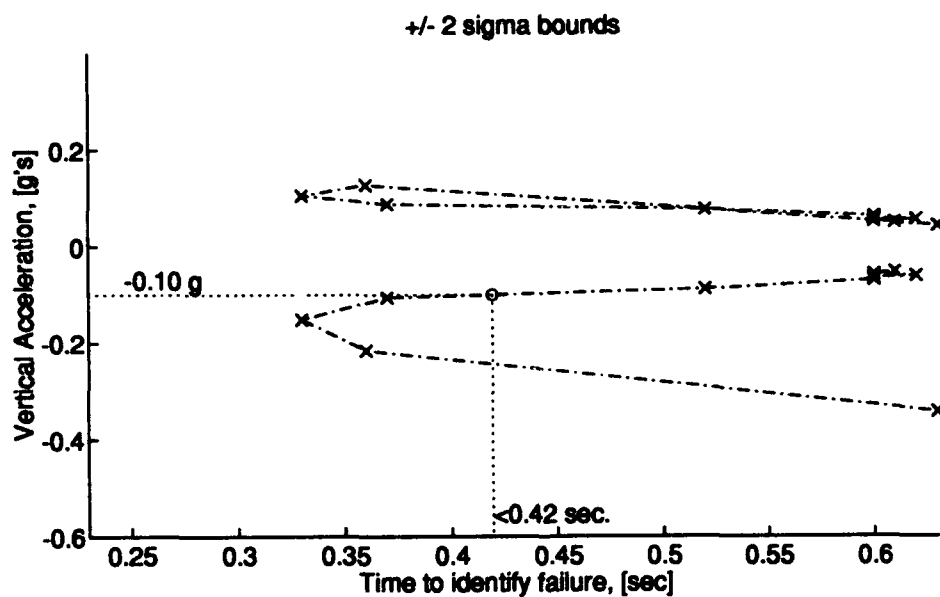
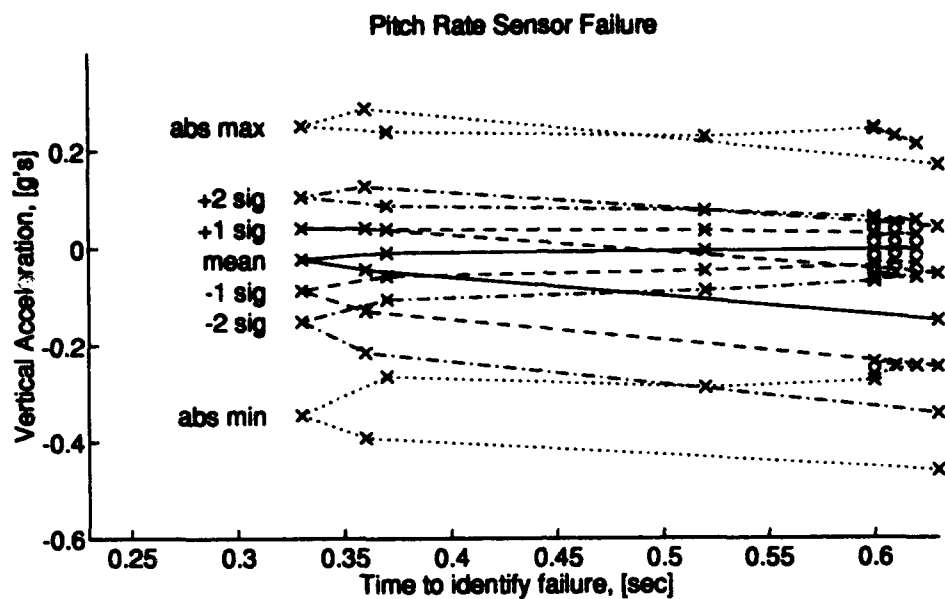


Figure 4.5 *g*-forces vs ID time for Pitch Rate Sensor failure as frequency changes.

Table 4.6 Results of varying dither frequency to alter Pitch Angle Sensor failure identification time and vertical g -forces.

Trial		1	2	3	4	5	6	7	8	9	10
Failure ID time [sec]		0.10	0.45	0.93	0.95	1.05	1.28	1.66	1.76	1.72	1.65
Elevator Dither											
Magnitude [deg/sec]		6.00	6.00	6.00	6.00	6.00	6.00	6.00	6.00	6.00	6.00
Frequency [rad/sec]		0.4163	0.8326	1.6653	3.3306	6.6611	12.6561	13.3222	16.6528	19.9833	26.6444
Vertical Acceleration [g 's]											
maximum occurrence		0.1698	0.2871	0.2510	0.2399	0.2286	0.2435	0.2466	0.2132	0.2432	0.2296
+2 σ		0.0425	0.1272	0.1053	0.0878	0.0767	0.0624	0.0572	0.0561	0.0519	0.0495
+1 σ		-0.0537	0.0415	0.0412	0.0394	0.0355	0.0294	0.0266	0.0267	0.0245	0.0239
mean		-0.1499	-0.0441	-0.0230	-0.0090	-0.0058	-0.0037	-0.0040	-0.0026	-0.0030	-0.0018
-1 σ		-0.2460	-0.1298	-0.0871	-0.0574	-0.0470	-0.0368	-0.0346	-0.0320	-0.0304	-0.0275
-2 σ		-0.3422	-0.2154	-0.1512	-0.1058	-0.0882	-0.0696	-0.0652	-0.0614	-0.0579	-0.0531
minimum occurrence		-0.4597	-0.3919	-0.3444	-0.2648	-0.2883	-0.2747	-0.2625	-0.2447	-0.2366	-0.2447

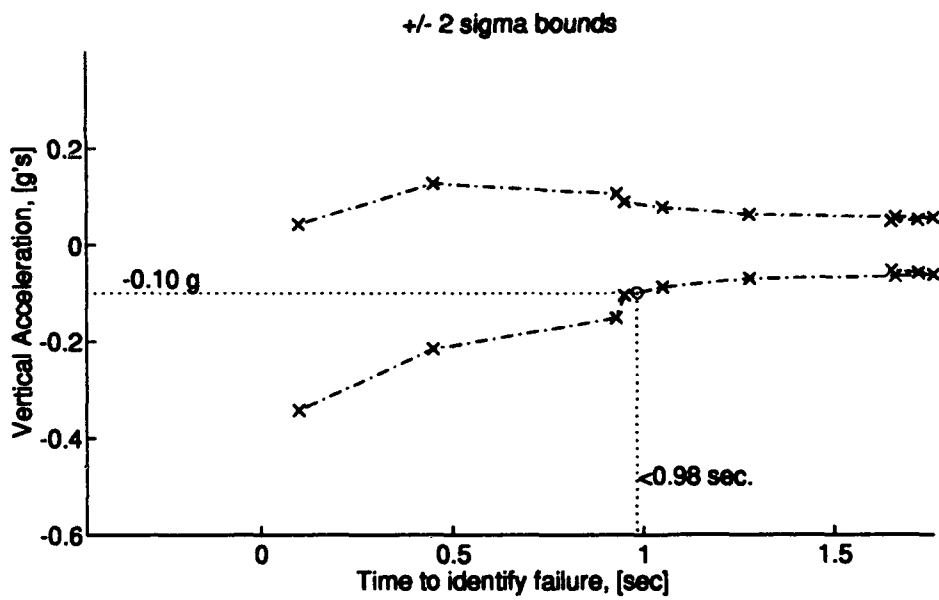
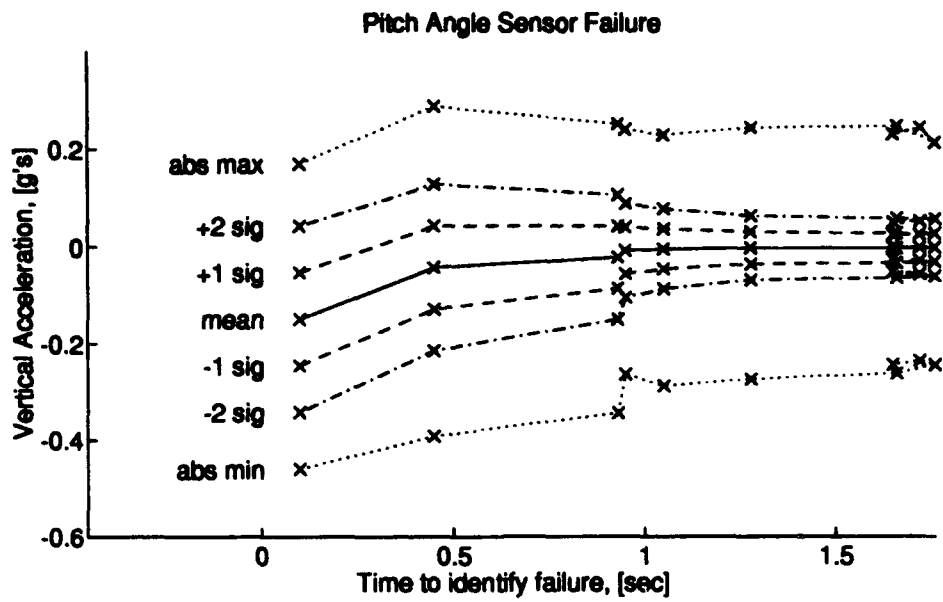


Figure 4.6 *g*-forces vs ID time for Pitch Angle Sensor failure as frequency changes.

Table 4.7 Results of varying dither frequency to alter Right Aileron Actuator failure identification time and horizontal g -forces.

Trial	1	2	3	4	5	6	7	8	9	10
Failure ID time [sec]	0.12	0.12	0.19	0.24	0.24	0.76	0.84	0.97	1.38	3.49
Aileron Dither										
Magnitude [deg/sec]	6.00	6.00	6.00	6.00	6.00	6.00	6.00	6.00	6.00	6.00
Frequency [rad/sec]	0.2262	0.4524	0.9048	1.8096	3.6193	6.8767	7.2386	9.0482	10.8579	14.4772
Horizontal Acceleration [g 's]										
maximum occurrence	1.0213	0.6315	0.7119	0.5459	0.7117	0.5410	0.5955	0.4925	0.4764	0.4967
+2 σ	0.7478	0.3367	0.3104	0.3055	0.3304	0.2479	0.1954	0.1275	0.1140	0.1058
+1 σ	0.5451	0.2188	0.1863	0.1696	0.1731	0.1291	0.1019	0.0675	0.0611	0.0557
mean	0.3424	0.1010	0.0623	0.0338	0.0158	0.0103	0.0085	0.0074	0.0083	0.0056
-1 σ	0.1398	-0.0169	-0.0618	-0.1021	-0.1416	-0.1084	-0.0849	-0.0526	-0.0446	-0.0445
-2 σ	-0.0629	-0.1348	-0.1859	-0.2379	-0.2989	-0.2272	-0.1784	-0.1126	-0.0975	-0.0946
minimum occurrence	-0.3622	-0.4607	-0.5458	-0.6222	-0.5920	-0.5108	-0.5675	-0.5087	-0.5025	-0.4797

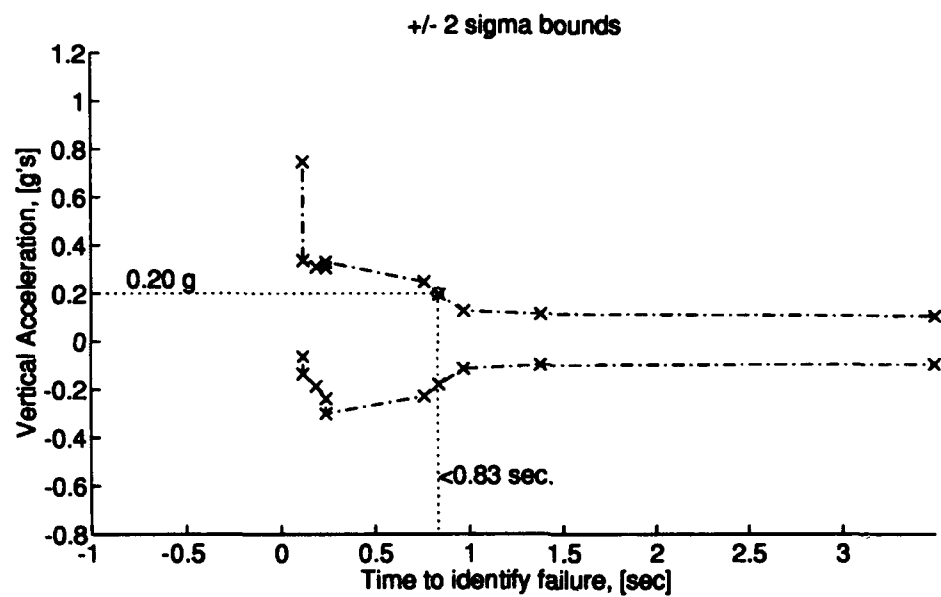
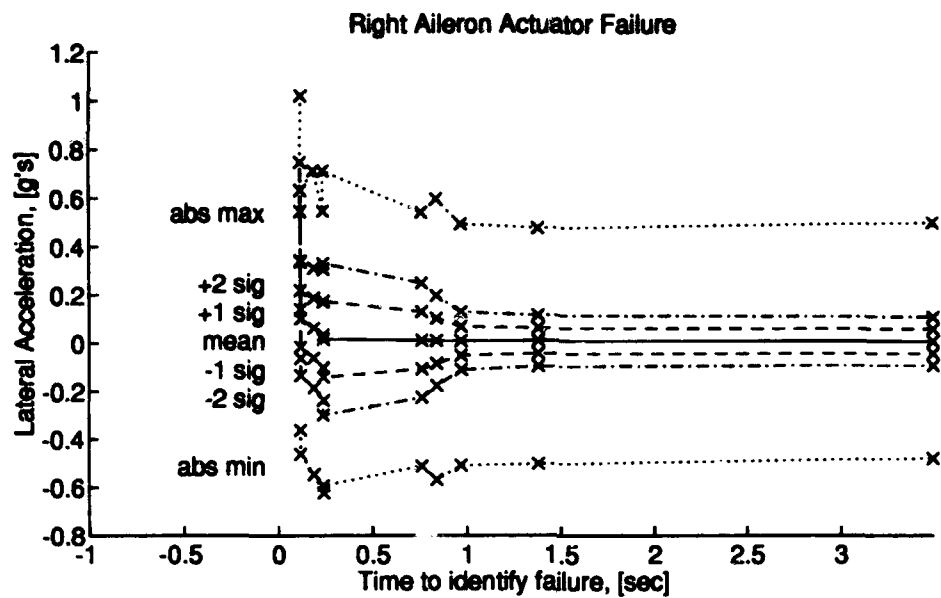


Figure 4.7 *g*-forces vs ID time for Right Aileron Actuator failure as frequency changes.

Table 4.8 Results of varying dither frequency to alter Left Aileron Actuator failure identification time and horizontal g -forces.

Trial	1	2	3	4	5	6	7	8	9	10
Failure ID time [sec]	0.12	0.12	0.17	0.23	0.23	0.68	0.75	0.78	0.75	1.42
Aileron Dither										
Magnitude [deg/sec]	6.00	6.00	6.00	6.00	6.00	6.00	6.00	6.00	6.00	6.00
Frequency [rad/sec]	0.2262	0.4524	0.9048	1.8096	3.6193	6.8767	7.2386	9.0482	10.8579	14.4772
Horizontal Acceleration [g 's]										
maximum occurrence	1.0213	0.6315	0.7119	0.5459	0.7117	0.5410	0.5955	0.4925	0.4764	0.4967
$+2\sigma$	0.7478	0.3367	0.3104	0.3055	0.3304	0.2479	0.1954	0.1275	0.1140	0.1058
$+1\sigma$	0.5451	0.2188	0.1863	0.1696	0.1731	0.1291	0.1019	0.0675	0.0611	0.0557
mean	0.3424	0.1010	0.0623	0.0338	0.0158	0.0103	0.0085	0.0074	0.0083	0.0056
-1σ	0.1398	-0.0169	-0.0618	-0.1021	-0.1416	-0.1084	-0.0849	-0.0526	-0.0446	-0.0445
-2σ	-0.0629	-0.1348	-0.1859	-0.2379	-0.2989	-0.2272	-0.1784	-0.1126	-0.0975	-0.0946
minimum occurrence	-0.3622	-0.4607	-0.5458	-0.6222	-0.5920	-0.5108	-0.5675	-0.5087	-0.5025	-0.4797

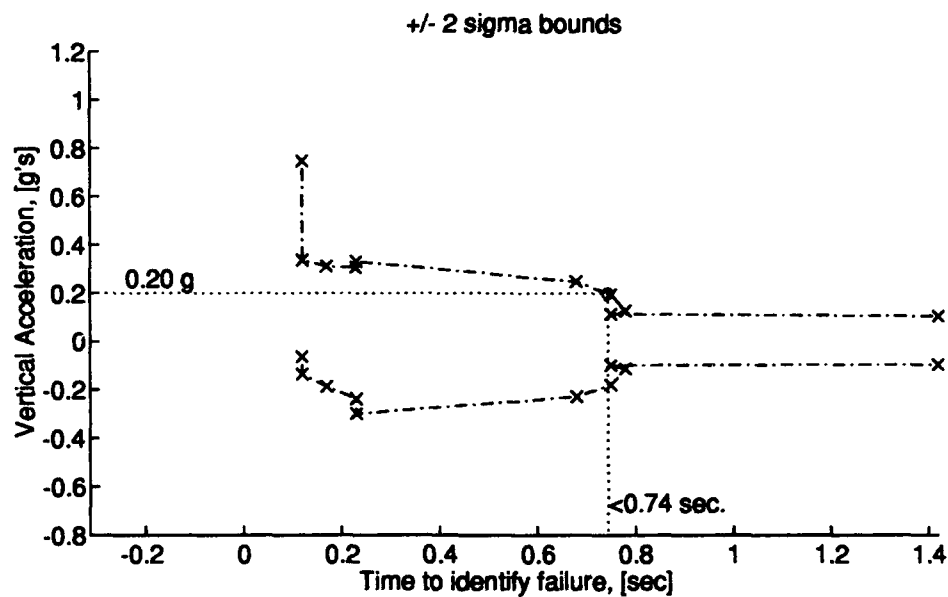
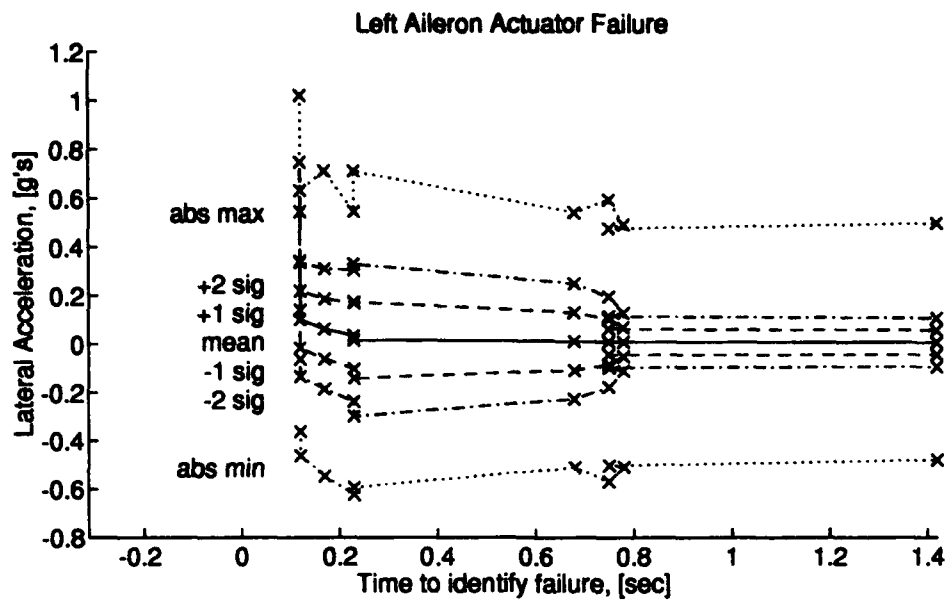


Figure 4.8 *g*-forces vs ID time for Left Aileron Actuator failure as frequency changes.

Table 4.9 Results of varying dither frequency to alter Right Rudder Actuator failure identification time and horizontal g -forces.

Trial	1	2	3	4	5	6	7	8	9	10
Failure ID time [sec]	0.22	0.33	0.26	0.32	0.56	2.50	2.75	8.00	8.00	8.00
Rudder Dither										
Magnitude [deg/sec]	6.00	6.00	6.00	6.00	6.00	6.00	6.00	6.00	6.00	6.00
Frequency [rad/sec]	0.2262	0.4524	0.9048	1.8096	3.6193	6.8767	7.2386	9.0482	10.8579	14.4772
Horizontal Acceleration [g 's]										
maximum occurrence	1.0213	0.6315	0.7119	0.5459	0.7117	0.5410	0.5955	0.4925	0.4764	0.4967
+2 σ	0.7478	0.3367	0.3104	0.3055	0.3304	0.2479	0.1954	0.1275	0.1140	0.1058
+1 σ	0.5451	0.2188	0.1863	0.1696	0.1731	0.1291	0.1019	0.0675	0.0611	0.0557
mean	0.3424	0.1010	0.0623	0.0338	0.0158	0.0103	0.0085	0.0074	0.0083	0.0056
-1 σ	0.1398	-0.0169	-0.0618	-0.1021	-0.1416	-0.1084	-0.0849	-0.0526	-0.0446	-0.0445
-2 σ	-0.0629	-0.1348	-0.1859	-0.2379	-0.2989	-0.2272	-0.1784	-0.1126	-0.0975	-0.0946
minimum occurrence	-0.3622	-0.4607	-0.5458	-0.6222	-0.5920	-0.5108	-0.5675	-0.5087	-0.5025	-0.4797

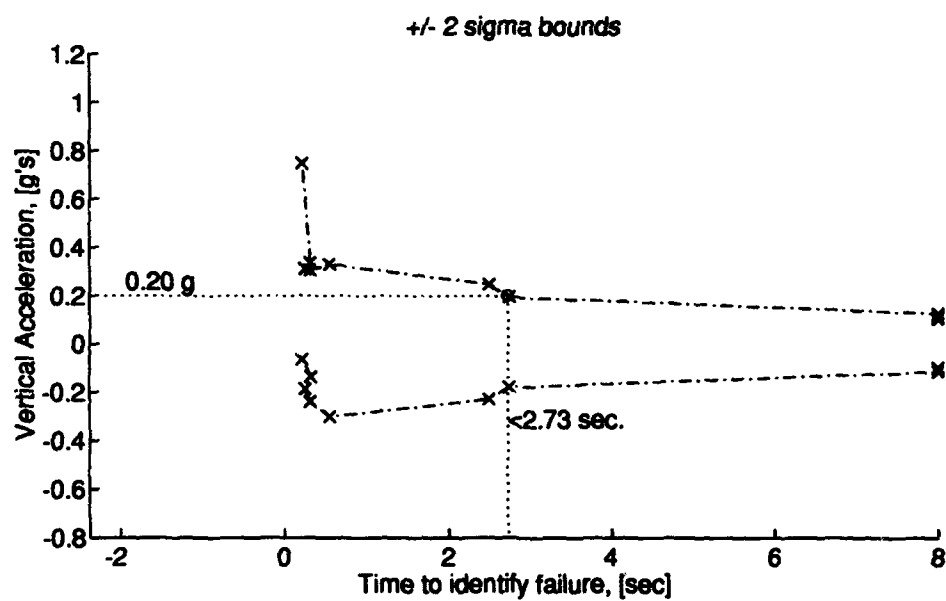
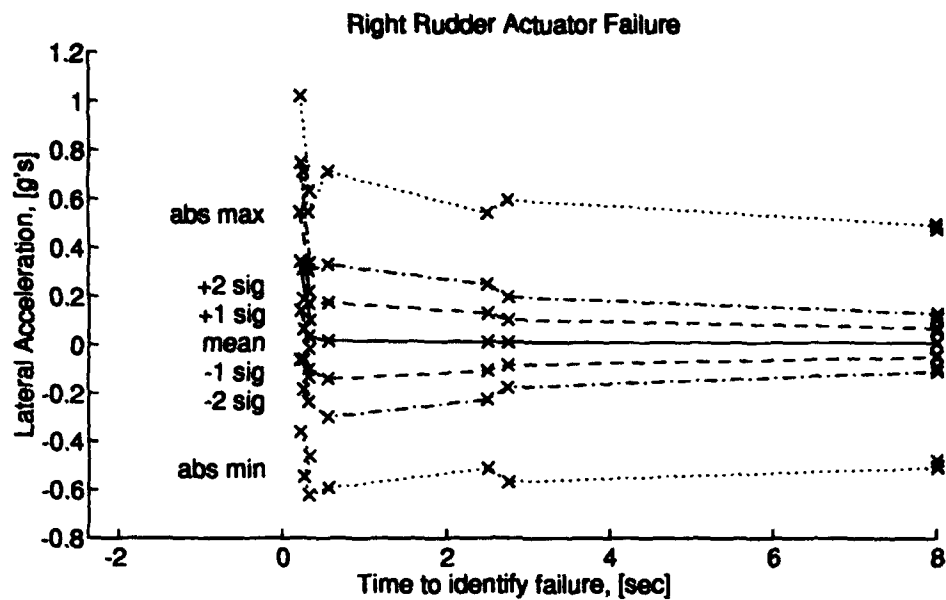


Figure 4.9 *g*-forces vs ID time for Right Rudder Actuator failure as frequency changes.

Table 4.10 Results of varying dither frequency to alter Left Rudder Actuator failure identification time and horizontal g -forces.

Trial	1	2	3	4	5	6	7	8	9	10
Failure ID time [sec]	0.23	0.31	0.26	0.33	0.53	3.73	5.34	8.00	8.00	8.00
Rudder Dither										
Magnitude [deg/sec]	6.00	6.00	6.00	6.00	6.00	6.00	6.00	6.00	6.00	6.00
Frequency [rad/sec]	0.2262	0.4524	0.9048	1.8096	3.6193	6.8767	7.2386	9.0482	10.8579	14.4772
Horizontal Acceleration [g 's]										
maximum occurrence	1.0213	0.6315	0.7119	0.5459	0.7117	0.5410	0.5955	0.4925	0.4764	0.4967
+2 σ	0.7478	0.3367	0.3104	0.3055	0.3304	0.2479	0.1954	0.1275	0.1140	0.1058
+1 σ	0.5451	0.2188	0.1863	0.1696	0.1731	0.1291	0.1019	0.0675	0.0611	0.0557
mean	0.3424	0.1010	0.0623	0.0338	0.0158	0.0103	0.0085	0.0074	0.0083	0.0056
-1 σ	0.1398	-0.0169	-0.0618	-0.1021	-0.1416	-0.1084	-0.0849	-0.0526	-0.0446	-0.0445
-2 σ	-0.0629	-0.1348	-0.1859	-0.2379	-0.2989	-0.2272	-0.1784	-0.1126	-0.0975	-0.0946
minimum occurrence	-0.3622	-0.4607	-0.5458	-0.6222	-0.5920	-0.5108	-0.5675	-0.5087	-0.5025	-0.4797

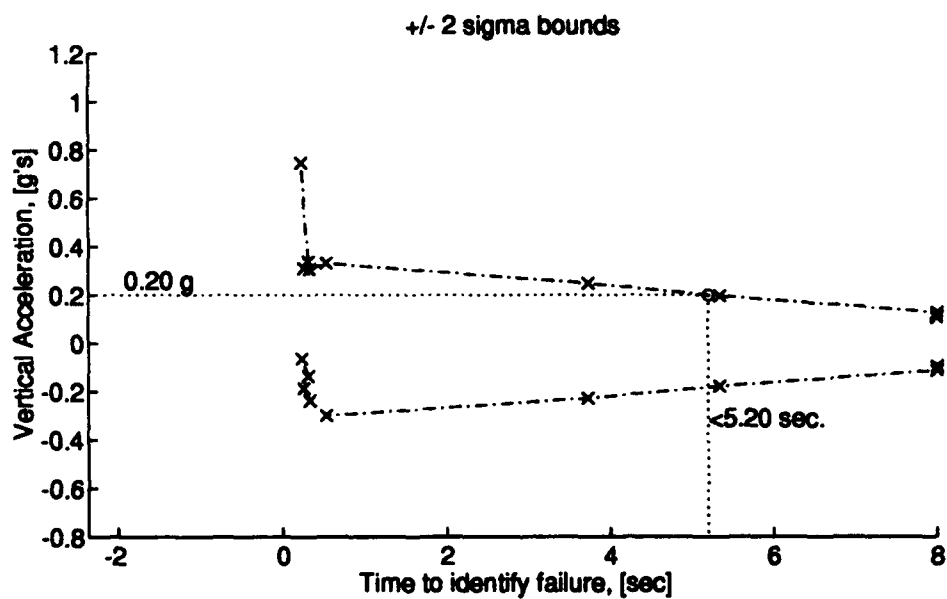
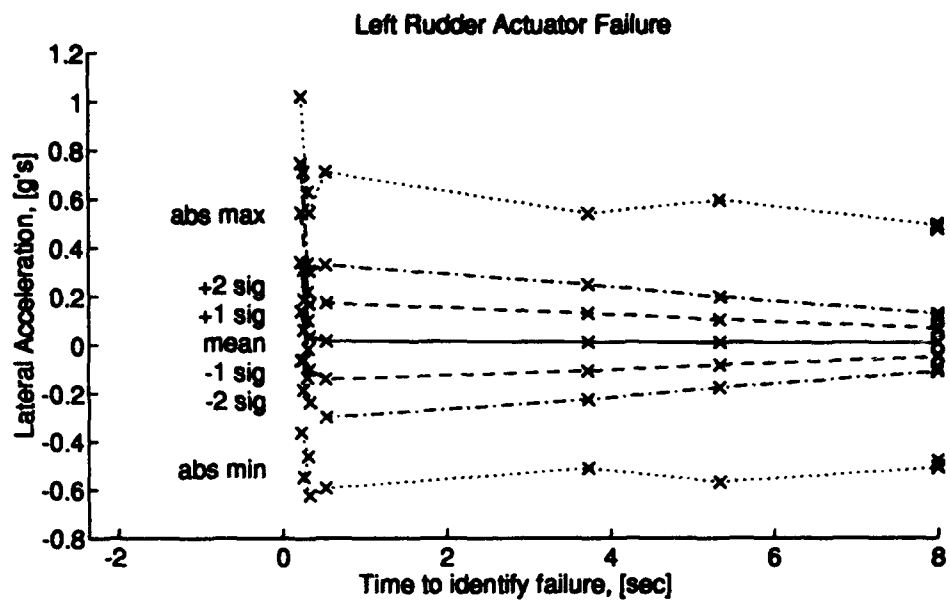


Figure 4.10 *g*-forces vs ID time for Left Rudder Actuator failure as frequency changes.

Table 4.11 Results of varying dither frequency to alter Sideslip Angle Sensor failure identification time and horizontal g -forces.

Trial	1	2	3	4	5	6	7	8	9	10
Failure ID time [sec]	1.89	1.04	1.98	1.25	1.77	3.58	3.43	3.89	3.86	3.90
Aileron Dither										
Magnitude [deg/sec]	6.00	6.00	6.00	6.00	6.00	6.00	6.00	6.00	6.00	6.00
Frequency [rad/sec]	0.2262	0.4524	0.9048	1.8096	3.6193	6.8767	7.2386	9.0482	10.8579	14.4772
Rudder Dither										
Magnitude [deg/sec]	6.00	6.00	6.00	6.00	6.00	6.00	6.00	6.00	6.00	6.00
Frequency [rad/sec]	0.2262	0.4524	0.9048	1.8096	3.6193	6.8767	7.2386	9.0482	10.8579	14.4772
Horizontal Acceleration [g 's]										
maximum occurrence	1.0213	0.6315	0.7119	0.5459	0.7117	0.5410	0.5955	0.4925	0.4764	0.4967
+2 σ	0.7478	0.3367	0.3104	0.3055	0.3304	0.2479	0.1954	0.1275	0.1140	0.1058
+1 σ	0.5451	0.2188	0.1863	0.1696	0.1731	0.1291	0.1019	0.0675	0.0611	0.0557
mean	0.3424	0.1010	0.0623	0.0338	0.0153	0.0103	0.0085	0.0074	0.0083	0.0056
-1 σ	0.1398	-0.0169	-0.0618	-0.1021	-0.1416	-0.1084	-0.0849	-0.0526	-0.0446	-0.0445
-2 σ	-0.0629	-0.1348	-0.1859	-0.2379	-0.2989	-0.2272	-0.1784	-0.1126	-0.0975	-0.0946
minimum occurrence	-0.3622	-0.4607	-0.5458	-0.6222	-0.5920	-0.5108	-0.5675	-0.5087	-0.5025	-0.4797

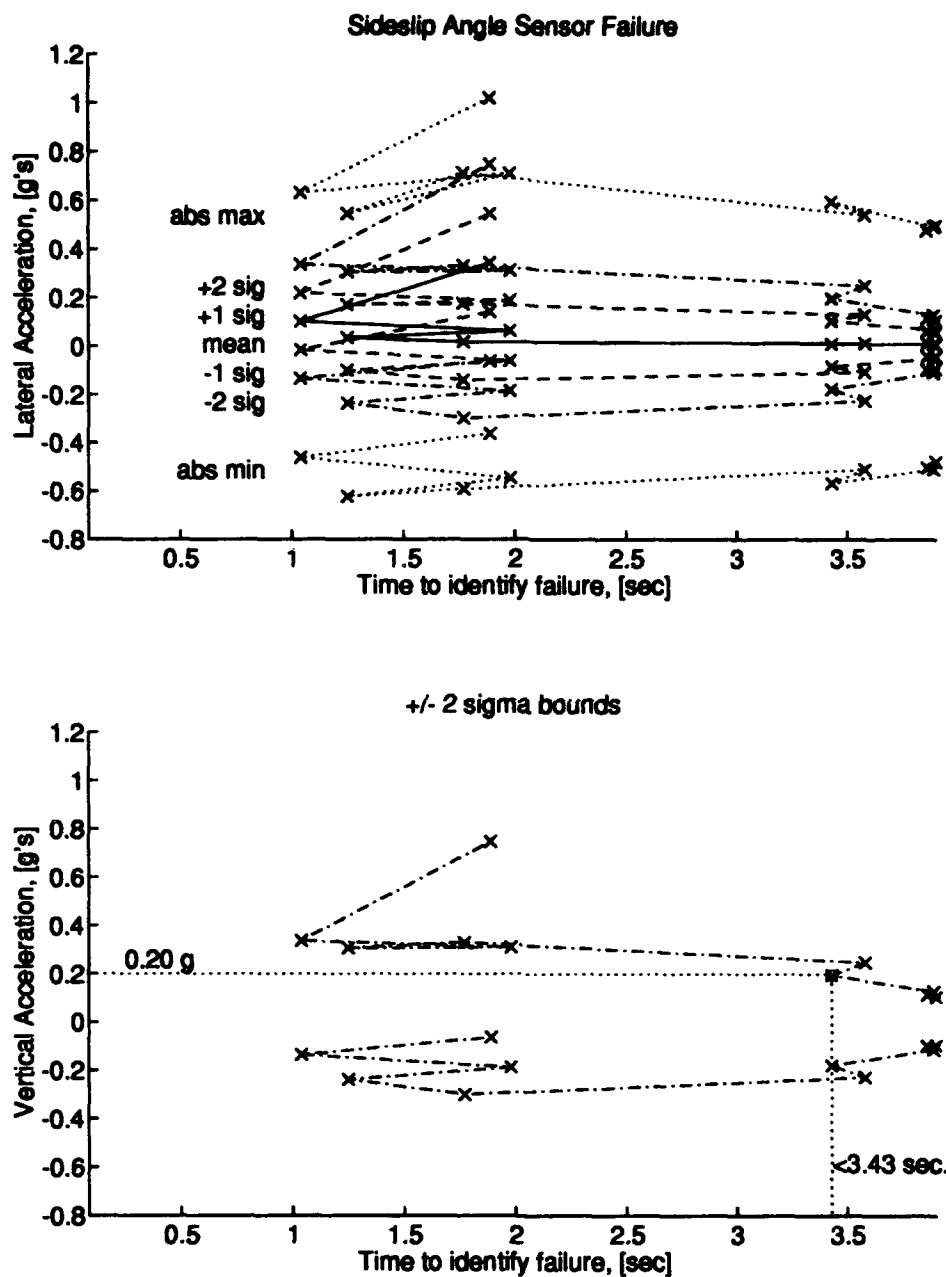


Figure 4.11 *g*-forces vs ID time for Sideslip Angle Sensor failure as frequency changes.

Table 4.12 Results of varying dither frequency to alter Roll Rate Sensor failure identification time and horizontal *g*-forces.

Trial	1	2	3	4	5	6	7	8	9	10
Failure ID time [sec]	0.29	0.68	0.72	0.72	0.70	0.72	0.87	0.72	0.67	0.83
Aileron Dither										
Magnitude [deg/sec]	6.00	6.00	6.00	6.00	6.00	6.00	6.00	6.00	6.00	6.00
Frequency [rad/sec]	0.2262	0.4524	0.9048	1.8096	3.6193	6.8767	7.2386	9.0482	10.8579	14.4772
Rudder Dither										
Magnitude [deg/sec]	6.00	6.00	6.00	6.00	6.00	6.00	6.00	6.00	6.00	6.00
Frequency [rad/sec]	0.2262	0.4524	0.9048	1.8096	3.6193	6.8767	7.2386	9.0482	10.8579	14.4772
Horizontal Acceleration [<i>g</i> 's]										
maximum occurrence	1.0213	0.6315	0.7119	0.5459	0.7117	0.5410	0.5955	0.4925	0.4764	0.4967
+2 σ	0.7478	0.3367	0.3104	0.3055	0.3304	0.2479	0.1954	0.1275	0.1140	0.1058
+1 σ	0.5451	0.2188	0.1863	0.1696	0.1731	0.1291	0.1019	0.0675	0.0611	0.0557
mean	0.3424	0.1010	0.0623	0.0338	0.0158	0.0103	0.0085	0.0074	0.0083	0.0056
-1 σ	0.1398	-0.0169	-0.0618	-0.1021	-0.1416	-0.1084	-0.0849	-0.0526	-0.0446	-0.0445
-2 σ	-0.0629	-0.1348	-0.1859	-0.2379	-0.2989	-0.2272	-0.1784	-0.1126	-0.0975	-0.0946
minimum occurrence	-0.3622	-0.4607	-0.5458	-0.6222	-0.5920	-0.5108	-0.5675	-0.5087	-0.5025	-0.4797

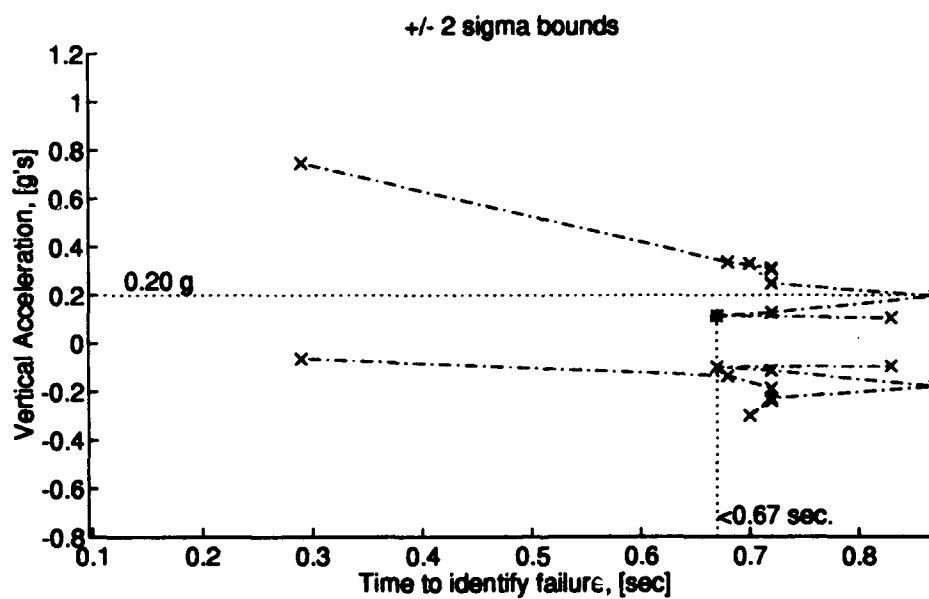
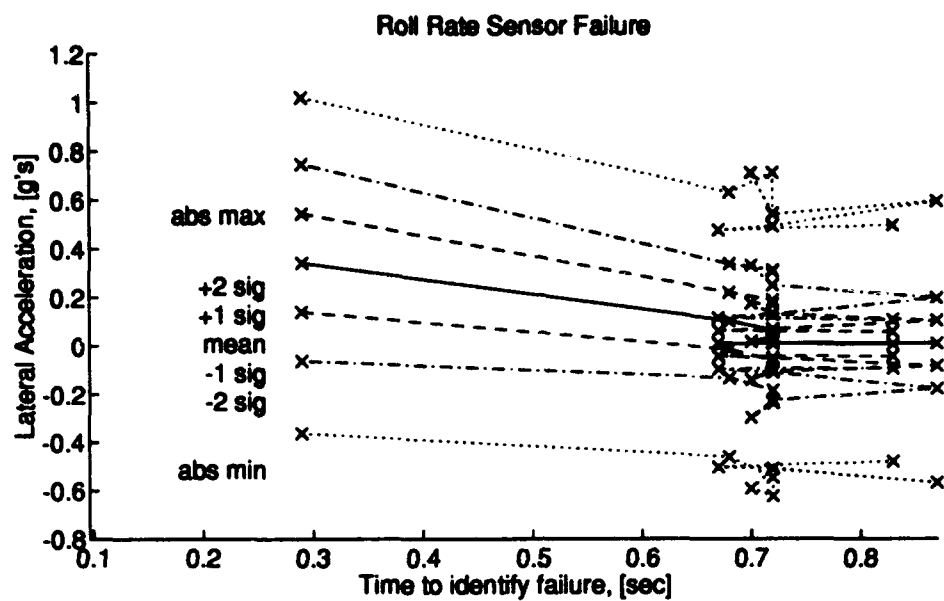


Figure 4.12 *g*-forces *vs* ID time for Roll Rate Sensor failure as frequency changes.

Table 4.13 Results of varying dither frequency to alter Roll Angle Sensor failure identification time and horizontal g -forces.

Trial	1	2	3	4	5	6	7	8	9	10
Failure ID time [sec]	0.10	0.10	0.20	0.17	0.80	1.01	1.19	0.96	1.07	1.28
Aileron Dither										
Magnitude [deg/sec]	6.00	6.00	6.00	6.00	6.00	6.00	6.00	6.00	6.00	6.00
Frequency [rad/sec]	0.2262	0.4524	0.9048	1.8096	3.6193	6.8767	7.2386	9.0482	10.8579	14.4772
Rudder Dither										
Magnitude [deg/sec]	6.00	6.00	6.00	6.00	6.00	6.00	6.00	6.00	6.00	6.00
Frequency [rad/sec]	0.2262	0.4524	0.9048	1.8096	3.6193	6.8767	7.2386	9.0482	10.8579	14.4772
Horizontal Acceleration [g 's]										
maximum occurrence	1.0213	0.6315	0.7119	0.5459	0.7117	0.5410	0.5955	0.4925	0.4764	0.4967
+2 σ	0.7478	0.3367	0.3104	0.3055	0.3304	0.2479	0.1954	0.1275	0.1140	0.1058
+1 σ	0.5451	0.2188	0.1863	0.1696	0.1731	0.1291	0.1019	0.0675	0.0611	0.0557
mean	0.3424	0.1010	0.0623	0.0338	0.0158	0.0103	0.0085	0.0074	0.0083	0.0056
-1 σ	0.1398	-0.0169	-0.0618	-0.1021	-0.1416	-0.1084	-0.0849	-0.0526	-0.0446	-0.0445
-2 σ	-0.0629	-0.1348	-0.1859	-0.2379	-0.2989	-0.2272	-0.1784	-0.1126	-0.0975	-0.0946
minimum occurrence	-0.3622	-0.4607	-0.5458	-0.6222	-0.5920	-0.5108	-0.5675	-0.5087	-0.5025	-0.4797

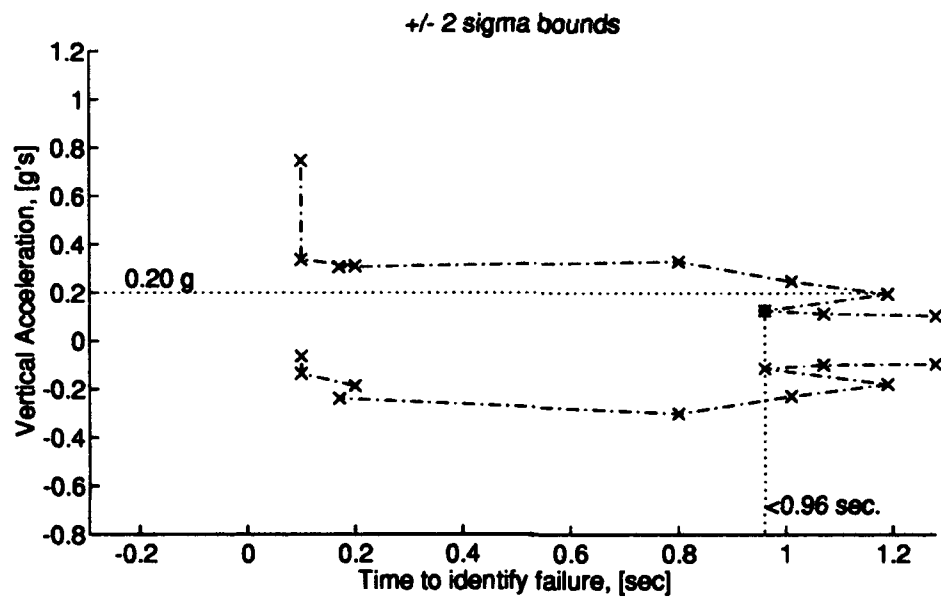
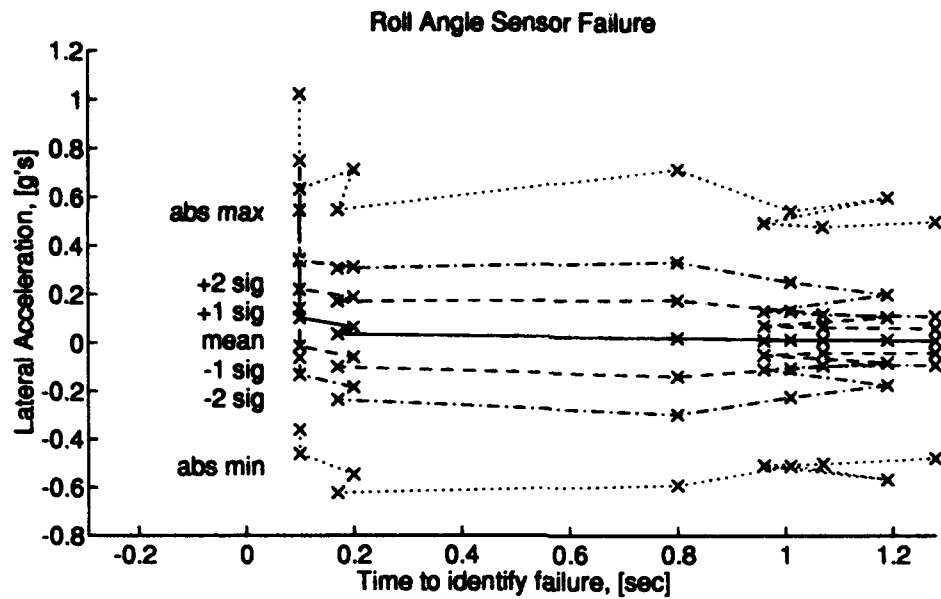


Figure 4.13 *g*-forces *vs* ID time for Roll Angle Sensor failure as frequency changes.

Table 4.14 Results of varying dither frequency to alter Yaw Rate Sensor failure identification time and horizontal g -forces.

	Trial									
	1	2	3	4	5	6	7	8	9	10
Failure ID time [sec]	0.79	0.94	1.18	0.83	0.75	1.18	1.17	1.25	1.26	1.30
Aileron Dither										
Magnitude [deg/sec]	6.00	6.00	6.00	6.00	6.00	6.00	6.00	6.00	6.00	6.00
Frequency [rad/sec]	0.2262	0.4524	0.9048	1.8096	3.6193	6.8767	7.2386	9.0482	10.8579	14.4772
Rudder Dither										
Magnitude [deg/sec]	6.00	6.00	6.00	6.00	6.00	6.00	6.00	6.00	6.00	6.00
Frequency [rad/sec]	0.2262	0.4524	0.9048	1.8096	3.6193	6.8767	7.2386	9.0482	10.8579	14.4772
Horizontal Acceleration [g 's]										
maximum occurrence	1.0213	0.6315	0.7119	0.5459	0.7117	0.5410	0.5955	0.4925	0.4764	0.4967
+2 σ	0.7478	0.3367	0.3104	0.3055	0.3304	0.2479	0.1954	0.1275	0.1140	0.1058
+1 σ	0.5451	0.2188	0.1863	0.1696	0.1731	0.1291	0.1019	0.0675	0.0611	0.0557
mean	0.3424	0.1010	0.0623	0.0338	0.0158	0.0103	0.0085	0.0074	0.0083	0.0056
-1 σ	0.1398	-0.0169	-0.0618	-0.1021	-0.1416	-0.1084	-0.0849	-0.0526	-0.0446	-0.0445
-2 σ	-0.0629	-0.1348	-0.1859	-0.2379	-0.2989	-0.2272	-0.1784	-0.1126	-0.0975	-0.0946
minimum occurrence	-0.3622	-0.4607	-0.5458	-0.6222	-0.5920	-0.5108	-0.5675	-0.5087	-0.5025	-0.4797

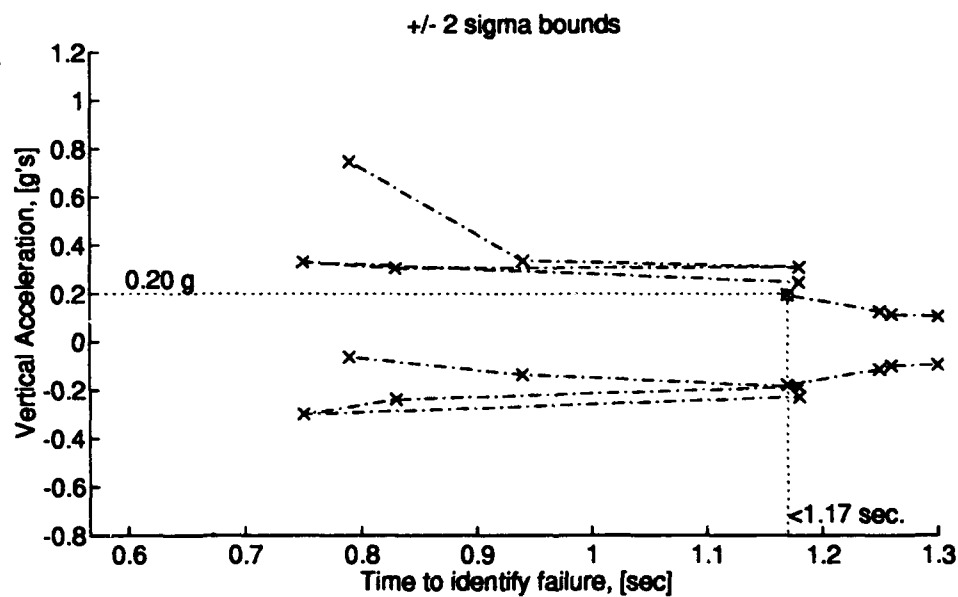
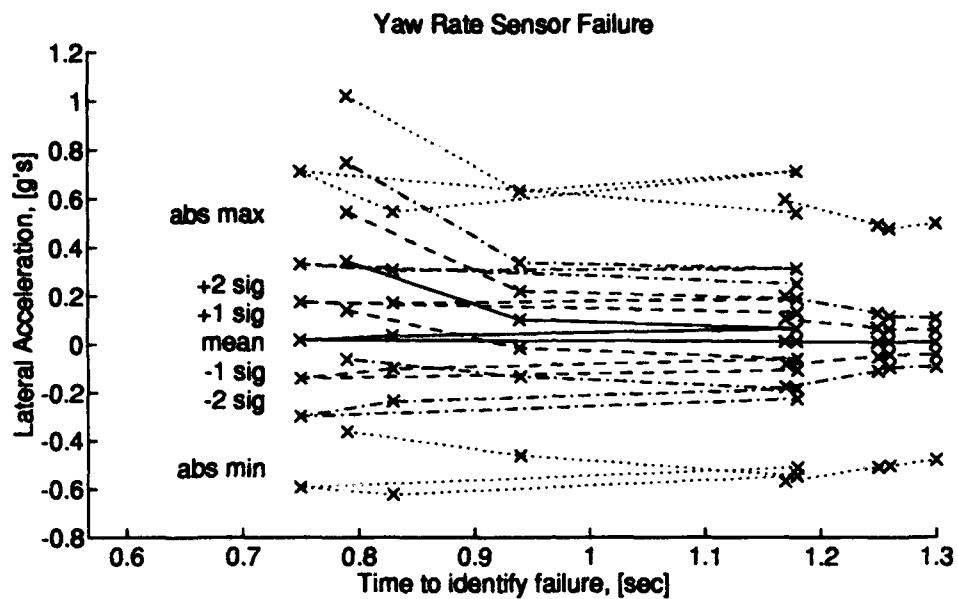


Figure 4.14 *g*-forces *vs* ID time for Yaw Rate Sensor failure as frequency changes.

4.2.1 Analysis of MMAE Performance Against Varying Dither Frequency. The data presented in the previous pages is now analyzed with the purpose of determining the optimal combination of sinusoidal dither frequency and magnitude. Criteria are that vertical g -forces do not exceed $0.1g$, horizontal g -forces do not exceed $0.2g$, the aircraft remains stable while being dithered in the fully functional configuration, false alarms are minimized, failure identification time is minimized, and travel limits on control surface deflections are not violated. MMAE performance on each failure condition is analyzed in detail to determine the best dither for the particular failure, then the results of the individual analyses are combined to arrive at a best overall dither. We begin with the longitudinal channel.

For the *right and left elevator actuator failures*, a trend toward faster failure identification times as frequency decreases is broken at Trial 3 where $\omega = 1.6653$, as seen in Figure 4.1 and Table 4.1, as well as Figure 4.2 and Table 4.2. Of special note here is that the commanded elevator angles violate the limits given in Table 3.2 at the low frequency dithers of Trials 1, 2, and 3.

The elevator travel limit violation is due to the out-of-phase dither and the effect of the flight control system. Recall that the longitudinal flight control system is divided into left and right channels (Section 3.2.2). While each channel *commands its own surface*, both channels are controlling the same aircraft state, q , pitch rate. If the pitch rate desired by both channels is not the same, extra elevator surface deflection is commanded by each flight control system channel to achieve their desired, but respectively different, commanded pitch rates. One channel tries to overpower the other. This is not a problem at higher frequencies because of the lag of the flight control system. Here, the high commanded pitch rate changes to a low rate before the elevator can be commanded to deflect outside of its limits. This lag effect ceases to keep elevator surfaces within limits at low frequencies. However, instead of stopping at the limit, our linearized discrete-time aircraft truth model of Equation (3.1) allows for out-of-limit commands. Therefore, responsibility lies with the researcher to check the commanded surface deflections manually. Routines to warn of control surface position and rate limits could have been added to the software, however, the additional computational load would increase the time required to run simulations, and the state-space model provided by Simulink [9] does not facilitate monitoring or modification of intermediate states easily.

Besides the limit violations at low frequencies, Figure 4.1 exhibits a shallow slope across the higher frequencies. This would indicate that failure identification time is not a function of g -loading. Rather, failure identification times seems to be more related to the degree of surface deflection. Indeed, detailed analysis reveals that the elevator surface movements occupy a greater percentage of the deflection range on simulations yielding shorter identification times than of those with longer identification times. And, as discussed above, lower frequency dithers result in greater surface deflection for the same dither magnitude.

For the *forward velocity sensor failure*, a random cluster of failure identification times between Trials 4 and 10 is noted in Figure 4.3 and Table 4.3. This lack of definite trend in failure identification times for frequencies above $\omega = 3.3306$ rad/sec may be explained by the Bode plot of forward velocity response to elevator deflections $|u(\omega)/\delta_e(\omega)|$ shown in Figure B.1. The response beyond $\omega = 3$ rad/sec is more than 50 dB below the peak magnitude. With such a small response to elevator input, one would expect the random system inputs to exercise more influence over MMAE failure identification times than the elevator dithers.

At the lower end of the spectrum for dither frequency, failure identification times go solidly to 0.10 sec, which is the shortest time possible with our MMAE design (see Subsection 3.3.1). Our conclusion, therefore, is that short forward velocity failure identification times will be realized with decreasing dither frequency.

For the *angle of attack sensor*, failure identification times are well correlated with the Bode plot of angle of attack response to elevator input shown in Figure B.2. Note that the $|\alpha(\omega)/\delta_e(\omega)|$ response has a steep drop-off after $\omega = 7$ rad/sec. This frequency corresponds closely with Trial 5 of Table 4.4. Failure identification times at lower frequencies are consistently short while those at higher frequencies are an order of magnitude longer. Thus, we see a close correlation between the $|\alpha(\omega)/\delta_e(\omega)|$ magnitude response and angle of attack failure identification time.

For the *pitch rate sensor failure*, a different trend is noted. Figure 4.5 and Table 4.5 show a definite reversal of the trend towards shorter failure identification times with lower frequency dithers. A study of the Bode plot for pitch rate response to elevator input $|q(\omega)/\delta_e(\omega)|$ shown in Figure B.3 does not explain this reversal. The magnitude response might suggest a failure identification time trend that is inverse to that of actual testing, considering only the discrete

frequencies tested. That is, the dip in response magnitude between 0.5 rad/sec and 3 rad/sec might lead one to predict longer failure identification times for these frequencies. However, this is not the case. Rather, the *best* identification times are found in this interval.

Why does the pitch rate sensor behave differently from the other sensors? An explanation is supported by the fact that the pitch rate state is controlled by and provides feedback to the flight control system. A thorough discussion is found in Section 5.2.

For the *pitch angle sensor failure*, the trend is consistent with that found for the forward velocity sensor. Indeed these two sensors have similar responses to elevator inputs (see Figures B.4 and B.1) and neither sensor provides feedback to the flight control system.

With the characteristics of each type of failure identification in mind, we now move toward selecting the optimal frequency and magnitude of the sinusoidal dither to be applied to the longitudinal channel. Only one set of parameters will be chosen because (a) elevators are the only means of inputting dithers, and (b) we must limit the scope of our research. A better solution may be to superimpose one sinusoid of differing frequency and magnitude on another sinusoid, by means of a linear combination for example.

For the elevators, the limiting factor is control surface travel limit violations at low frequencies. The best dither could be at $\omega = 3.3306$ or $\omega = 6.6611$. Both Trials 4 and 5 of Table 4.1 show that the vertical g -limits of 0.1 g are not violated except in Trial 4 where -2σ is 0.1058, accepted as within limits due to the course discretization of the test parameter space. The forward velocity sensor, angle of attack sensor, and pitch angle sensor failures are more quickly identified at very low frequencies. So, this factor will direct us to a lower frequency, if given a choice.

Finally, the fastest pitch angle failure identification time is detected at a dither frequency of $\omega = 1.6653$. However, the vertical g -limits are broken at this frequency, as shown in Trial 3 at Table 4.5. The elevator failure identification time at this frequency is not significantly different from that of $\omega = 3.3306$. The elevator surface travel limit violation at this frequency may be resolved by lowering the magnitude of dither at $\omega = 1.6653$, which must be done anyway to reduce g -loading to within limits. So, we are left with a choice: in order to meet the vertical g -limits, do we lower the dither magnitude at $\omega = 1.6653$, or do we increase the dither frequency to $\omega = 3.3306$?

Table 4.15 Comparison of Reducing Dither Magnitude *versus* Increasing Dither Frequency to Reduce Vertical *g*-forces.

Trial	3	3.1	3.2	4
Elevator Dither				
Magnitude [deg/sec]	6.00	5.00	4.00	6.00
Frequency [rad/sec]	1.6653	1.6653	1.6653	3.3306
Failure ID Time [sec]				
A1	0.24	0.29	0.33	0.22
A2	0.23	0.25	0.29	0.20
S1	0.58	0.83	0.93	1.17
S2	0.10	1.34	2.26	0.68
S3	0.33	0.42	0.47	0.37
S4	0.93	1.05	1.19	0.95
Vertical Acceleration [<i>g</i>'s]				
+2 σ	0.1053	0.0839	0.0722	0.0878
-2 σ	-0.1512	-0.0904	-0.0777	-0.1058

Additional simulations with $\omega = 1.6553$ and dither magnitudes of 5 deg/sec and 4 deg/sec were made. The results are found in Appendix D but are compiled in Table 4.15 for our convenience. Trials 3.1, 3.2, and 4 all fall within *g*-limits. Trial 3.2 merely illustrates the trend toward longer failure identification times with decreasing dither magnitude. So, of Trial 3.1 (reduced magnitude) and Trial 4 (increased frequency), which yields better failure identification times in general? Except for the forward velocity sensor, S1, all failures were identified more quickly at a dither with a magnitude of 6 deg/sec and at a frequency of 3.3306 rad/sec. Thus, our optimal longitudinal dither is concluded and stated in Equation (4.6), on page 4-42.

Our next task is to find an optimal dither for the lateral channel by specifying a sinusoidal frequency and magnitude. This dither will be applied to both channels of the roll rate command and both channels of yaw angle command, as shown in Figure 3.1.

First, we consider the *aileron actuator failures*. Unlike the elevators, the aileron surfaces were never commanded outside of their limits (see Table 3.2) for any set of test conditions. However, 63% of their range is used when dithering at the low frequency of 0.2262 rad/sec and roll rate dither magnitude is 6 rad/sec. As seen in Figures 4.7 and 4.8 and Tables 4.7 and 4.8, shorter failure identification times are realized with lower frequency dithers. As frequency decreases though, the "brick wall" effect is seen at about Trial 5 where $\omega = 3.6193$. Similar analysis applies to the *rudder*

actuator failures. Trial 5 marks the point where little gain in failure identification time is realized for a large penalty in horizontal g -loading. Still, the $\pm 2\sigma$ bounds of Trial 5 are outside of the ± 0.20 horizontal g -limit. Frequency must be increased to 7.2386 rad/sec, as in Trial 7, before the $\pm 2\sigma$ bounds of g -loading are within limits.

The *sideslip angle sensor failure* data is shown in Figure 4.11 and Table 4.11. This sensor provides feedback to the flight control system so that the sideslip angle aircraft state may be controlled. The erratic distribution of failure identification times at both ends of the spectrum might be explained by the poor quality of sideslip angle sensor measurements. As seen in Table 3.3 on page 3-7, the variance associated with the sideslip angle sensor, R_β , is the worst of all angle sensors. If sensor measurements are very noisy, the Kalman filter is more inclined to believe its internal model rather than the information found in incoming measurements. The fully functional filter residuals generally remain unchanged in character through an induced sideslip angle sensor failure, except for the r_β residual. This residual generates a short duration spike which is likely to be disregarded by the Kalman filter. The only remaining clue to a change in performance is found in the r_β residual of the filter hypothesizing a sideslip angle sensor failure, which immediately goes to zero-mean, low variance. There is a definite shift of failure times to the right with increasing dither frequency in Figure 4.11. This information is useful in helping us to select Trial 4 or 5 as having the best, most reliable dither parameters.

For the *roll rate sensor failure*, Figure 4.12 and Table 4.12 show that the identification times are clustered around 0.7 and 0.8 seconds. Were it not for Trial 1, no trend could be detected. Therefore, we will not conclude that there is a trend except that, regardless of frequency chosen, an identification time of around 0.75 seconds will result. Again, this sensor provides feedback to the flight control system.

The *roll angle sensor failure* identification times can be correlated to the Bode plot of $|\phi(\omega)/\delta_a(\omega)|$ in Figure B.7. At low frequencies there are high gains and short identification times.

The $\pm 2\sigma$ trace of Figure 4.13 has a "Z"-shape around Trials 6, 7, 8, and 9. This gives the impression that there is some notch dither frequency where the MMAE has better response than at the surrounding dither frequencies. This is not likely to be the case. Random effects of wind gusting may play a bigger part in failure identification times since the aileron surfaces are commanded to

deflect over only 8% of their travel range for each of Trials 6 through 10. The useful conclusion here is that lower frequency dithers yield better failure identification times.

The *yaw rate sensor failure* is a unique situation. Although the yaw rate sensor provides feedback to the flight control system, the low frequency output of this sensor is attenuated by the washout filter. This is a high pass filter with a break frequency at about 1 rad/sec. The impact is that, for rudder dither frequencies below 1 rad/sec, a yaw rate sensor failure might be treated like the failure of a sensor that is not providing feedback to the flight control system. That is, under this condition, scalar residual monitoring in the fully-functional-aircraft filter could be used effectively.

Table 4.14 and Figure 4.14 reveal a definite "Z"-shape pattern with Trials 1, 2, and 3 making up the top, Trials 3, 4, and 5 defining the diagonal, and Trials 5, 6, and 7 tracing the bottom. An interesting correlation is made with the Bode plot of Figure B.12. Specifically, the magnitude transition from the local minimum at 0.4 rad/sec to the local maximum at 3.7 rad/sec contains the frequencies of Trials 3, 4, and 5, the diagonal of the "Z" of Figure 4.14. Further study provides one with convincing evidence that the Bode log-magnitude plot correlates with the failure identification times. So, even though the yaw rate sensor provides feedback to the flight control system, because the low frequencies are attenuated, this allows the MMAE response to a yaw rate sensor failure to be more like that of a sensor that does not provide feedback to the flight control system. The "Z" of Figure 4.14 is valid, so our best dither for the yaw rate sensor failure is that of Trial 5.

In summation, the lateral channel components compel us to choose the dither frequency of Trial 5, 3.6193 rad/sec, as the best candidate for optimal dither. However, the horizontal g -load caused by the parameters of Trial 5 are outside of the $\pm 0.2g$ limits. Again, we must decide whether to lower the dither magnitude or increase the dither frequency to that of Trial 7 in order to meet this criterion. Table 4.16 presents the compiled results of varying dither magnitude at the Trial 5 frequency, along with the results of Trial 7 for comparison. The details of Trials 5 through 5.3 are presented in Figures D.7 through D.14, with companion Tables D.7 through D.14, in Appendix D. Referring to Table 4.16, we see that the 5-series trial with the lowest failure identification times and g -forces within limits is Trial 5.2. The $+2\sigma$ bound is violated but judged acceptable in light of the coarsely discretized dither magnitude space. Comparison of the failure identification times

Table 4.16 Comparison of Reducing Dither Magnitude *versus* Increasing Dither Frequency to Reduce Horizontal *g*-forces.

Trial	5	5.1	5.2	5.3	7
Aileron Dither					
Magnitude [deg/sec]	6.00	4.00	3.00	2.00	6.00
Frequency [rad/sec]	3.6193	3.6193	3.6193	3.6193	7.2386
Rudder Dither					
Magnitude [deg/sec]	6.00	4.00	3.00	2.00	6.00
Frequency [rad/sec]	3.6193	3.6193	3.6193	3.6193	7.2386
Failure ID Time [sec]					
A3	0.24	0.52	0.79	1.87	0.84
A4	0.23	0.30	0.36	0.99	0.75
A5	0.56	0.90	1.20	1.72	2.75
A6	0.53	1.00	1.40	2.38	5.34
S5	1.77	2.42	2.78	3.53	3.43
S6	0.70	0.75	0.69	0.73	0.87
S7	0.80	0.27	0.22	1.51	1.19
S8	0.75	0.85	0.97	1.11	1.17
Horizontal Acceleration [<i>g</i>'s]					
+2 σ	0.3304	0.2631	0.2043	0.1476	0.1954
-2 σ	-0.2989	-0.1802	-0.1399	-0.1343	-0.1784

in Trial 5.2 with Trial 7 tells us that the best choice is to reduce the dither magnitude rather than increase the dither frequency to meet the *g*-limits.

Therefore, the optimal dither for the lateral channel will have magnitude 3 deg/sec and frequency 3.6193 rad/sec for the roll rate command, and magnitude 3 degrees and frequency 3.6193 rad/sec for the sideslip angle command. Actual performance of our optimal dither is evaluated in the next section.

Possibly, a better solution for the lateral channel would feature separate dither parameters for the rudder and ailerons. Indeed, the roll rate and roll angle aircraft states respond to low frequency dithers, which could be applied to the ailerons, while the higher frequency of Trial 5 could be applied to the rudders for quick response of the MMAE to sideslip angle sensor and yaw rate sensor failures. Furthermore, two sinusoids of different frequencies and magnitude could be superimposed to stimulate the MMAE to respond to both high- and low-frequency-sensitive failures.

A much more complicated analysis is required to investigate these proposals, so in the interest of time, they are not pursued in this thesis.

4.2.2 Optimal Dither. The optimal dither performance is shown in Figure 4.15. Each plot shows the response of the MMAE for the filter that matches the failure induced. An expanded presentation is provided in Appendix E. The command inputs are dithered with the signals shown in Equation (4.6):

$$\begin{aligned}
 \text{Right pitch rate command} &= 6.0 \times \sin(3.3306t + \phi_{er}) \text{ deg/sec} \\
 \text{Left pitch rate command} &= 6.0 \times \sin(3.3306t + \phi_{el}) \text{ deg/sec} \\
 \text{Right roll rate command} &= 3.0 \times \sin(3.6193t + \phi_{er}) \text{ deg/sec} \\
 \text{Left roll rate command} &= 3.0 \times \sin(3.6193t + \phi_{el}) \text{ deg/sec} \\
 \text{Right sideslip angle command} &= 3.0 \times \sin(3.6193t + \phi_{rr}) \text{ deg} \\
 \text{Left sideslip angle command} &= 3.0 \times \sin(3.6193t + \phi_{rl}) \text{ deg}
 \end{aligned} \tag{4.6}$$

Note that the longitudinal sensor responses, S2, S3, and S4, are not as fast as would be predicted by Trial 4 of Tables 4.4 through 4.6. This may be attributed to two factors. Consider that Trial 4 of Tables 4.4 through 4.6 had elevator dithering at $\omega = 3.3306$ rad/sec and aileron dithering at $\omega = 1.0896$ rad/sec, a lower frequency than that of the elevators. Recall that the ailerons are cross coupled into the longitudinal channel according to terms in B of Equation (3.1). Next, recall that longitudinal sensors had the best failure identification times at lower frequencies such as $\omega = 0.8326$ (see Trial 2 of Tables 4.3 and 4.6) and $\omega = 1.6653$ (see Trial 3 of Tables 4.4 and 4.5). The two factors of low frequency aileron dithering and aileron cross coupling into the longitudinal axis can account for the seemingly good failure identification times of Trial 4. Once the low frequency component was removed, as in our proposed optimal dither (Equation (4.6)), the longitudinal sensors responded more slowly to the higher frequency as in Trial 5 of Tables 4.4 through 4.6.

Obviously, in the interest of obtaining consistent test results, our frequency response tests should have been conducted with the aircraft being subjected to only one frequency at a time. The base frequencies mentioned in Section 4.2 should have been identical for the elevators, ailerons, and the rudders. With the preceding analysis re-accomplished under these conditions, an optimal dither would have been more accurately predicted. However, the analysis of the preceding paragraph

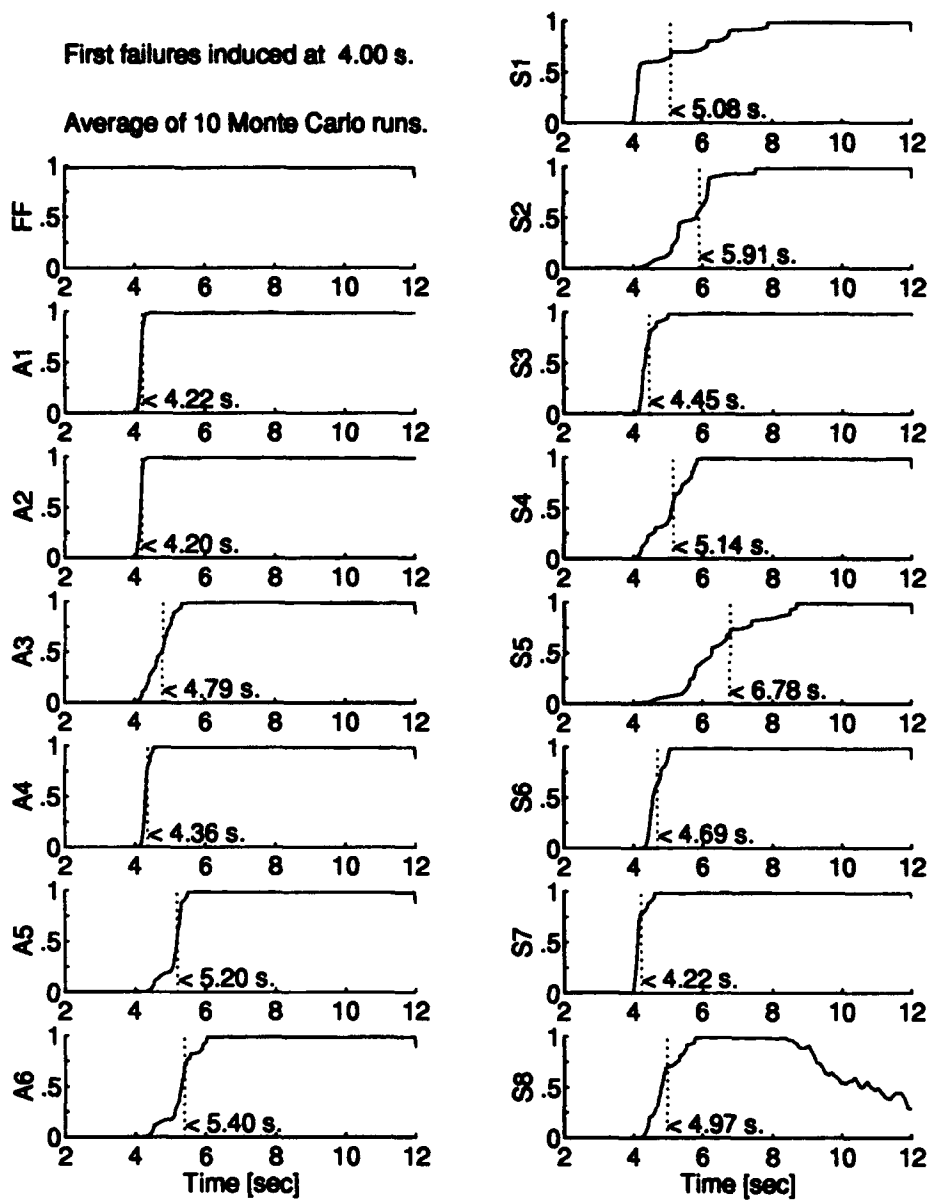


Figure 4.15 MMAE Filter Probability Plots with the Optimal Dither Technique.

indicates that one might successfully use ailerons to induce the low-frequency excitation into the longitudinal channel to improve MMAE response to S2, S3, and S4 failures while maintaining a higher frequency, low-magnitude dither on the elevators for good elevator actuator failure detection. This is a complex relationship because the aileron dither also affects failure identification times for sensors S5-S8 and the aileron actuators. Therefore, we restrict the design of aileron dither to provide excitation for only lateral sensors, and elevator dither design to excite only longitudinal sensors. However, a linear combination type of dither signal might warrant investigation in the future.

4.3 Pilot Command Inputs

During normal flying operations, the LAMBDA pilot is constantly providing command inputs to the flight control system. To see what the effects of his/her input commands are on the aircraft in terms of g -loading and MMAE performance, flight data was obtained from Wright Laboratories [26] to apply to the truth model and MMAE program. The command input data provided was in the form of an ASCII file with vectors of single channel stick inputs for pitch rate, roll rate, and sideslip angle. The data was recorded in real time at 60 Hz, even though the LAMBDA FCS operates at 50 Hz as our truth model does. To convert the 60 Hz data to 50 Hz data, every sixth datum was removed from each vector. This method of conversion was used in preference to curve fitting and re-discretizing because of its simplicity. Of more concern is that these pilot inputs are being applied against computer-generated wind perturbations to which this pilot is not reacting. Without actually flying an MMAE-equipped LAMBDA in real-time simulation, the effectiveness of pilot command inputs as a dither technique will remain an unknown.

A further modification is that the single channel data for each control axis was simply duplicated and applied to the two channels of each control axis of our truth model. The applied command inputs are shown in Figure 4.16 along with the g -loadings calculated by our truth model.

The data series was taken from a pitch-up maneuver. The complete maneuver consists of a positive-negative doublet applied to the pitch rate input, followed by commands to level and straighten the flight path. The portion of data shown in Figure 4.16 and used in the present simulation is only the part to level and straighten the flight path. The ordinate labels are defined

as follows: $E_{cmd\ Rt}$ – right channel pitch rate command (E for elevator); $E_{cmd\ Lt}$ – left channel pitch rate command; A_z – vertical acceleration; $A_{cmd\ Rt}$ – right channel roll rate command (A for aileron); $A_{cmd\ Lt}$ – left channel roll rate command; $R_{cmd\ Rt}$ – right channel sideslip angle command (R for rudder); $R_{cmd\ Lt}$ – left channel sideslip angle command; and A_y – horizontal acceleration. Each of the failed conditions are applied to the truth model at 4.0 seconds. The MMAE filter probability traces are shown in Figure 4.17.

Only one Monte Carlo run was made for each failure condition because we desire to present a *representation* of what would happen on one real flight, without the added complications of compressing many runs into a plot of averages. Wind was included at the same strength as for previous simulations. Note the difficulty the fully functional filter has in maintaining lock on a fully functional aircraft. Even so, no false declarations were made. For actuator failures only, the right elevator and left aileron were identified in 2.24 and 1.04 seconds, respectively, while the left elevator and right aileron were not correctly identified. Figure 4.18 shows a solid 50-50 sharing of probability between failed rudder filters when either rudder is failed by itself. Because neither one nor the other attained a probability of greater than $p_{TRIG} = 0.5$, no failure was identified. However, the algorithm has, in fact, correctly identified that a rudder failure has occurred in both cases, but it is not sure which one failed. This is a clear indication of the need for out-of-phase dithers when cross-coupling terms are not included in the model.

All sensors were correctly identified and all identification times except that of the sideslip angle sensor failure were better than those of the optimal dither in Figure 4.15. However, note that the vertical acceleration limit of 0.1 g has been severely violated in the A_z plot of Figure 4.16. Also, the horizontal g -limit of 0.2 g is severely violated in the A_y plot. These violations disqualify this particular pilot dither routine from being called an “optimal dither”. Note finally that the spiking beginning at 9 seconds in the S_8 plot is a result of the aircraft going unstable. This phenomenon is discussed in Section 5.1.

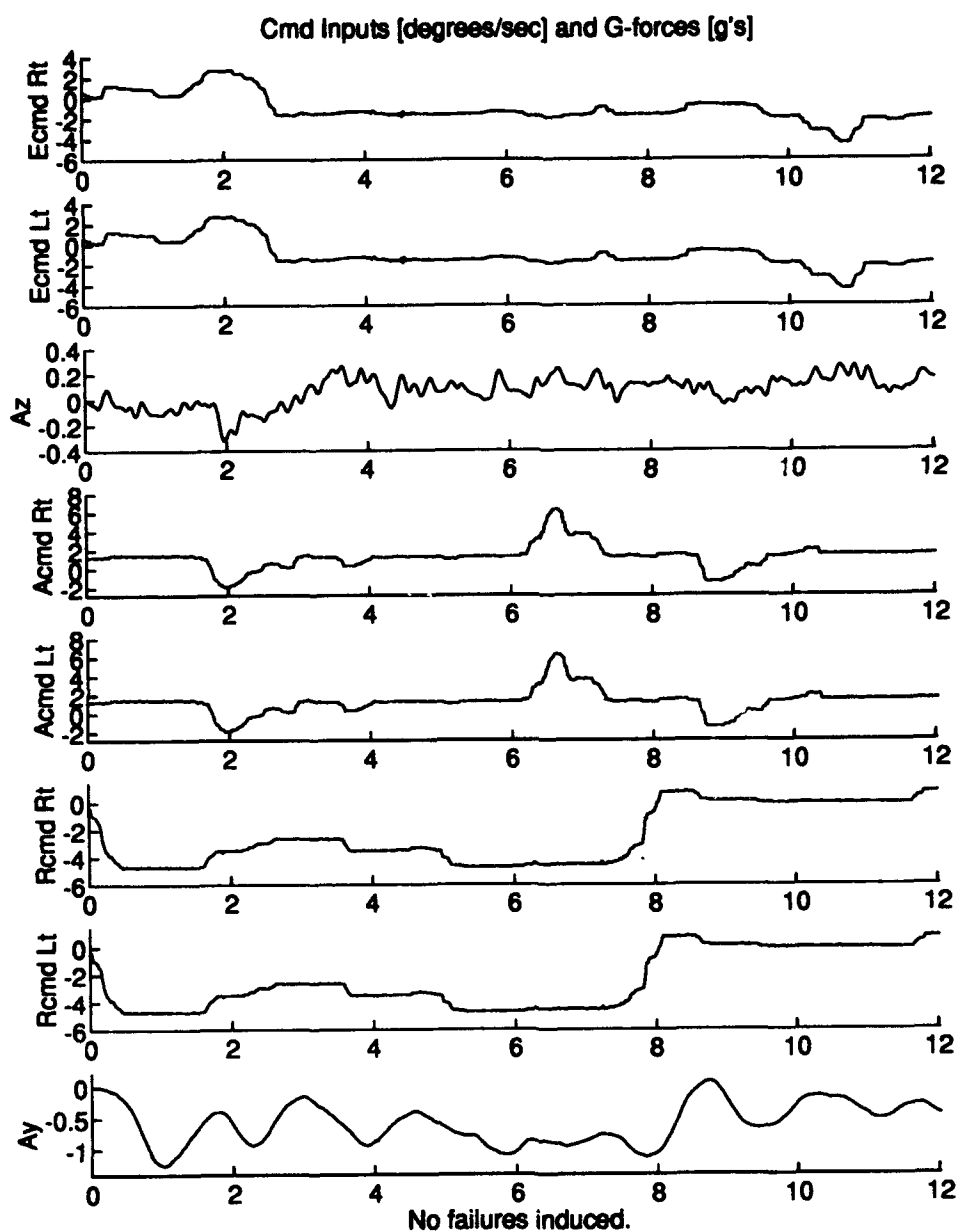


Figure 4.16 Command Input Plots of LAMBDA Pilot's Effort to Fly Straight and Level.

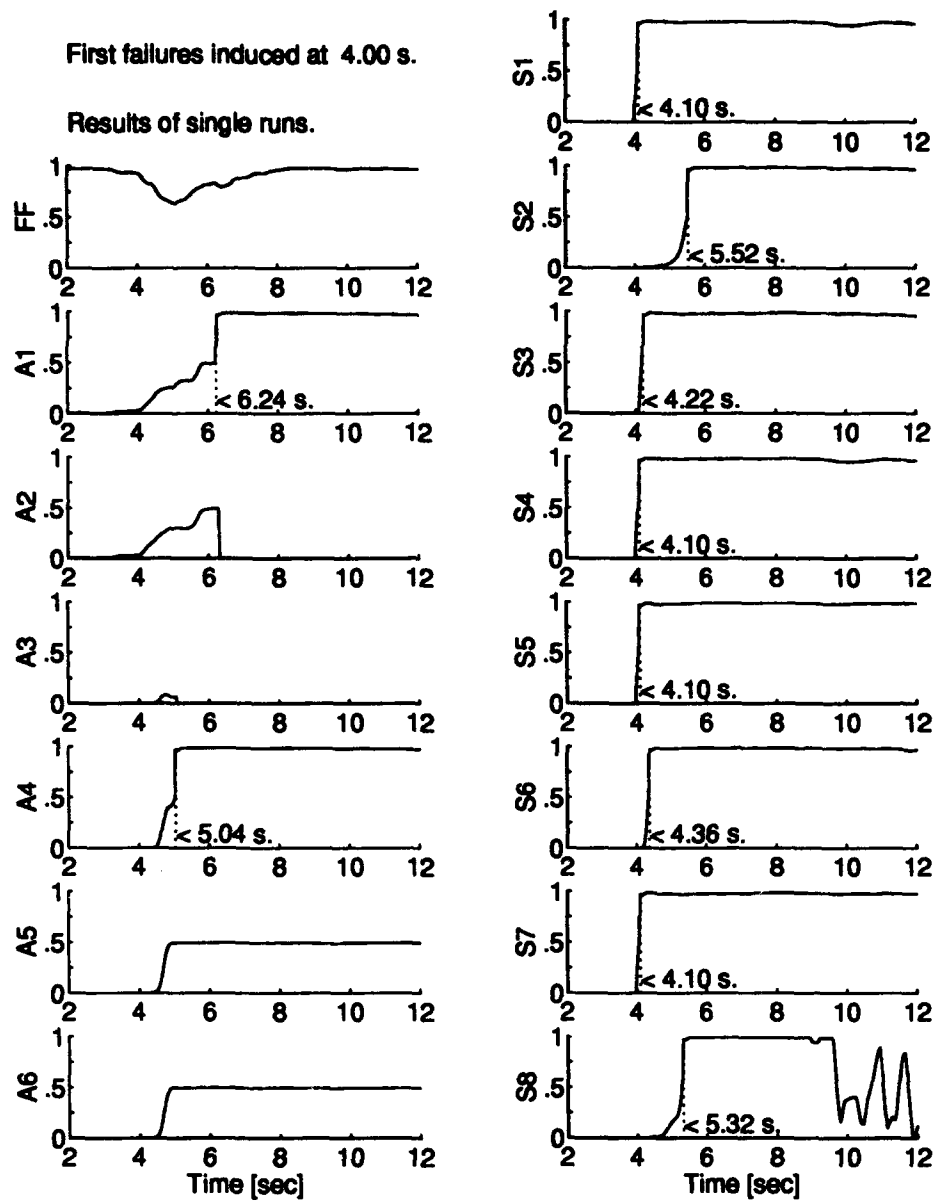


Figure 4.17 MMAE Filter Probability Plots when Command Input is Pilot's Effort to Fly Straight and Level.

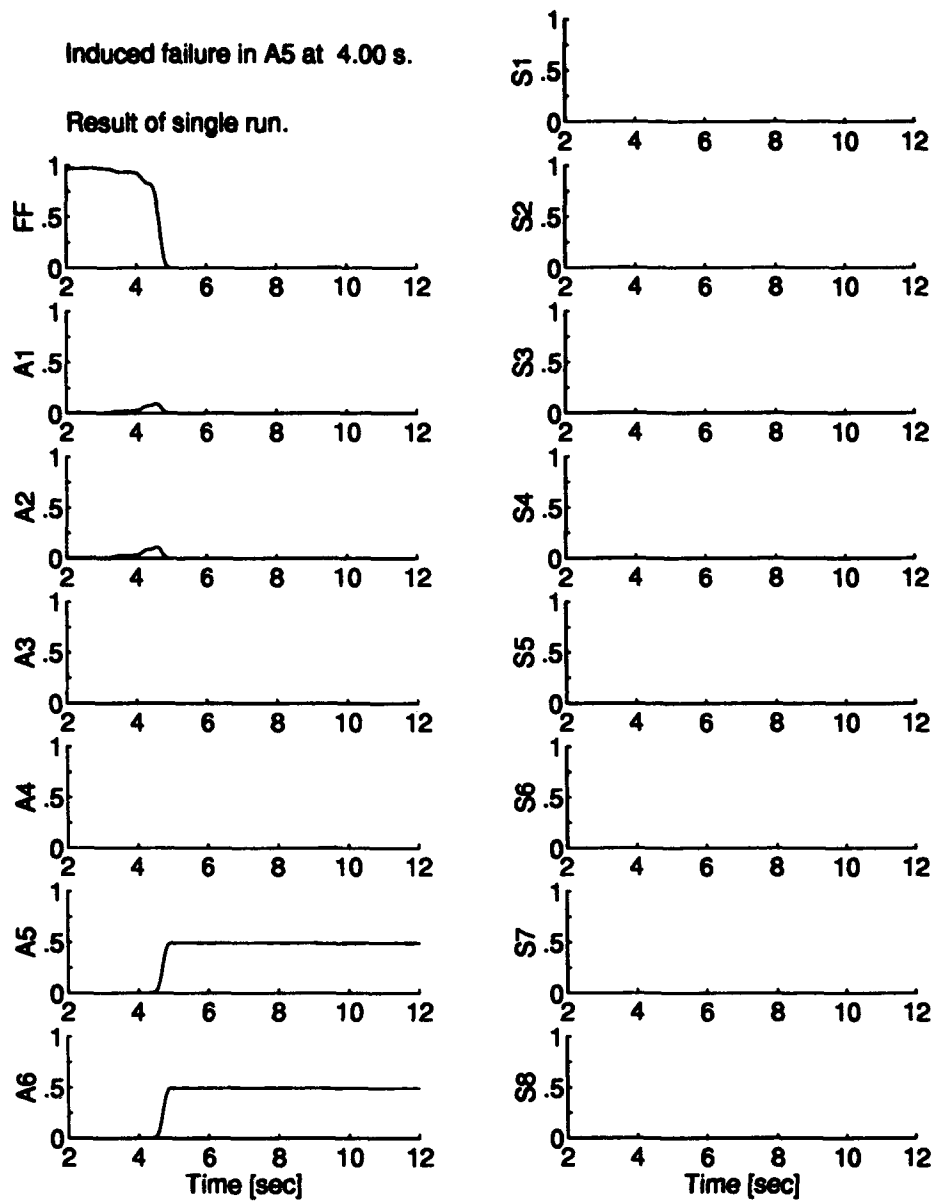


Figure 4.18 MMAE Filter Probability Plots for all Bank 0 Filters when only the Right Rudder Failure is Induced at 4.00 seconds. Command Input is Pilot's Effort to Fly Straight and Level. Note Shared Probability between Right and Left Rudder Filters.

4.4 Dual Failure Performance

The optimal dither technique of Subsection 4.2.2 is used to command the truth model when it is subjected to two failures spaced apart by 1 second. All combinations of all fourteen possible actuator and sensor failures are tested in simulation. Criteria for successful performance is that a filter hypothesizing both the induced first failure and the induced second failure holds a window-averaged probability (see Subsection 3.3.1) above the trigger limit of $p_{TRIG} = 0.5$ at the end of the 12 second simulation, with no false alarms in between.

The presentation format allows the reader to view averages of ten Monte Carlo runs. As an example, consider Figure 4.19. When the fault declarations are consistent from run to run, this format is clear and easily understood. Each pair of plots in a row are the average probabilities of the set of ten runs with the same failure parameters. The plot in the first column is the probability of the filter that was declared to have the first failure. This filter is a secondary filter in level-0, which becomes the primary filter in level-1 at the time of the first failure declaration. The plot in the second column starts off as the probability of a secondary filter in level-0 but changes to the secondary filter in level-1 which hypothesizes the first failure detected *and* the second failure detected. The change is denoted by a vertical dash-dot line. This compact format eliminates the need to display all of the non-relevant filter probabilities from both level-0 and level-1. However, this format does become confusing when the order of MMAE fault declaration changes from run to run. In this case, acceptable performance may have been achieved, but the only way to represent this graphically is to show probabilities from each Monte Carlo run. Therefore, a short narrative is given to make clear what is not evident in the plots.

Two pages are devoted to all of the simulations with identical first failures. The first page of the pair shows performance with actuators as the second failures (Figure 4.19); the second page shows performance with sensors as second failures (Figure 4.20).

When the first failure is of the *right elevator actuator*, A1, all actuators as second failures are successfully identified. A2, the left elevator actuator, is identified as the second failure 0.56 seconds after it is induced. This is a longer time that it took to identify A2 as the first failure, as shown in Figure 4.15 even though MMAE probabilities seem to be solidly at steady state after the first failure. This extended failure identification time may be explained by noting that the filter tuning

process favors the identification of a fully functional filter which is still present in the level-1 bank. So, when the second failure occurs, probability must not only be transferred to the new dual failure filter, it must avoid going back to the fully functional filter.

Another explanation for the longer identification time required for a second failure is that this failure is induced at 5 seconds in the dual tests rather than at 4 seconds, as in the single failure tests. The impact is that the dither signal inputs are making different transitions at these two times. The conjecture is that a failure is more quickly identified if it is induced during a period when the time differential of the input is high. To draw a parallel, this condition exists between two simulations with different dither signal magnitudes. In the cases shown in Appendix D, it is clear that the higher magnitude inputs result in quicker failure identification times, as anticipated.

The rest of the dual failure probability plots are presented in Appendix F, which has the filter codes of Table 3.4 re-printed as an aid, but discussion is presented below. All dual failures were correctly identified and no false alarms were detected with the *left elevator actuator* as the first failure. Figure F.1 shows good MMAE performance when the left elevator fails first and actuators fail second. Figure F.2, as consistent with Figure 4.20, reveals that excellent identification of longitudinal sensors is obtained when one elevator actuator is failed. Loss of one elevator actuator gives the remaining control surface complete control of the longitudinal states without competition from out-of-phase deflections the opposite surface. The result is that these states are excited *more*, which leads to enhanced failure detection.

All dual failures were correctly identified and no false alarms were detected with the *right aileron actuator* as the first failure. Figures F.3 and F.4, however, do not necessarily give that impression. Consider the top row of two plots in Figure F.3. The actual results are that the A1 filter was identified as the *first* failure in 2 of the 8 Monte Carlo runs in which the A3 filter was correctly identified second. Similarly, in the plots of row 7 of Figure F.4, the corresponding test result was that the S7 filter came first in 3 of 10 runs.

Understanding the highly condensed information contained in the dual failure plots takes careful consideration. The reader is encouraged to pause at this point and refer back to the hierarchical structure in Figure 1.2 on page 1-14. Recall that all level-0 filters hypothesize only one

First failure induced is A1 at 4.00 s.
 Second failures induced at 5.00 s.
 Average of 10 Monte Carlo runs.

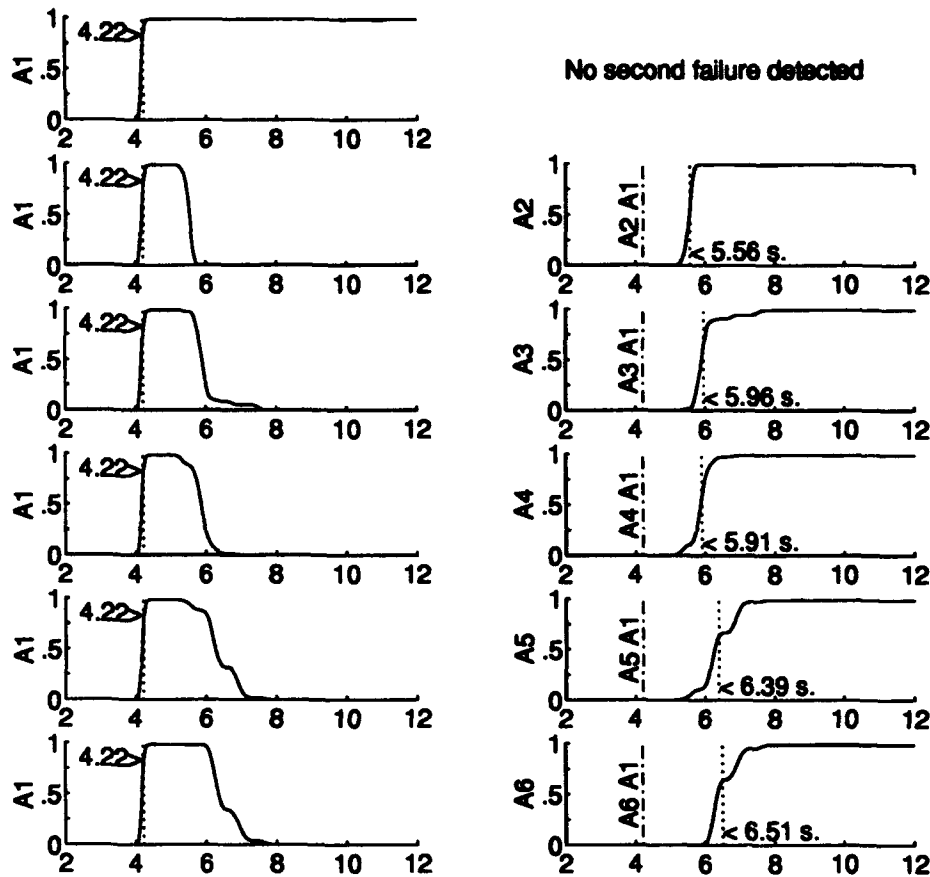


Figure 4.19 Dual Failure MMAE filter Probability Plots with the Right Elevator Actuator Failing at 4.00 sec. and Each Actuator Failing at 5.00 sec.

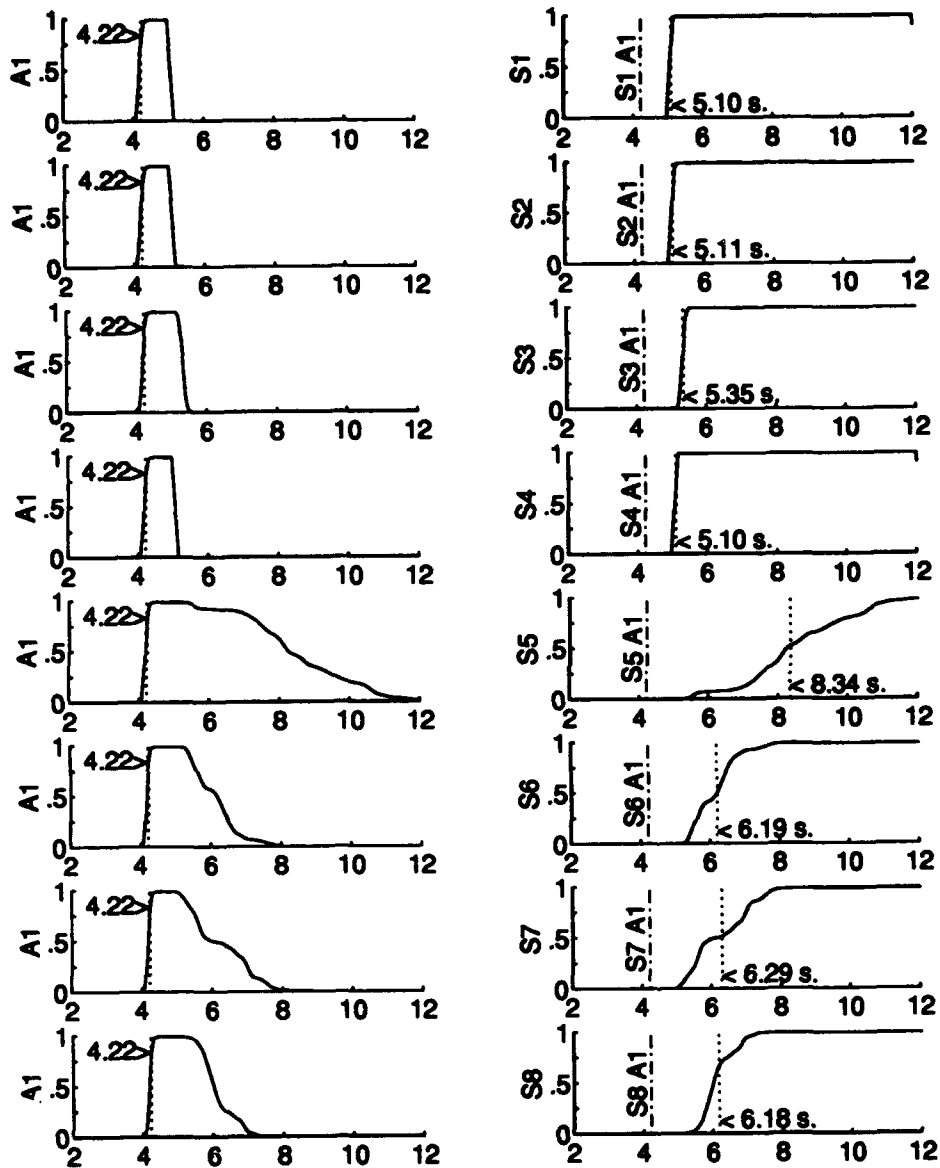


Figure 4.20 Dual Failure MMAE filter Probability Plots with the Right Elevator Actuator Failing at 4.00 sec. and Each Sensor Failing at 5.00 sec.

or zero component failures. When two unidentified failures are present, as is the case when the first failure of our test is not identified in less than one second, the MMAE algorithm has a choice. In the present situation, it may choose the A3 failure and switch to the A3 bank or it may choose the A1 failure and switch to the A1 bank. Upon switching to a new bank, our data gathering routine continues to use the same 15 storage locations to track probabilities of level-1 filters as it did to track level-0 probabilities. Data for the A1 filter in level-0 is appended with data for the A3A1 filter when the bank is switched to the A3 level-1 bank. Data for the A1 filter continues to be A1 filter data when the bank is switched to the A1 level-1 bank. This is not a problem when all of the ten Monte Carlo runs switch banks in the same order. However, if there is an order reversal between runs, the reader must realize that the averaged probability plot starting out as the A3 filter ends up as averaged probability composed of 80% from the A3 filter (when the MMAE switched to bank A3 first in 8 of 10 runs) and 20% from the A1A3 filter (when the MMAE switched to bank A1 first in 2 of 10 runs).

Massive amounts of data would have to be published in order to gain a completely clear understanding. Therefore, this reliable and detailed narrative should be followed closely.

All dual failures were correctly identified and no false alarms were detected with the *left aileron actuator* as the first failure. Trends of Figures F.5 and F.6 are similar to those for the right aileron actuator as the first failure.

All dual failures were correctly identified with the *right rudder actuator* as the first failure. However, false alarms of a left rudder actuator failure were detected when the second failure was the yaw rate sensor, S8. This is to be expected since the aircraft becomes unstable with a yaw rate sensor failure; see Section 5.1. Detailed data from simulations with these failed components show that the false alarms came up after 10 seconds, well after the two correct identifications were made.

All dual failures were correctly identified with the *left rudder actuator* as the first failure. On one run with the left rudder actuator failed first and the right aileron failed second, a unusual event occurred. A left aileron actuator failure was falsely identified first, the right aileron actuator failure was correctly identified second and subsequently, 9 failure status switches occurred between the A4-A3 filter and A4-A6 filters. Both of these filters are incorrect. The correct final filter should be the A6-A3 filter or the A3-A6 filter, depending on the order of correct failure identification.

Since the incorrect filter was identified first, the MMAE switched to the wrong level-1 bank which contained neither of the correct filters that match the actual dual failure status. As a result, the MMAE became indecisive about the next best decision, given that the absolute best choice was not available. This accounts for the wavering of probability on the row 3 plots of Figure F.9. There were three runs with false alarms for the right rudder actuator when the yaw rate sensor was failed second. This is easily attributed to the aircraft instability caused by the loss of the yaw rate sensor feedback to the flight control system (see Section 5.1). The only peculiarity is that there are fewer false alarms when the yaw rate sensor is failed along with a rudder actuator. This does make sense when one considers that the flight control system uses the rudder actuators to induce this aircraft instability.

All dual failures were correctly identified with the *forward velocity sensor* as the first failure. On one run with the right aileron actuator failing second, the left aileron was incorrectly identified as the first failure, the right aileron was correctly identified as the second failure. Again, the incorrect *first* failure declaration prohibited the MMAE from declaring the correct dual failure status because the selected level-1 bank of elemental filters, having a failed A4 as its primary hypothesis, does not include the correct dual failure hypotheses of A3-S1 or S1-A3. MMAE filter probability shifts between filters A4-A3, A4-S1, and A4-FF six times before the end of this one particular simulation. Proper detections occurred on all other runs with the same failure parameters. The yaw rate sensor as the second failure produced 4 false alarms of the right aileron actuator in 3 of 10 runs. In all cases, the first two failures declared were correct, with the false alarms coming at a later time, which we will consider as sufficient criterion for proper MMAE performance when a yaw rate sensor failure is involved. See Figures F.11 and F.12.

There is a software "bug" that was corrected by forcing the MMAE algorithm to change filter banks only once. The problem is that the algorithm switches filter banks on *every* failure declaration. The software correction prohibits a switch to another bank after two failures have been declared. If bank changes were allowed on every failure declaration, dual failures would cause constant switching between level-1 banks without settling on just one filter hypothesizing both failures. On the other hand, if the MMAE *needs* to switch banks more than once, it is deduced that the system has probably failed any test proposed in this research. Had this limitation been lifted, an identification of the A4-FF filter would have led to a switch to the level-0 bank. The

opportunity to identify the correct dual failure status might then have been taken. This limitation will be suspended to illustrate an important MMAE capability as dual failures with sideslip angle sensors are analyzed shortly.

All dual failures were correctly identified with the *angle of attack sensor* as the first failure. There were only three false alarms of a right aileron actuator after correct dual failure status was declared when the yaw rate sensor failed second. The correct dual failure status was declared following these false alarms as well. See Figures F.13 and F.14.

All dual failures were correctly identified with the *pitch rate sensor* as the first failure. Only once did the MMAE identify the left aileron as being failed second when it should have identified the right aileron. Note that the algorithm correctly identified that an aileron failure had occurred, but it required some additional time to disambiguate between a right and a left aileron failure. This is observed as a recurrent phenomenon. The algorithm subsequently identified the right aileron correctly without further problems. See Figures F.15 and F.16.

All dual failures were correctly identified with the *pitch angle sensor* as the first failure. On only one run with the left aileron actuator as the second failure did the MMAE declare a failed right aileron. The correct failed aileron actuator was subsequently identified. See Figures F.17 and F.18.

All dual failures were correctly identified with the *sideslip angle sensor* as the first failure with one exception. In this particular case of one run, the sideslip angle sensor failure (S5) was induced first at 4.00 seconds. The right aileron actuator failure (A3) was induced second at 5.00 seconds. During this simulation, the MMAE identified the failure of the left aileron actuator (A4) incorrectly at 5.36 seconds and switched to that level-1 bank of filters. At 5.88 seconds, the MMAE identified the fully-functional aircraft filter as the true failure hypothesis, but this time, on a special run, we allowed the algorithm to switch banks more than one time, so the MMAE switched back to the level-0 bank. This action shown in Figure 4.21 illustrates the MMAE's ability to recover from a false first declaration. As the simulation continued, the right aileron actuator was correctly identified at 6.70 seconds, then the sideslip angle sensor was identified as failed at 8.20 seconds. So, the MMAE probability ended up with filter A4-S5, which is the desired result. It is important to note that such a recovery was only required on 3 of 1960 runs, this is less than a 0.2% rate of

false first detection. For an overview of MMAE performance with the sideslip angle sensor failure as the first of two failures, see Figures F.19 and F.20.

All dual failures except one were correctly identified and no false alarms were detected with the *roll rate sensor* as the first failed component. The missed failure identification was that of a failed right aileron actuator on one run. There was also one run that switched twice between correct and partially correct declarations. This was also associated with the right aileron actuator failure. See Figures F.21 and F.22.

All dual failures were correctly identified with the *roll angle sensor* as the first failure. One false alarm was detected in which the left aileron actuator failure was identified second instead of a right aileron actuator failure. The correct failure was subsequently identified. See Figures F.23 and F.24.

See Figures F.25 and F.26 for MMAE probabilities when the *yaw rate sensor* is the first failure. One false alarm was detected in which the left aileron actuator failure was identified instead of a right aileron actuator failure. The correct actuator was *not* subsequently identified. On three runs involving the sideslip angle sensor as the second failure, the MMAE algorithm did not make any failure declaration. The sideslip angle sensor is used to provide feedback to the flight control system sideslip angle control loop, as is the yaw rate sensor. The conclusions to be seen in Section 5.2 that sensors used in flight control feedback are more difficult to identify because of the unusual residual characteristics may be applied here. Indeed, the residuals corresponding to the sideslip angle sensor and the yaw rate sensor develop a tighter variance in the fully functional filter *after* these sensors are failed. This makes it more difficult to shift probability from the fully functional filter to the correct filter which develops a change in only one of its residuals.

The additional failure declarations observed may be attributed the aircraft instability caused by the failure of the yaw rate sensor (see Section 5.1). Therefore, except for dual failures involving the sideslip angle sensor, Figures F.25 or F.26 show good MMAE performance with dual failures which include the yaw rate sensor.

Conclusions drawn from our observation of MMAE performance against dual failures are the following. The hierarchical structure is very effective in identifying two failures in the face of wind gust uncertainty and sensor noise uncertainty. The hierarchical structure allows the MMAE

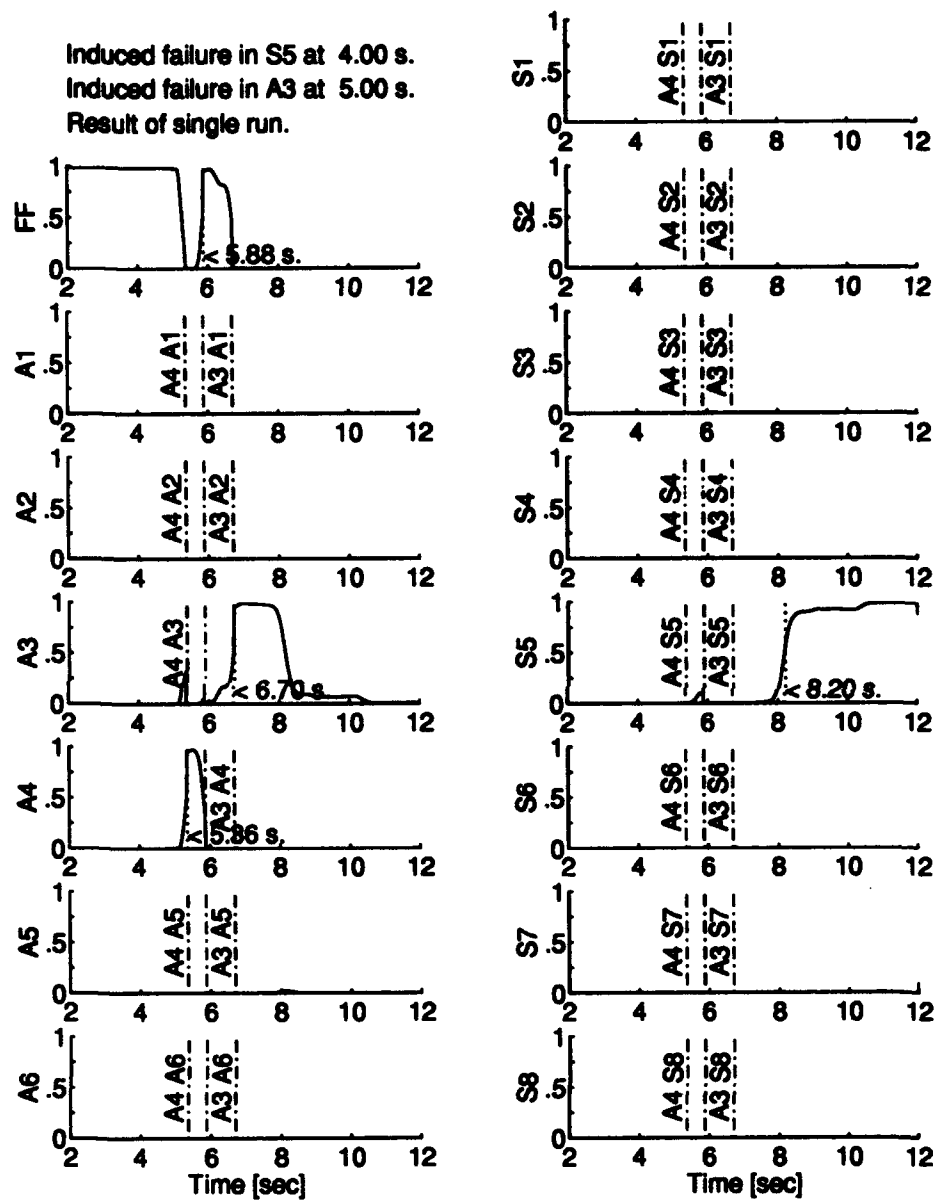


Figure 4.21 One Run Dual Failure MMAE filter Probability Plots with the Sideslip Angle Sensor Failing at 4.00 sec. and the Right Aileron Actuator Failing at 5.00 sec. Note MMAE Recovery from False First Detection.

algorithm to identify failures out of the order in which they are induced. No time is wasted in identifying obvious failures while ambiguity might exist in identifying another failure.

The several missed and false alarms observed were associated with the ailerons in which left was confused with right. This could be attributed to the fact that, with the optimal dither used in this test sequence, the ailerons are not commanded to move very much. Had more dynamic range of the aileron control surfaces been utilized, better identification of left and right aileron actuator failures would have resulted.

There were three isolated incidents of the MMAE algorithm making false first failure declarations. This caused the incorrect level-1 filter bank to be brought on-line. Due to a software problem, subsequent bank switches were not allowed. However, this limitation was lifted on one simulation to illustrate the MMAE's ability to recover from a false failure declaration and go on to make the correct dual failure identification.

4.5 Chapter Summary

The results of extensive testing and analysis have been recorded in this chapter in support of the objectives presented in Section 1.5. In addition, the experience of tuning the elemental Kalman filters is recorded. The tuning algorithm of Section 4.1 was developed out of necessity. A complicated wind disturbance model made it difficult to tune manually the zero-order wind disturbances accurately enough to prevent the extremes of sluggish or volatile MMAE performance. The automatic tuning algorithm proved to be quite effective in maximizing MMAE performance.

The search for an optimal dither technique led to the study of the effects of varying frequency and magnitude in the sinusoidal command input dithers. The frequency study reveals interesting relationships between failure identification times and Bode magnitude responses in the identification of sensor failures. Sensors involved in feedback to the flight control system have different failure identification characteristics as dither frequency is altered. A more in-depth study of this phenomenon will come in the following chapter. The knowledge gained in the study of various dither frequencies and magnitudes enabled us to conclude the parameters of an optimal dither. This dither is optimal with respect to failure identification time, while not violating constraints on g -loading.

As an exploratory study, command inputs derived from a real pilot's efforts to fly the airborne LAMBDA were used to command the computer model of LAMBDA. MMAE failure performance was evaluated with the pilot's inputs acting as the dither routine. The need for out-of-phase dithers on the left and right control channels became evident when attempting to identify actuator failures. However, exceptionally good failure identification times were realized with the aircraft data sensor failures.

Finally, dual failure performance with the optimal dither was studied. Our conclusion is that dual failures can be successfully identified with the MMAE algorithm and a hierarchical filter bank structure. Though failures were not always identified in the order of their introduction, the correct dual failure hypothesis was consistently declared. Also, one incident of the MMAE's ability to recover from a false alarm was illustrated.

V. Secondary Analyses

Chapter IV provided an extensive discussion of the primary objective of this thesis. In the present chapter, many secondary issues brought up in Chapter IV will be studied. These topics include the effect of a failed yaw rate sensor on the stability of the aircraft, an in-depth look at MMAE performance in the face of failures of feedback sensors, and finally, a study of MMAE response to phugoid frequency dithers at very low magnitude.

5.1 Failure of Yaw Rate Sensor

The failure of any single component used in our failure simulations will result in a controllable aircraft except for the yaw rate sensor failure, S8. Refer to Figure 5.1. On all MMAE filter probability plots involving a yaw rate sensor failure, the probability will rise through its transient response and remain at a level which correctly identifies the yaw rate sensor as failed. After a few seconds though, the probability drops from a solid identification and deteriorates as time goes on. This is not due to a faulty characteristic of the MMAE algorithm. Rather, this happens because the aircraft itself is going unstable.

When the yaw rate sensor is disabled, the flight control system (Figure 3.1) loses its input to the washout filter which is a compensator in the feedback loop. The stability of the lateral system is therefore compromised. Dissection shows that the discrete-time state transition matrix for the augmented truth model with a yaw rate sensor failure has an eigenvalue which lies outside of the unit circle. The purpose of this thesis is not to stabilize the aircraft under such conditions as the aircraft would go unstable whether an MMAE system were in place or not. The point is that the MMAE algorithm correctly identifies the failure well in advance of the aircraft becoming uncontrollable. The flight control system designer is left with the task of reconfiguring the flight control system once he/she has been warned about this failed condition.

The reader is therefore warned that the filter probability for the failed yaw rate sensor filter will always drop off after having shown a solid identification. Know that the cause is due to the augmented aircraft's instability, not the MMAE's deficiency.

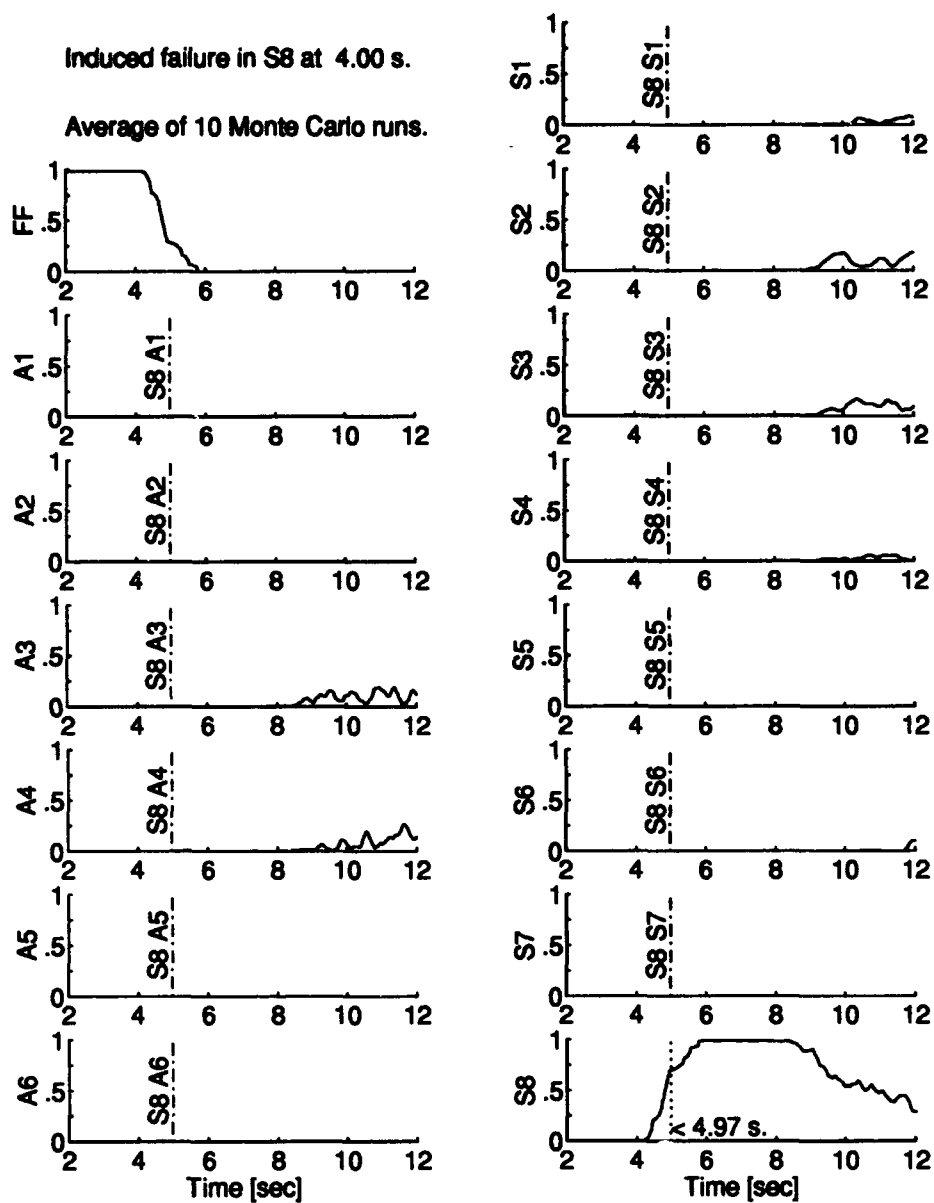


Figure 5.1 MMAE Probabilities for All Filters Subjected to Yaw Rate Sensor Failure.

5.2 Failure of Feedback Sensors

A trend is detected concerning the relative identification time of sensors used for FCS feedback compared with those not integrated into the FCS. That is, in the longitudinal channel, we see that failures associated with the pitch rate sensor take longer to identify than failures of the forward velocity, angle of attack, and pitch angle sensors. In the lateral directional channel, this trend is seen in the sideslip angle sensor, yaw rate sensor, and roll rate sensor failures having a tendency to lag in their identification times behind that of the roll angle sensor. One might expect that this angle sensor would lag behind the other rate sensors because it is the integral of a rate aircraft state variable. The intent of the following investigation is to modify our beliefs about residual monitoring on sensor failures when the sensor provides feedback to the FCS.

To establish a baseline for discussion, Figure 5.2 is presented to show the residuals of the fully functional aircraft filter that is given measurements and control inputs from a truth model that represents a fully functional aircraft.

Figure 5.3 shows the classical response of a Kalman filter's residuals to a sensor failure. Residuals from the filter hypothesizing a fully functional aircraft are plotted versus time. At 4.00 seconds, the pitch angle sensor failure is induced and the effect is clearly seen in the pitch angle residual, θ . A severe discontinuity of the character described in Subsection 1.3.4 is evident. No significant effect can be detected in any other sensor residual except perhaps that of the forward velocity sensor. The trace of u appears to oscillate after 4.00 seconds but it is exactly the same as it would be with no failure induced. Refer to Figure 5.2. So, the induced sensor failure results is exactly what one would expect: a jump discontinuity followed by oscillations in the residual of the failed sensor with no change in any other residuals.

The filter hypothesizing the pitch angle sensor failure produces the residuals in Figure 5.4 when receiving measurements and actuator command inputs (see Figure 5.6) identical to those processed by the fully functional filter of Figure 5.3. The pitch angle residual of Figure 5.4 clearly shows a change to zero-mean while the other residuals remain unchanged. Figure 5.5 shows the dithers applied to the flight control system of Figure 3.1. These plots can be used to pick out dither oscillations in residuals. When the hypothesis of the filter matches the condition of the truth model, residuals look white and zero-mean; when the hypothesis does not match, residuals display

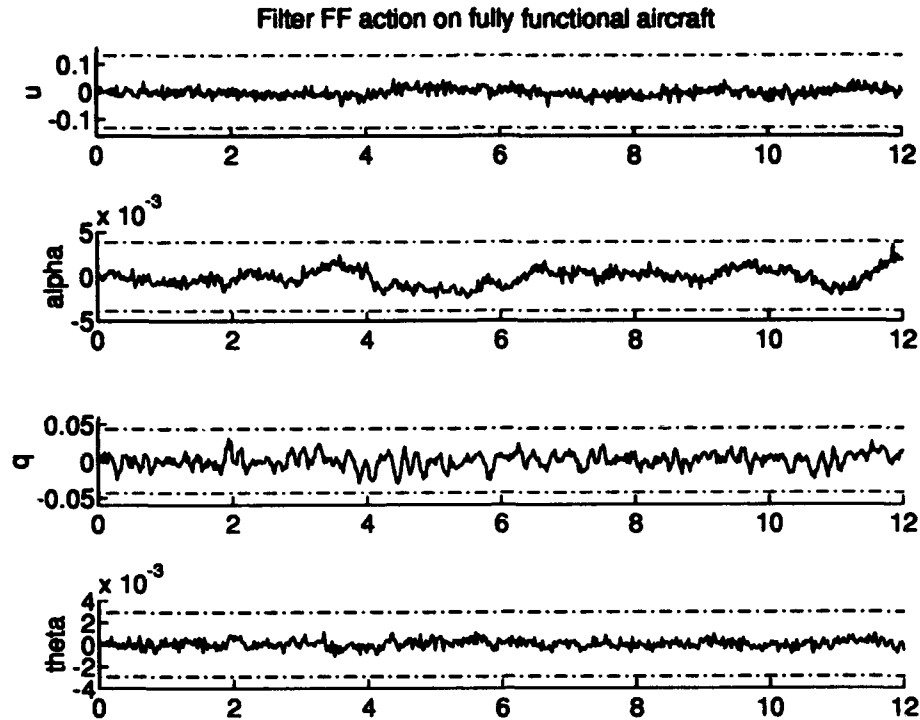


Figure 5.2 Longitudinal Residuals of Fully Functional Filter Acting on Fully Functional Aircraft. Pitch Command Dither Has Amplitude ± 4 deg/sec and Frequency 6.6611 rad/sec.

dither oscillations because they are not compensated correctly by the filter. This is easily seen in the the plot of the theta residual in Figure 5.3. The aircraft sensors give the outputs shown in Figure 5.6 when the pitch angle sensor is failed at 4.00 seconds. Note that the aircraft continues along its flight path with no change in trajectory despite this sensor failure. The dash-dot lines of the bottom two plots represent the limits imposed on the elevator surface deflection.

Now consider the failure of the pitch rate sensor. This situation is different because the pitch rate sensor provides feedback to the flight control system which is responding to a commanded pitch rate (see Figure 3.1). Conversely, the pitch angle sensor is not incorporated into the FCS. The residuals produced by the filter holding the fully functional hypothesis are shown in Figure 5.7 with the introduction of a pitch rate sensor failure at 4.00 seconds. Even though this is a sensor failure, there is no jump discontinuity in the q residual. In fact, we see that the residuals of the failed sensor on the fully functional filter get *better* than they were before the failure. Moreover,

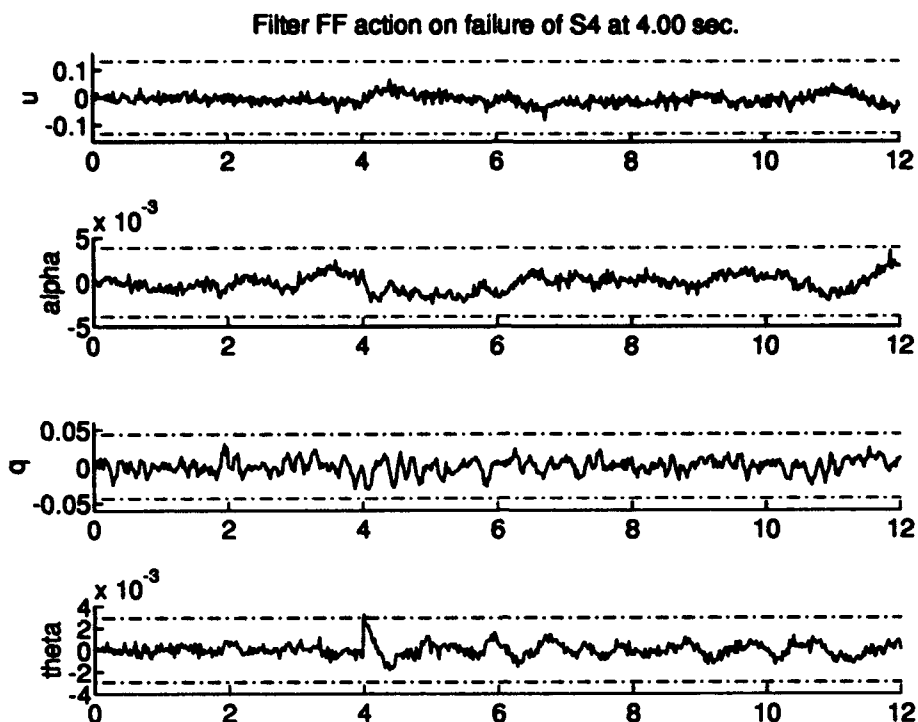


Figure 5.3 Longitudinal Residuals of Fully Functional Filter Acting on Pitch Angle Sensor Failure Which Occurs at 4.00 sec. Pitch Command Dither Has Amplitude ± 4 deg/sec and Frequency 6.6611 rad/sec.

distinct changes occur in the pitch angle sensor residuals, theta, and the angle of attack sensor residuals, alpha. Three questions come to mind: Why do the failed sensor residuals get better on the filter with the wrong hypothesis? Why are other residuals affected? And, why does the MMAE algorithm still make the correct failure identification, regardless?

The answer to the last question is found in a study of the failed pitch rate sensor filter's residuals shown in Figure 5.8. Here, observations similar to those made of Figure 5.4 for the correct filter responding to a non-feedback sensor failure are made. The residuals of q, the failed pitch rate sensor, develop zero mean and small magnitude characteristics while the other residuals seem to be affected to a much smaller degree.

So, the conclusion is that the MMAE is able to identify the failed pitch rate sensor correctly because (a) residuals of sensors other than those of the failed sensor get large on the fully functional

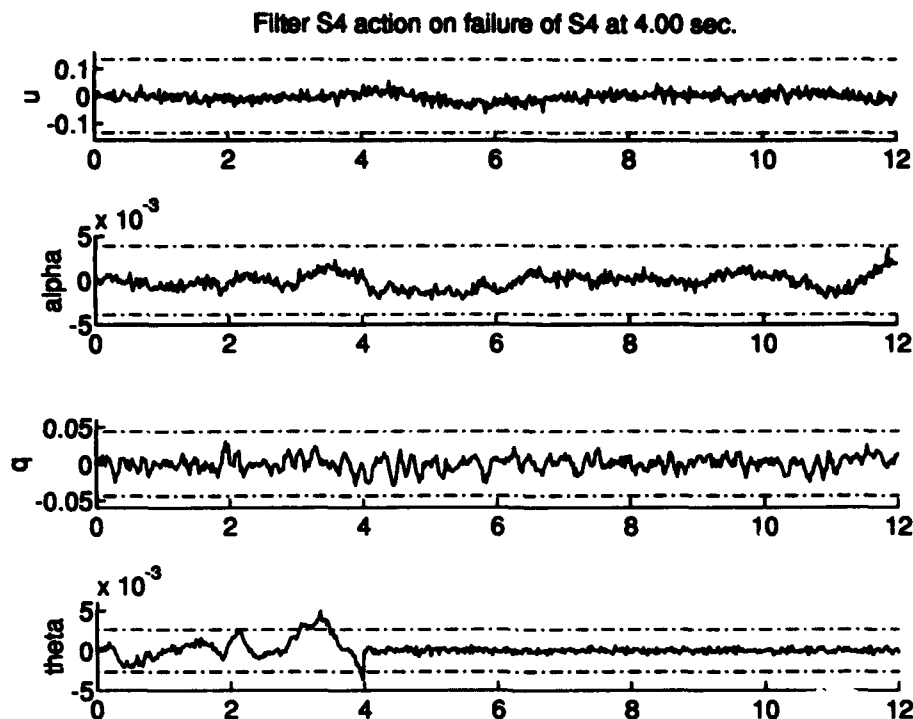


Figure 5.4 Longitudinal Residuals of Failed Pitch Angle Sensor Filter Acting on Pitch Angle Sensor Failure Which Occurs at 4.00 sec. Pitch Command Dither Has Amplitude ± 4 deg/sec and Frequency 6.6611 rad/sec.

filter and (b) the characteristic sensor failure response of a zero mean and reduced magnitude residual is evident on the failed sensor filter. Our original question of why does the pitch rate sensor take more time to identify than all other longitudinal sensors can be answered with the following explanation. Instead of watching for an increase in one residual on the fully functional filter and a decrease in the respective residual on the failed sensor filter, the MMAE must overcome the *decrease* in the failed sensor residual on the fully functional filter by waiting for other residuals on that filter to get large. The correct filter, as before, only shows a decrease in the residual of its hypothesized sensor failure. Its resulting change in probability is not large enough to compete with the complex changes in the fully functional filter. So, it seems that the MMAE's identification strategy is to wait for the incorrect filters to diverge rather than make a quick identification of the

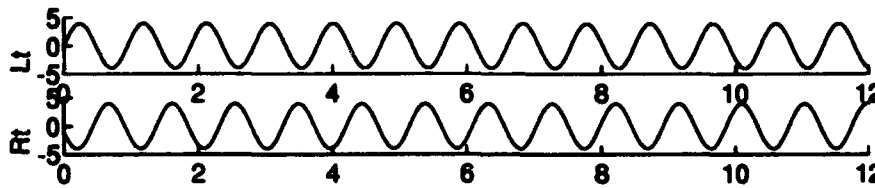


Figure 5.5 Pitch Command Dither [degrees/second] with Amplitude ± 4 deg/sec and Frequency 6.6611 rad/sec. Right Is 195° Out of Phase With Left.

correct filter. The length of time taken by the incorrect filters to diverge is dictated by the size of the $r_k^T A_k^{-1} r_k$ in each of the elemental filters.

To be sure, the hypothesis of a failed pitch angle sensor suggested by the residual theta in Figure 5.7 is not believed by the MMAE because the residuals for the filter of this hypothesis get large, as seen in Figure 5.10, just as those of the fully functional filter.

With the primary questions answered, a short explanation is given of why the other residuals are affected and why they get so large on the fully functional filter. Since the FCS controls pitch rate by adding a pitch rate feedback signal to pitch command to form an error signal, elevator coordination with pitch command is lost if the sensor measurements loose all correlation with the true aircraft pitch rate state. As an aside, this situation could be improved by running MMAE-estimated pitch rate into the FCS instead of the output of the failed pitch rate sensor.

The correlation of elevator actuator commands to pitch rate before the sensor failure is illustrated in Figure 5.10 by looking at q , Lt Elev, and Rt Elev at around the 2.00 second mark. A sharp increase then decrease is seen in q and the resulting command to the elevators can be seen to have a similar transition. After 4.00 seconds though, the Lt Elev and Rt Elev plots seem to loose some frequency content that was present before. This is attributed to the loss of pitch rate information in the development of elevator actuator commands. As a result, the commands applied to the elevator actuators will not control pitch rate as desired. In this condition, the aircraft no longer has the desired response of remaining on the original trajectory. The significant effects are seen in Figure 5.10 as the drop off of velocity, u , the increase in pitch angle, theta, and the erratic

behavior of angle of attack, α . The plot of q is the sensor measurement of pitch rate: the pitch rate *state* is not shown in Figure 5.10. For comparison, the aircraft pitch rate state is shown alone in Figure 5.11 to verify the intuitive conclusion that this state must develop a bias (since θ ramps) and exhibit an uncontrolled behavior.

Now consider that residuals are the difference between actual measurement and filter-predicted measurement. If the sensors are registering such huge displacements from the nominal, the fully functional filter will indeed track them but the residual magnitudes will be large as compared to filter tracking sensor measurements closer to the nominal. This is the effect seen in Figure 5.7, which was discussed above.

In summary, our presumptions about residual monitoring for sensor failures must be modified to account for the effect of failed sensors providing feedback to control the aircraft. The discontinuity in the failed sensor residual will not be present in the fully functional filter, but it will be present in the filter with the failed sensor hypothesis. Also, longer identification times can be expected for such sensor failures due to the complex reactions of the fully functional filter.

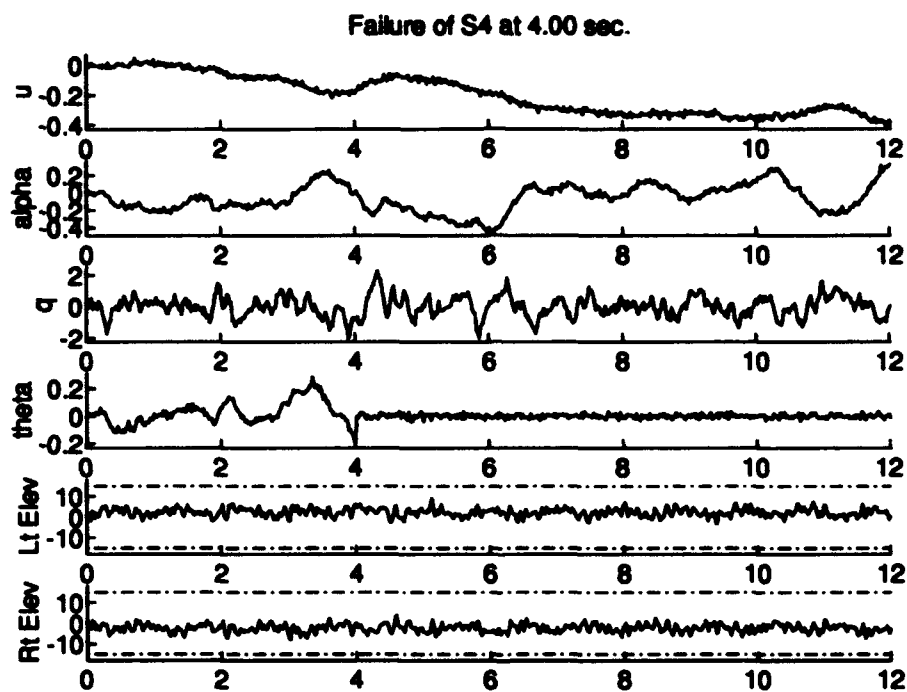


Figure 5.6 Longitudinal Flight Data Sensors Responding to Pitch Angle Sensor Failure Occurring at 4.00 sec. FCS Commands to Actuators Are Shown in Bottom Two Plots. Pitch command dither has amplitude ± 4 deg/sec and frequency 6.6611 rad/sec.

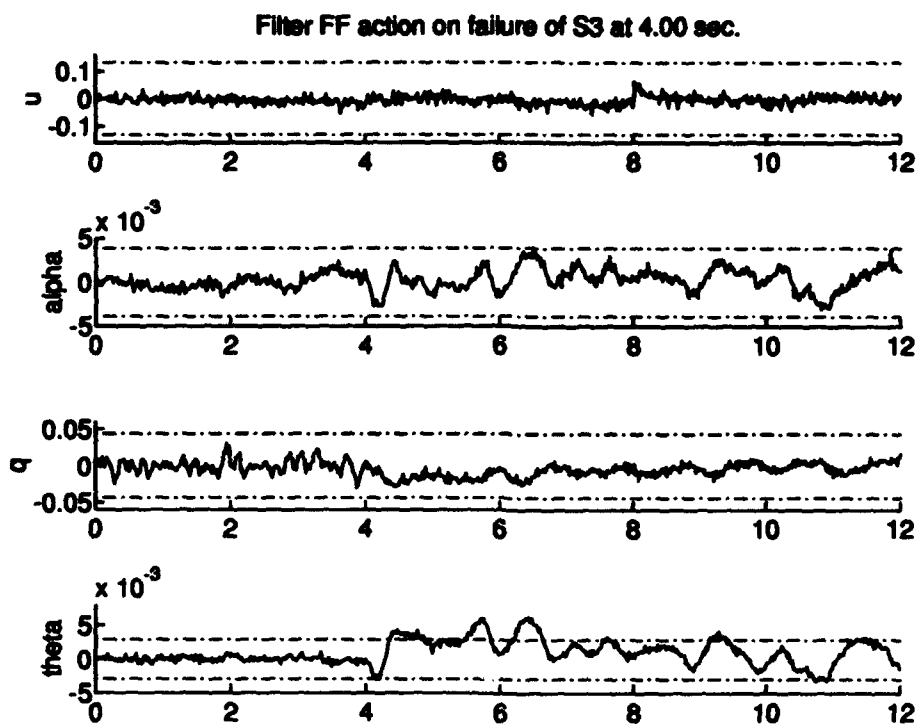


Figure 5.7 Longitudinal Residuals of Fully Functional Filter Acting on Pitch Rate Sensor Failure Which Occurs at 4.00 sec. Pitch Command Dither Has Amplitude ± 4 deg/sec and Frequency 6.6611 rad/sec.

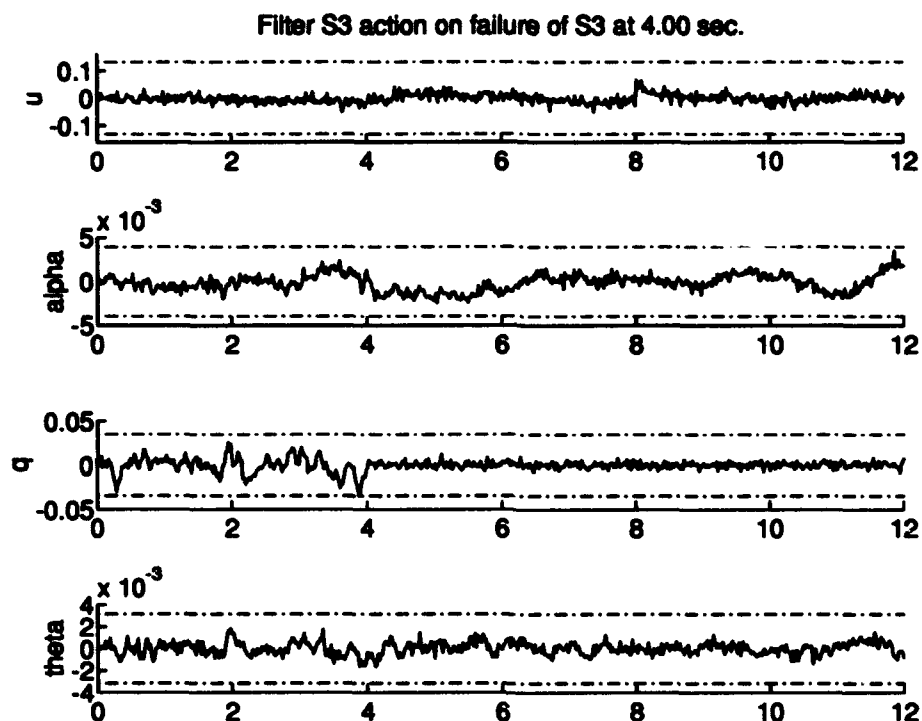


Figure 5.8 Longitudinal Residuals of Failed Pitch Rate Sensor Filter Acting on Pitch Rate Sensor Failure Which Occurs at 4.00 sec. Pitch Command Dither Has Amplitude ± 4 deg/sec and Frequency 6.6611 rad/sec.

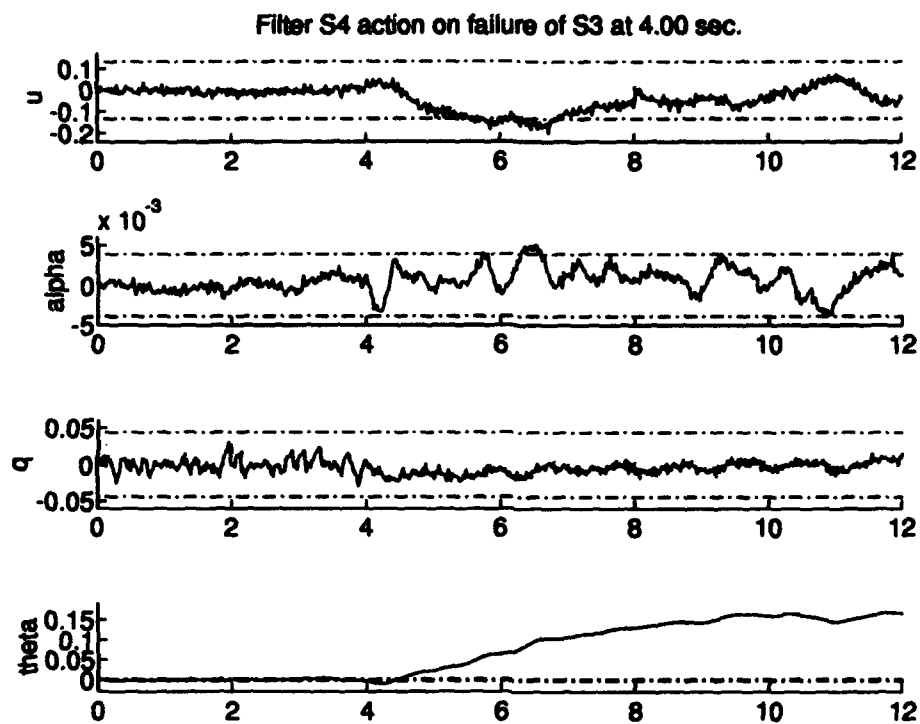


Figure 5.9 Longitudinal Residuals of Failed Pitch Angle Sensor Filter Acting on Pitch Rate Sensor Failure Which Occurs at 4.00 sec. Pitch Command Dither Has Amplitude ± 4 deg/sec and Frequency 6.6611 rad/sec.

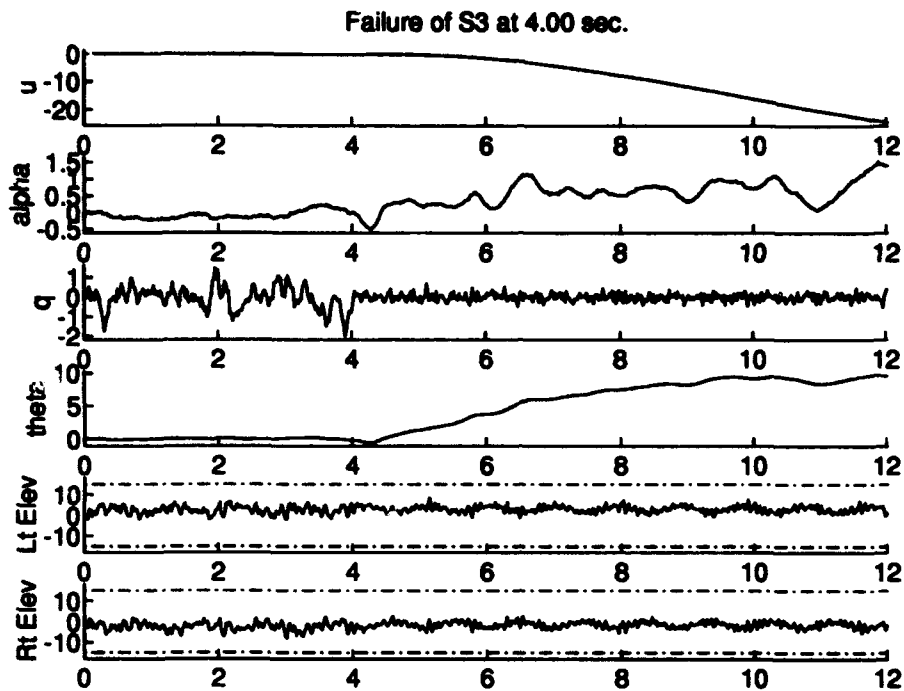


Figure 5.10 Longitudinal Flight Data Sensors Responding to Pitch Rate Sensor Failure Occurring at 4.00 sec. Flight Control System Commands to Actuators are Shown in Bottom Two Plots. Pitch Command Dither Has Amplitude ± 4 deg/sec and Frequency 6.6611 rad/sec.

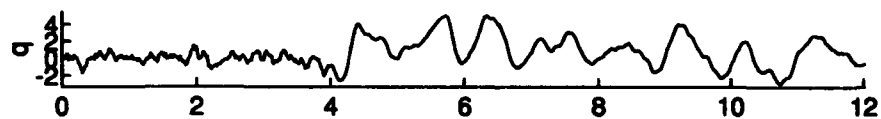


Figure 5.11 Aircraft Pitch Rate State Resulting from Failed Pitch Rate Sensor Failure Occurring at 4.00 sec. Pitch Command Dither Has Amplitude ± 4 deg/sec and Frequency 6.6611 rad/sec.

5.3 Dithering at the Phugoid Frequency and Low Magnitude

The problems of short simulation duration caused the very low frequency trials to be all but discarded when plotting the failure identification times *vs* acceleration for the various test frequencies. Also, because of the large magnitude on the dither sinusoids, the elevator control surfaces were commanded out of their limits. To perform a partial investigation of what was missing, a very low magnitude dither at the phugoid frequency ($\omega = 0.2484$) was used for a set of test runs. Dither signals applied to the command input are represented by Equation (5.1):

$$\begin{aligned}
 \text{Right pitch rate command} &= 0.3 \times \sin(0.2484t + \phi_{er}) \text{ deg/sec} \\
 \text{Left pitch rate command} &= 0.3 \times \sin(0.2484t + \phi_{el}) \text{ deg/sec} \\
 \text{Right roll rate command} &= 1.0 \times \sin(0.2484t + \phi_{er}) \text{ deg/sec} \\
 \text{Left roll rate command} &= 1.0 \times \sin(0.2484t + \phi_{el}) \text{ deg/sec} \\
 \text{Right sideslip angle command} &= 1.0 \times \sin(0.2484t + \phi_{rr}) \text{ deg} \\
 \text{Left sideslip angle command} &= 1.0 \times \sin(0.2484t + \phi_{rl}) \text{ deg}
 \end{aligned} \tag{5.1}$$

The resulting failure identification times are significant reductions from those of our optimal dither in Figure 4.15. See Figure 5.12. The pitch rate magnitude of 0.3 deg/sec causes the elevators to move through 63% of their $\pm 15^\circ$ range with the left elevator nearly breaking the upper limit and the right elevator nearly breaking the lower limit. The ailerons and rudders utilize less than 20% of their ranges when commanded with the dither signals given in Equation (5.1). Note, however, from Table 5.1 that the *g*-limits have not been broken, as is the case with the Trials of Section 4.2 in which low frequencies cause severe *g*-limit violations.

Table 5.1 Lateral and Vertical Acceleration Statistics Resulting from One Complete Cycle of Phugoid Frequency Dither.

Component	A_y [G's]	A_z [G's]
Maximum Occurrence	0.6706	0.2306
+2 σ	0.1359	0.0597
+1 σ	0.0797	0.0298
mean	0.0234	-0.0002
-1 σ	-0.0329	-0.0301
-2 σ	-0.0892	-0.0600
Minimum Occurrence	-0.7328	-0.2331

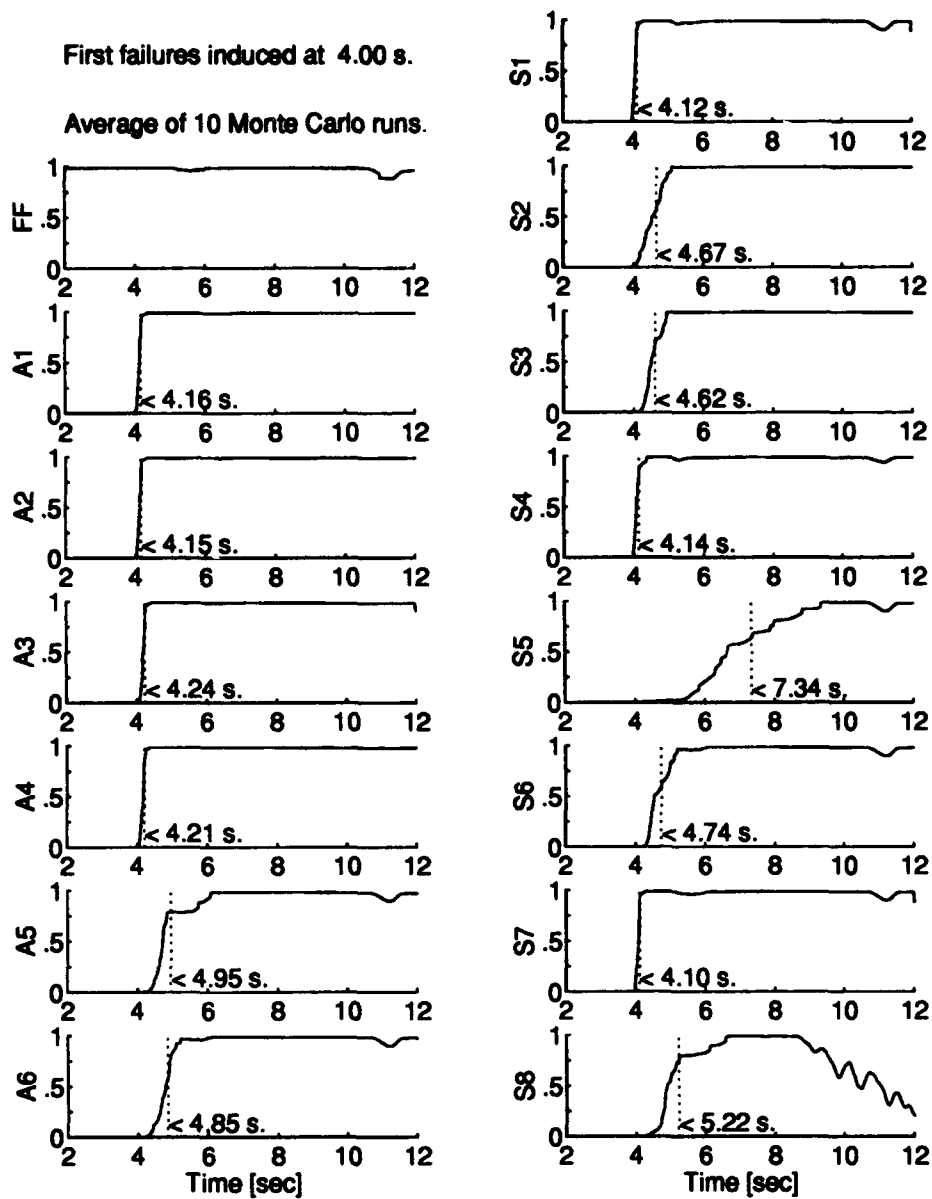


Figure 5.12 MMAE Filter Probability Histories when Dithering at Phugoid Frequency.

Figure 5.13 shows the flight control system command inputs and the g -loading resulting from those inputs. The ordinate labels are defined as follows: Ecnd Rt – right channel pitch rate command; Ecnd Lt – left channel pitch rate command; avg Az – average vertical acceleration from 10 Monte Carlo runs; Acnd Rt – right channel roll rate command; Acnd Lt – left channel roll rate command; Rcnd Rt – right channel sideslip angle command; Rcnd Lt – left channel sideslip angle command; and avg Ay – average horizontal acceleration from 10 Monte Carlo runs.

For the fully functional aircraft, there were no false alarms in ten Monte Carlo runs of 12 seconds duration each. There were false alarms when testing the MMAE against right and left elevators. On Run 4 with the induction of a right elevator actuator failure at 4.00 seconds, the correct filter was identified at 4.22 seconds. 5.60 seconds later, the left elevator was identified but probability subsequently returned to the correct filter. Similarly, three runs with a left elevator actuator failure induced, produced false alarms for angle of attack sensor and right elevator actuator failures. There is no consistent pattern and, of 140 separate runs, there were only these four false alarms. This neglects the aircraft instability and false alarms caused by a failed yaw rate sensor as seen in the probability plot of filter S8 in Figure 5.12.

The false alarm of the left elevator on Run 4 was investigated in-depth. No explanation could be found for this false alarm. The filter residuals for the correct filter were zero-mean Gaussian, as expected, and the residuals for the falsely declared filter were well outside their $\pm 2\sigma$ bounds. The only deviation from a normal run is that the remaining operational elevator is commanded to deflect 8° outside of its travel limits of $\pm 15^\circ$. The limit is broken at 7.26 seconds and rises smoothly to a maximum of 128% of the elevator deflection range. The limit is broken well after the first correct failure is declared but before the false second failure is declared. The phase relationship between the two elevator control surfaces is lost when one surface fails. This gives the remaining surface complete authority over the controlled aircraft state, pitch rate. Why the remaining elevator is commanded to deflect even more than when it was competing with opposing commands to the other elevator is a mystery. Our investigations reveal no explanations. However, this event does add credibility to the idea that a different dithers should be employed when the aircraft already has one failed component. Dithers for the fully functional aircraft were designed with all control surfaces and sensors intact. It therefore follows to reason that dithers for partially disabled aircraft should be designed according to the available flight control components.

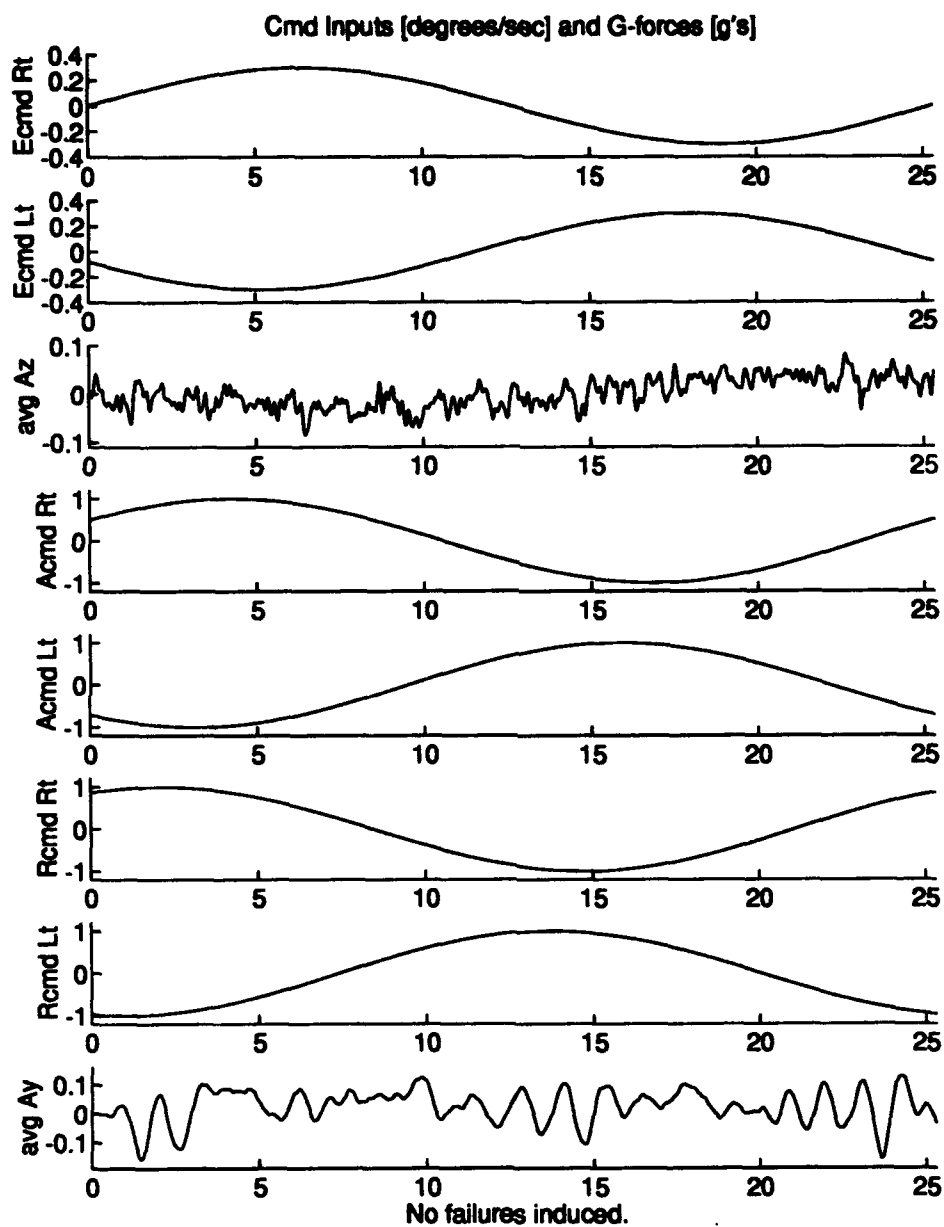


Figure 5.13 Command Inputs and Resulting Vertical and Horizontal Accelerations when Dithering at Phugoid Frequency.

Referring to Figure 5.13, we can see the unusual effect of dithering at the phugoid frequency. The vertical g -load has the high frequency content associated with wind gusting but it also has the low frequency component of the phugoid. The range of vertical acceleration samples does not exceed the limit of $0.1\ g$. It is important to note that a full cycle of command input is complete at the end of the simulation, which runs for 25.30 seconds. Other simulations in this thesis stop at 12.02 seconds. Even though the statistics only represent one cycle, they are more representative of the true effect than statistics from a partial cycle.

With the exception of the lateral control surface actuator failures and the angle of attack sensor failure, better MMAE performance was obtained with the shorter frequency dithers of Equation (4.6). Therefore, in light of the false alarms and small improvement in some failure identification times, we are more inclined to view the optimal dither of Figure 4.15 as the best dither possible within the scope of our work.

5.4 Chapter Summary

There were observations made in Chapter IV which have merited further study to provide credible substance to the explanations given concerning the primary research objectives. The first is unusual MMAE performance resulting from a failed yaw rate sensor. A separate analysis concludes that no problem exists with the MMAE algorithm in this particular situation, but that a failed yaw rate sensor causes the aircraft to go unstable in the lateral channel. This explanation must be kept in mind wherever yaw rate sensor failures are induced.

Sensors providing a feedback signal to the flight control system seemed to take longer to identify than sensors that do not provide feedback. One might suppose that, since the failure of these sensors has an effect on all aircraft states, they might have quicker failure identification times. The converse is true, and the detailed analysis in this chapter revealed that the residual of the failed sensor in the fully functional filter actually has a decrease in variance once a failure is induced. The MMAE must wait for all of the other residuals to deviate from zero-mean before it is able to declare the correct failure.

Finally, the problem of elevator control surfaces breaking their travel limits when dithered at low frequencies is corrected. The phugoid frequency is chosen as the dither frequency and the

dither magnitudes are adjusted so that the travel limits are not broken. With this correction, MMAE performance is re-evaluated against low frequency dithers. Some improvement was gained in failure identification times, although an exceptionally long time was taken to identify a failed sideslip angle sensor, which is not surprising since this sensor has a great deal of additive noise in its output.

VI. Conclusions and Recommendations

Our investigation of the MMAE algorithm has revealed several interesting characteristics about the nature of MMAE and its application to a dynamic system with rather significant random inputs. This chapter will review the findings of the research with respect to the initial objectives, summarize the conclusions drawn from the Kalman filter tuning experience, and present a suggested course of action to implement MMAE on-board the real LAMBDA. Finally, topics for further research are presented.

6.1 Summary of Findings

A review of the research objectives established in Section 1.5 is now presented along with a review of the actual findings.

What is the form of the dither input that causes the quickest convergence of the MMAE algorithm to a correct failure hypothesis?

It appears that the sinusoidal signal possesses the best characteristics for dithering a system to enhance MMAE failure identification. The first reason is that the sinusoid has a constantly changing first derivative. This has advantages above the square wave and triangle wave in that the system is constantly being excited rather than just relying on the transients of the system for excitation. Secondly, the excitation may be confined to a single frequency rather than a band. A square wave produces system excitation that has the frequency components of the period between pulses, the duration of the pulse, and the natural frequency of the system, as well as high frequency content due to the sharp change. With the sinusoid, we have shown that failure identification times may be correlated with the frequency of dither. Thus, there is no need to add in several different frequencies to enhance MMAE failure identification. However, if a combination of frequencies is found to be useful in failure identification, some linear combination of sinusoids could be designed so that all frequency components could be controlled.

What magnitude of lateral and vertical g-forces would be considered to be "subliminal" to the aircrew?

Our research in determining the limits of "subliminal" g-loading was restricted to the findings in published literature and personal interviews with authorities on human factors engineering. The

limit of 0.10 g 's in the vertical direction and 0.20 g 's in the horizontal direction was based mainly on Menke's statement [15] and supported by various other sources mentioned in Subsection 3.4.2.

What is the best balance between subliminality and failure identification time?

The plots of acceleration *versus* MMAE failure identification time in Section 4.2 generally have a breaking point where the accelerations become very large for very little improvement in failure identification time. We note that the issues to balance are really failure identification time and aircraft state excitation rather than applied g -forces. Accelerations in the vertical and horizontal directions are derived from state excitation. Also, failure identification times for control surfaces depend on control surface deflections which, with the QFT flight control system, is a function of offset between right and left control input channels. As discussed in Subsection 4.2.1, the relationship between applied g -forces and failure identification time is different from failed component to failed component. Therefore, a compromise must be made in defining the optimal dither for *all* component failure identifications.

What format of dither input will provide the best overall performance in terms of failure protection, aircrew convenience, and comfort?

In terms of best overall MMAE performance, the optimal dither of Equation (4.6) provides the best protection for all failed component identifications if only constant magnitude, frequency, and phase are used. In terms of aircrew comfort, this optimal dither also limits aircraft g -loads to less than the established limits for this thesis. However, considering that the LAMBDA is an unmanned, remotely piloted vehicle, the limit of g -forces simply demonstrates that they *can* be limited, as is desired for manned aircraft, while providing good MMAE failure identification performance. The question of convenience was not addressed for the lack of immediate resources and lack of concern with respect to the unmanned LAMBDA.

Does the MMAE hierarchical-structured failure detection algorithm converge to the correct dual failure hypothesis?

The hierarchical structure performs well when the aircraft system is controlled with our optimal dither of Equation (4.6). Although there were a few false alarms, there was no pattern of consistent false alarms or missed alarms.

Does the algorithm converge to the correct dual failure hypothesis quickly enough to prevent incorrect failure hypotheses declarations or severely degraded control of the aircraft?

A fortunate example available to illustrate that a failure can be identified *before* the aircraft goes out of control is that of the yaw rate sensor failure. The problems of aircraft stability associated with this failure are discussed in Section 5.1. It is proven that a yaw rate sensor failure can be identified by the MMAE within one second and the aircraft will remain stable for up to 4 seconds after the failure. This allows 3 seconds for flight control system re-configuration which, in this case, may simply be to null the flight control systems' commands to the rudder control surfaces. We have also proven that two failures spaced in time by 1 second are identified correctly with the MMAE hierarchical structure.

Is the algorithm's performance path-dependent for the identification of simultaneous dual failures?

Simultaneous dual failures were not tested. However, it is noted that the order of failures does impact the time to identify them.

The difficulties encountered while tuning the elemental Kalman filters led to the development of a computer algorithm to accomplish this task. The objective is to allow for unknown wind perturbations of state variables while keeping elemental Kalman filters tightly tuned. This was accomplished by tuning against a portion of the simulated wind conditions against which the MMAE-augmented LAMBDA model is flown. The strategy is to reduce the entire Q matrix incrementally so that MMAE probability of fully functional filter does not drop below 2% of its maximum value during 60 seconds of simulation.

A peculiarity of using MMAE on a system augmented with a control system was found. The left and right flight control systems, when subjected to out-of-phase dithers, attempt to compensate for the unrealized change in a single controlled aircraft state by increasing the deflection of their respective control surface. Even though the flight control system input magnitudes are kept the same, there was a big difference between the amount of control surface deflection that was commanded for different frequencies. So, the effect is that as dither frequency varied, so did the magnitude of aircraft state excitation which, we know, also plays a predictable roll in failure identification time.

An optimal dither routine was deduced by testing the time to identify all types of single failures against different frequencies and magnitudes of input dither. The first task was to alter frequency while input dither magnitude remained constant. Actuator failures are best identified with higher frequency dithers at about the 3 rad/sec. Sensor failures have a dither frequency relationship with failure identification time that can be predicted by looking at the Bode plot response of the corresponding aircraft state to the dithering control surface. That is, for dither frequencies in the high-gain region of the Log-magnitude plot, one can expect quick failure identification times. However, if a sensor is included in the feedback loop of the flight control system, the time to identify the failure of that sensor does not correlate with the Log-magnitude Bode plot. A study of this phenomenon was accomplished and the findings are that the scalar residual behavior exhibited by a non-feedback sensor is not characteristic of that of a feedback sensor. Rather, as with control surface failures, more than one residual of the fully functional filter will begin to deviate. In addition, the scalar residual of the failed sensor may have a reduced variation in the fully functional filter. The impact is that scalar residual monitoring must be accomplished in the filter which hypothesizes the failure of the sensor.

An optimal dither format was developed based on a balance of best frequency and magnitude of dither for each type of failure in each channel. Rudder and aileron dithers were synchronised in frequency to simplify analysis, but there is the possibility that using separate dither characteristics for these control surfaces will yield better failure identification by taking advantage of the sideslip angle and yaw rate response to low frequency.

A sample of the LAMBDA's pilot control stick inputs was obtained and applied to the inputs of our truth model. The intent was to see what MMAE performance would be if no automatic dither is applied and the only flight control system inputs are those of the pilot in his/her effort to maintain a straight and level flight path. In this study, there was no phase difference between left and right channel control inputs. Under that condition, the MMAE was unable to distinguish a left actuator from a right actuator failure effectively. However, sensor failures were identified quickly. Of note is that the pilot's commands resulted in *g*-loading outside of our established limits.

6.2 *Suggestions for Implementing an Effective MMAE on LAMBDA*

The optimal dither routine has been established for the flight conditions simulated in the software designed with the uncertainty characteristics specified by the Dryden Wind Gust Model. MMAE performance varied greatly according to how this model was represented by zero-order approximations in the elemental Kalman filter models. No work in this thesis makes any attempt to verify that this model represents the conditions encountered by the LAMBDA in actual test flights. Therefore, it is important to acquire actual flight data and use the tuning algorithm described in Section 4.1 to develop the steady state Kalman filter gains required for good MMAE performance in actual wind conditions. At least, the tuning derived in our research should be verified against such data.

The controllability of the LAMBDA must be verified from an operator's perspective while undergoing automatic dithers. This could be done by using the computerized LAMBDA flight simulator found at Wright Laboratory Flight Controls Division, Flight Controls Techniques Branch. It must be established that the video display is not too jittery for the pilot to track a desired course comfortably and effectively. Our studies verified that the g -loading on a hypothetical pilot on-board the LAMBDA is not uncomfortable. This was done to extend the application and effectiveness of an MMAE dither to manned aircraft with the assumption that the same dither would not cause the ground-based LAMBDA pilot problems in controlling the unmanned aircraft.

Finally, the type of actuator failures simulated in this thesis are realized by floating or missing control surfaces. That is, the zeroing out of a column in the B matrix means that no aerodynamic forces are applied by the control surface. If failed actuators are realized by control surfaces *fixed* in the neutral (or worse, non-neutral) position rather than failing to free-stream, unmodeled forces would be applied and poor actuator failure identification would result.

6.3 *Recommended Topics for Further Research*

Since the MMAE identification time for each component subject to failure depends on the frequency and magnitude of dither, it would be advantageous to alter the dither parameters according to the type failure suspected. For instance, if the longitudinal channel has lost the use of one elevator, it would be meaningless to continue to dither the aircraft as a frequency and magnitude that

is suited to enhance MMAE identification of a failed elevator actuator. Rather, a dither designed strictly for sensor failure identification should begin. Furthermore, appropriate dithers for partially disabled aircraft should be designed while keeping in mind which flight control components are available.

An aspect of subliminality is the lack of annoyance to the pilot. Because the human body is able to perceive very small angular acceleration and linear acceleration, it may be futile to develop an effective dither signal that is imperceptible. On the other hand, we can design a dither signal that may not be an annoyance to the pilot. Considering the nature of wind, with its unpredictability, an effective dither signal might be designed to have the *feel* of atmospheric turbulence of a level just above that through which the aircraft is currently flying. This would provide the aircraft state excitation required for effective MMAE failure identification, and it would not subject the pilot to unfamiliar or nauseating dynamics.

Dithers having the form of swept sine waves or band-limited noise dithers may provide the aircraft state excitation required for MMAE failure identification and be unpredictable enough to avoid pilot annoyance. As shown in our research, there are several frequencies in each axis that facilitate good MMAE performance. A dither signal that sweeps across these frequencies will cover the best frequency for each component at time intervals, instead of just dithering at some compromise frequency as we have done. A random frequency sweep may make the dither signal indistinguishable from wind disturbance. Another suggestion is to form a linear combination of sinusoids. The sensitive frequencies for several types of failure identifications could be superimposed on one dither signal to form a linear combination, so that the best dither for all components is applied continuously.

While testing failure identification times as dither frequency and magnitude are varied, a coarse discretization of frequency/magnitude points was used to form the test parameter space. Finer discretization may clear up problems of identifying trends in identification times related to the roll rate sensor failure and yaw rate sensor failure. Another solution to creating more consistent trends would be to force the failure being tested to occur at exactly the same phase angle of each different frequency of dither. This would ensure that the MMAE attempts to identify failures at similar dynamic changes for all frequencies.

Another proposal for altering our experimental procedure to provide more consistent results is to set the dither phase offset to zero, then test for sensor failure responses. The strategy is to note the degree of aircraft state excitation required for good sensor failure identification. This will establish the amount of aircraft state excitation that should remain constant from dither frequency to dither frequency. In the experiments of this thesis, input dither magnitude was kept constant over all frequencies while aircraft state excitation magnitude was allowed to vary greatly. The effect of dither frequency changes could be isolated further by altering input dither magnitude to keep aircraft state excitation magnitude constant over various dither frequencies.

More study should be undertaken to establish the best phase relationship between left and right control channels. This could be accomplished by offsetting opposite control surface dithers by 180° and performing only actuator failures as dither magnitude is increased from zero. A minimum degree of control surface deflection for good actuator failure identification should be established by experimentation. The 180° phase between channels should promote maximum efficiency in identifying left from right actuator failures. Since left and right channels will attempt to cancel each other out, the effect on aircraft state excitation should be minimal with all actuators operational. The next step is to shift the phase from 180° , thereby increasing aircraft state excitation to the point established by experiment as described in the previous paragraph. The result should be a dither magnitude and *phase* that provide a balanced system input for the best MMAE failure identification for both actuators and sensors.

An important suggestion is to dither all surfaces at the same frequency for each test. This assures that no other frequencies are introduced from one channel through the cross coupling terms of the other channel. All surfaces must be dithered in each test, however. Zero excitation in one channel will lead to an unreliable MMAE response for that channel, which will detract from MMAE probabilities being formed in the channel that is being dithered.

It was demonstrated in Section 5.1 that the MMAE is able to identify the failure of a critical flight control system component, the yaw rate sensor. Loss of its feedback signal to the washout filter caused the aircraft to go unstable. The MMAE readily provides good estimates of the yaw rate sensor signal despite the sensor's failure. It follows that these estimates may *replace* the yaw rate sensor signal in the event of such a failure and thus provide stable control of the aircraft.

Similarly, the pitch rate sensor measurement could be replaced by an MMAE estimate of the pitch rate state in case of a pitch rate sensor failure. Although the aircraft is not unstable with this failure, improved flight control system performance can be realized. An investigation into MMAE state estimate replacement of sensor signals is recommended.

Finally, knowing the behavior of scalar residuals with respect to their correspondence to feedback or non-feedback sensors allows one to devise a strategy for effective residual monitoring. This is especially important when dealing with sensors that provide feedback to the QFT flight control system, since their failures have a tendency to take longer to identify than those of non-feedback sensors.

6.4 Report Summary

The research in this thesis seeks to identify the best dither routine for enhancing MMAE failure identification and to investigate the performance of a hierarchical structure in the MMAE identification of dual failures. The theory behind MMAE is presented in Chapter I along with the research objectives. A review of previous MMAE research was undertaken to establish what is known and what is as yet unknown about MMAE, so that the present work will serve to build on that knowledge. The methods for achieving the research objectives were presented in Chapter III, along with justification for the structure of models used in computer simulations. In Chapter IV, the results of testing are presented and analyzed with respect to the research objectives. Support for secondary conclusions not related to the primary research objectives is provided in Chapter V. A summation of conclusions is found in the present chapter. Supporting appendices give complete insight to all results and conclusions reported.

Appendix A. Dimensional Stability Derivatives

The primed dimensional stability derivatives used in the LAMBDA truth model for this thesis are the result of an analysis of data from LAMBDA flights conducted by WL/FIGS [26]. Table 1.1 gives the nominal flight conditions corresponding to the the values in Tables A.1 and A.2. They are to be used in Equation (3.1) which describes the LAMBDA's aerodynamic characteristics in state space format. Also, the wind states to aircraft states transformation matrix of Equation (3.24) makes use of these same stability derivatives.

Table A.1 LAMBDA longitudinal primed dimensional stability derivatives.

Symb.	Value	Definition
X'_u	-0.413963×10^{-1}	Change in longitudinal force due to change in velocity
X'_α	4.51655	Change in longitudinal force due to change in angle of attack
X'_q	2.76989	Change in longitudinal force due to change in pitch rate
X'_θ	-32.1700	Change in longitudinal force due to change in pitch angle
$X'_{\delta_{e,l}}$	-0.300342	Change in longitudinal force due to change in left elevator angle
$X'_{\delta_{e,r}}$	-0.300342	Change in longitudinal force due to change in right elevator angle
$X'_{\delta_{a,l}}$	0.970785×10^{-1}	Change in longitudinal force due to change in left aileron angle
$X'_{\delta_{a,r}}$	0.970785×10^{-1}	Change in longitudinal force due to change in right aileron angle
Z'_u	-0.265210×10^{-2}	Change in vertical force due to change in velocity
Z'_α	-4.01458	Change in vertical force due to change in angle of attack
Z'_q	0.977740	Change in vertical force due to change in pitch rate
Z'_θ	0	Change in vertical force due to change in pitch angle
$Z'_{\delta_{e,l}}$	-0.150277	Change in vertical force due to change in left elevator angle
$Z'_{\delta_{e,r}}$	-0.150277	Change in vertical force due to change in right elevator angle
$Z'_{\delta_{a,l}}$	-0.304528	Change in vertical force due to change in left aileron angle
$Z'_{\delta_{a,r}}$	-0.304528	Change in vertical force due to change in right aileron angle
M'_u	-0.228065×10^{-2}	Change in pitching moment due to change in velocity
M'_α	-45.4757	Change in pitching moment due to change in angle of attack
M'_q	-3.38135	Change in pitching moment due to change in pitch rate
M'_θ	0	Change in pitching moment due to change in pitch angle
$M'_{\delta_{e,l}}$	-23.2027	Change in pitching moment due to change in left elevator angle
$M'_{\delta_{e,r}}$	-23.2027	Change in pitching moment due to change in right elevator angle
$M'_{\delta_{a,l}}$	-3.91485	Change in pitching moment due to change in left aileron angle
$M'_{\delta_{a,r}}$	-3.91485	Change in pitching moment due to change in right aileron angle

Table A.2 LAMBDA lateral primed dimensional stability derivatives.

Symb.	Value	Definition
Y'_β	-0.185589	Change in lateral force due to change in sideslip angle
Y'_p	-0.167993×10^{-1}	Change in lateral force due to change in roll rate
Y'_ϕ	0.190265	Change in lateral force due to change in roll angle
Y'_r	-0.995281	Change in lateral force due to change in yaw rate
$Y'_{\delta_{a,l}}$	0	Change in lateral force due to change in left elevator angle
$Y'_{\delta_{a,r}}$	0	Change in lateral force due to change in right elevator angle
$Y'_{\delta_{a,l}}$	0	Change in lateral force due to change in left aileron angle
$Y'_{\delta_{a,r}}$	0	Change in lateral force due to change in right aileron angle
Y'_{δ_r}	0.138001	Change in lateral force due to change in rudder angle
L'_β	-8.84221	Change in rolling moment due to change in sideslip angle
L'_p	-11.1274	Change in rolling moment due to change in roll rate
L'_r	2.00065	Change in rolling moment due to change in yaw rate
$L'_{\delta_{a,l}}$	3.01717	Change in rolling moment due to change in left elevator angle
$L'_{\delta_{a,r}}$	-3.01717	Change in rolling moment due to change in right elevator angle
$L'_{\delta_{a,l}}$	66.3312	Change in rolling moment due to change in left aileron angle
$L'_{\delta_{a,r}}$	-66.3312	Change in rolling moment due to change in right aileron angle
L'_{δ_r}	-0.662067	Change in rolling moment due to change in rudder angle
N'_β	12.8746	Change in yawing moment due to change in sideslip angle
N'_p	-0.226784	Change in yawing moment due to change in roll rate
N'_r	-0.864736	Change in yawing moment due to change in yaw rate
$N'_{\delta_{a,l}}$	-0.280877×10^{-1}	Change in yawing moment due to change in left elevator angle
$N'_{\delta_{a,r}}$	0.280877×10^{-1}	Change in yawing moment due to change in right elevator angle
$N'_{\delta_{a,l}}$	-2.15844	Change in yawing moment due to change in left aileron angle
$N'_{\delta_{a,r}}$	2.15844	Change in yawing moment due to change in right aileron angle
N'_{δ_r}	-21.9503	Change in yawing moment due to change in rudder angle

Appendix B. Bode Plots of Actuator Transfer Functions

The natural amplitude ratio response of the eight aircraft states to control surface inputs is presented in this appendix in the form of logarithmic magnitude Bode plots. This data is used in the analysis of Section 4.2.1 as a means of correlating MMAE failure identification times to the natural response of aircraft states to dither inputs.

Each caption indicates the input and output of the transfer function used in generating the indicated plot. A constant log-magnitude line derived by subtracting 20 dB from the peak magnitude is drawn in each plot. The crossing of this line with the log-magnitude response indicates the bandwidth of the response. Bandwidth could be derived using other methods, but this one seems to generate more consistent results as each state is excited by different control surfaces.

The frequency of the peak log-magnitude is indicated in the caption by ω_{pk} given in radians per second, as is the bandwidth, ω_{BW} . When required, an upper bandwidth frequency is indicated by $\omega_{BW_{upper}}$ and a lower bandwidth frequency by $\omega_{BW_{lower}}$.

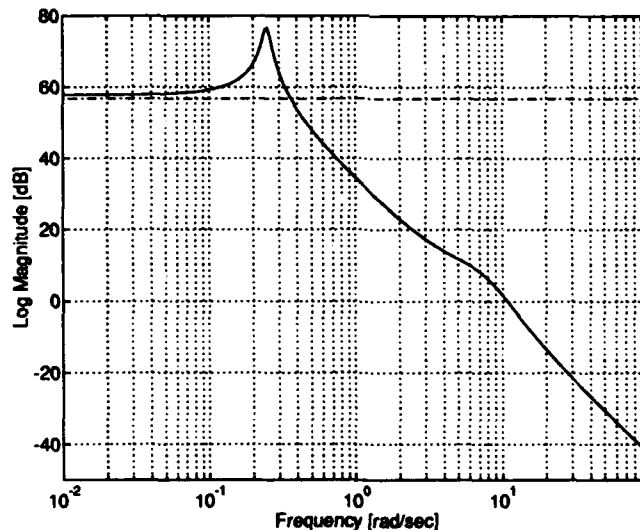


Figure B.1 Log Magnitude Response of forward velocity to Left Elevator. Peak Magnitude Minus 20 dB is 56.72 dB. $\omega_{pk} = 0.25$ and $\omega_{BW} = 0.36$ rad/sec.

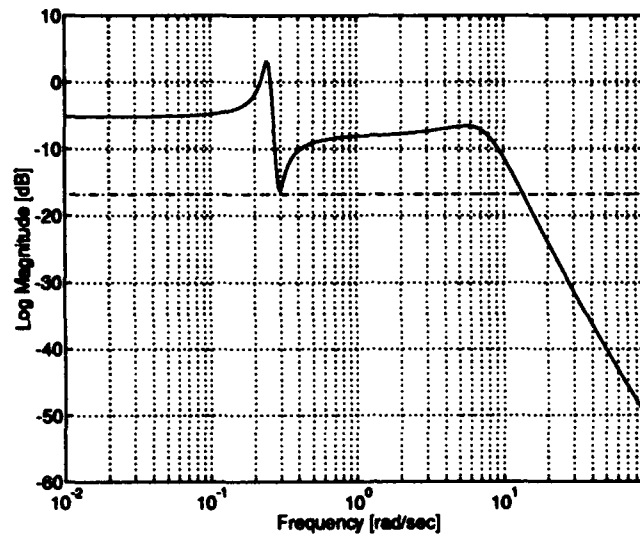


Figure B.2 Log Magnitude Response of Angle of attack to Left Elevator. Peak Magnitude Minus 20 dB is -16.78 dB. $\omega_{pk} = 0.24$ and $\omega_{BW} = 13.55$ rad/sec.

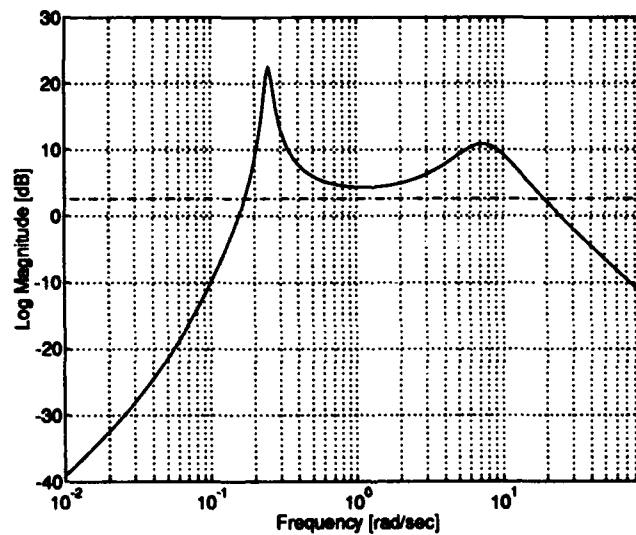


Figure B.3 Log Magnitude Response of Pitch Rate to Left Elevator. Peak Magnitude Minus 20 dB is 2.62 dB. $\omega_{pk} = 0.25$, $\omega_{BW_{lower}} = 0.17$ and $\omega_{BW_{upper}} = 18.91$ rad/sec.

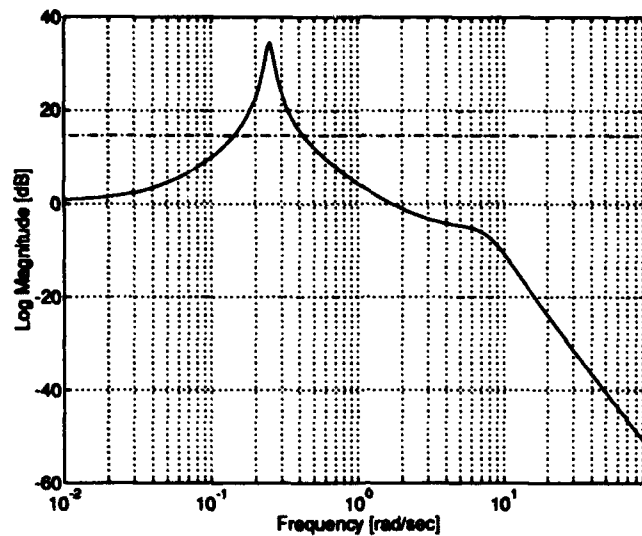


Figure B.4 Log Magnitude Response of Pitch Angle to Left Elevator. Peak Magnitude Minus 20 dB is 14.66 dB. $\omega_{pk} = 0.25$, $\omega_{BW_{lower}} = 0.14$ and $\omega_{BW_{upper}} = 0.42$ rad/sec.

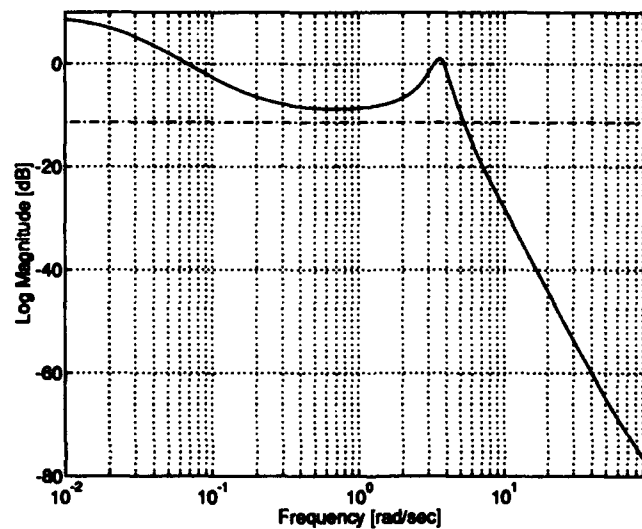


Figure B.5 Log Magnitude Response of Sideslip Angle to Left Aileron. Peak Magnitude Minus 20 dB is -11.40 dB. $\omega_{pk} = 0.01$ and $\omega_{BW} = 5.26$ rad/sec.

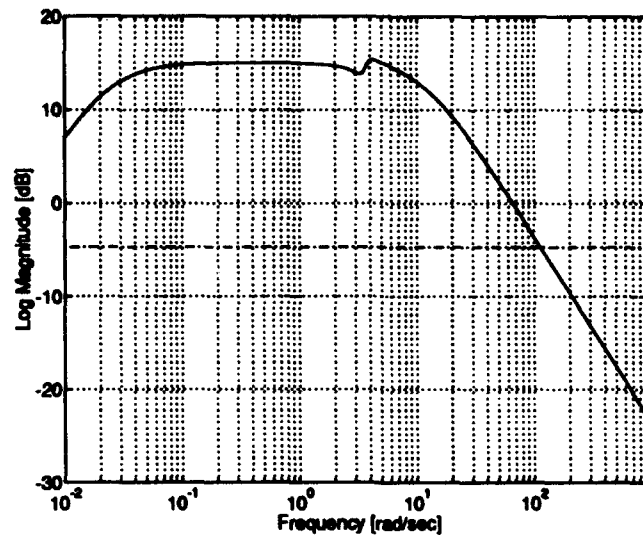


Figure B.6 Log Magnitude Response of Roll Rate to Left Aileron. Peak Magnitude Minus 20 dB is -4.68 dB. $\omega_{pk} = 4.20$ and $\omega_{BW} = 113.20$ rad/sec.

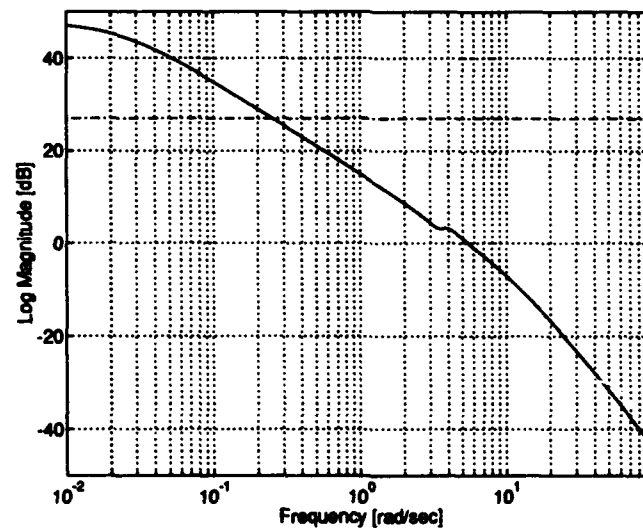


Figure B.7 Log Magnitude Response of Roll Angle to Left Aileron. Peak Magnitude Minus 20 dB is 27.00 dB. $\omega_{pk} = 0.01$ and $\omega_{BW} = 0.25$ rad/sec.

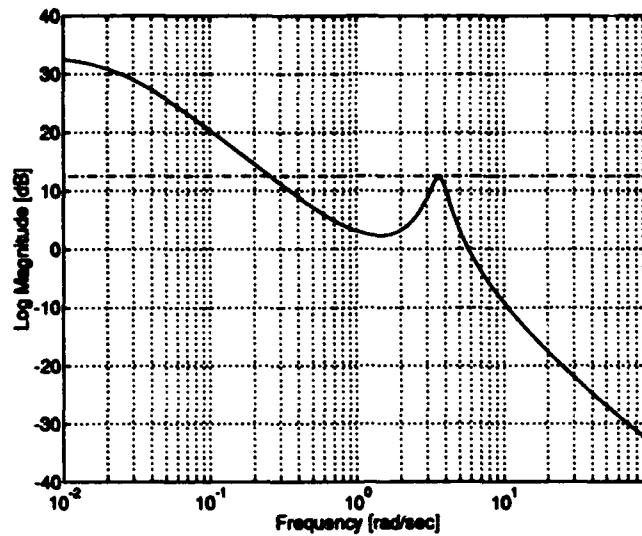


Figure B.8 Log Magnitude Response of Yaw Rate to Left Aileron. Peak Magnitude Minus 20 dB is 12.53 dB. $\omega_{pk} = 0.01$ and $\omega_{BW} = 0.26$ rad/sec.

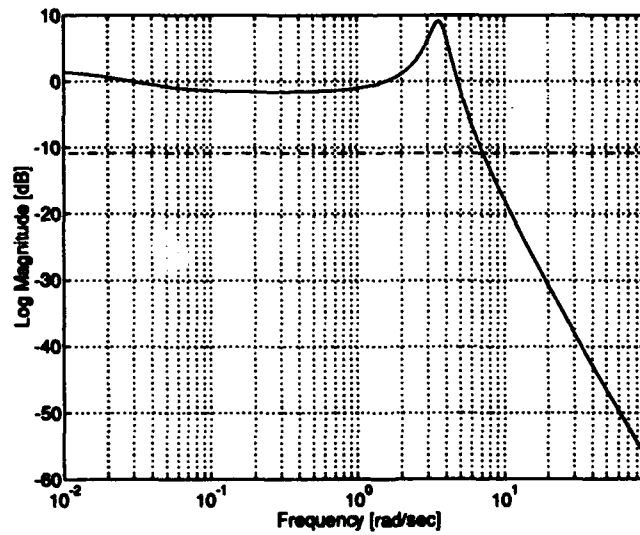


Figure B.9 Log Magnitude Response of Sideslip Angle to Left Rudder. Peak Magnitude Minus 20 dB is -10.88 dB. $\omega_{pk} = 3.60$ and $\omega_{BW} = 7.16$ rad/sec.

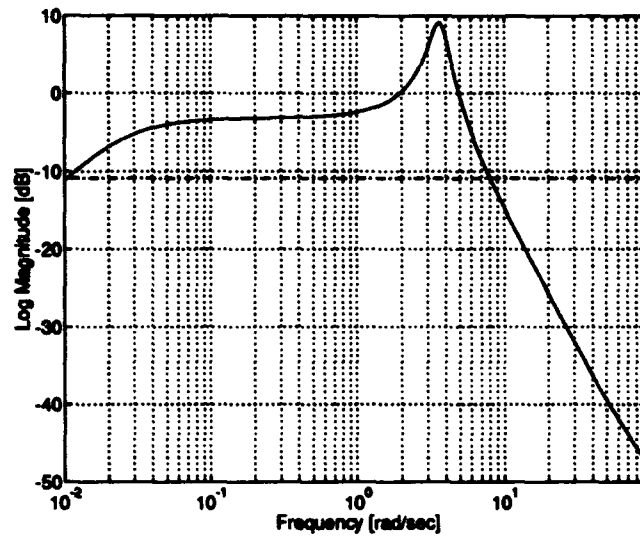


Figure B.10 Log Magnitude Response of Roll Rate to Left Rudder. Peak Magnitude Minus 20 dB is -10.87 dB. $\omega_{pk} = 3.60$, $\omega_{BW_{lower}} = 0.01$ and $\omega_{BW_{upper}} = 8.00$ rad/sec.

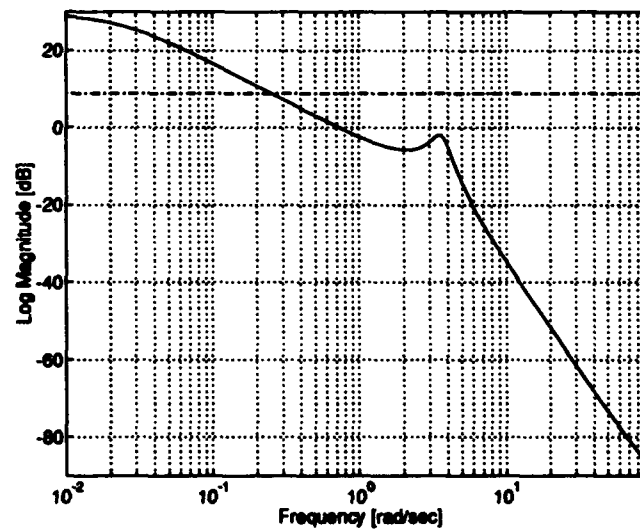


Figure B.11 Log Magnitude Response of Roll Angle to Left Rudder. Peak Magnitude Minus 20 dB is 8.83 dB. $\omega_{pk} = 0.01$ and $\omega_{BW} = 0.25$ rad/sec.

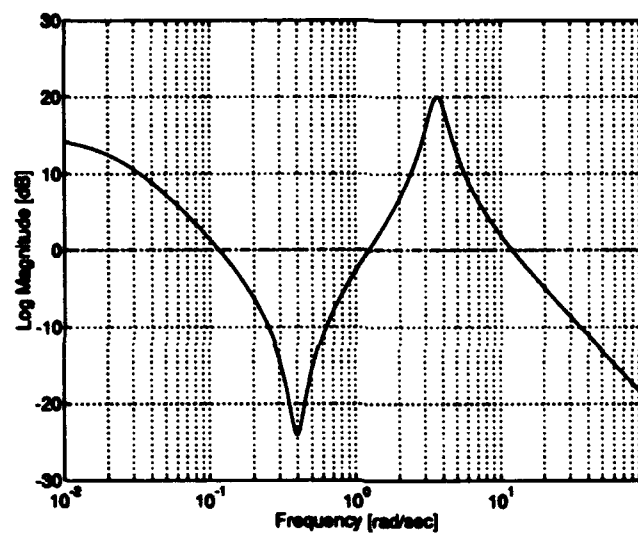


Figure B.12 Log Magnitude Response of Yaw Rate to Left Rudder. Peak Magnitude Minus 20 dB is 0.14 dB. $\omega_{pk} = 3.70$ and cross-over frequencies are at $\omega_{BW} = 0.11, 1.23$, and 11.87 rad/sec.

Appendix C. Difference Equations for QFT Prefilters and Compensators

Listed in this appendix are the difference equations for the prefilters, compensators, and washout filters for the Quantitative Feedback Theory flight control system designed by Capt Rasmussen [26]. The sample time of this design is $T_s = 20$ msec. Refer to Figure 3.1 for a high-level block diagram of this flight control system.

Prefilter F₁₁ has the input Pitch Rate Command, PITCHCMD, and the output F11C which is summed with the Pitch Rate Measurement, PITCH_RATE, to form the Pitch Rate Error, QERR.

$$\begin{aligned} F11A(k) = & 8.9573 \times 10^{-1} \times F11A(k-1) + 1.000 \times PITCHCMD(k) - \\ & 9.1388 \times 10^{-1} \times PITCHCMD(k-1) \end{aligned} \quad (C.1a)$$

$$\begin{aligned} F11B(k) = & 8.1818 \times 10^{-1} \times F11B(k-1) + 1.000 \times F11A(k) + \\ & 1.0000 \times F11A(k-1) \end{aligned} \quad (C.1b)$$

$$\begin{aligned} F11C(k) = & 8.3486 \times 10^{-1} \times F11C(k-1) + 9.0874 \times 10^{-3} \times F11B(k) + \\ & 9.0874 \times 10^{-3} \times F11B(k-1) \end{aligned} \quad (C.1c)$$

Summing block:

$$QERR(k) = F11C(k) - PITCH_RATE(k) \quad (C.2)$$

Compensator G₁₁ has the input Pitch Rate Error, QERR, and the output G11D which is range limited to produce the Elevator Command, ELEVATOR_CMD.

$$\begin{aligned} G11A(k) = & 1.1111 \times 10^{-1} \times G11A(k-1) + 1.0000 \times QERR(k) - \\ & 8.0180 \times 10^{-1} \times QERR(k-1) \end{aligned} \quad (C.3a)$$

$$\begin{aligned} G11B(k) = & 9.6078 \times 10^{-1} \times G11B(k-1) + 1.0000 \times G11A(k) - \\ & 8.4332 \times 10^{-1} \times G11A(k-1) \end{aligned} \quad (C.3b)$$

$$\begin{aligned} G11C(k) = & 6.1538 \times 10^{-1} \times G11C(k-1) - 3.0769 \times 10^{-1} \times G11C(k-2) + \\ & 1.0000 \times G11B(k) - 1.8462 \times G11B(k-1) + \\ & 8.5741 \times 10^{-1} \times G11B(k-2) \end{aligned} \quad (C.3c)$$

$$G11D(k) = 1.0000 \times G11D(k-1) + 3.7457 \times G11C(k) +$$

$$3.7457 \times G11C(k-1) \quad (C.3d)$$

Limit $G11D(k)$ (and consequently $G11D(k-1)$) to $\pm 15^\circ$.

$$ELEVATOR_CMD(k) = G11D(k) \quad (C.4)$$

Prefilter F.22 has the input Roll Rate Command, $ROLLCMD$, and the output $F22A$ which is summed with the Roll Rate Measurement, $ROLL_RATE$, to form the Pitch Rate Error, $PERR$.

$$F22A(k) = 1.0000 \times ROLLCMD(k) \quad (C.5)$$

Summing block:

$$PERR(k) = F22A(k) - ROLL_RATE(k) \quad (C.6)$$

Compensator G.22 has the input Roll Rate Error, $PERR$, and the output $G22C$ which is range limited to produce the Aileron Command, $AILERON_CMD$.

$$\begin{aligned} G22A(k) = & 1.0884 \times G22A(k-1) - 3.9225 \times 10^{-1} \times G22A(k-2) + \\ & 1.0000 \times PERR(k) - 1.6083 \times PERR(k-1) + \\ & 6.4242 \times 10^{-1} \times PERR(k-2) \end{aligned} \quad (C.7a)$$

$$\begin{aligned} G22B(k) = & 9.9860 \times 10^{-1} \times G22B(k-1) + 1.0000 \times G22A(k) - \\ & 9.990 \times 10^{-1} \times G22A(k-1) \end{aligned} \quad (C.7b)$$

$$\begin{aligned} G22C(k) = & 9.9860 \times 10^{-1} \times G22C(k-1) + 5.3345 \times 10^{-2} \times G22B(k) + \\ & 5.3345 \times 10^{-2} \times G22B(k-1) \end{aligned} \quad (C.7c)$$

Limit $G22C(k)$ (and consequently $G22C(k-1)$) to $\pm 15^\circ$.

$$AILERON_CMD(k) = G22C(k) \quad (C.8)$$

Prefilter F.33 has the input Sideslip Angle Command, $BETA_CMD$, and the output $F33B$ which is summed with the Sideslip Angle Measurement, $BETA$, to form the Sideslip Angle Error,

BERR.

$$\begin{aligned} F33A(k) = & 9.4175 \times 10^{-1} \times F33A(k-1) + 1.0000 \times BETA_CMD(k) - \\ & 7.3913 \times 10^{-1} \times BETA_CMD(k-1) \end{aligned} \quad (C.9a)$$

$$\begin{aligned} F33B(k) = & 9.6078 \times 10^{-1} \times F33B(k-1) + 1.5471 \times 10^{-1} \times F33A(k) - \\ & 1.3719 \times 10^{-1} \times F33A(k-1) \end{aligned} \quad (C.9b)$$

Summing block:

$$BERR(k) = F33B(k) - BETA(k) \quad (C.10)$$

Compensator G.33 has the input Sideslip Angle Error, BERR, and the output G33B.

$$\begin{aligned} G33A(k) = & 6.6667 \times 10^{-1} \times G33A(k-1) + 1.0000 \times BERR(k) + \\ & 10.0000 \times 10^{-1} \times BERR(k-1) \end{aligned} \quad (C.11a)$$

$$\begin{aligned} G33B(k) = & 6.6667 \times 10^{-1} \times G33B(k-1) - 3.8194 \times 10^{-2} \times G33A(k) - \\ & 3.8194 \times 10^{-2} \times G33A(k-1) \end{aligned} \quad (C.11b)$$

The Washout Filter has the input Yaw Rate Measurement, YAW_RATE, and the output Yaw Damper Feedback, YD, which is summed with the output of compensator G.33, G33B, and range limited to produce the Rudder Command, RUDDER_CMD.

$$\begin{aligned} YD(k) = & 9.8020 \times 10^{-1} \times YD(k-1) + 3.9604 \times 10^{-1} \times YAW_RATE(k) - \\ & 3.9604 \times 10^{-1} \times YAW_RATE(k-1) \end{aligned} \quad (C.12)$$

Summing block:

$$RUDDER_CMD(k) = G33B(k) - YD(k) \quad (C.13)$$

Appendix D. Failure ID Time vs g-forces as Dither Magnitude Changes

The figures and tables of this appendix are the results of studies similar to those of Section 4.2 except that magnitude instead of frequency is being changed from trial to trial. Trial numbers have varying decimal digits to indicate changes in dither *magnitude*. Identical digits in the units position of the trial numbers indicate simulations with identical dither *frequencies*.

A complete analysis of the following data is accomplished in Subsection 4.2.1. In particular, the tradeoff between adjusting dither magnitude or dither frequency is considered. Information contained in Tables D.1 through D.6 is condensed in Table 4.15 found on page 4-38. Likewise, information contained in Tables D.7 through D.14 is condensed in Table 4.16 on page 4-41.

Table D.1 Results of varying dither magnitude to alter Right Elevator Actuator failure identification time and vertical g -forces.

Trial	4	4.1	4.2
Failure ID time [sec]	0.24	0.29	0.33
Elevator Dither			
Magnitude [deg/sec]	6.00	5.00	4.00
Frequency [rad/sec]	1.6653	1.6653	1.6653
Vertical Acceleration [g's]			
maximum occurrence	0.2510	0.2778	0.2726
+2σ	0.1053	0.0839	0.0722
+1σ	0.0412	0.0403	0.0347
mean	-0.0230	-0.0032	-0.0028
-1σ	-0.0871	-0.0468	-0.0402
-2σ	-0.1512	-0.0904	-0.0777
minimum occurrence	-0.3444	-0.2828	-0.2712

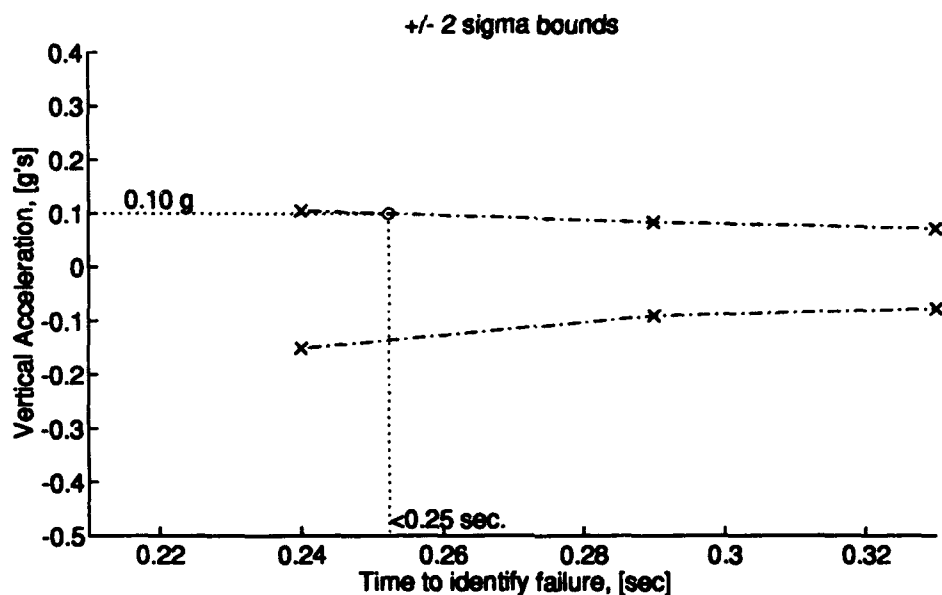
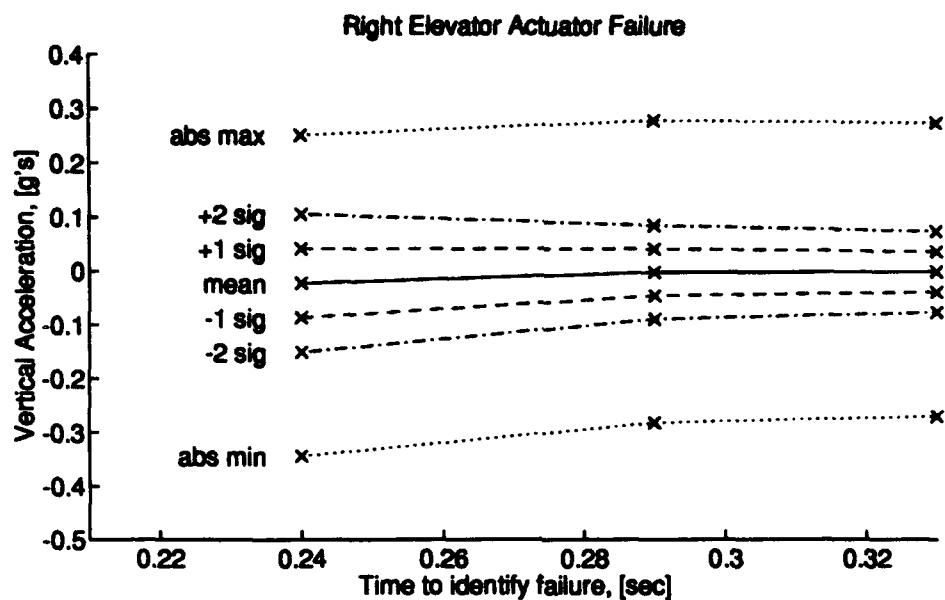


Figure D.1 *g*-forces vs ID time for Right Elevator Actuator failure as magnitude changes.

Table D.2 Results of varying dither magnitude to alter Left Elevator Actuator failure identification time and vertical g -forces.

Trial	4	4.1	4.2
Failure ID time [sec]	0.23	0.25	0.29
Elevator Dither			
Magnitude [deg/sec]	6.00	5.00	4.00
Frequency [rad/sec]	1.6653	1.6653	1.6653
Vertical Acceleration [g's]			
maximum occurrence	0.2510	0.2778	0.2726
+2σ	0.1053	0.0839	0.0727
+1σ	0.0412	0.0403	0.0347
mean	-0.0230	-0.0032	-0.0028
-1σ	-0.0871	-0.0468	-0.0402
-2σ	-0.1512	-0.0904	-0.0777
minimum occurrence	-0.3444	-0.2828	-0.2712

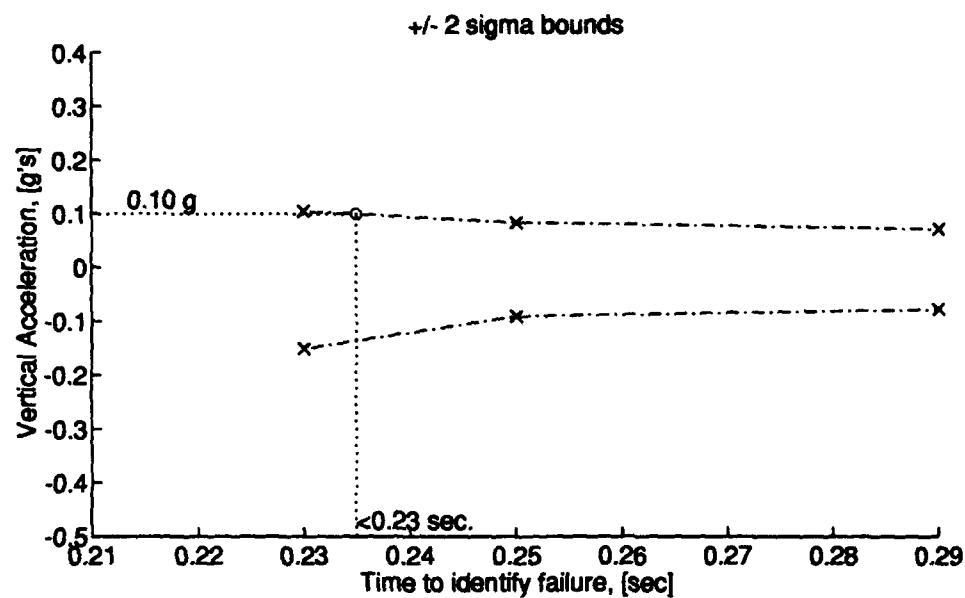
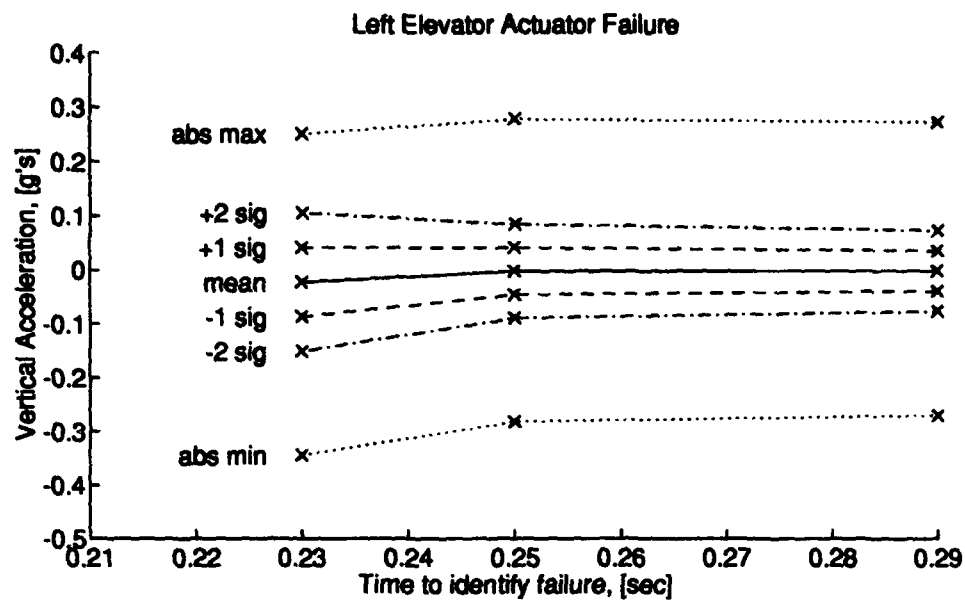


Figure D.2 *g*-forces vs ID time for Left Elevator Actuator failure as magnitude changes.

Table D.3 Results of varying dither magnitude to alter Forward Velocity Sensor failure identification time and vertical g -forces.

Trial	4	4.1	4.2
Failure ID time [sec]	0.58	0.83	0.93
Elevator Dither			
Magnitude [deg/sec]	6.00	5.00	4.00
Frequency [rad/sec]	1.6653	1.6653	1.6653
Vertical Acceleration [g's]			
maximum occurrence	0.2510	0.2778	0.2726
+2σ	0.1053	0.0839	0.0722
+1σ	0.0412	0.0403	0.0347
mean	-0.0230	-0.0032	-0.0028
-1σ	-0.0871	-0.0468	-0.0402
-2σ	-0.1512	-0.0904	-0.0777
minimum occurrence	-0.3444	-0.2828	-0.2712

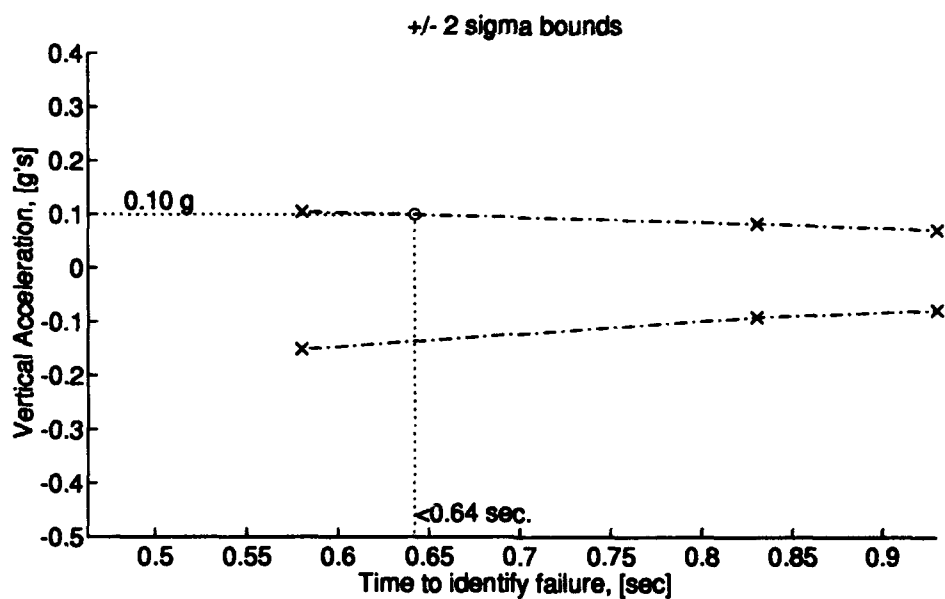
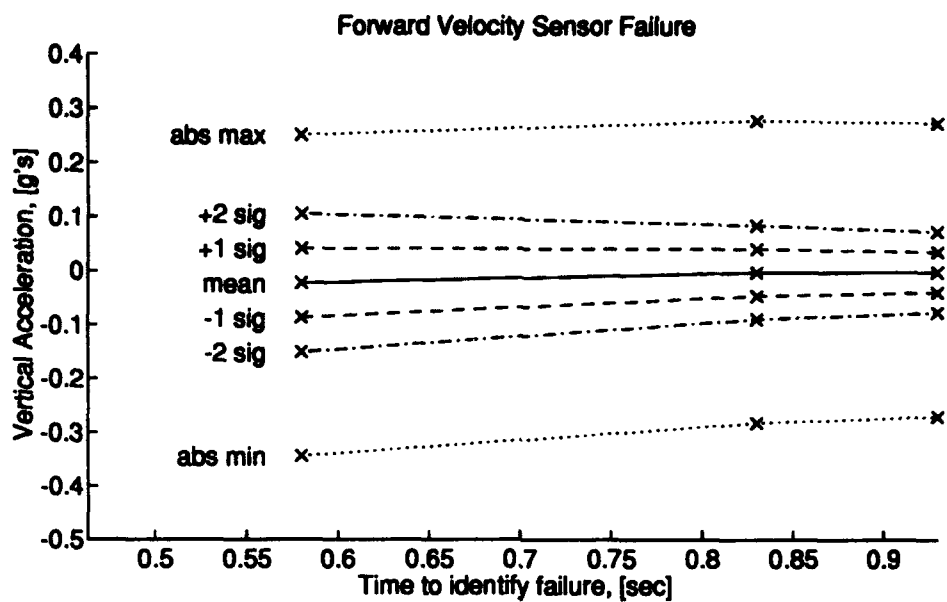


Figure D.3 *g*-forces vs ID time for Forward Velocity Sensor failure as magnitude changes.

Table D.4 Results of varying dither magnitude to alter Angle of Attack Sensor failure identification time and vertical g -forces.

Trial	4	4.1	4.2
Failure ID time [sec]	0.10	1.34	2.26
Elevator Dither			
Magnitude [deg/sec]	6.00	5.00	4.00
Frequency [rad/sec]	1.6653	1.6653	1.6653
Vertical Acceleration [g's]			
maximum occurrence	0.2510	0.2778	0.2726
+2σ	0.1053	0.0839	0.0722
+1σ	0.0412	0.0403	0.0347
mean	-0.0230	-0.0032	-0.0028
-1σ	-0.0871	-0.0468	-0.0402
-2σ	-0.1512	-0.0904	-0.0777
minimum occurrence	-0.3444	-0.2828	-0.2712

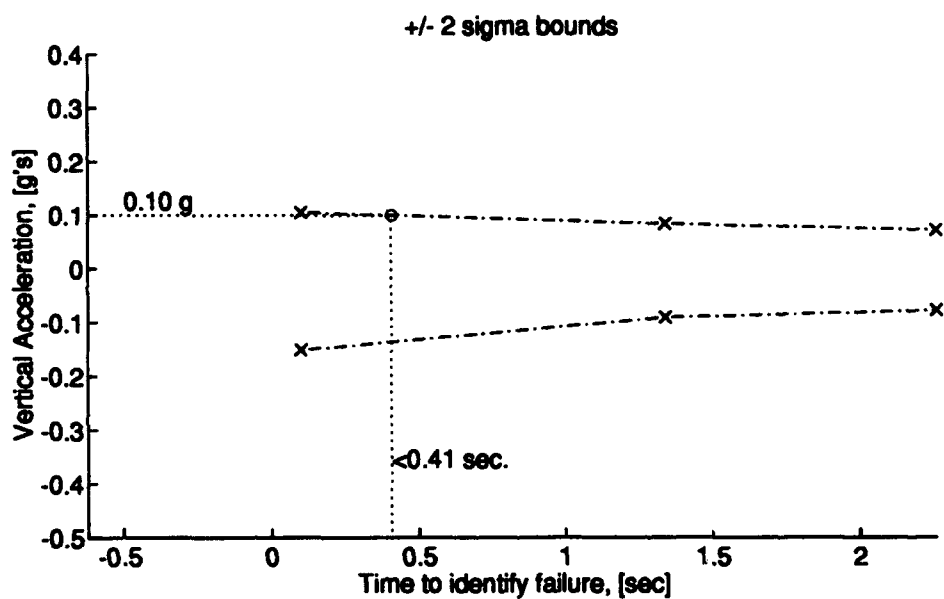
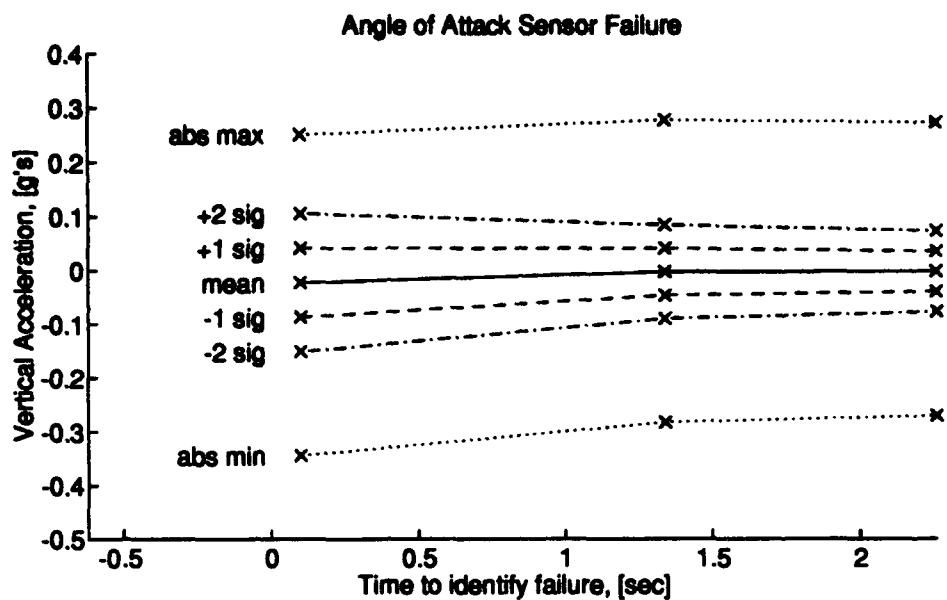


Figure D.4 *g*-forces vs ID time for Angle of Attack Sensor failure as magnitude changes.

Table D.5 Results of varying dither magnitude to alter Pitch Rate Sensor failure identification time and vertical g -forces.

Trial	4	4.1	4.2
Failure ID time [sec]	0.33	0.42	0.47
Elevator Dither			
Magnitude [deg/sec]	6.00	5.00	4.00
Frequency [rad/sec]	1.6653	1.6653	1.6653
Vertical Acceleration [g's]			
maximum occurrence	0.2510	0.2778	0.2726
+2σ	0.1053	0.0839	0.0722
+1σ	0.0412	0.0403	0.0347
mean	-0.0230	-0.0032	-0.0028
-1σ	-0.0871	-0.0468	-0.0402
-2σ	-0.1512	-0.0904	-0.0777
minimum occurrence	-0.3444	-0.2828	-0.2712

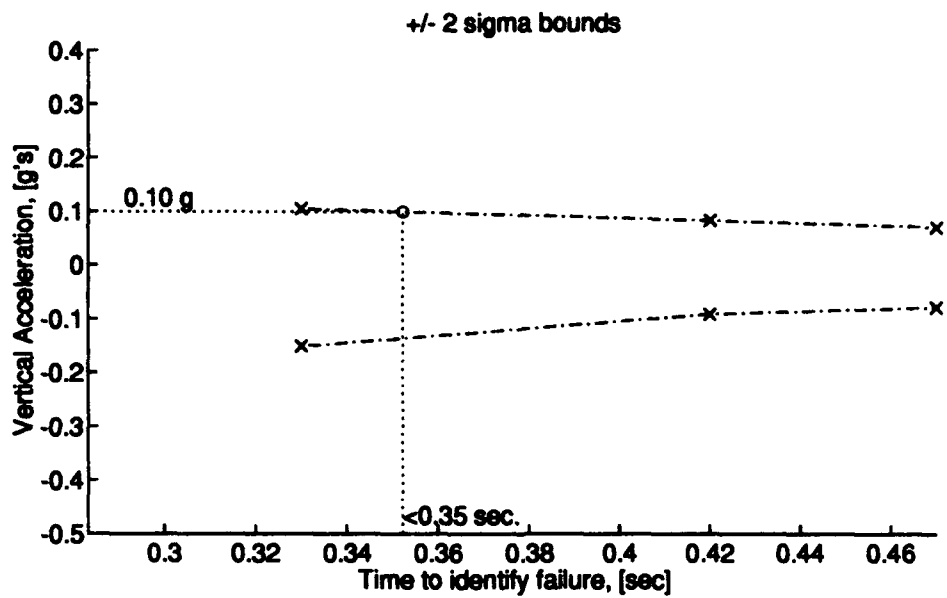
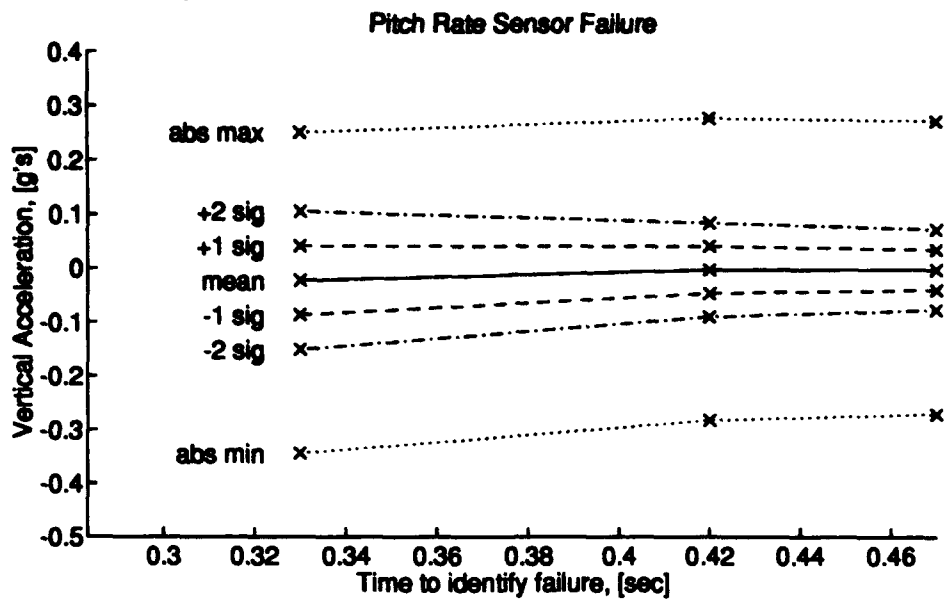


Figure D.5 *g*-forces vs ID time for Pitch Rate Sensor failure as magnitude changes.

Table D.6 Results of varying dither magnitude to alter Pitch Angle Sensor failure identification time and vertical g -forces.

Trial	4	4.1	4.2
Failure ID time [sec]	0.93	1.05	1.19
Elevator Dither			
Magnitude [deg/sec]	6.00	5.00	4.00
Frequency [rad/sec]	1.6653	1.6653	1.6653
Vertical Acceleration [g's]			
maximum occurrence	0.2510	0.2778	0.2726
+2σ	0.1053	0.0839	0.0722
+1σ	0.0412	0.0403	0.0347
mean	-0.0230	-0.0032	-0.0028
-1σ	-0.0871	-0.0468	-0.0402
-2σ	-0.1512	-0.0904	-0.0777
minimum occurrence	-0.3444	-0.2828	-0.2712

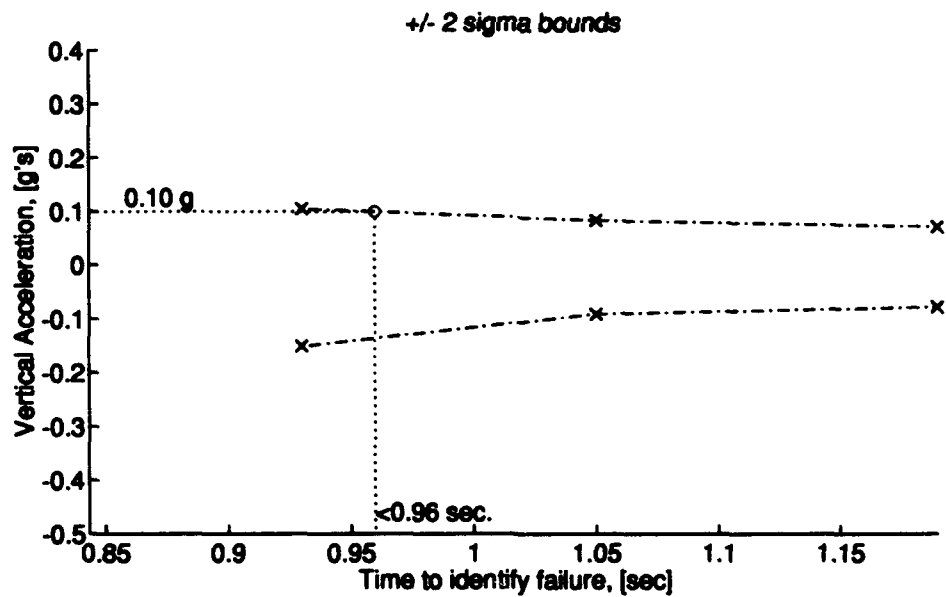
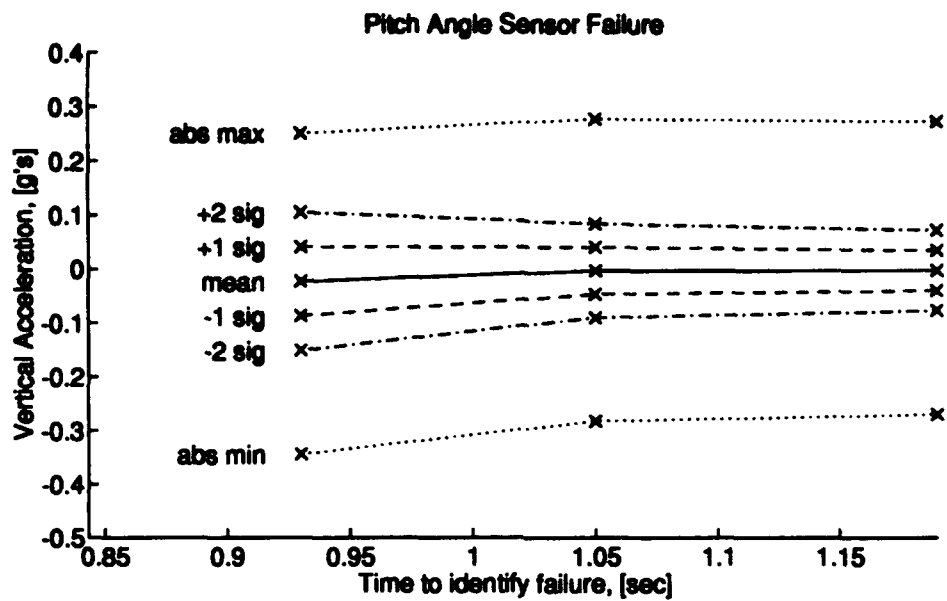


Figure D.6 *g*-forces vs ID time for Pitch Angle Sensor failure as magnitude changes.

Table D.7 Results of varying dither magnitude to alter Right Aileron Actuator failure identification time and horizontal g -forces.

Trial	5	5.1	5.2	5.3
Failure ID time [sec]	0.24	0.52	0.79	1.87
Aileron Dither				
Magnitude [deg/sec]	6.00	4.00	3.00	2.00
Frequency [rad/sec]	3.6193	3.6193	3.6193	3.6193
Horizontal Acceleration [g's]				
maximum occurrence	0.7117	0.6878	0.6187	0.5590
+2σ	0.3304	0.2631	0.2043	0.1476
+1σ	0.1731	0.1523	0.1182	0.0771
mean	0.0158	0.0415	0.0322	0.0067
-1σ	-0.1416	-0.0693	-0.0538	-0.0638
-2σ	-0.2989	-0.1802	-0.1399	-0.1343
minimum occurrence	-0.5920	-0.5185	-0.5011	-0.4979

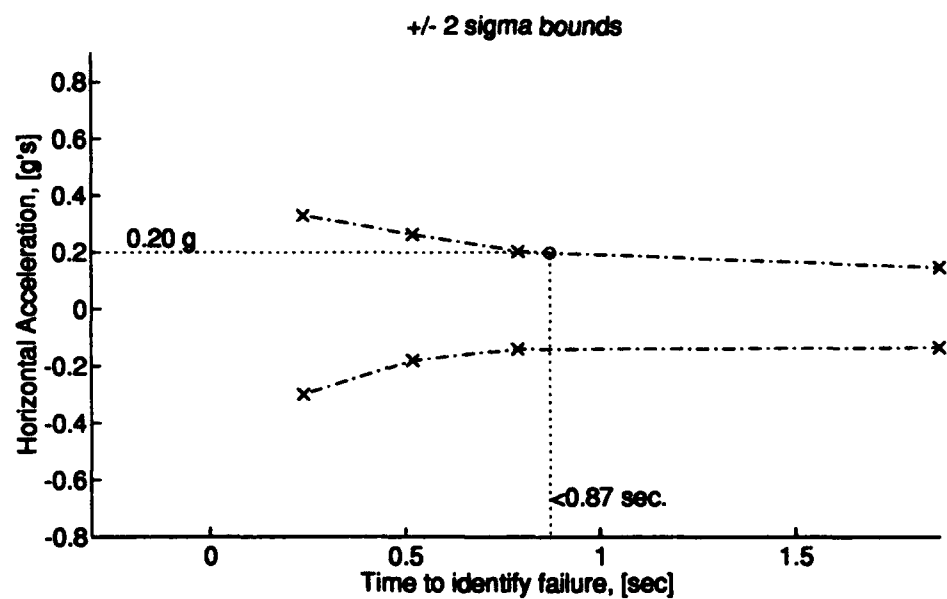
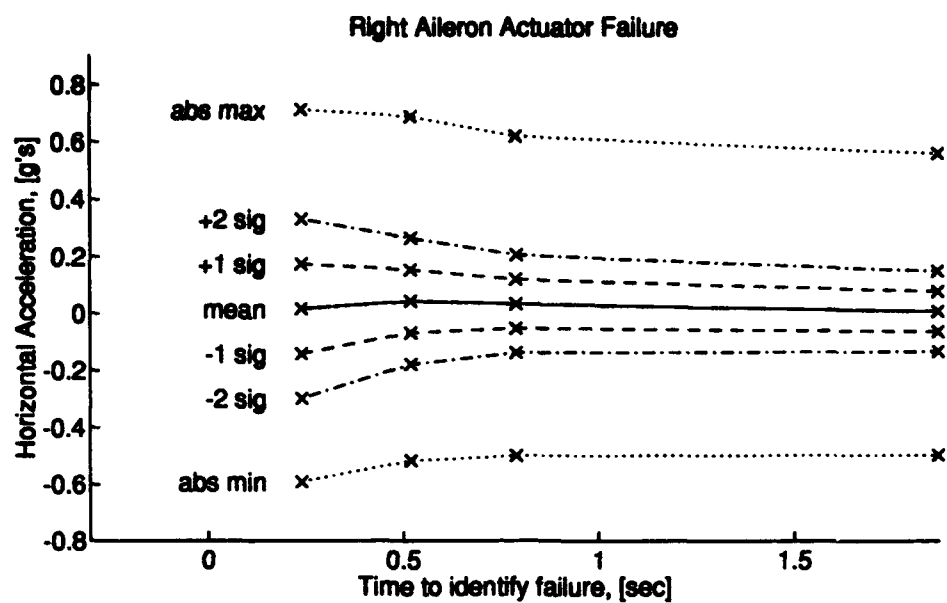


Figure D.7 *g*-forces vs ID time for Right Aileron Actuator failure as magnitude changes.

Table D.8 Results of varying dither magnitude to alter Left Aileron Actuator failure identification time and horizontal g -forces.

Trial	5	5.1	5.2	5.3
Failure ID time [sec]	0.23	0.30	0.36	0.99
Aileron Dither				
Magnitude [deg/sec]	6.00	4.00	3.00	2.00
Frequency [rad/sec]	3.6193	3.6193	3.6193	3.6193
Horizontal Acceleration [g's]				
maximum occurrence	0.7117	0.6878	0.6187	0.5590
+2σ	0.3304	0.2631	0.2043	0.1476
+1σ	0.1731	0.1523	0.1182	0.0771
mean	0.0158	0.0415	0.0322	0.0067
-1σ	-0.1416	-0.0693	-0.0538	-0.0638
-2σ	-0.2989	-0.1802	-0.1399	-0.1343
minimum occurrence	-0.5920	-0.5185	-0.5011	-0.4979

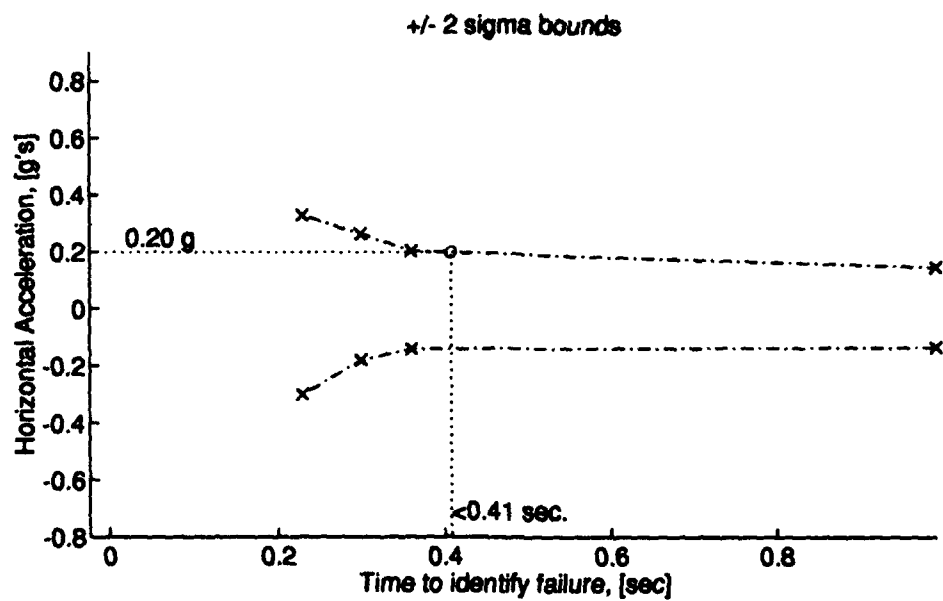
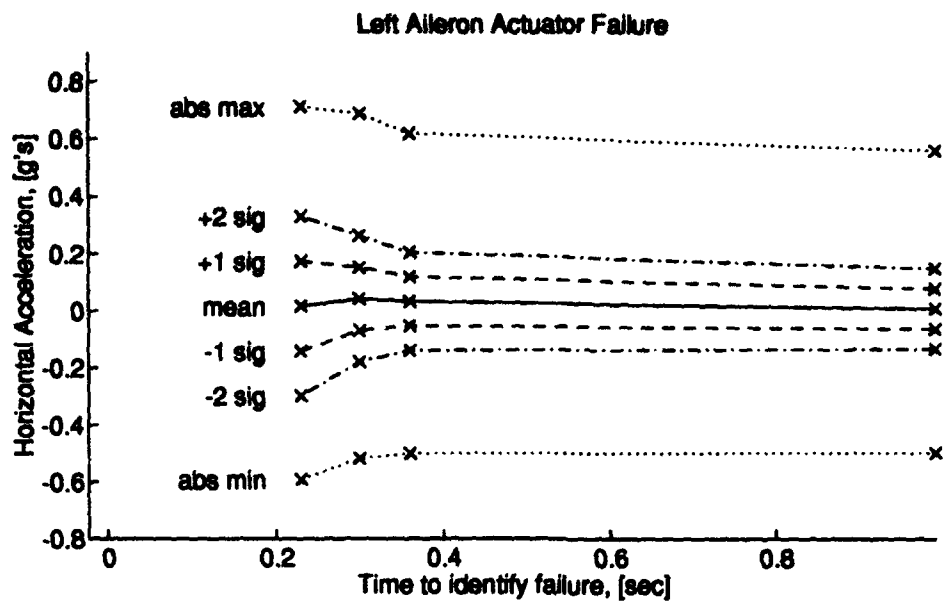


Figure D.8 *g*-forces vs ID time for Left Aileron Actuator failure as magnitude changes.

Table D.9 Results of varying dither magnitude to alter Right Rudder Actuator failure identification time and horizontal g -forces.

Trial	5	5.1	5.2	5.3
Failure ID time [sec]	0.56	0.90	1.20	1.72
Rudder Dither				
Magnitude [deg/sec]	6.00	4.00	3.00	2.00
Frequency [rad/sec]	3.6193	3.6193	3.6193	3.6193
Horizontal Acceleration [g's]				
maximum occurrence	0.7117	0.6878	0.6187	0.5590
+2σ	0.3304	0.2631	0.2043	0.1476
+1σ	0.1731	0.1523	0.1182	0.0771
mean	0.0158	0.0415	0.0322	0.0067
-1σ	-0.1416	-0.0693	-0.0538	-0.0638
-2σ	-0.2989	-0.1802	-0.1399	-0.1343
minimum occurrence	-0.5920	-0.5185	-0.5011	-0.4979

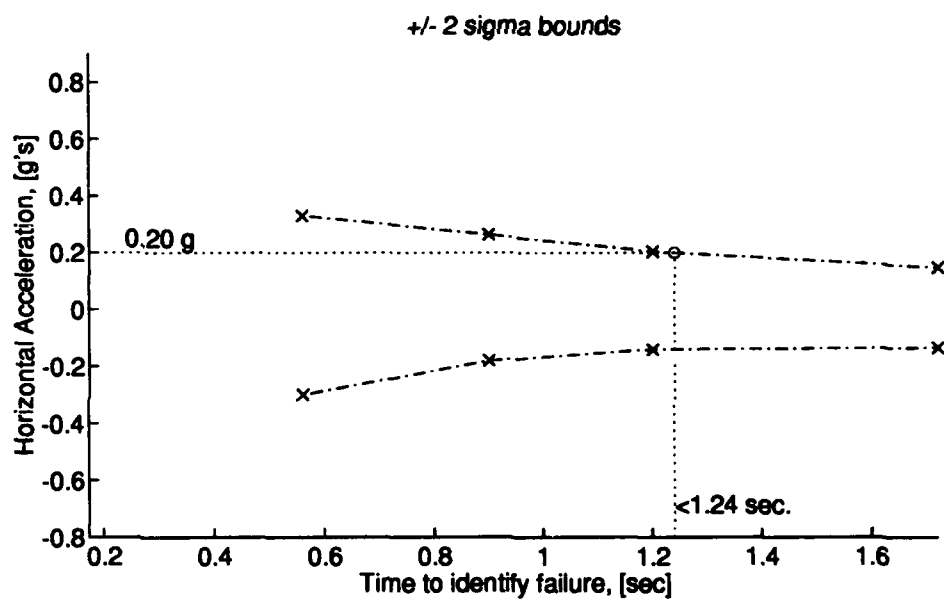
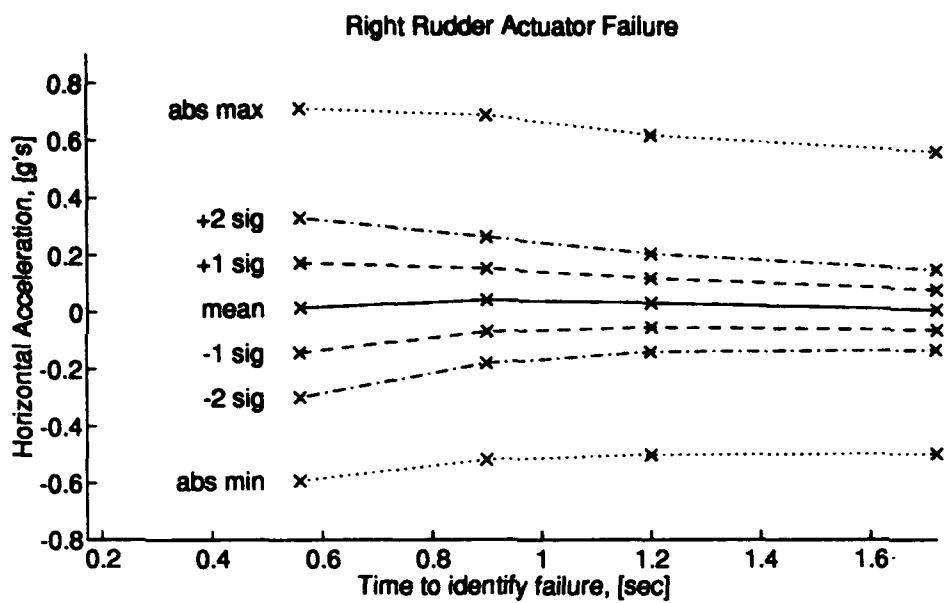


Figure D.9 *g*-forces vs ID time for Right Rudder Actuator failure as magnitude changes.

Table D.10 Results of varying dither magnitude to alter Left Rudder Actuator failure identification time and horizontal g -forces.

Trial	5	5.1	5.2	5.3
Failure ID time [sec]	0.53	1.00	1.40	2.38
Rudder Dither				
Magnitude [deg/sec]	6.00	4.00	3.00	2.00
Frequency [rad/sec]	3.6193	3.6193	3.6193	3.6193
Horizontal Acceleration [g's]				
maximum occurrence	0.7117	0.6878	0.6187	0.5590
+2σ	0.3304	0.2631	0.2043	0.1476
+1σ	0.1731	0.1523	0.1182	0.0771
mean	0.0158	0.0415	0.0322	0.0067
-1σ	-0.1416	-0.0693	-0.0538	-0.0638
-2σ	-0.2989	-0.1802	-0.1399	-0.1343
minimum occurrence	-0.5920	-0.5185	-0.5011	-0.4979

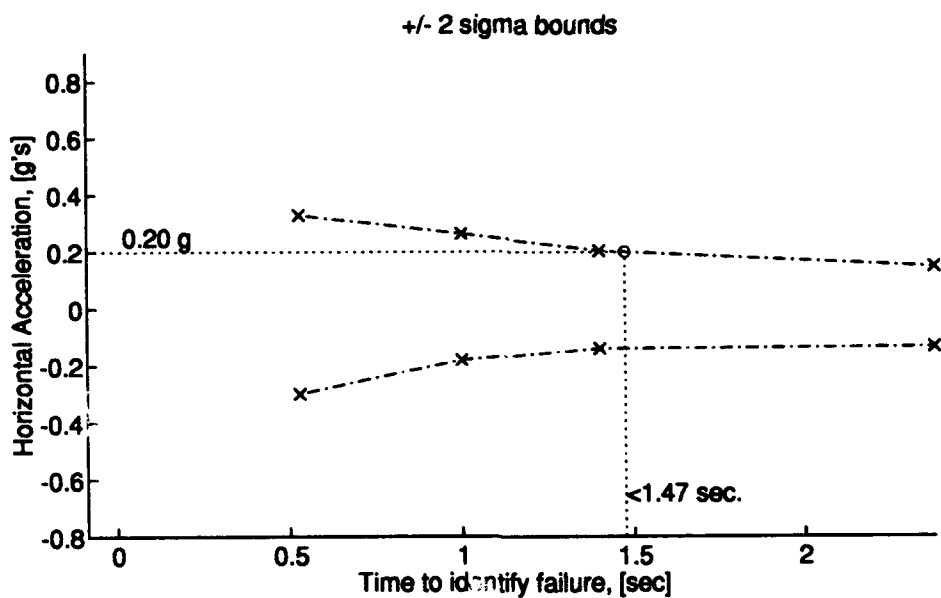
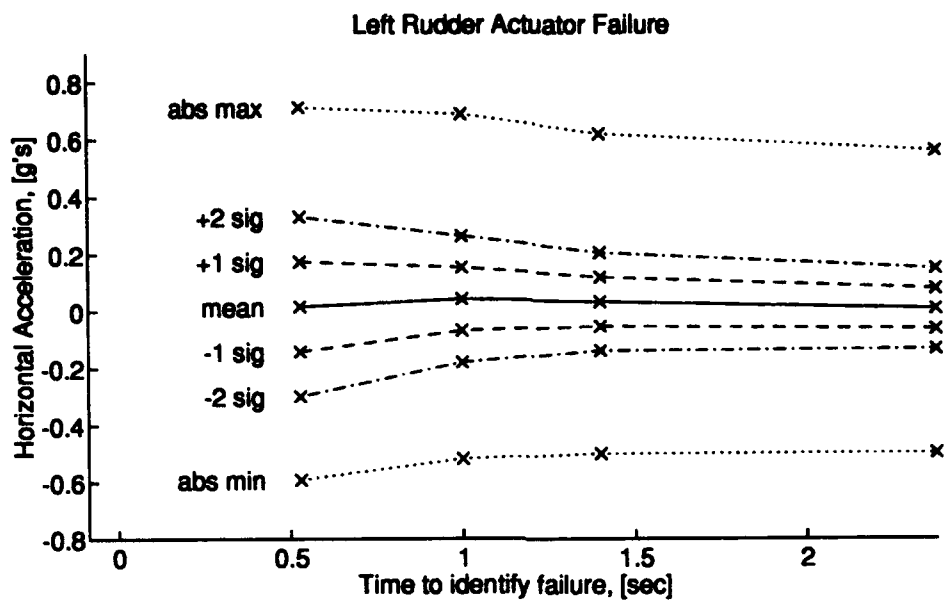


Figure D.10 *g*-forces vs ID time for Left Rudder Actuator failure as magnitude changes.

Table D.11 Results of varying dither magnitude to alter Sideslip Angle Sensor failure identification time and horizontal g -forces.

Trial	5	5.1	5.2	5.3
Failure ID time [sec]	1.77	2.42	2.78	3.53
Aileron Dither				
Magnitude [deg/sec]	6.00	4.00	3.00	2.00
Frequency [rad/sec]	3.6193	3.6193	3.6193	3.6193
Rudder Dither				
Magnitude [deg/sec]	6.00	4.00	3.00	2.00
Frequency [rad/sec]	3.6193	3.6193	3.6193	3.6193
Horizontal Acceleration [g's]				
maximum occurrence	0.7117	0.6878	0.6187	0.5590
$+2\sigma$	0.3304	0.2631	0.2043	0.1476
$+1\sigma$	0.1731	0.1523	0.1182	0.0771
mean	0.0158	0.0415	0.0322	0.0067
-1σ	-0.1416	-0.0693	-0.0538	-0.0638
-2σ	-0.2989	-0.1802	-0.1399	-0.1343
minimum occurrence	-0.5920	-0.5185	-0.5011	-0.4979

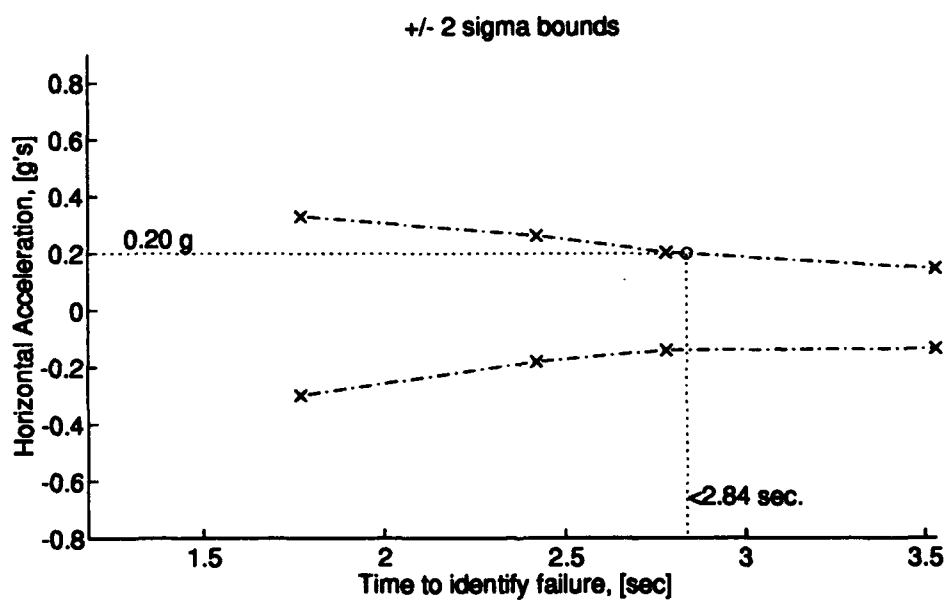
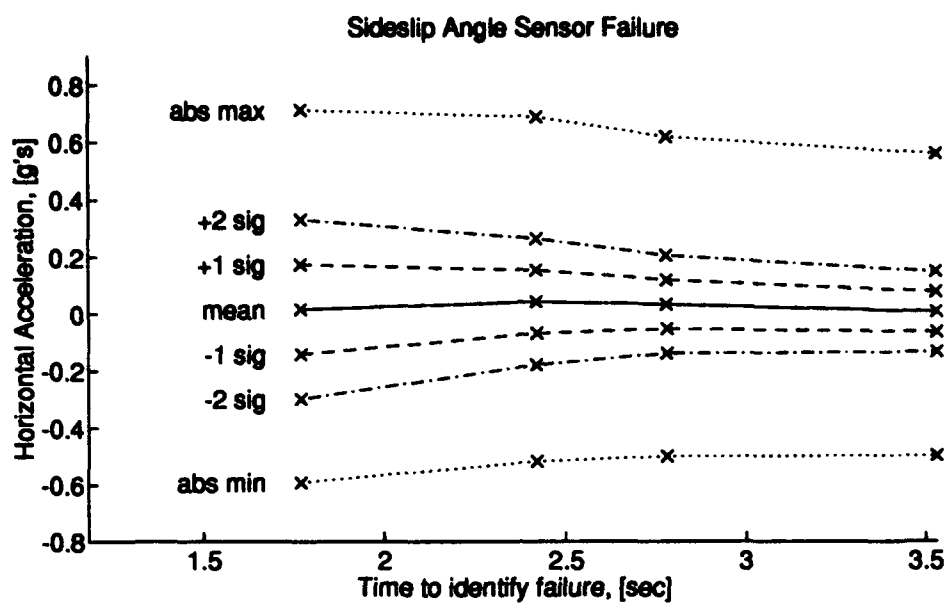


Figure D.11 *g*-forces vs ID time for Sideslip Angle Sensor failure as magnitude changes.

Table D.12 Results of varying dither magnitude to alter Roll Rate Sensor failure identification time and horizontal g -forces.

Trial	5	5.1	5.2	5.3
Failure ID time [sec]	0.70	0.75	0.69	0.73
Aileron Dither				
Magnitude [deg/sec]	6.00	4.00	3.00	2.00
Frequency [rad/sec]	3.6193	3.6193	3.6193	3.6193
Rudder Dither				
Magnitude [deg/sec]	6.00	4.00	3.00	2.00
Frequency [rad/sec]	3.6193	3.6193	3.6193	3.6193
Horizontal Acceleration [g's]				
maximum occurrence	0.7117	0.6878	0.6187	0.5590
+2σ	0.3304	0.2631	0.2043	0.1476
+1σ	0.1731	0.1523	0.1182	0.0771
mean	0.0158	0.0415	0.0322	0.0067
-1σ	-0.1416	-0.0693	-0.0538	-0.0638
-2σ	-0.2989	-0.1802	-0.1399	-0.1343
minimum occurrence	-0.5920	-0.5185	-0.5011	-0.4979

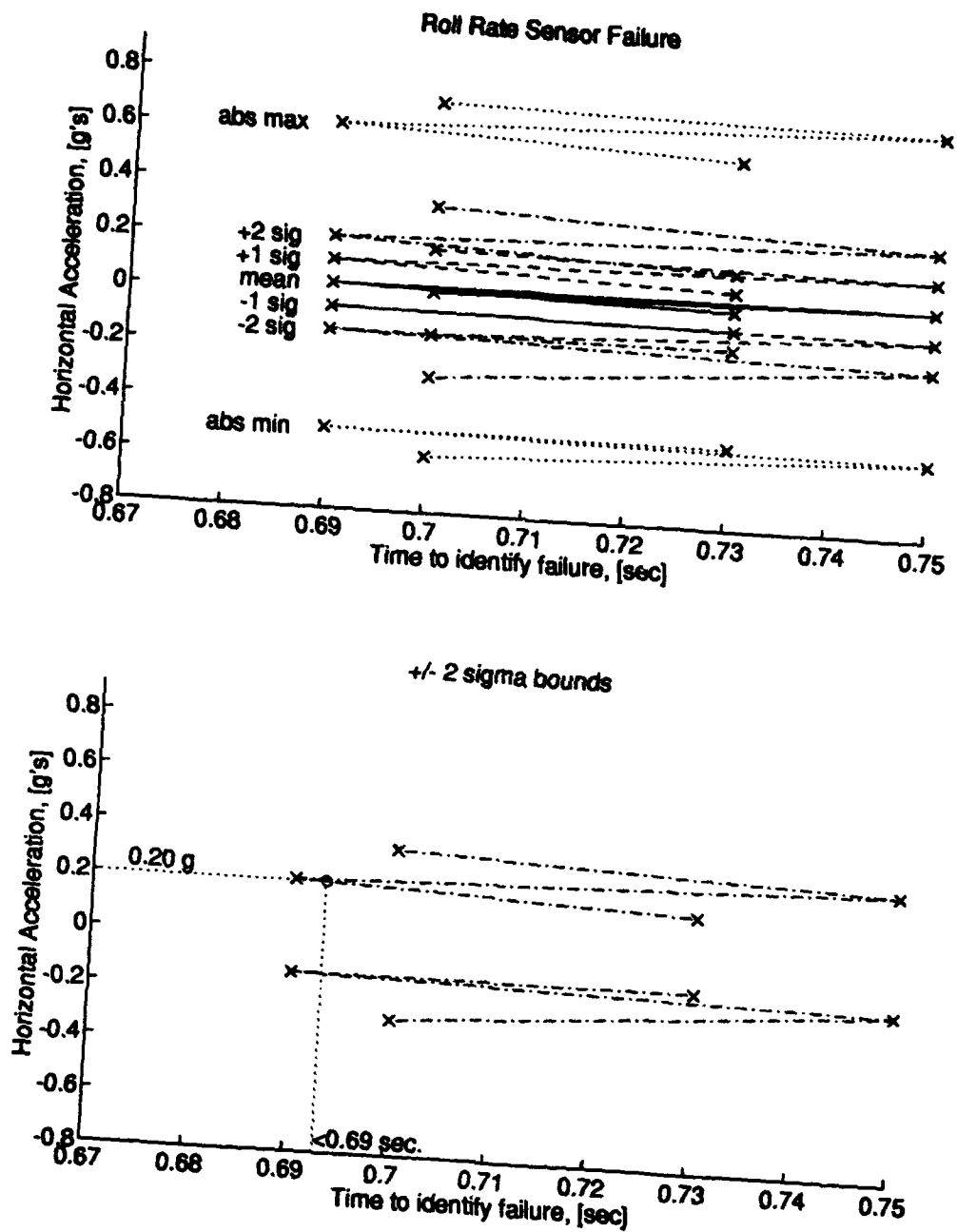


Figure D.12 *g-forces vs ID time for Roll Rate Sensor failure as magnitude changes.*

Table D.13 Results of varying dither magnitude to alter Roll Angle Sensor failure identification time and horizontal g -forces.

Trial	5	5.1	5.2	5.3
Failure ID time [sec]	0.80	0.27	0.22	1.51
Aileron Dither				
Magnitude [deg/sec]	6.00	4.00	3.00	2.00
Frequency [rad/sec]	3.6193	3.6193	3.6193	3.6193
Rudder Dither				
Magnitude [deg/sec]	6.00	4.00	3.00	2.00
Frequency [rad/sec]	3.6193	3.6193	3.6193	3.6193
Horizontal Acceleration [g's]				
maximum occurrence	0.7117	0.6878	0.6187	0.5590
+2σ	0.3304	0.2631	0.2043	0.1476
+1σ	0.1731	0.1523	0.1182	0.0771
mean	0.0158	0.0415	0.0322	0.0067
-1σ	-0.1416	-0.0693	-0.0538	-0.0638
-2σ	-0.2989	-0.1802	-0.1399	-0.1343
minimum occurrence	-0.5920	-0.5185	-0.5011	-0.4979

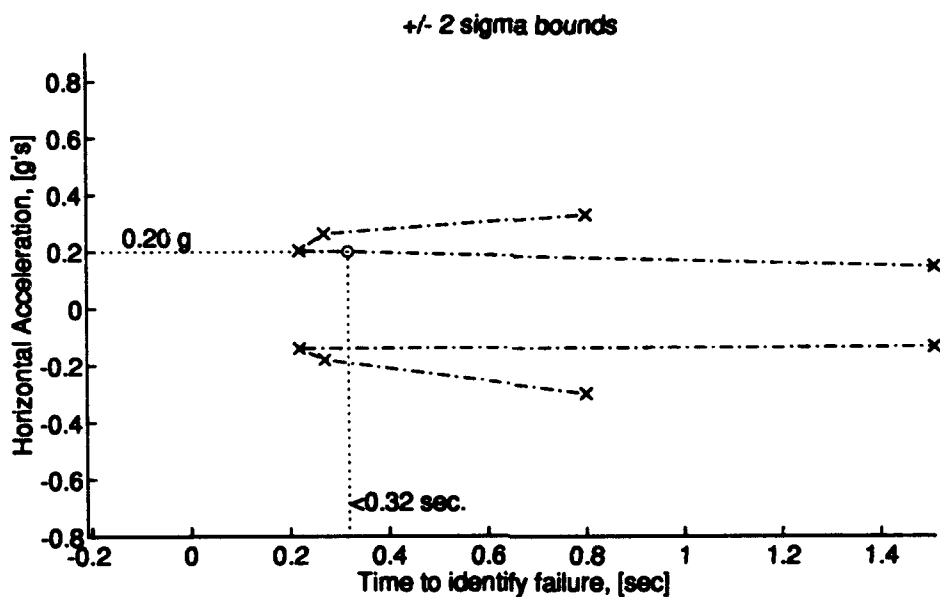
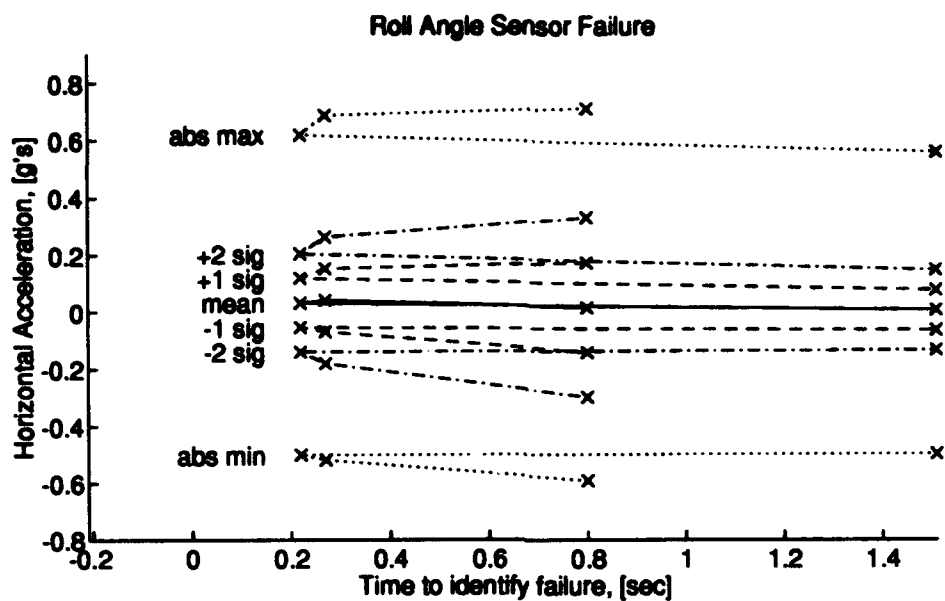


Figure D.13 *g*-forces vs ID time for Roll Angle Sensor failure as magnitude changes.

Table D.14 Results of varying dither magnitude to alter Yaw Rate Sensor failure identification time and horizontal g -forces.

Trial	5	5.1	5.2	5.3
Failure ID time [sec]	0.75	0.85	0.97	1.11
Aileron Dither				
Magnitude [deg/sec]	6.00	4.00	3.00	2.00
Frequency [rad/sec]	3.6193	3.6193	3.6193	3.6193
Rudder Dither				
Magnitude [deg/sec]	6.00	4.00	3.00	2.00
Frequency [rad/sec]	3.6193	3.6193	3.6193	3.6193
Horizontal Acceleration [g's]				
maximum occurrence	0.7117	0.6878	0.6187	0.5590
+2σ	0.3304	0.2631	0.2043	0.1476
+1σ	0.1731	0.1523	0.1182	0.0771
mean	0.0158	0.0415	0.0322	0.0067
-1σ	-0.1416	-0.0693	-0.0538	-0.0633
-2σ	-0.2989	-0.1802	-0.1399	-0.1343
minimum occurrence	-0.5920	-0.5185	-0.5011	-0.4979

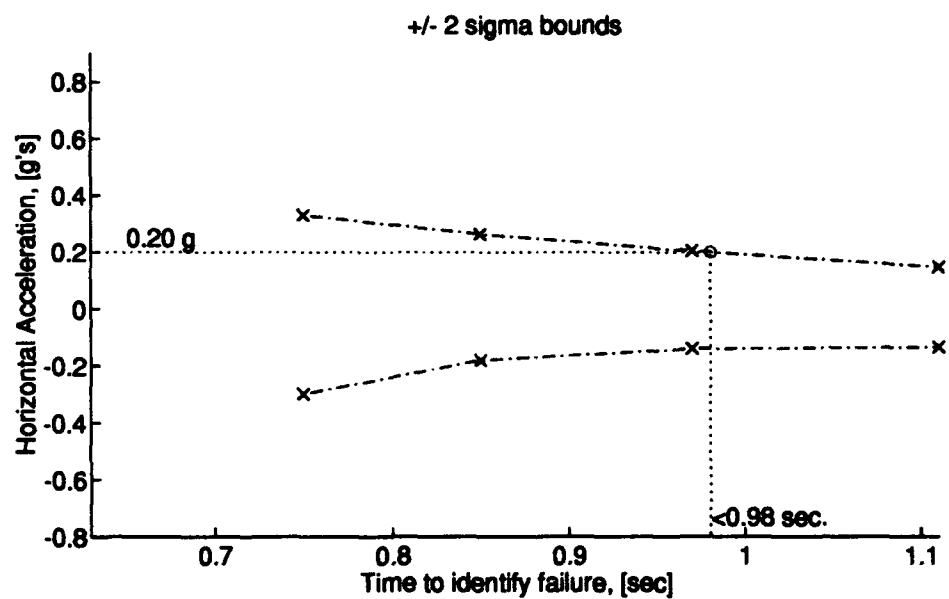
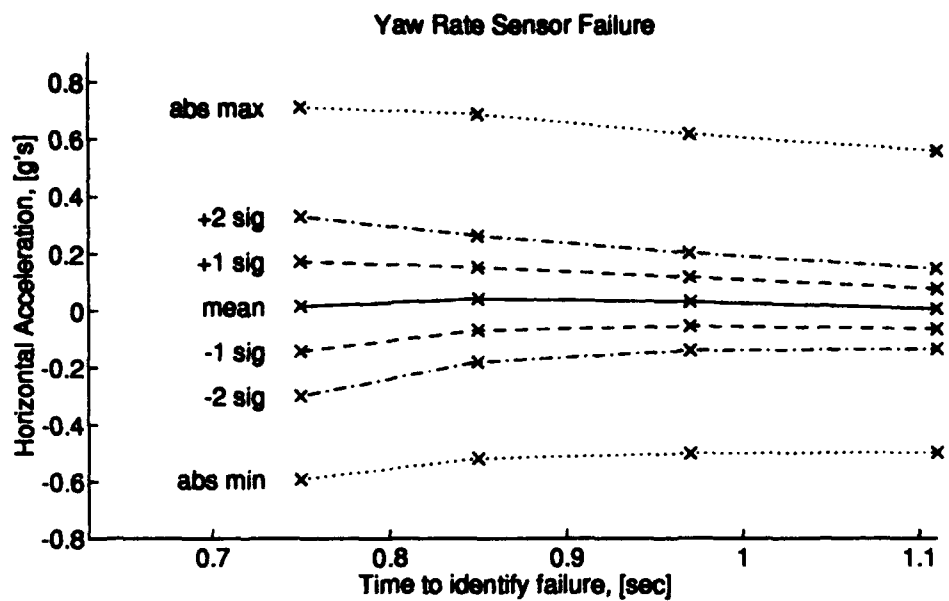


Figure D.14 *g*-forces vs ID time for Yaw Rate Sensor failure as magnitude changes.

Appendix E. Single Failure Probability Plots

MMAE performance against single failures with the optimal dither of Equation (4.6) is presented in a more expanded form in this appendix than in Figure 4.15 on page 4-43. An average probability of ten Monte Carlo runs is presented in each of the following plots. For convenience, Table 3.4 is repeated below as Table E.1 so that the codes in the plots are easily interpreted as the indicated filters. Two codes next to each other as in A2S4 indicate a secondary filter of a level-1 bank which hypothesizes two failed components.

Table E.1 MMAE Kalman Filter Codes.

Code	Filter Model Represents:
FF	fully functional aircraft
A1	right elevator actuator failure
A2	left elevator actuator failure
A3	right aileron actuator failure
A4	left aileron actuator failure
A5	right rudder actuator failure
A6	left rudder actuator failure
S1	forward velocity sensor failure
S2	angle of attack sensor failure
S3	pitch rate sensor failure
S4	pitch angle sensor failure
S5	sideslip angle sensor failure
S6	roll rate sensor failure
S7	roll angle sensor failure
S8	yaw rate sensor failure

Each figure has fifteen averaged-probability plots. Simulations begin with the level-0 bank of filters as indicated by the single codes on the left. As the first failure is detected, a dotted vertical line indicates the filter which holds the declared hypothesis. At that time, the MMAE switches to the level-1 bank of filters with the filter of the first declared failure as the primary filter. All other plots except that of the fully functional aircraft filter switch to secondary filters of the level-1 bank. This is indicated by the vertical dash-dot line and the dual codes.

The "stepping" phenomenon especially evident in the upper right plot of Figure E.8. This is caused by the averaging of ten Monte Carlo runs. The "steps" occur where individual Monte Carlo runs have failure declarations and this filter is re-assigned the maximum probability.

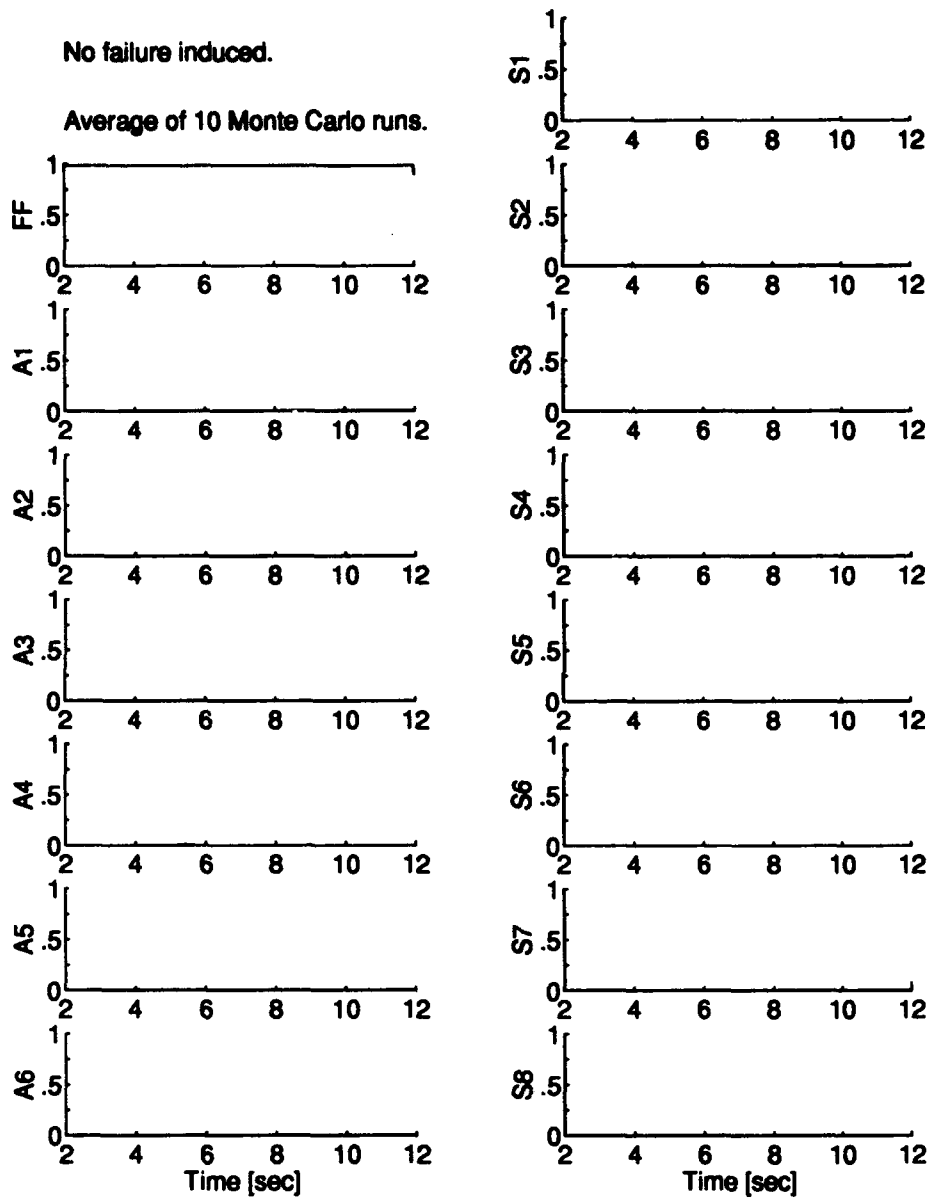


Figure E.1 MMAE Performance With Fully Functional Aircraft Failure at 4.00 Seconds Using Optimal Dither.

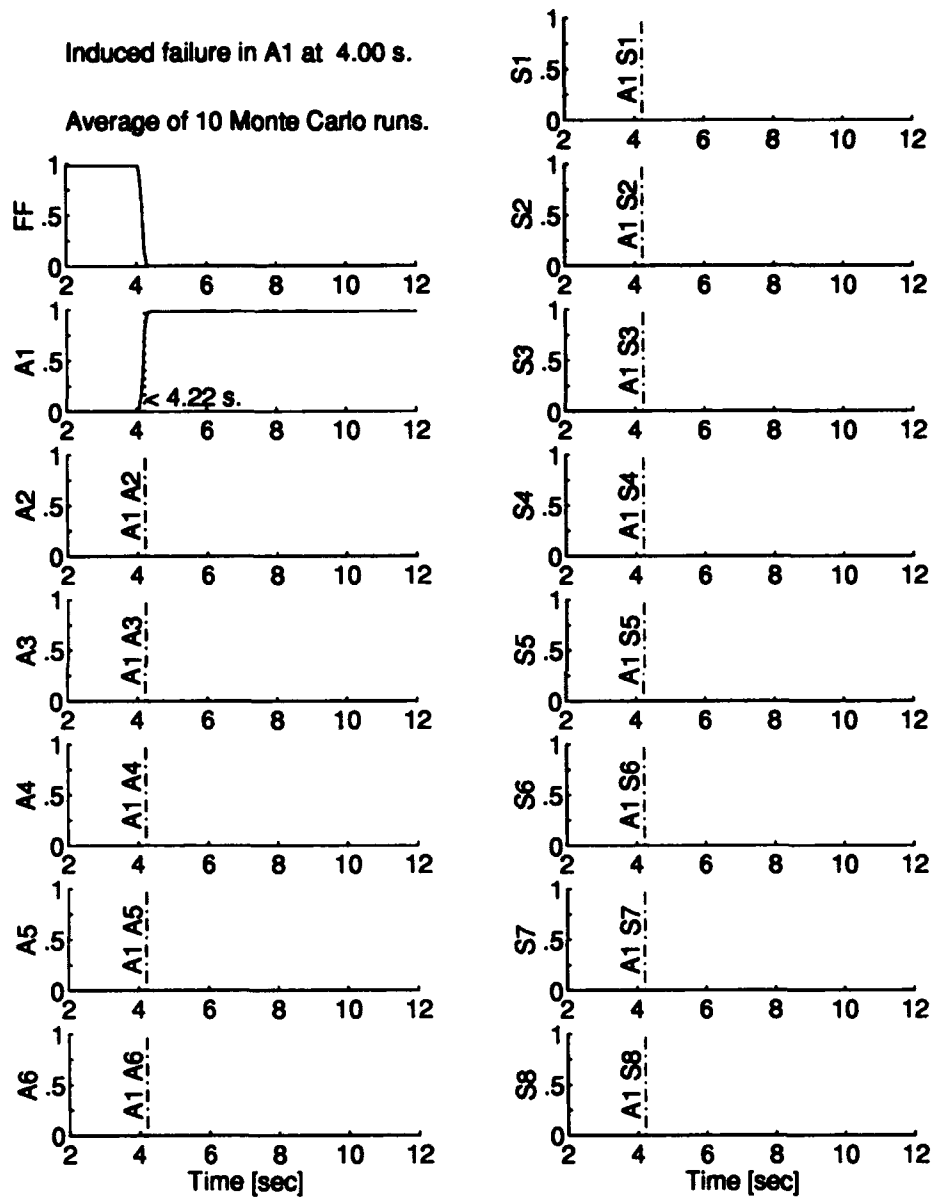


Figure E.2 MMAE Performance With Right Elevator Actuator Failure at 4.00 Seconds Using Optimal Dither.

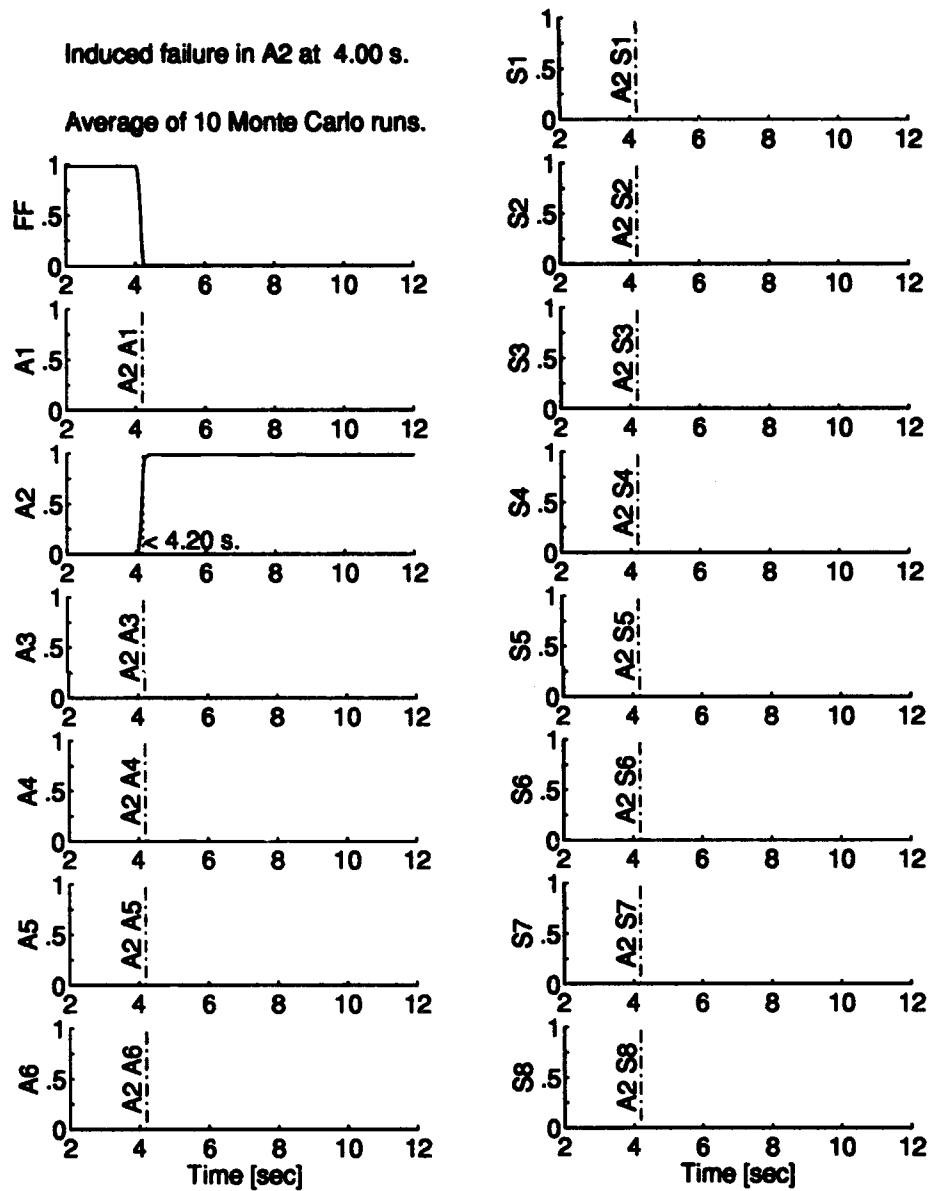


Figure E.3 MMAE Performance With Left Elevator Actuator Failure at 4.00 Seconds Using Optimal Dither.

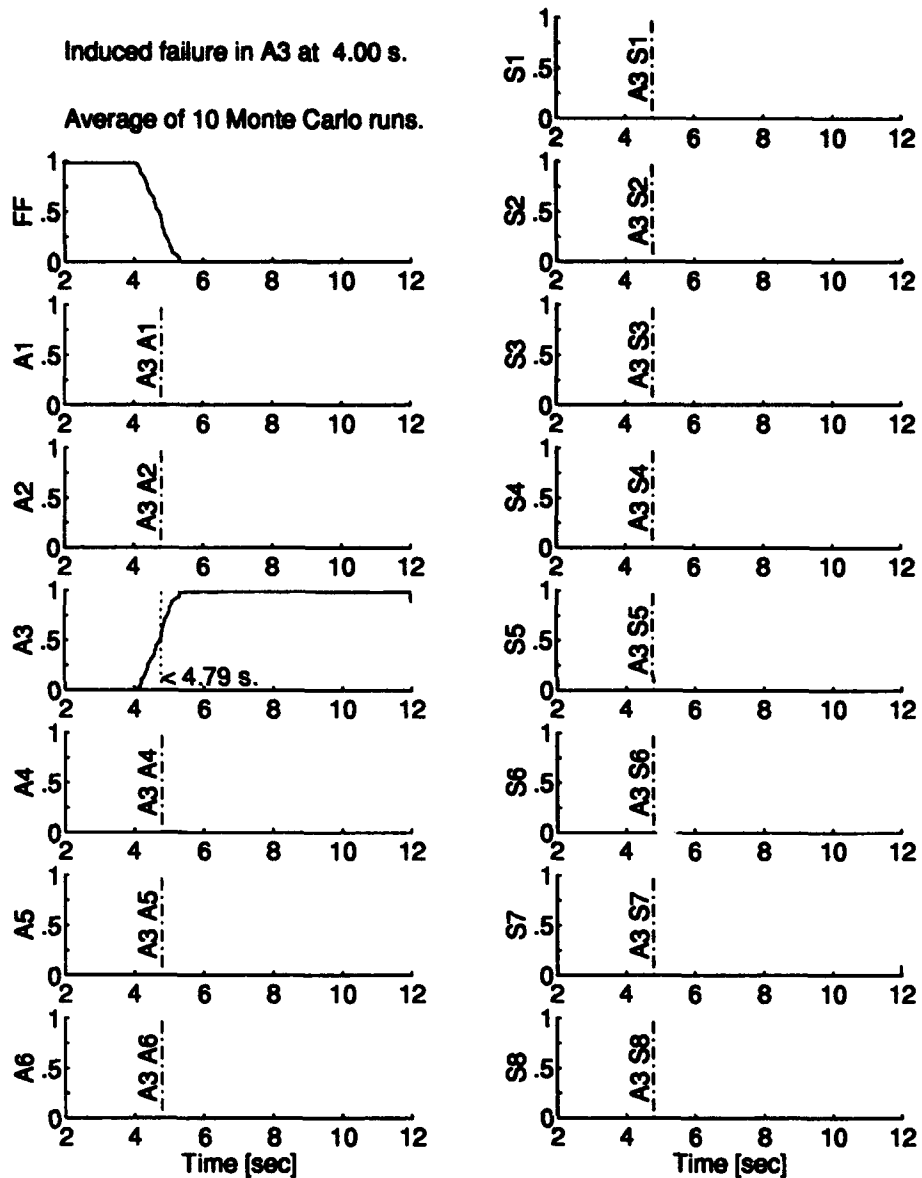


Figure E.4 MMAE Performance With Right Aileron Actuator Failure at 4.00 Seconds Using Optimal Dither.

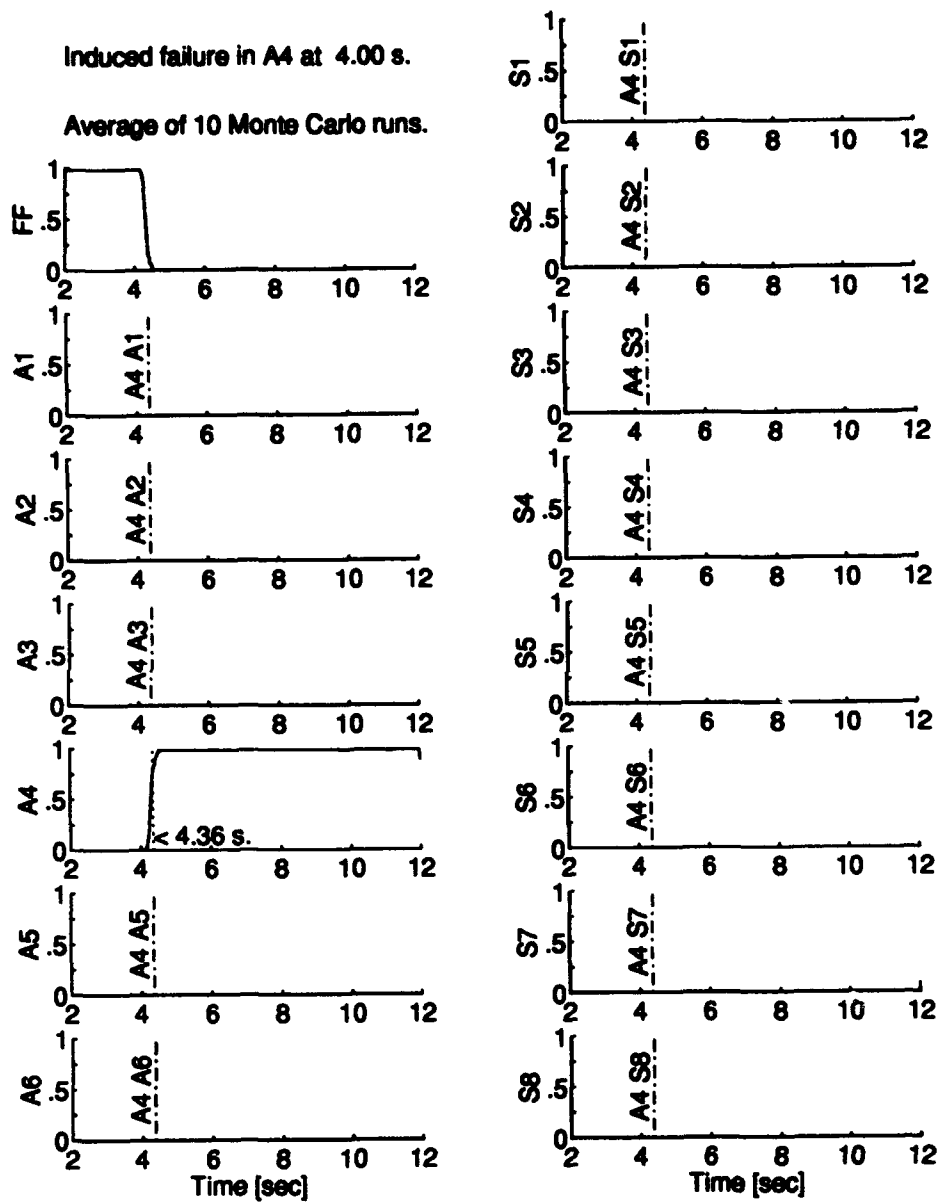


Figure E.5 MMAE Performance With Left Aileron Actuator Failure at 4.00 Seconds Using Optimal Dither.

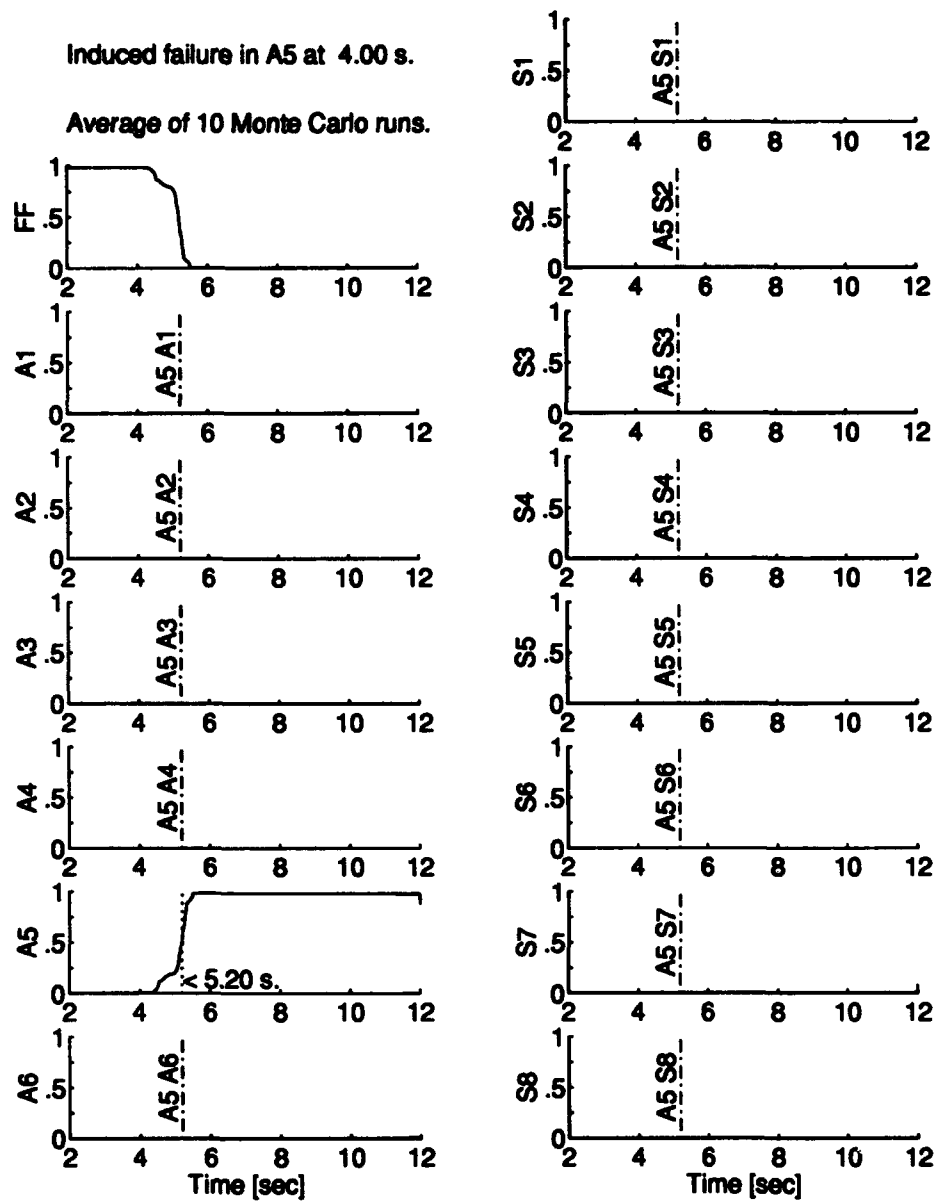


Figure E.6 MMAE Performance With Right Rudder Actuator Failure at 4.00 Seconds Using Optimal Dither.

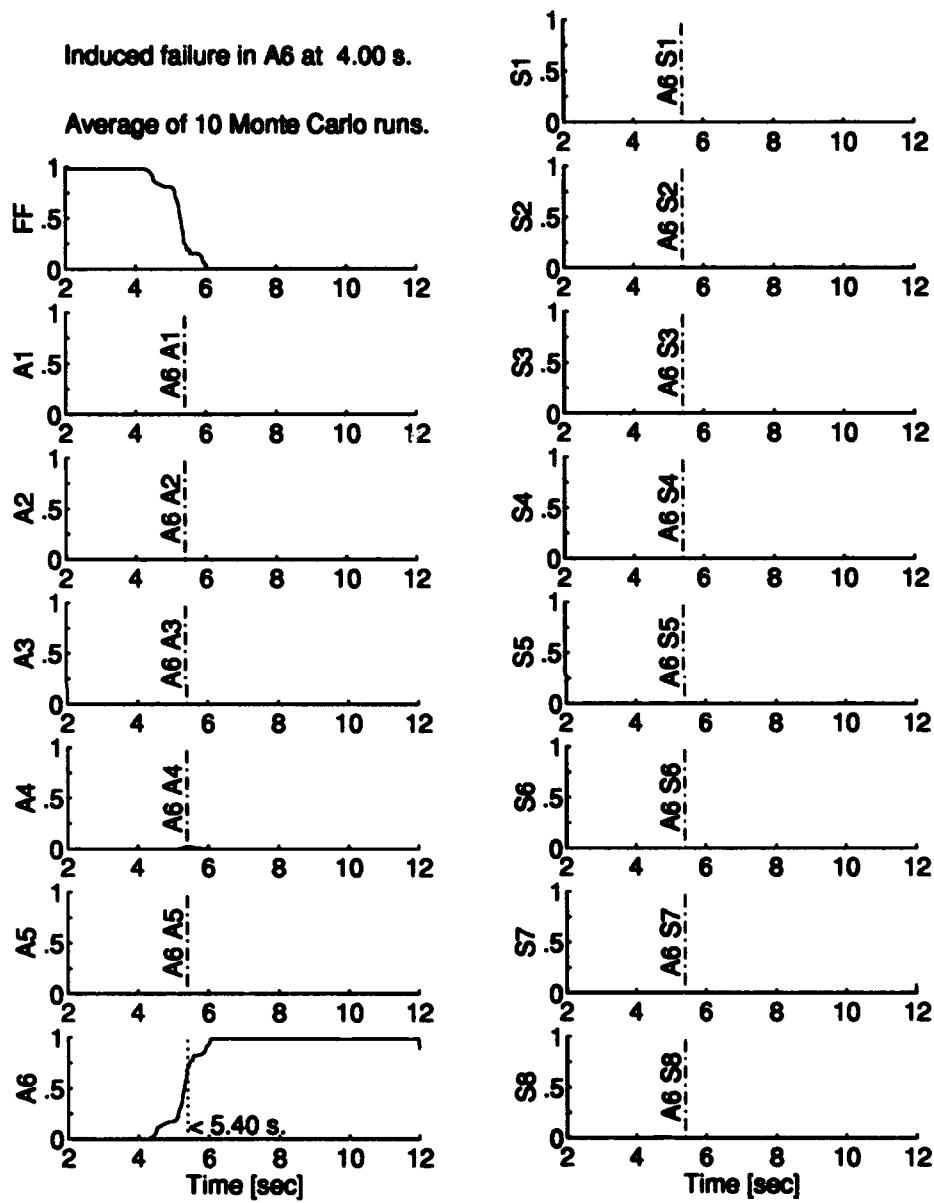


Figure E.7 MMAE Performance With Left Rudder Actuator Failure at 4.00 Seconds Using Optimal Dither.

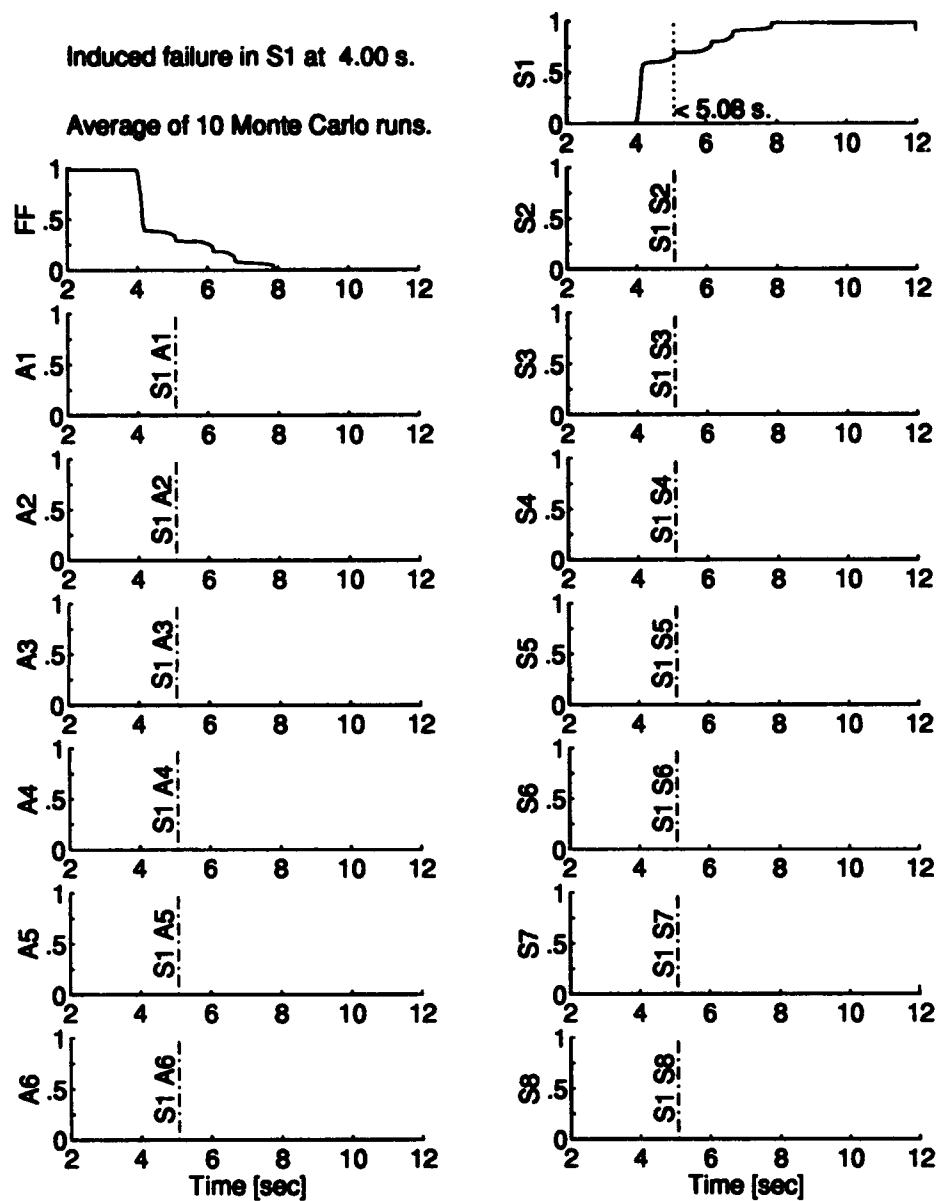


Figure E.8 MMAE Performance With Forward Velocity Sensor Failure at 4.00 Seconds Using Optimal Dither.

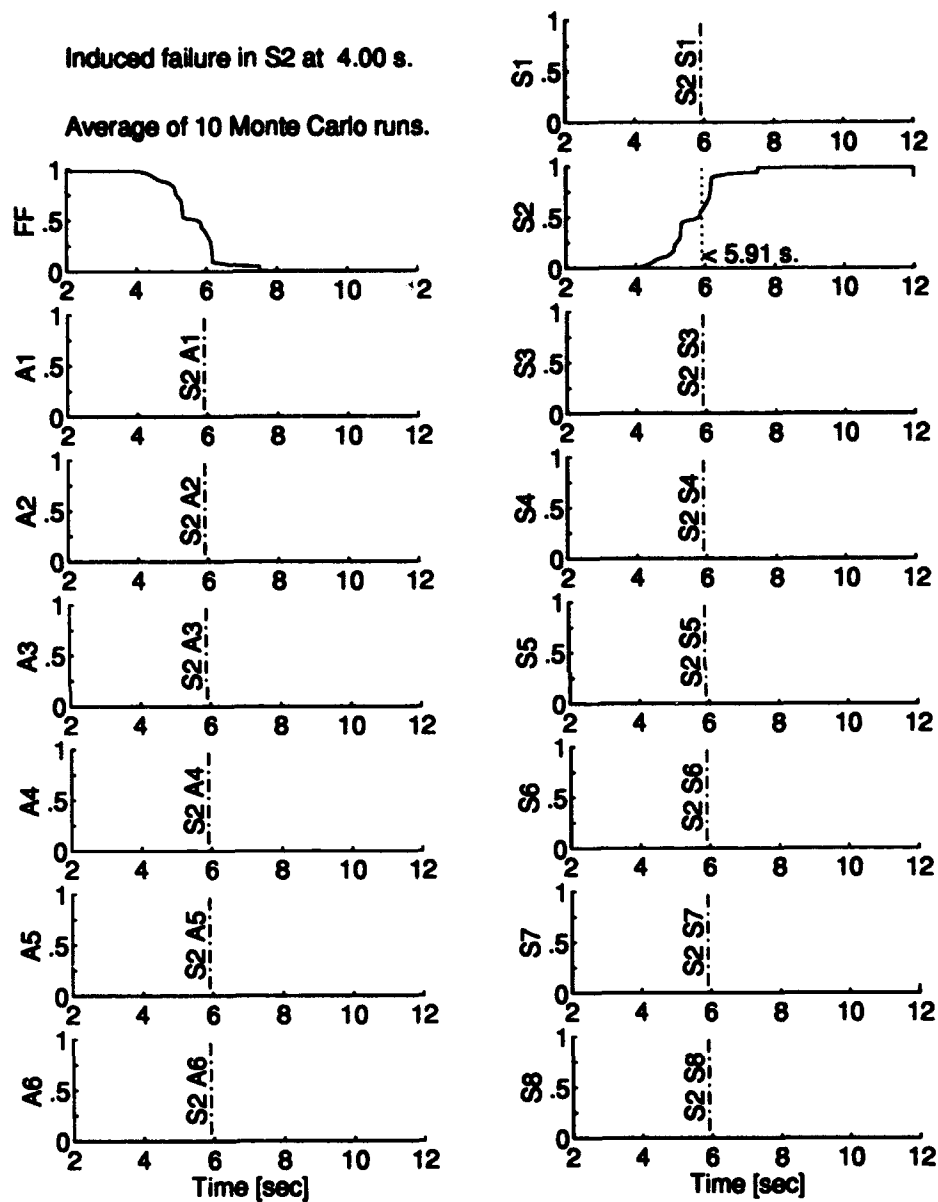


Figure E.9 MMAE Performance With Angle of Attack Sensor Failure at 4.00 Seconds Using Optimal Dither.

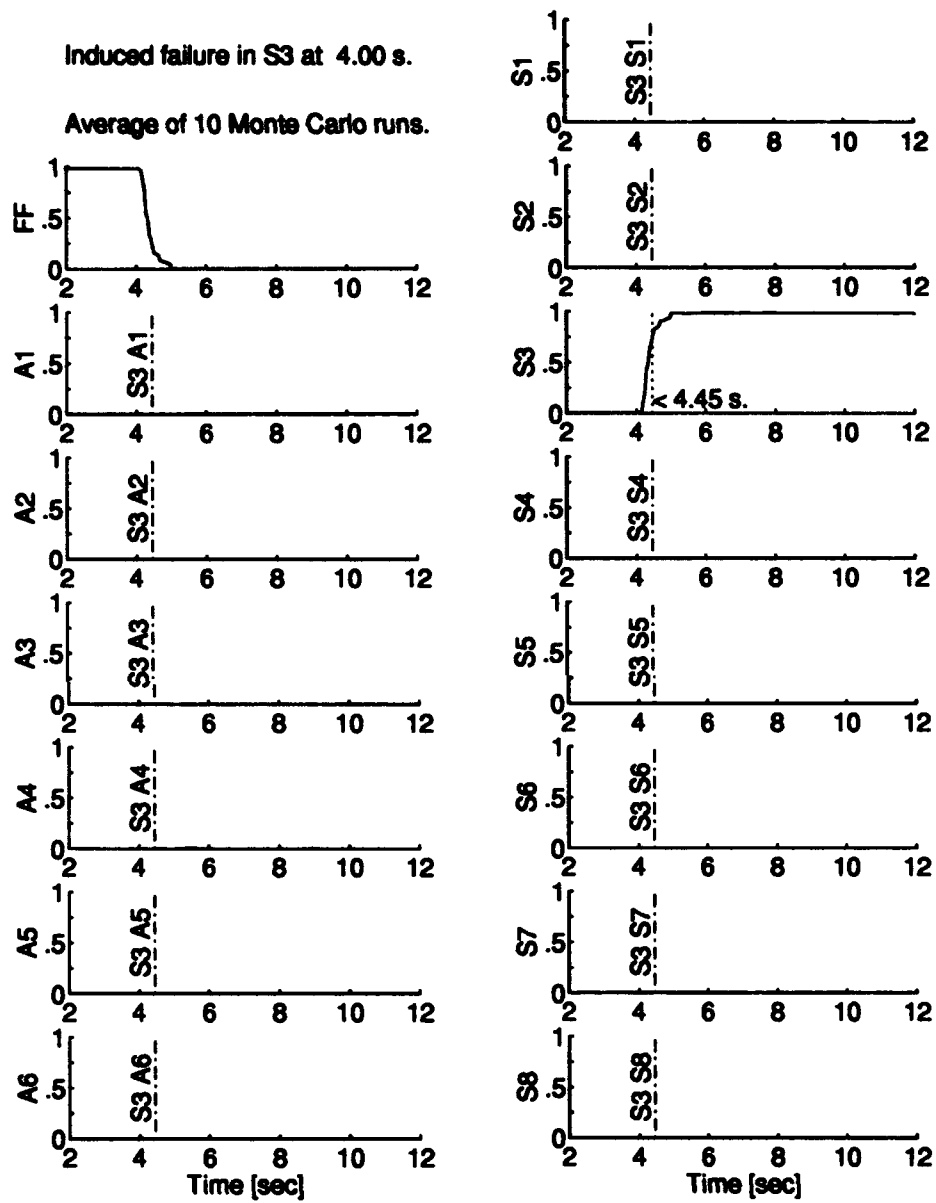
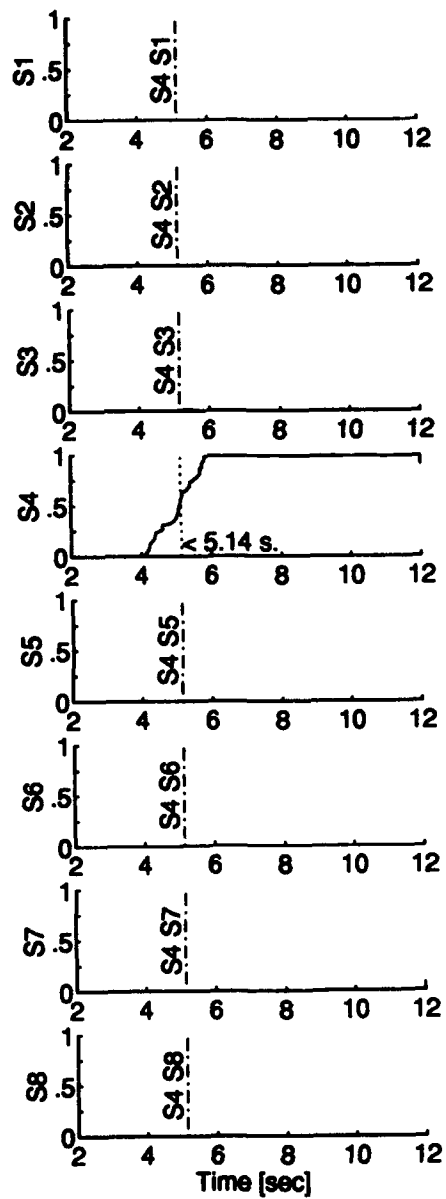
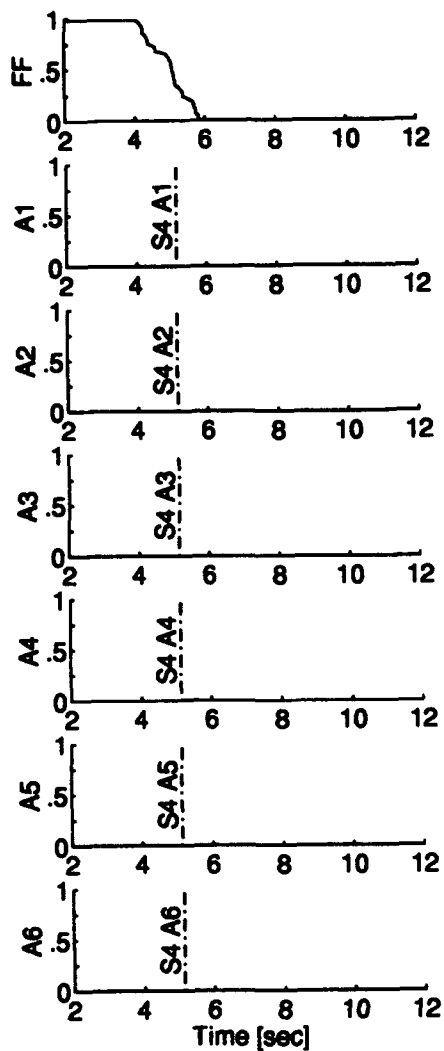


Figure E.10 MMAE Performance With Pitch Rate Sensor Failure at 4.00 Seconds Using Optimal Dither.

Average of 10 Monte Carlo runs.



E-12

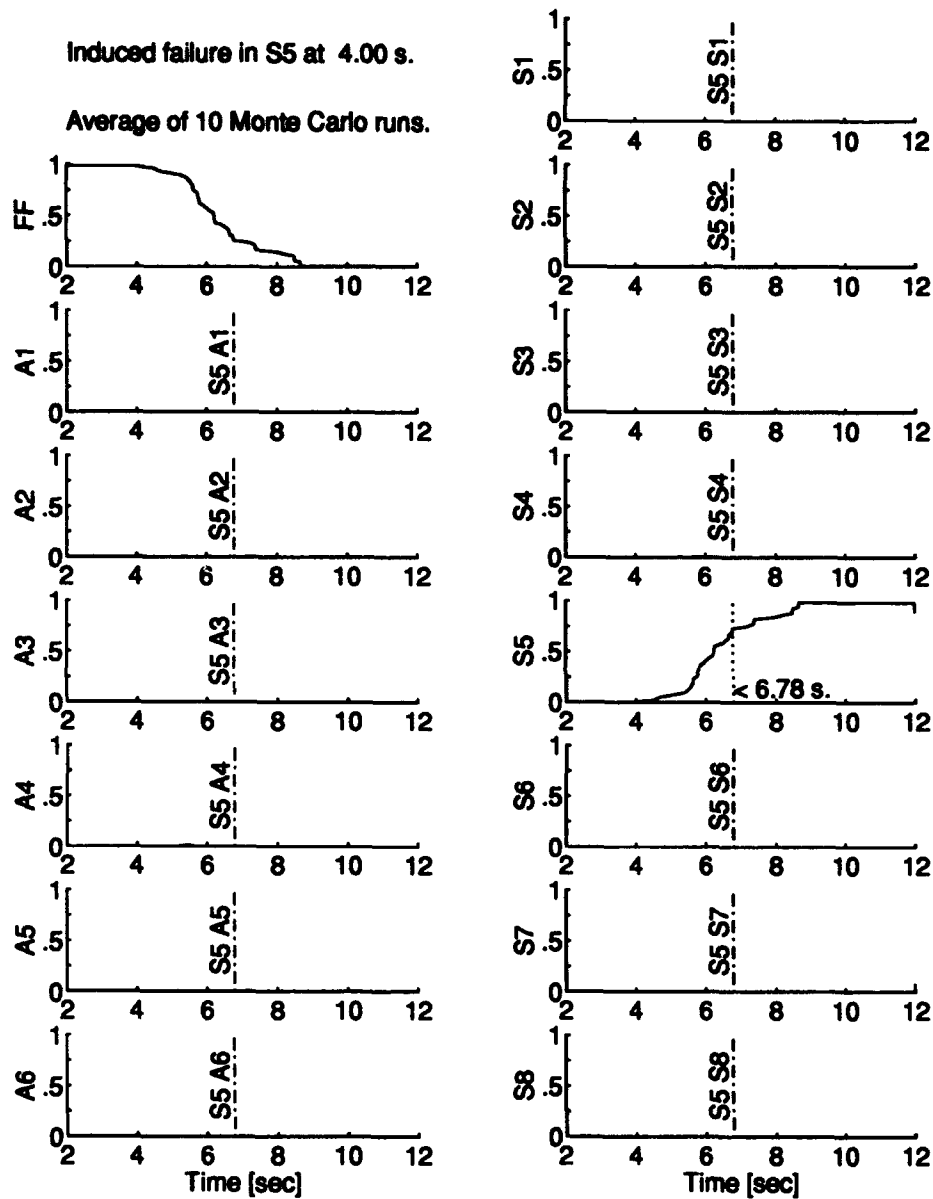


Figure E.12 MMAE Performance With Sideslip Angle Sensor Failure at 4.00 Seconds Using Optimal Dither.

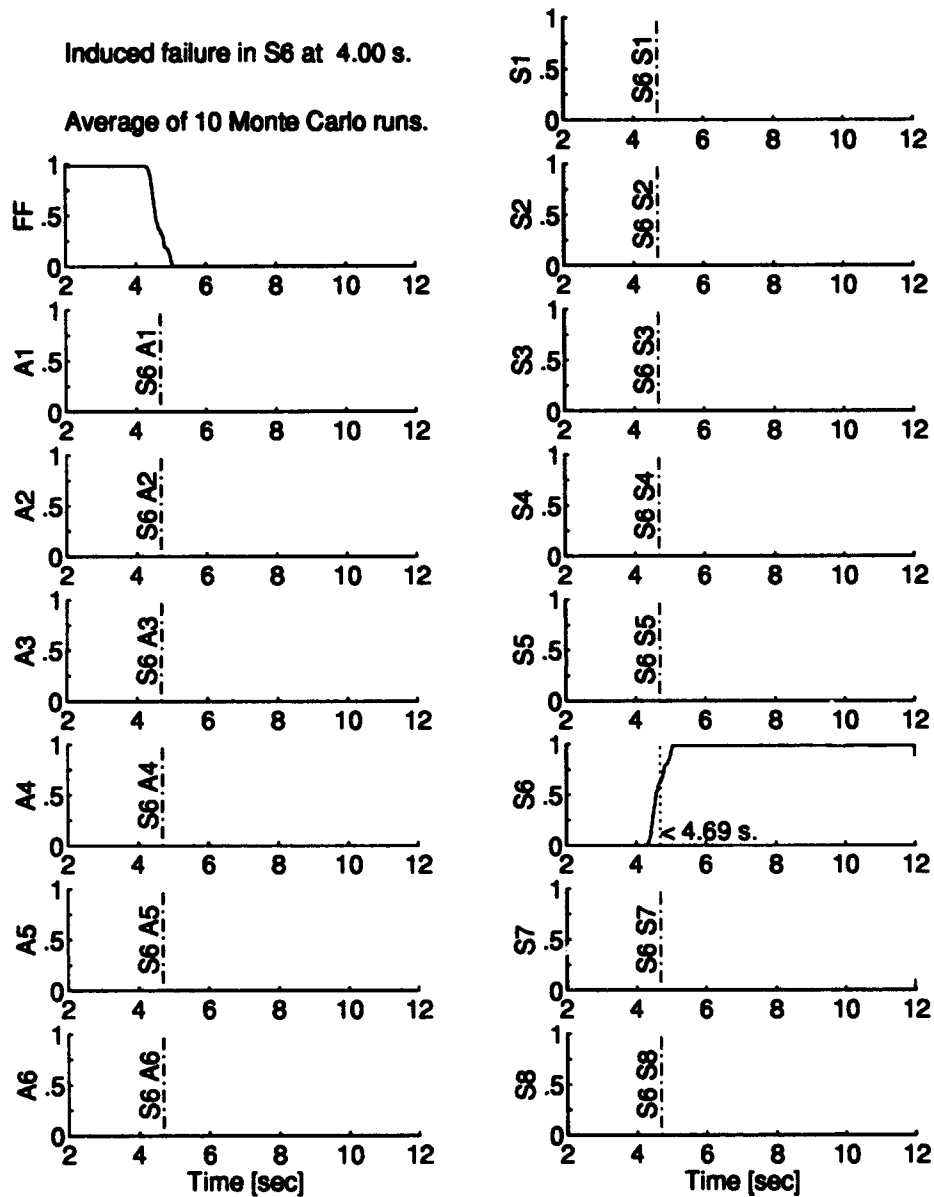


Figure E.13 MMAE Performance With Roll Rate Sensor Failure at 4.00 Seconds Using Optimal Dither.

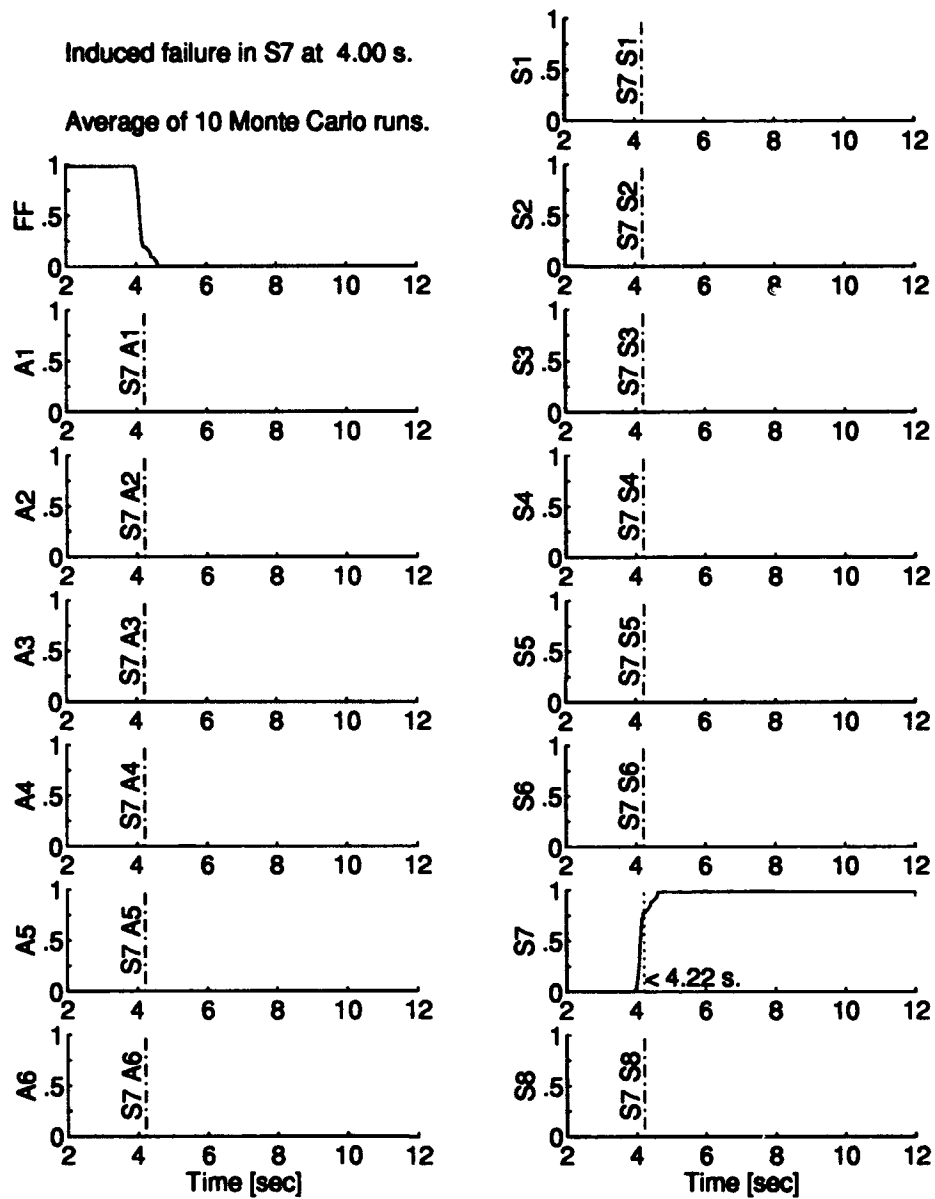


Figure E.14 MMAE Performance With Roll Angle Sensor Failure at 4.00 Seconds Using Optimal Dither.

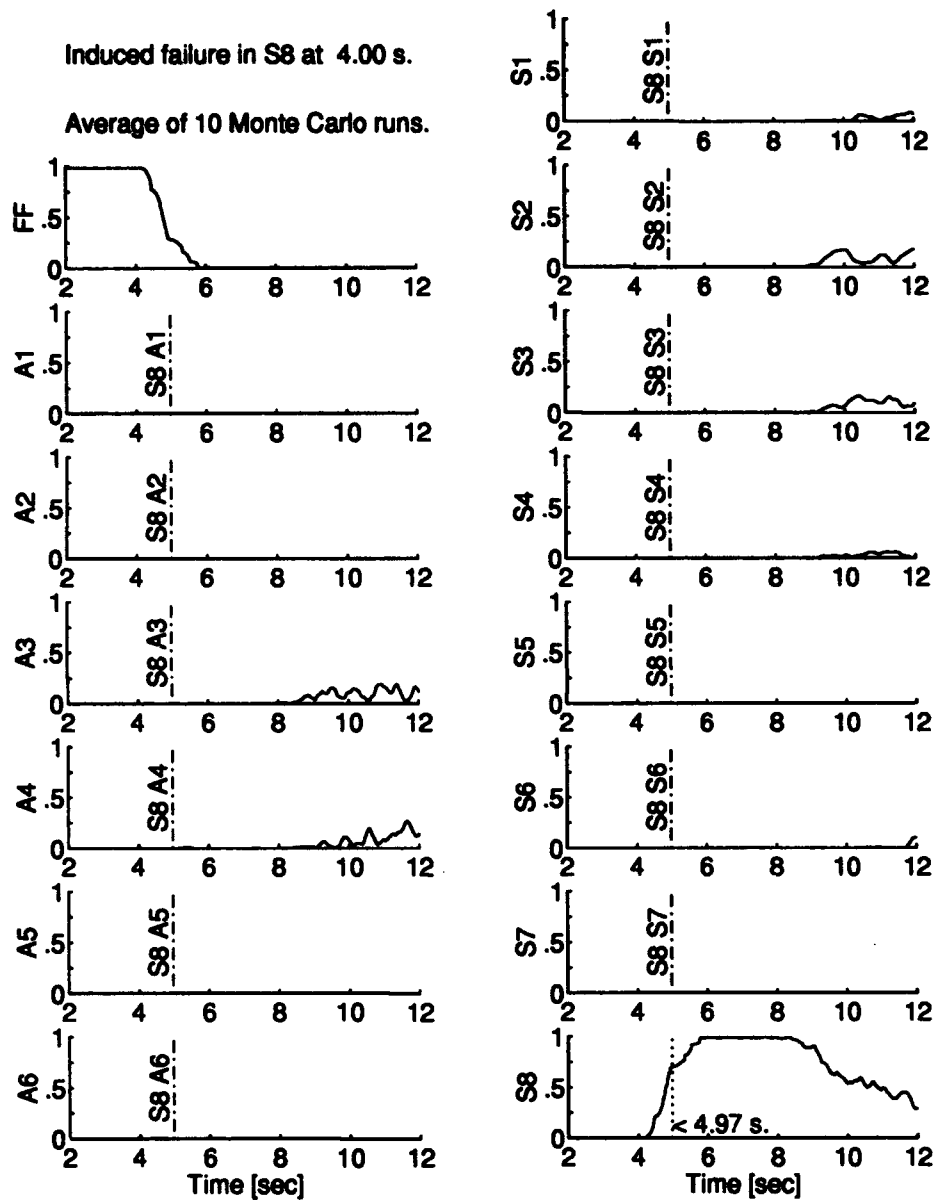


Figure E.15 MMAE Performance With Yaw Rate Sensor Failure at 4.00 Seconds Using Optimal Dither.

Appendix F. Dual Failure Probability Plots

MMAE filter probabilities for dual failures are presented in this appendix. The plots are ordered according to first failure induced. For a complete explanation and plots for performance with right elevator actuator failure induced first, see Section 4.4.

For convenience, Table 3.4 is repeated below as Table F.1 so that the codes in the plots are easily interpreted as the indicated filters. Two codes next to each other as in A2S4 indicate a secondary filter of a level-1 bank which hypothesizes two failed components.

Table F.1 MMAE Kalman Filter Codes.

Code	Filter Model Represents:
FF	fully functional aircraft
A1	right elevator actuator failure
A2	left elevator actuator failure
A3	right aileron actuator failure
A4	left aileron actuator failure
A5	right rudder actuator failure
A6	left rudder actuator failure
S1	forward velocity sensor failure
S2	angle of attack sensor failure
S3	pitch rate sensor failure
S4	pitch angle sensor failure
S5	sideslip angle sensor failure
S6	roll rate sensor failure
S7	roll angle sensor failure
S8	yaw rate sensor failure

First failure induced is A2 at 4.00 s.
 Second failures induced at 5.00 s.
 Average of 10 Monte Carlo runs.

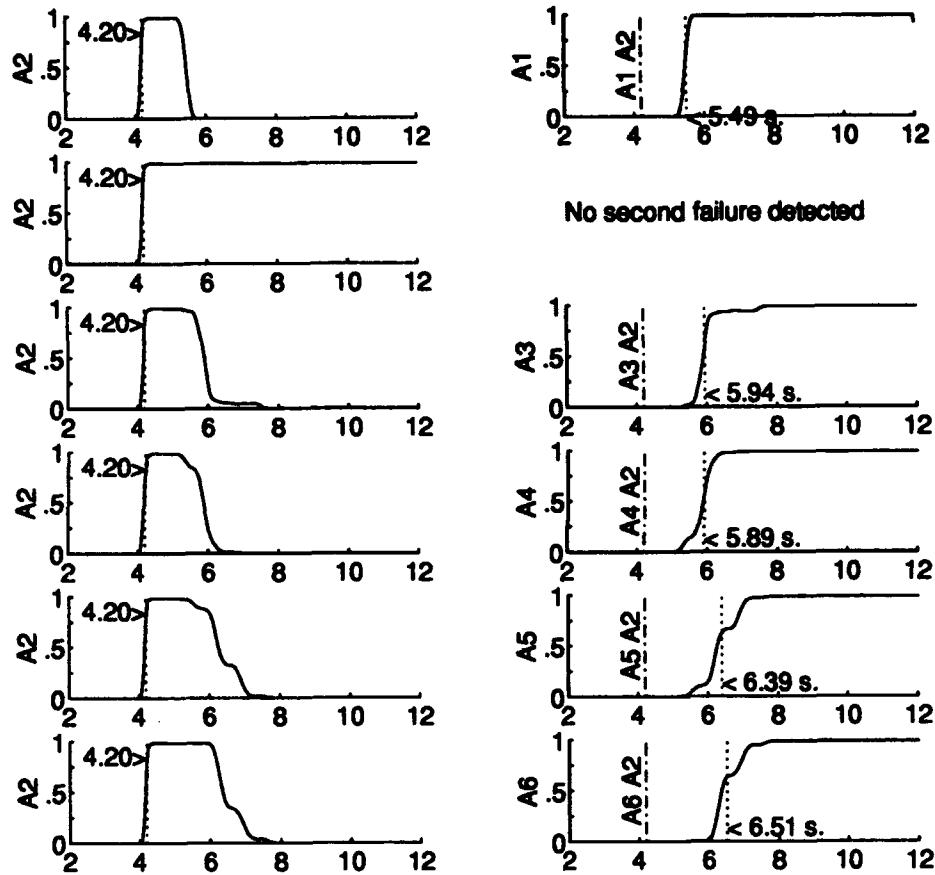


Figure F.1 Dual Failure MMAE filter Probability Plots with the Left Elevator Actuator Failing at 4.00 sec. and Each Actuator Failing at 5.00 sec.

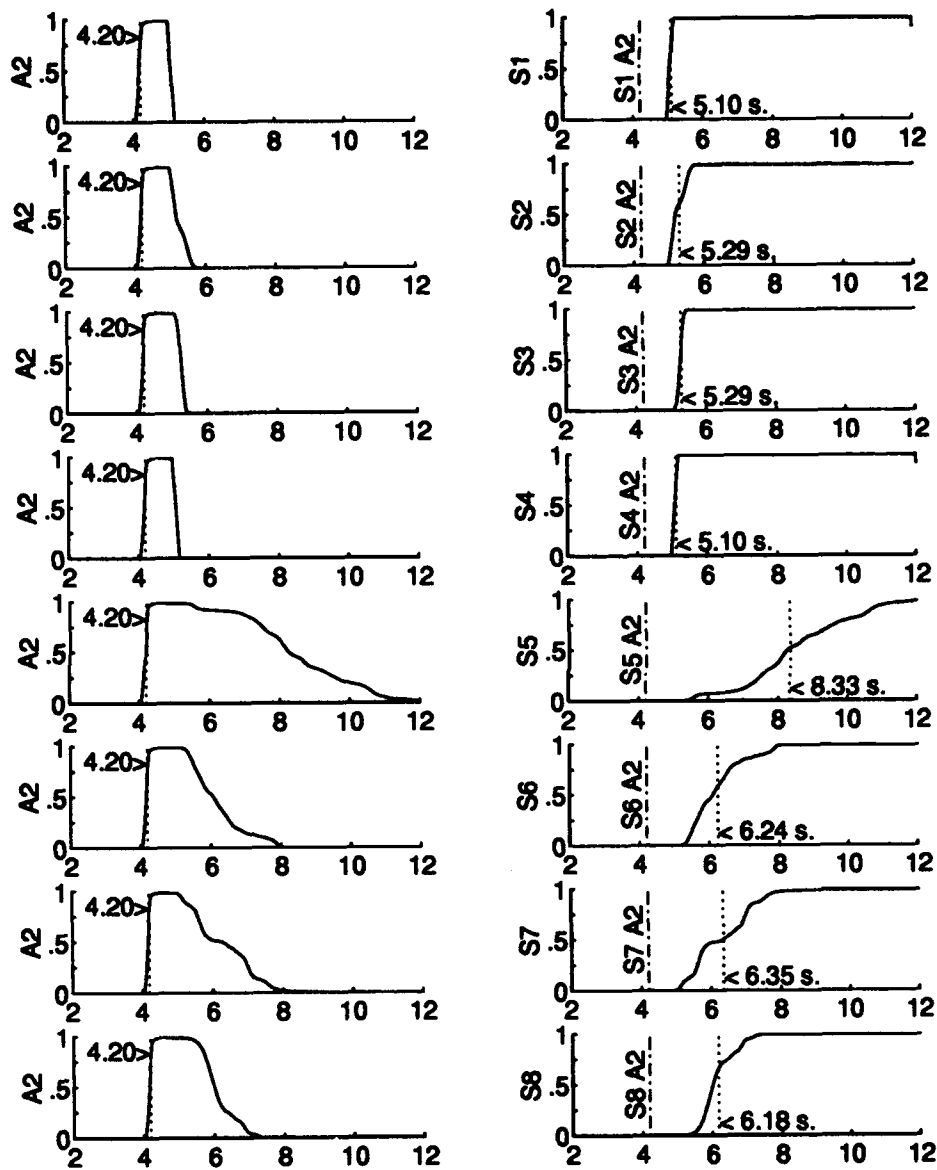


Figure F.2 Dual Failure MMAE filter Probability Plots with the Left Elevator Actuator Failing at 4.00 sec. and Each Sensor Failing at 5.00 sec.

First failure induced is A3 at 4.00 s.
 Second failures induced at 5.00 s.
 Average of 10 Monte Carlo runs.

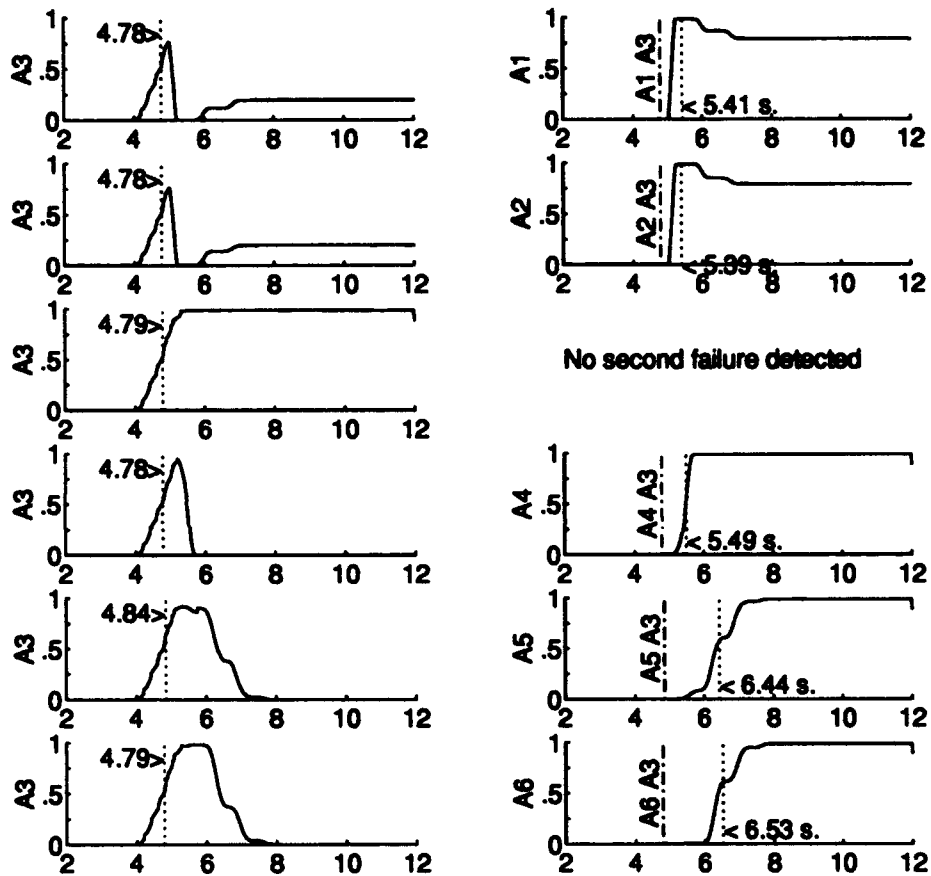


Figure F.3 Dual Failure MMAE filter Probability Plots with the Right Aileron Actuator Failing at 4.00 sec. and Each Actuator Failing at 5.00 sec.

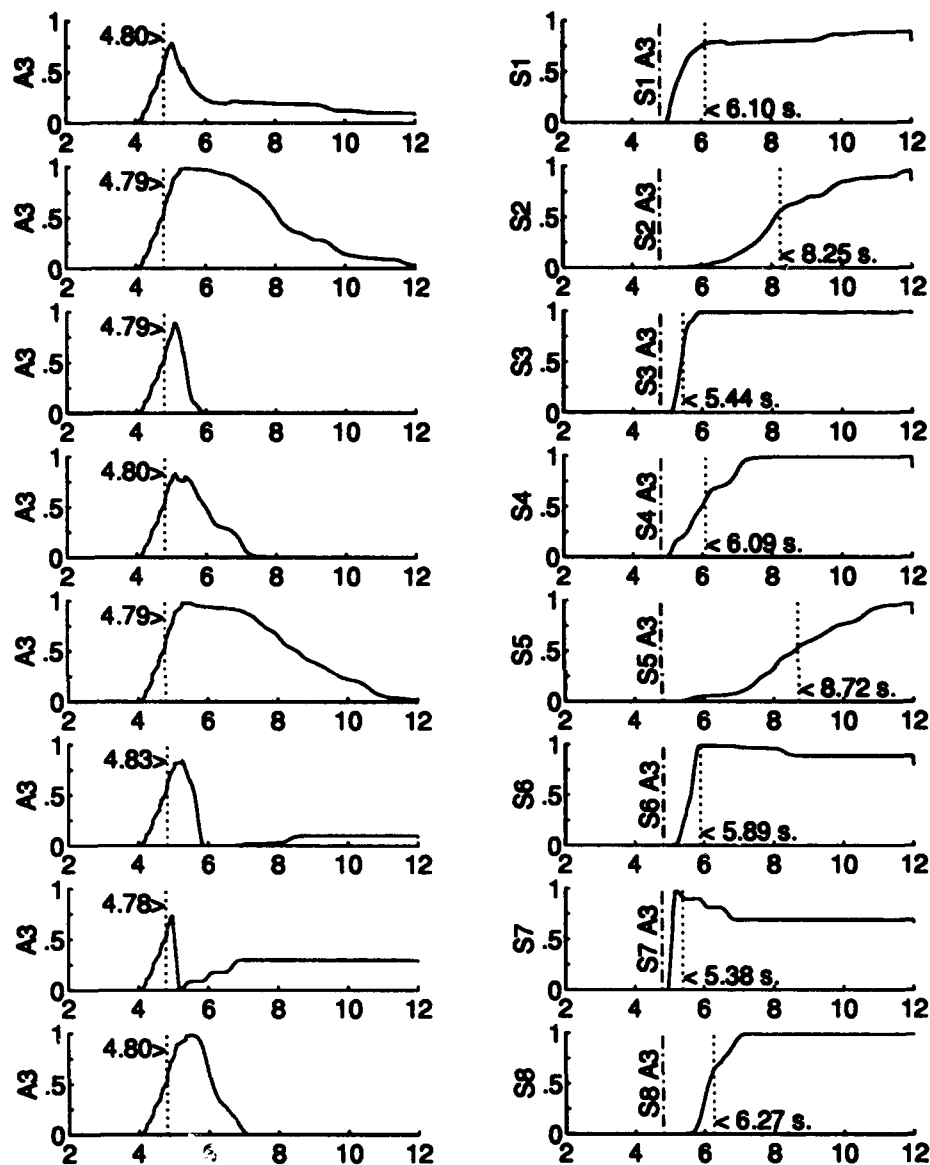


Figure F.4 Dual Failure MMAE filter Probability Plots with the Right Aileron Actuator Failing at 4.00 sec. and Each Sensor Failing at 5.00 sec.

First failure induced is A4 at 4.00 s.
 Second failures induced at 5.00 s.
 Average of 10 Monte Carlo runs.

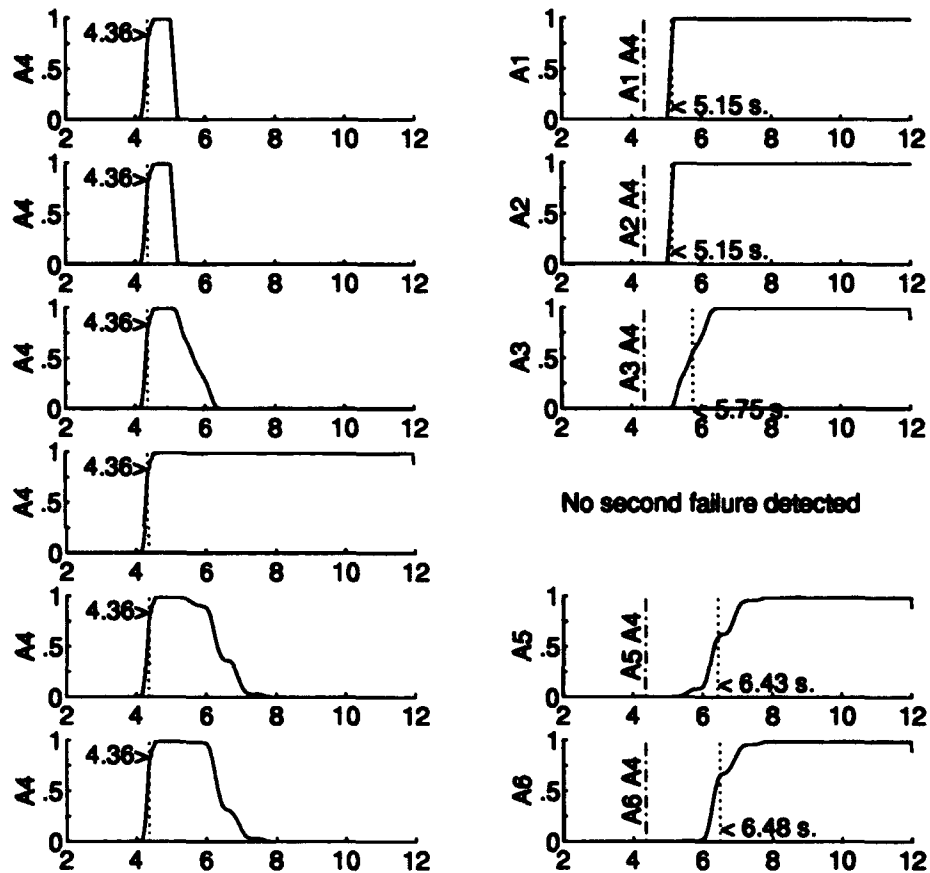


Figure F.5 Dual Failure MMAE filter Probability Plots with the Left Aileron Actuator Failing at 4.00 sec. and Each Actuator Failing at 5.00 sec.

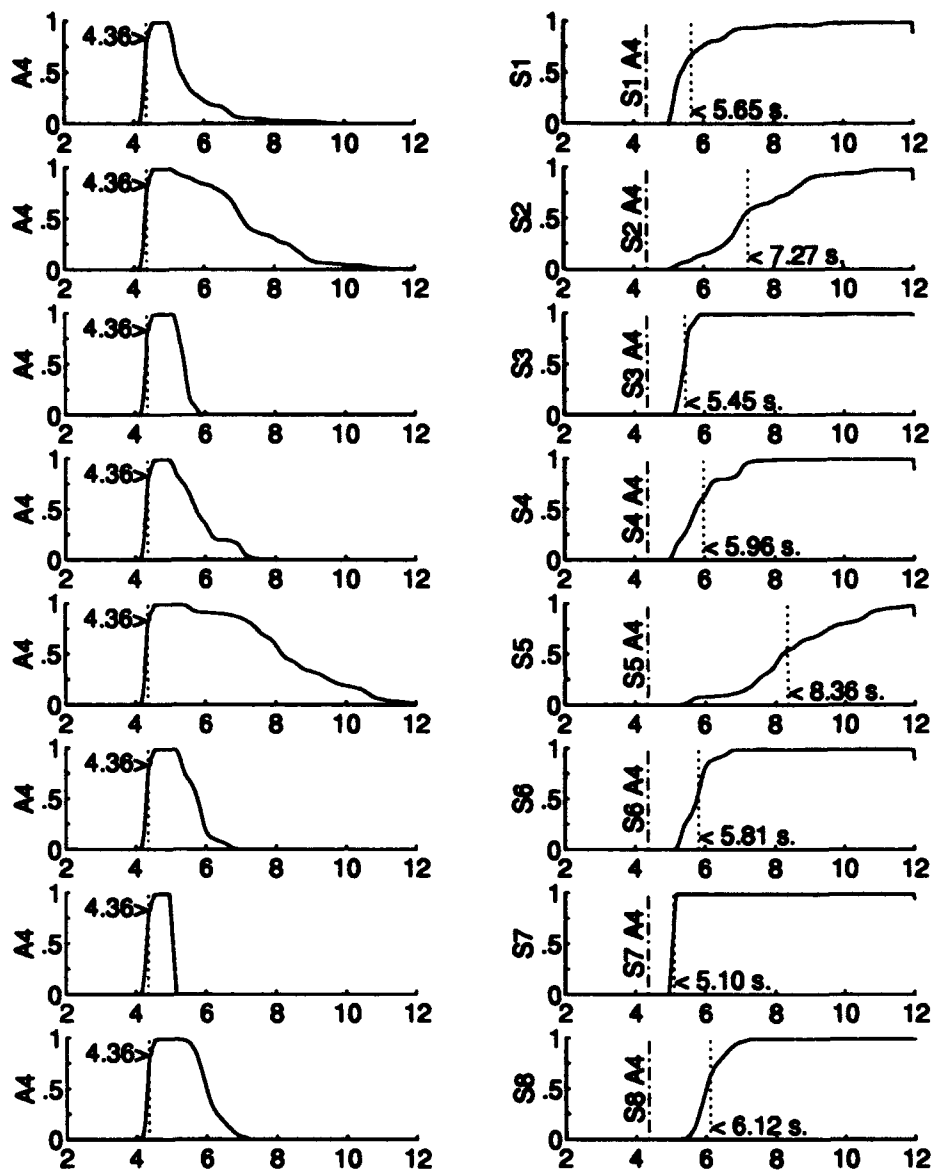


Figure F.6 Dual Failure MMAE filter Probability Plots with the Left Aileron Actuator Failing at 4.00 sec. and Each Sensor Failing at 5.00 sec.

First failure induced is A5 at 4.00 s.
 Second failures induced at 5.00 s.
 Average of 10 Monte Carlo runs.

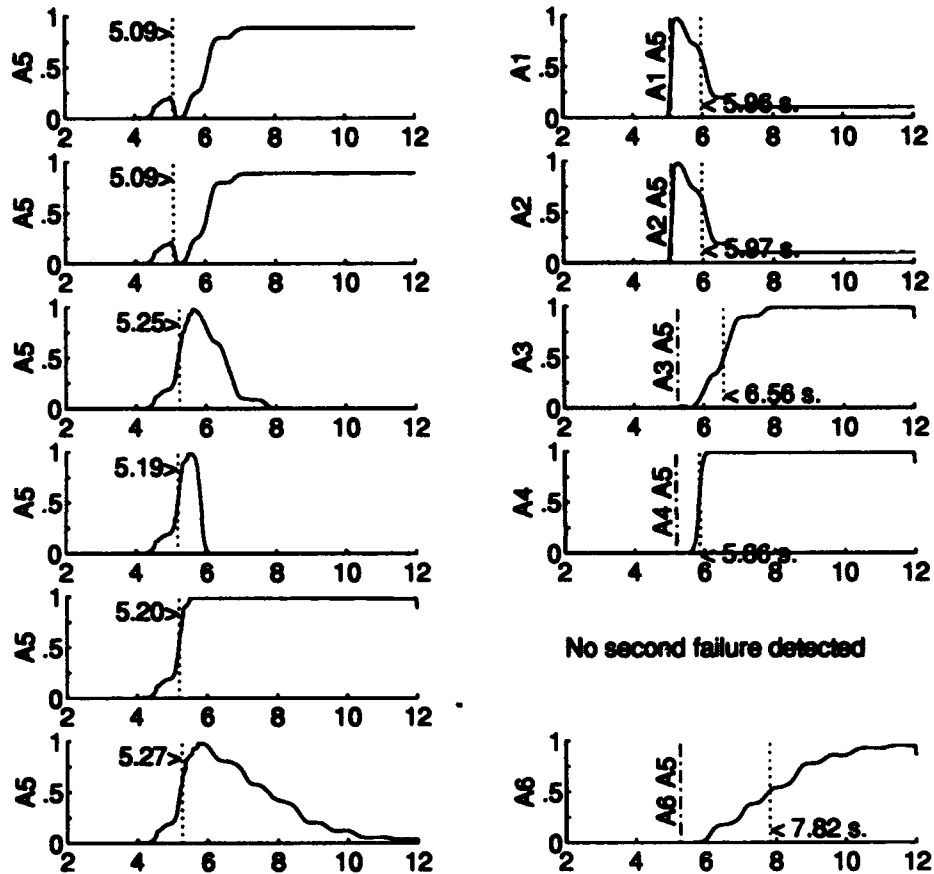


Figure F.7 Dual Failure MMAE filter Probability Plots with the Right Rudder Actuator Failing at 4.00 sec. and Each Actuator Failing at 5.00 sec.

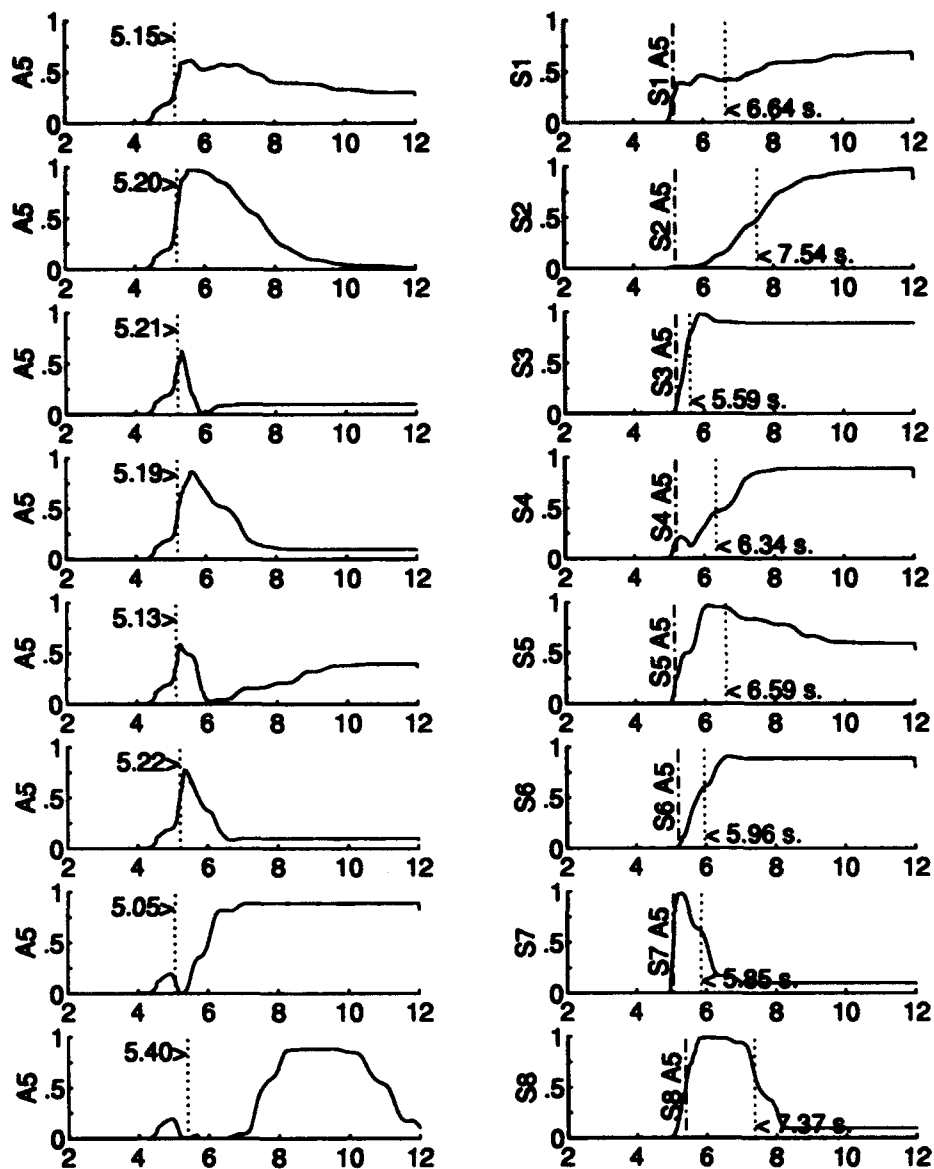


Figure F.8 Dual Failure MMAE filter Probability Plots with the Right Rudder Actuator Failing at 4.00 sec. and Each Sensor Failing at 5.00 sec.

First failure induced is A6 at 4.00 s.
 Second failures induced at 5.00 s.
 Average of 10 Monte Carlo runs.

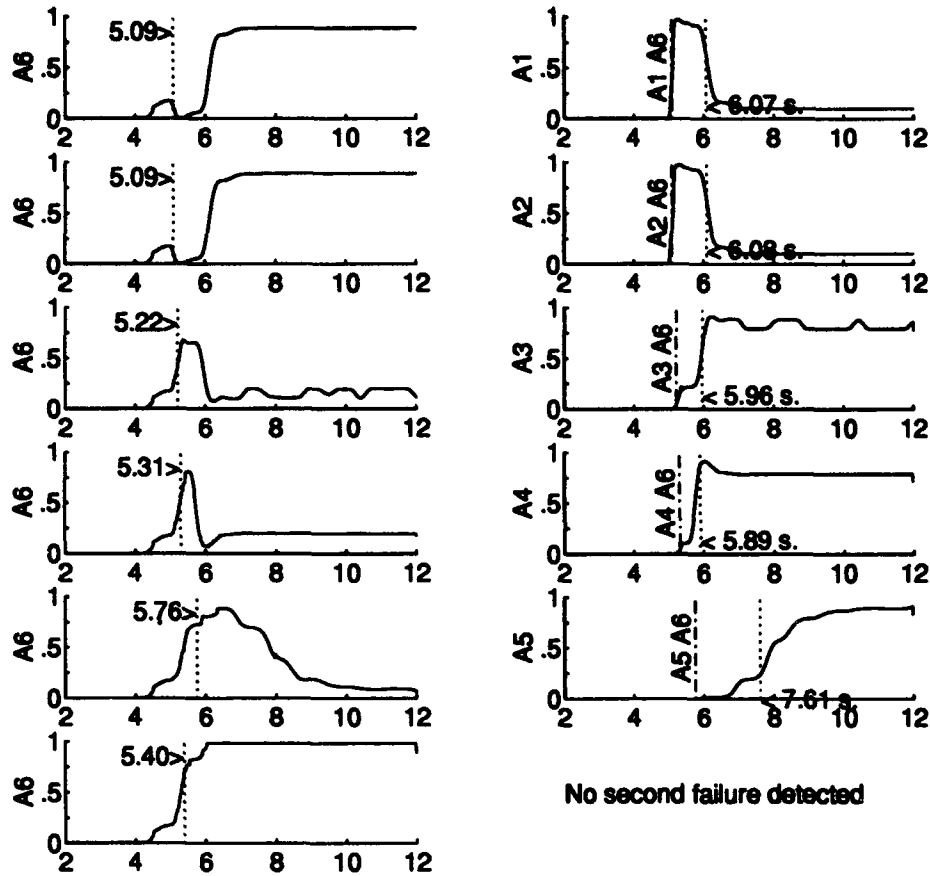


Figure F.9 Dual Failure MMAE filter Probability Plots with the Left Rudder Actuator Failing at 4.00 sec. and Each Actuator Failing at 5.00 sec.

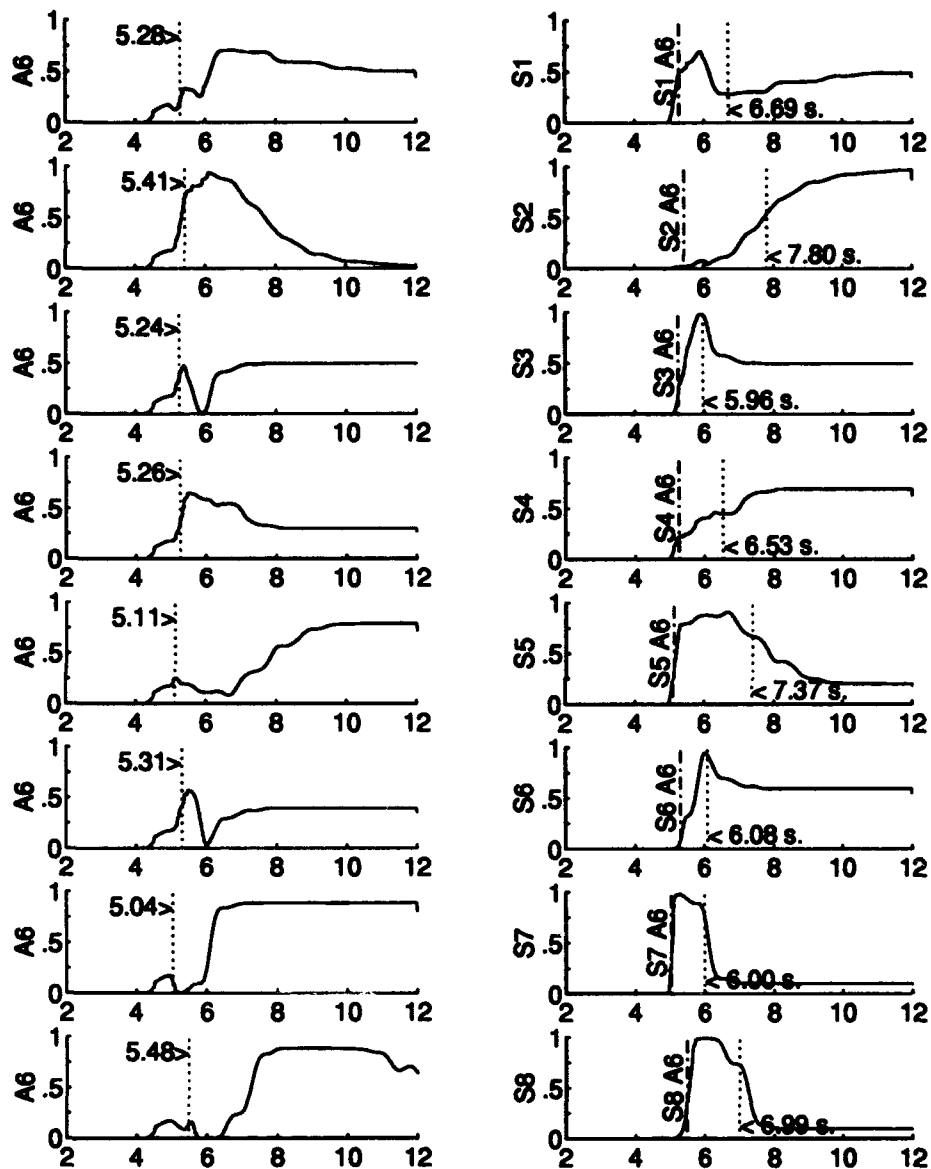


Figure F.10 Dual Failure MMAE filter Probability Plots with the Left Rudder Actuator Failing at 4.00 sec. and Each Sensor Failing at 5.00 sec.

First failure induced is S1 at 4.00 s.
 Second failures induced at 5.00 s.
 Average of 10 Monte Carlo runs.

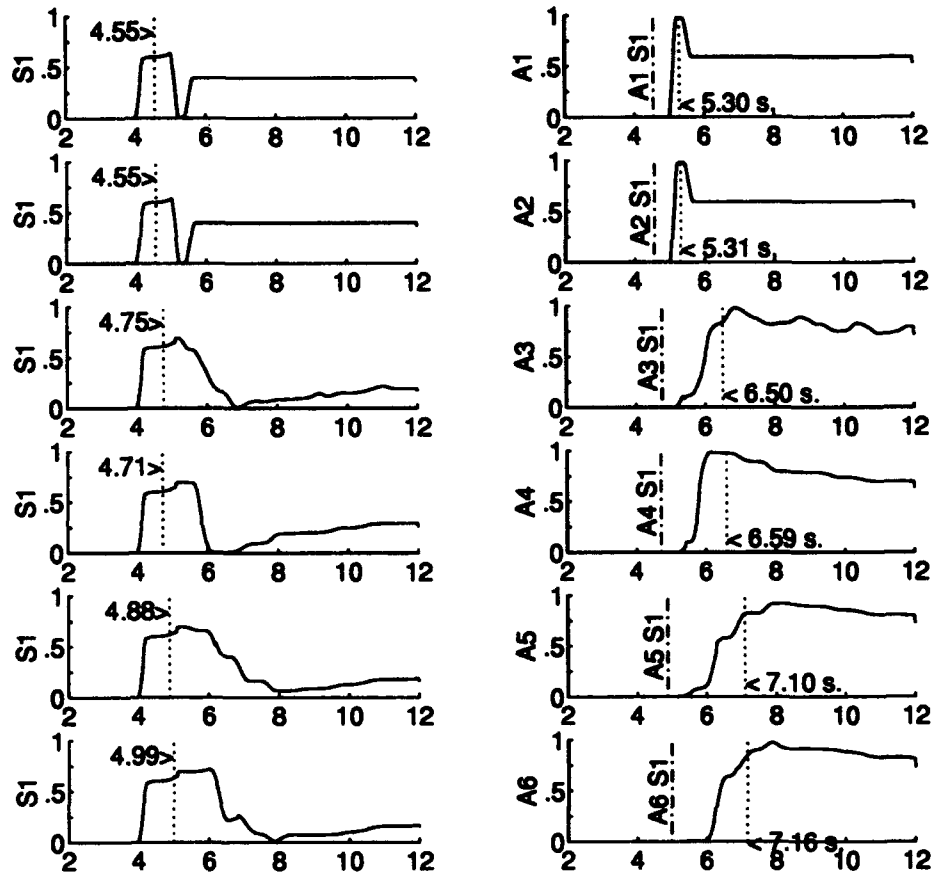


Figure F.11 Dual Failure MMAE filter Probability Plots with the Forward Velocity Sensor Failing at 4.00 sec. and Each Actuator Failing at 5.00 sec.

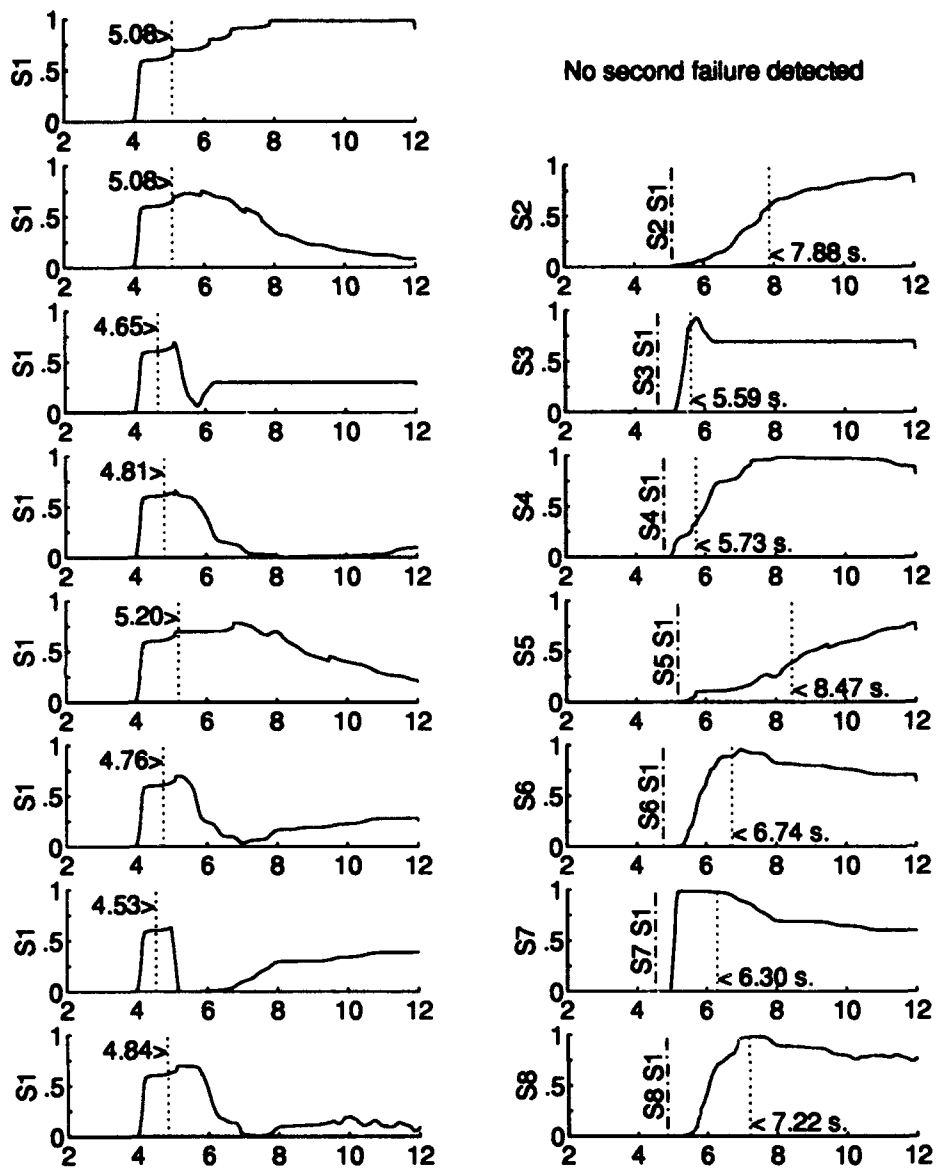


Figure F.12 Dual Failure MMAE filter Probability Plots with the Forward Velocity Sensor Failing at 4.00 sec. and Each Sensor Failing at 5.00 sec.

First failure induced is S2 at 4.00 s.
 Second failures induced at 5.00 s.
 Average of 10 Monte Carlo runs.

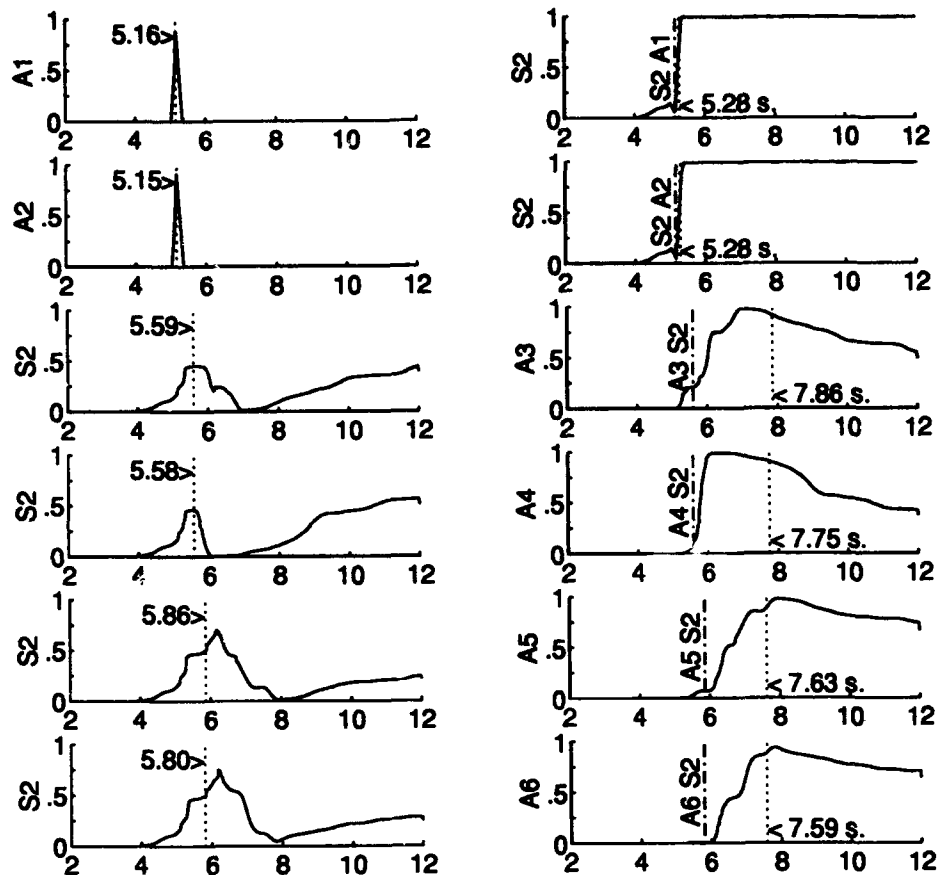


Figure F.13 Dual Failure MMAE filter Probability Plots with the Angle of Attack Sensor Failing at 4.00 sec. and Each Actuator Failing at 5.00 sec.

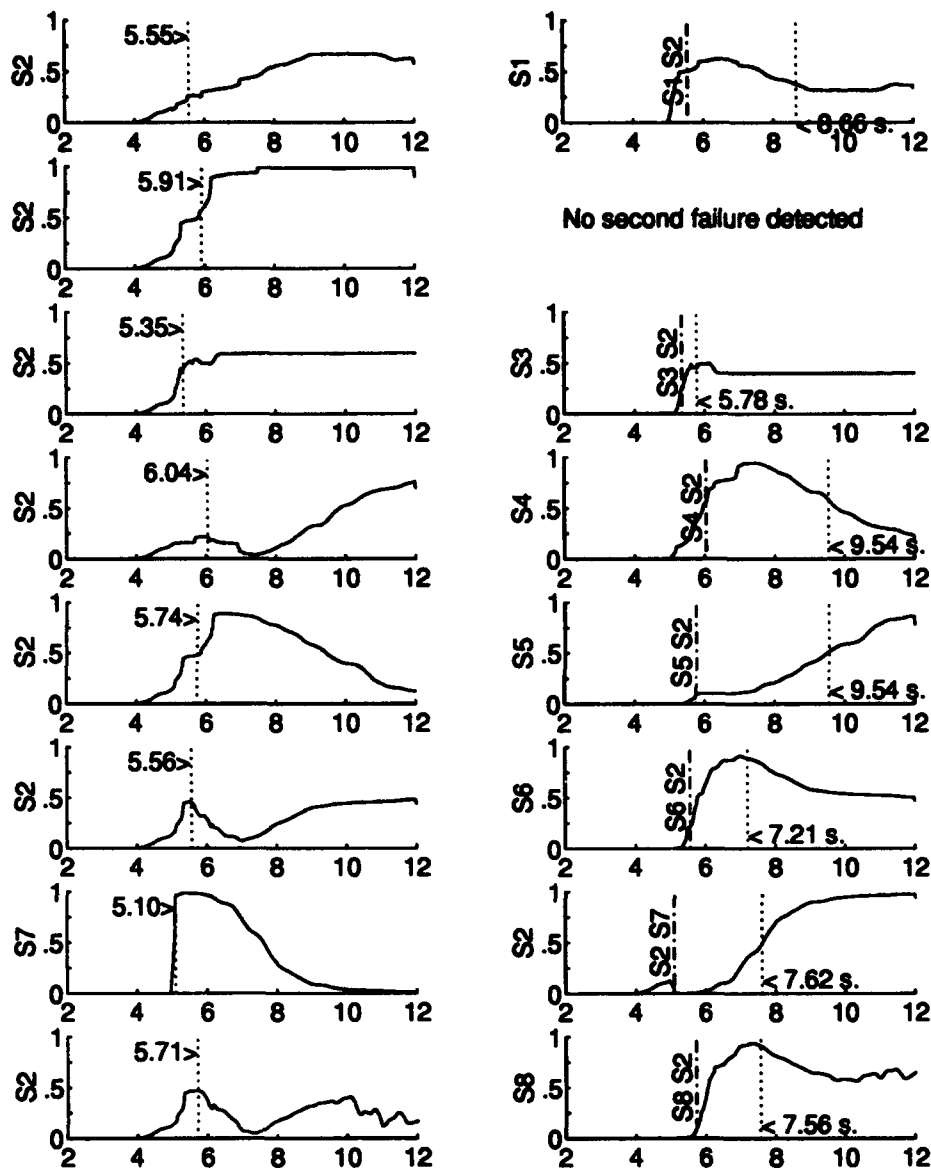


Figure F.14 Dual Failure MMAE filter Probability Plots with the Angle of Attack Sensor Failing at 4.00 sec. and Each Sensor Failing at 5.00 sec.

First failure induced is S3 at 4.00 s.
 Second failures induced at 5.00 s.
 Average of 10 Monte Carlo runs.

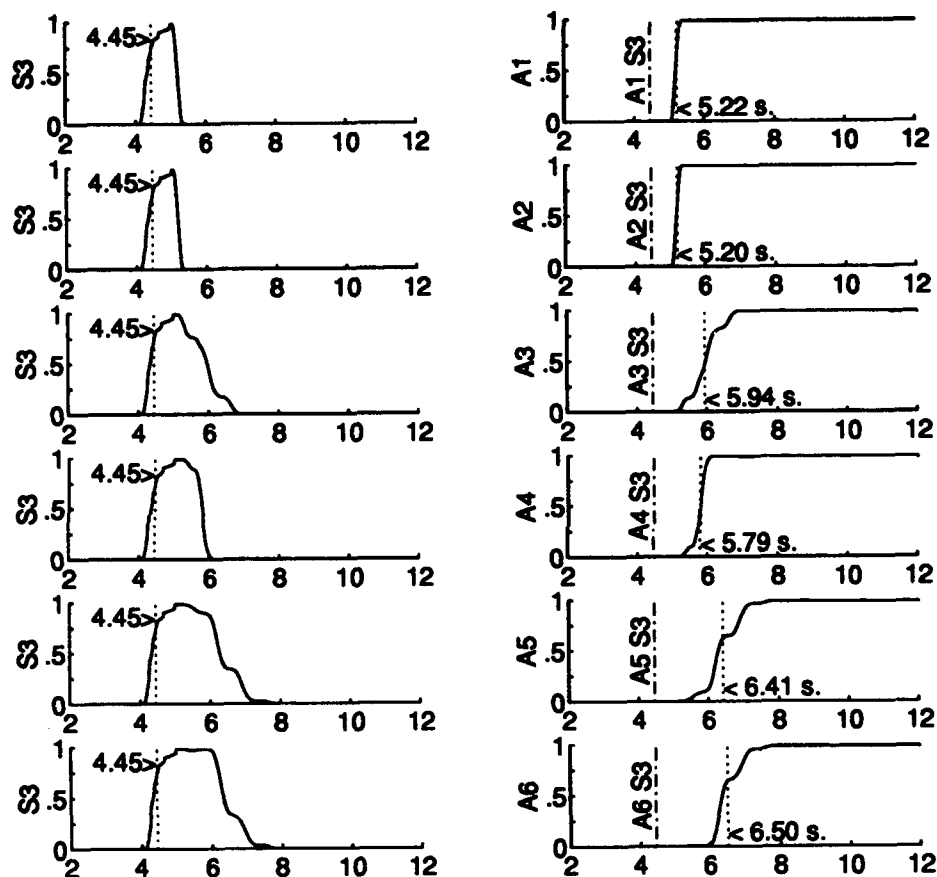


Figure F.15 Dual Failure MMAE filter Probability Plots with the Pitch Rate Sensor Failing at 4.00 sec. and Each Actuator Failing at 5.00 sec.

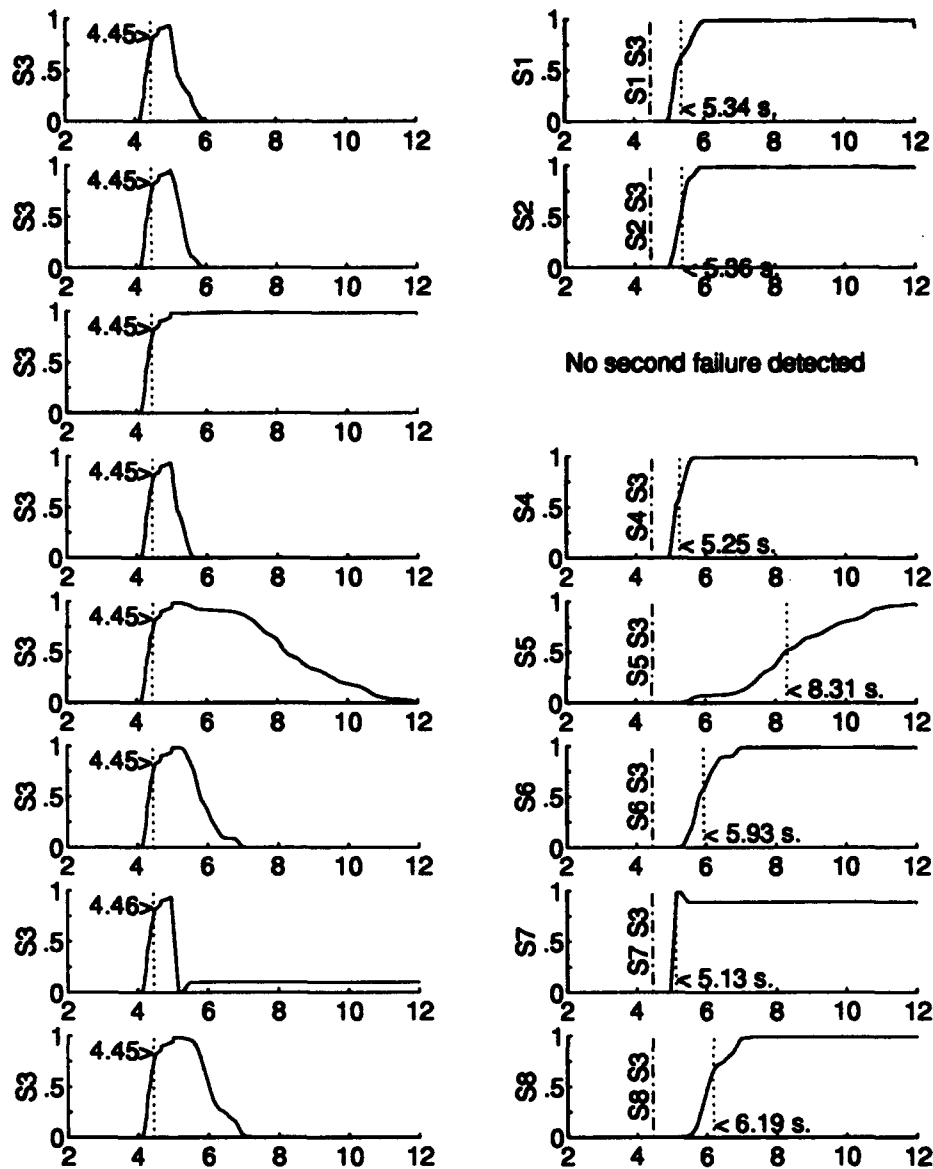


Figure F.16 Dual Failure MMAE filter Probability Plots with the Pitch Rate Sensor Failing at 4.00 sec. and Each Sensor Failing at 5.00 sec.

First failure induced is S4 at 4.00 s.
 Second failures induced at 5.00 s.
 Average of 10 Monte Carlo runs.

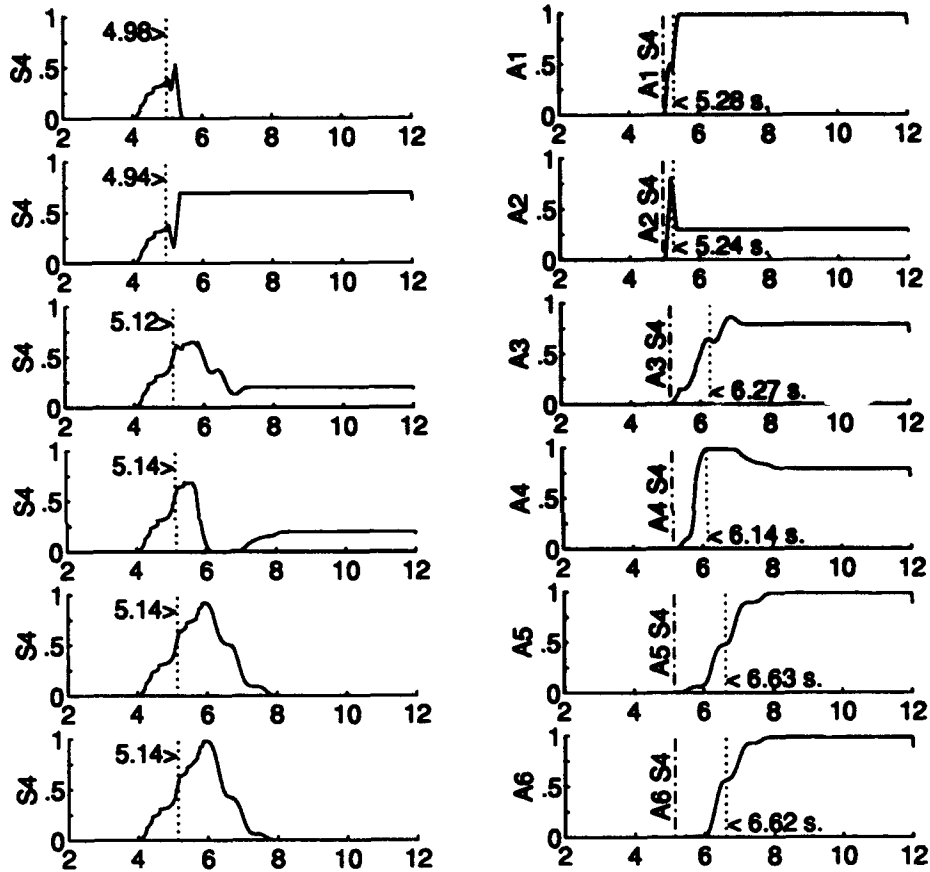


Figure F.17 Dual Failure MMAE filter Probability Plots with the Pitch Angle Sensor Failing at 4.00 sec. and Each Actuator Failing at 5.00 sec.

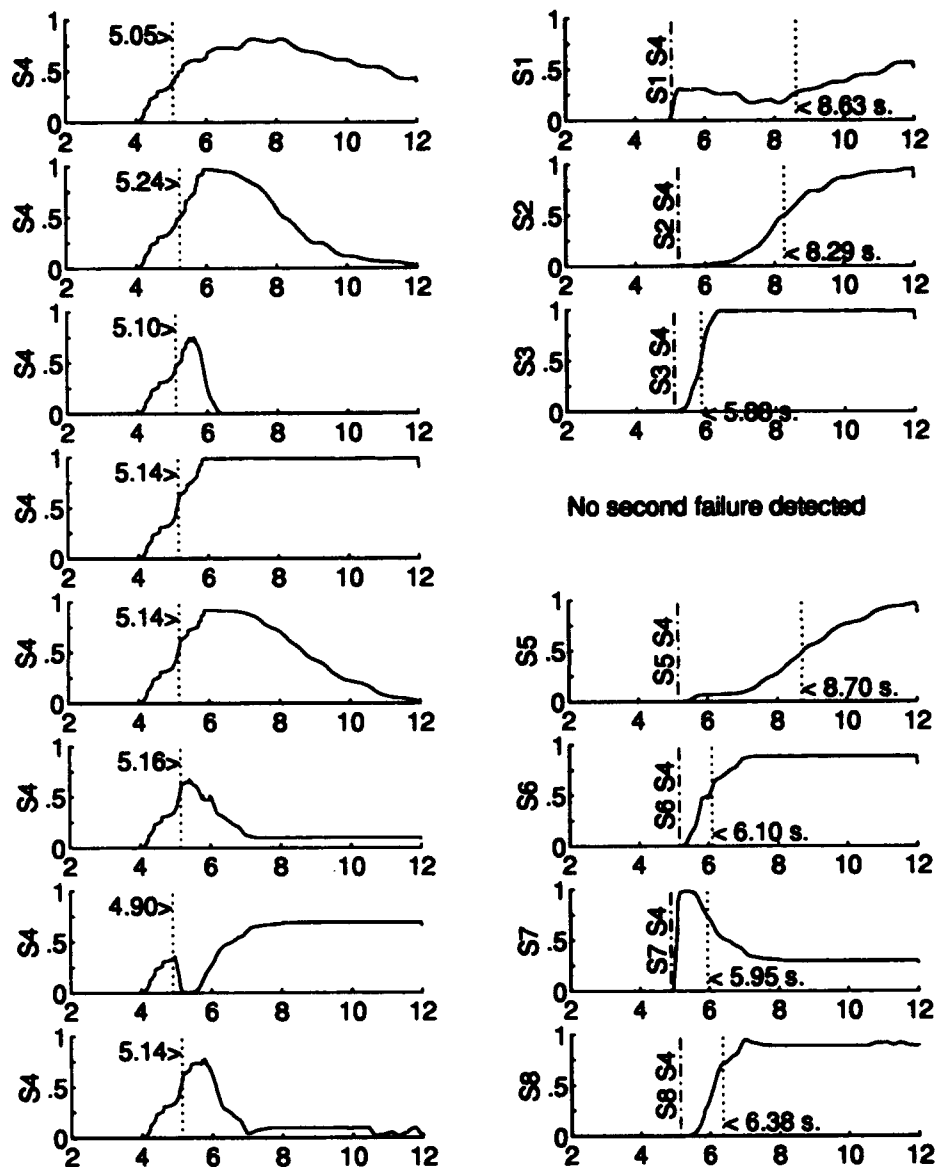


Figure F.18 Dual Failure MMAE filter Probability Plots with the Pitch Angle Sensor Failing at 4.00 sec. and Each Sensor Failing at 5.00 sec.

First failure induced is S5 at 4.00 s.
 Second failures induced at 5.00 s.
 Average of 10 Monte Carlo runs.

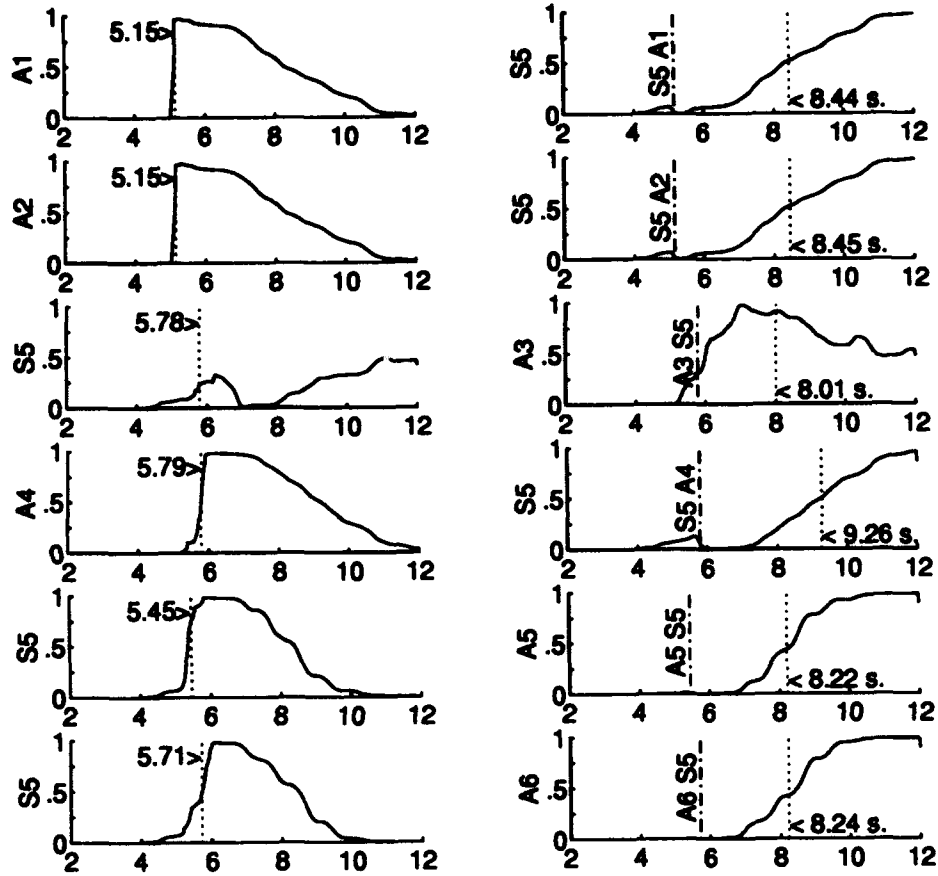


Figure F.19 Dual Failure MMAE filter Probability Plots with the Sideslip Angle Sensor Failing at 4.00 sec. and Each Actuator Failing at 5.00 sec.

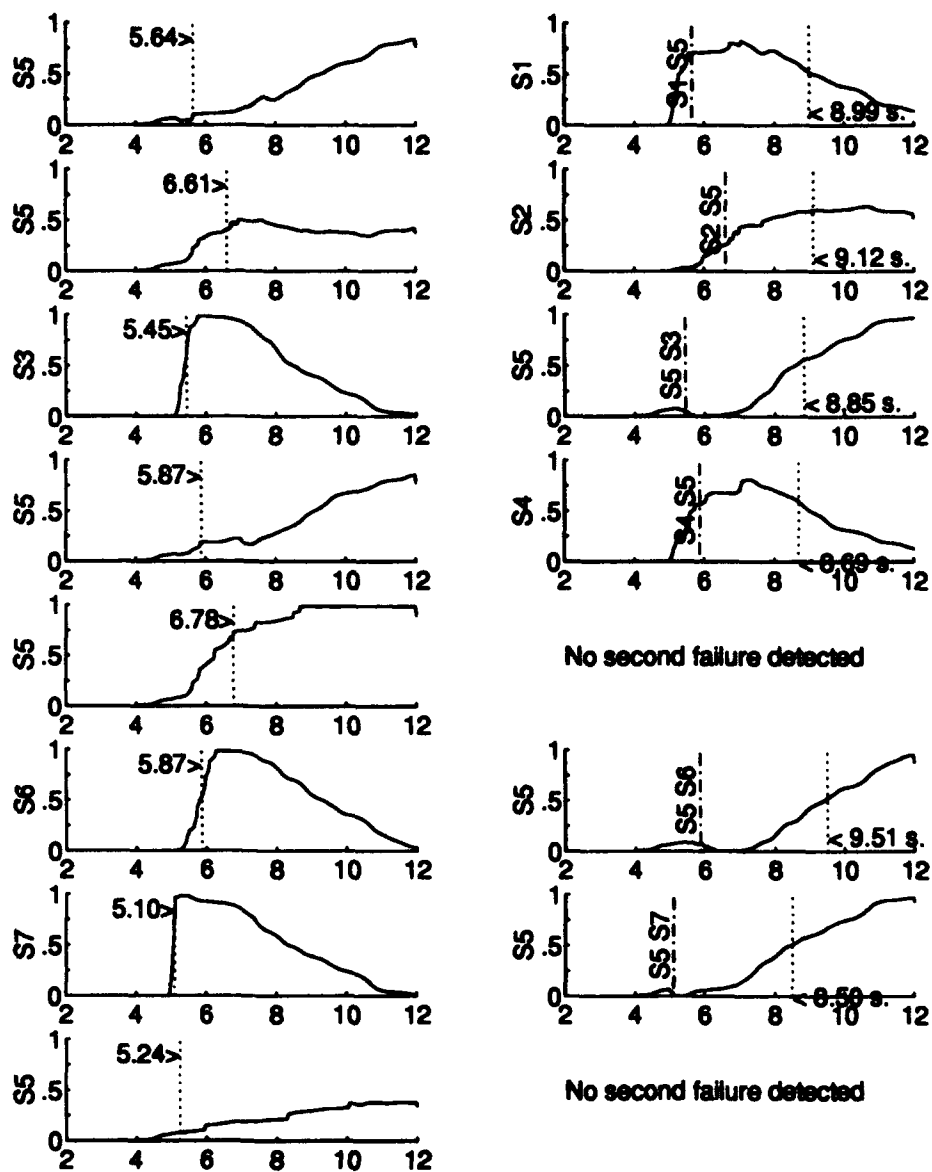


Figure F.20 Dual Failure MMAE filter Probability Plots with the Sideslip Angle Sensor Failing at 4.00 sec. and Each Sensor Failing at 5.00 sec.

First failure induced is S6 at 4.00 s.
 Second failures induced at 5.00 s.
 Average of 10 Monte Carlo runs.

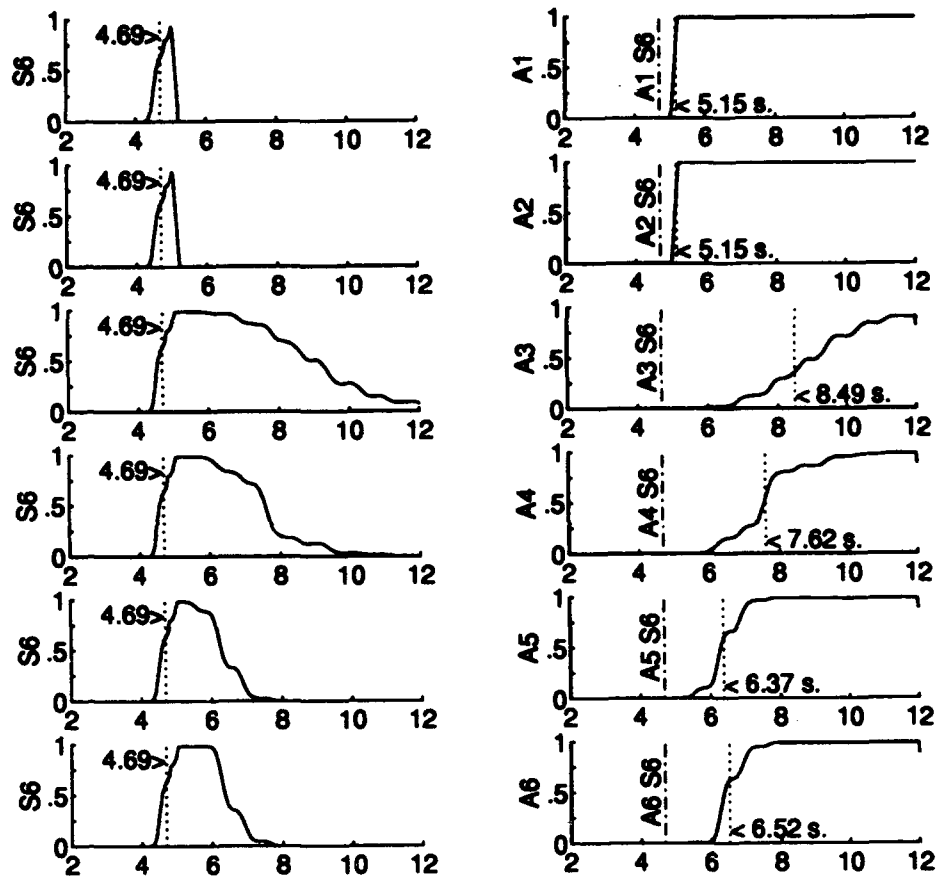


Figure F.21 Dual Failure MMAE filter Probability Plots with the Roll Rate Sensor Failing at 4.00 sec. and Each Actuator Failing at 5.00 sec.

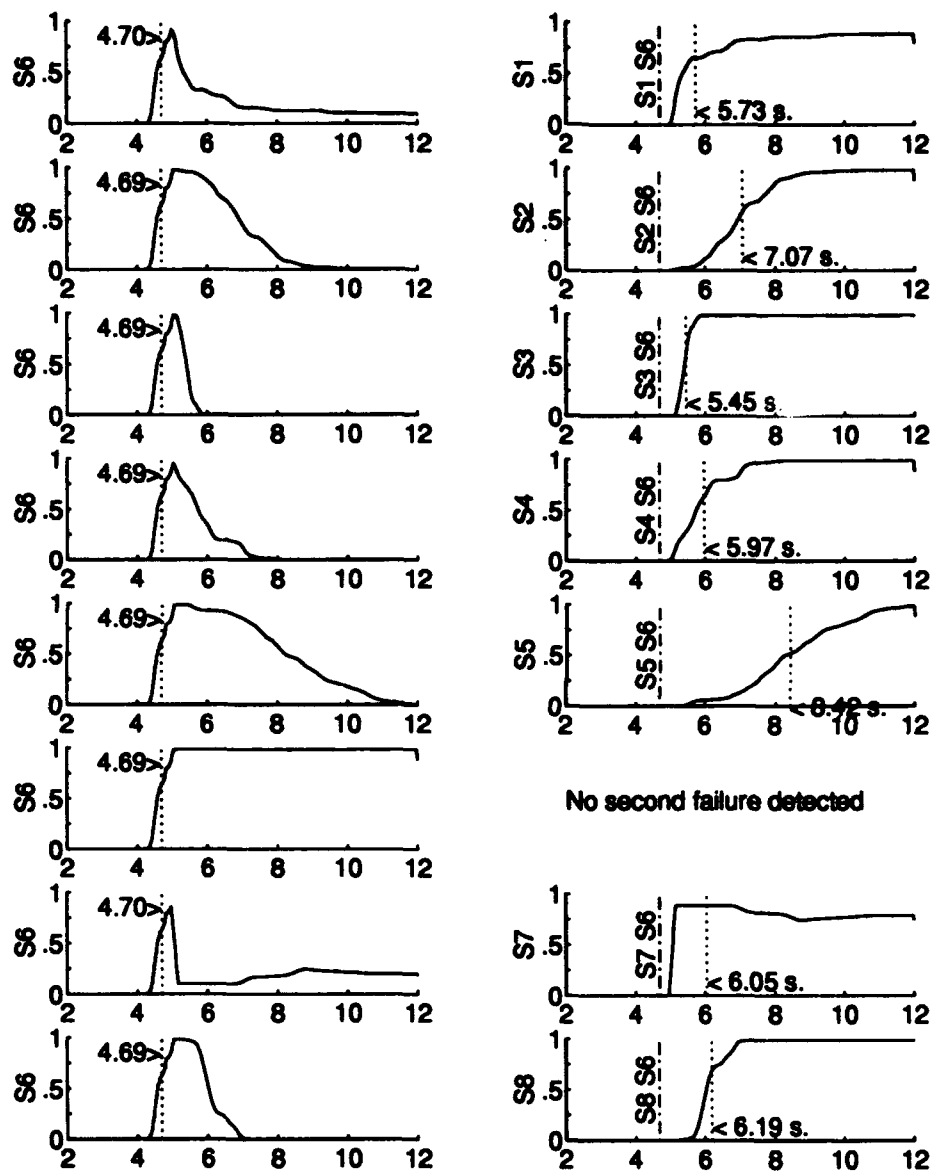


Figure F.22 Dual Failure MMAE filter Probability Plots with the Roll Rate Sensor Failing at 4.00 sec. and Each Sensor Failing at 5.00 sec.

First failure induced is S7 at 4.00 s.
 Second failures induced at 5.00 s.
 Average of 10 Monte Carlo runs.

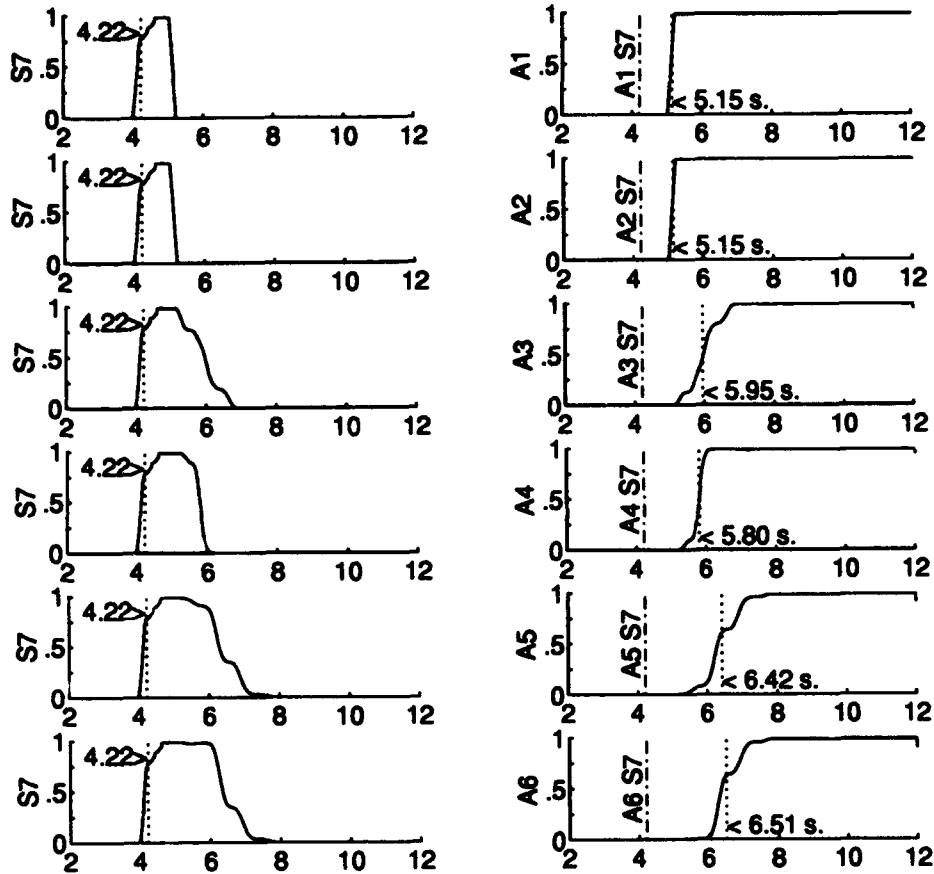


Figure F.23 Dual Failure MMAE filter Probability Plots with the Roll Angle Sensor Failing at 4.00 sec. and Each Actuator Failing at 5.00 sec.

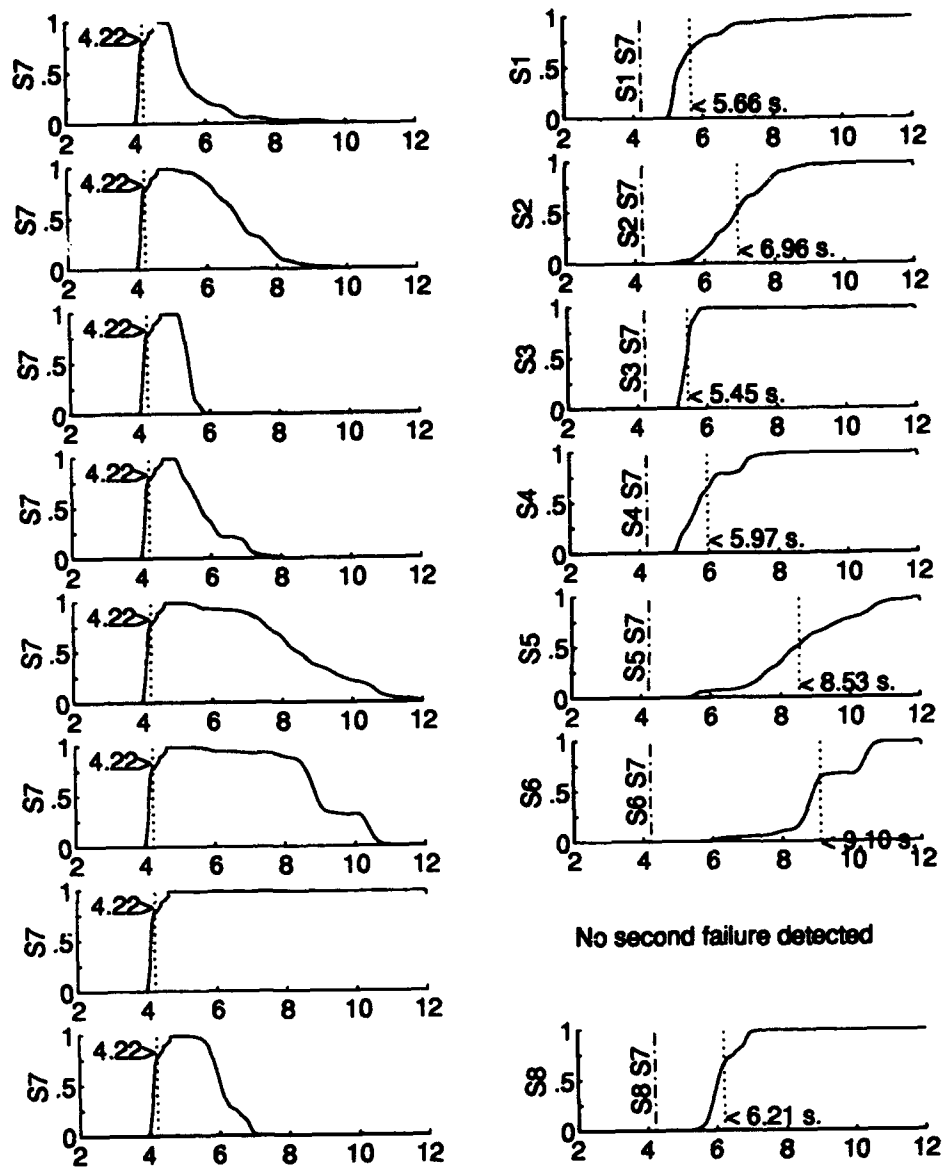


Figure F.24 Dual Failure MMAE filter Probability Plots with the Roll Angle Sensor Failing at 4.00 sec. and Each Sensor Failing at 5.00 sec.

First failure induced is S8 at 4.00 s.
 Second failures induced at 5.00 s.
 Average of 10 Monte Carlo runs.

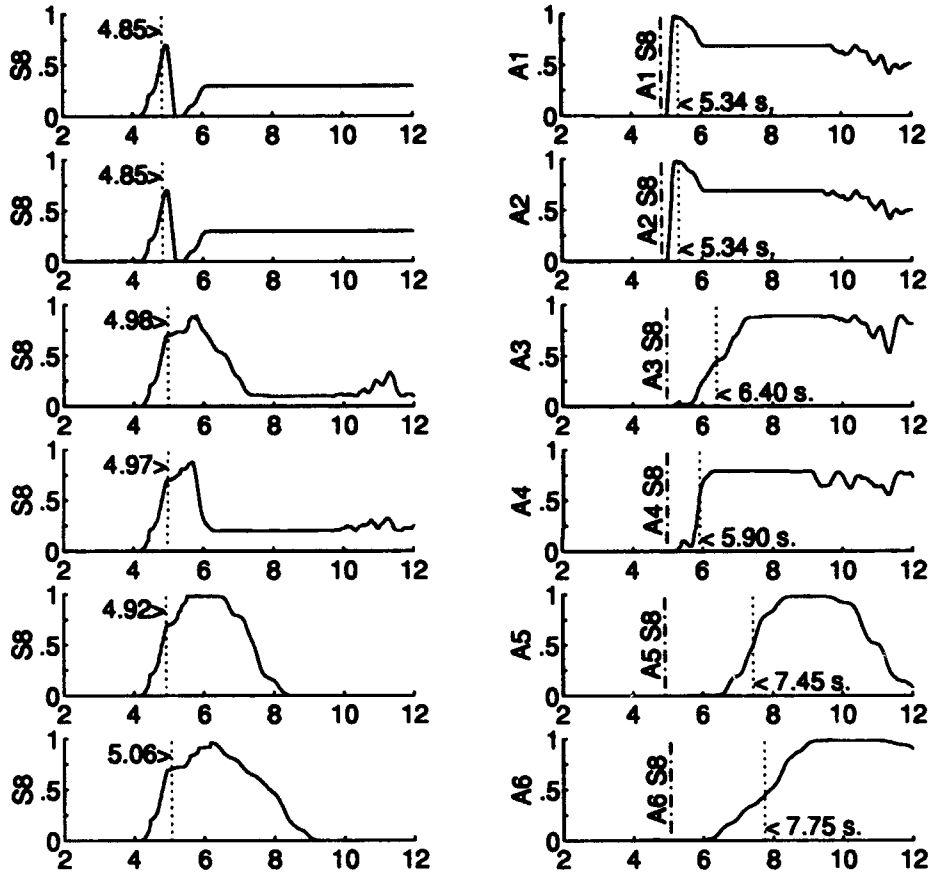


Figure F.25 Dual Failure MMAE filter Probability Plots with the Yaw Rate Sensor Failing at 4.00 sec. and Each Actuator Failing at 5.00 sec.

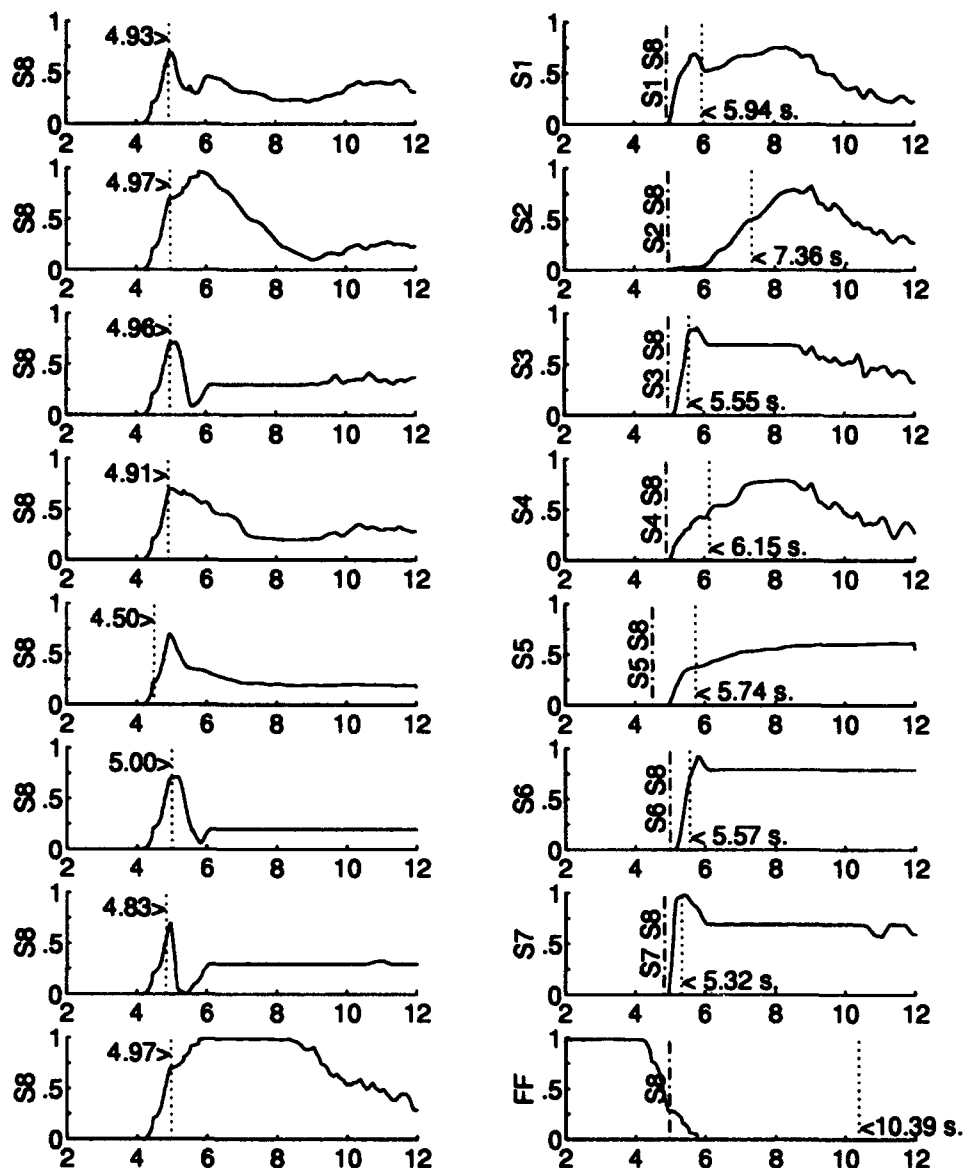


Figure F.26 Dual Failure MMAE filter Probability Plots with the Yaw Rate Sensor Failing at 4.00 sec. and Each Sensor Failing at 5.00 sec.

Bibliography

1. Athans, M., et. al. "The Stochastic Control of the F-8C Aircraft Using a Multiple Model Adaptive Control (MMAC) Method - Part I: Equilibrium Flight," *IEEE Transactions on Automatic Control*, AC-22(5):768-780 (October 1977).
2. Dunn, H. J. and R. C. Montgomery. "A Moving Window Parameter Adaptive Control System for the F8-DFBW Aircraft," *IEEE Transactions on Automatic Control*, AC-22(5):788-795 (October 1977).
3. Hanlon, Capt Peter D. *Failure Identification Using Multiple Model Adaptive Estimation for the LAMBDA Flight Vehicle*. MS thesis, Air Force Institute of Technology, Wright-Patterson AFB, OH, December 1992.
4. Integrated Systems, Inc. *MATRIX*, (registered trademark) (Version 3.0 Edition), 1992.
5. Lane, Capt David W. "Interview with Captain Jim Wicker, USAF." Captain Wicker, a C-141 pilot with the 3950th Test Wing at Wright-Patterson AFB, Ohio, provided insight on aircraft motion and its effect on aircrew comfort., March 1992.
6. Magill, D.T. "Optimal Adaptive Estimation of Sample Stochastic Processes," *IEEE Transactions on Automatic Control*, AC-10(4):434-439 (October 1965).
7. Martin, Capt Richard Maurice. *LQG Synthesis of Elemental Controllers for AFT'/F-16 Adaptive Flight Control*. MS thesis, Air Force Institute of Technology, Wright-Patterson AFB, OH, December 1990.
8. The MathWorks, Inc. *MATLAB* (registered trademark) (Version 4.0a Edition), December 1992.
9. The MathWorks, Inc. *SIMULINK model analysis and construction functions* (Version 1.2b Edition), November 1992.
10. Maybeck, Peter S. *Stochastic Models, Estimation, and Control, I*. Academic Press, Inc., 1979.
11. Maybeck, Peter S. *Stochastic Models, Estimation, and Control, II*. Academic Press, Inc., 1982.
12. Maybeck, Peter S. and Capt Peter D. Hanlon. "Performance Enhancement of a Multiple Model Adaptive Estimator," *IEEE Conference on Decision and Control* (1993).
13. Maybeck, Peter S. and Capt Donald L. Pogoda. "Multiple Model Adaptive Controller for the STOL F-15 with Sensor/Actuator Failures," *Proceedings of the 28th Conference on Decision and Control*, 1566-1572 (December 1989).
14. Maybeck, Peter S. and Richard D. Stevens. "Reconfigurable Flight Control Via Multiple Model Adaptive Control Methods," *Proceedings of the IEEE National Aerospace and Electronics Conference, Dayton, Ohio*, 441-448 (May 1992).
15. Menke, Timothy E. *Multiple Model Adaptive Estimation Applied to the VISTA F-16 with Actuator and Sensor Failures*. MS thesis, Air Force Institute of Technology, Wright-Patterson AFB, OH, June 1992.

16. Menke, Timothy E. and Peter S. Maybeck. "Multiple Model Adaptive Estimation Applied to the VISTA F-16 Flight Control System with Actuator and Sensor Failures," *IEEE Trans. on Aerospace and Electronic Systems*, AES-27, No. 3:470-480 (May 1991).
17. Menke, Timothy E. and Peter S. Maybeck. "Sensor/Actuator Failure Detection in the VISTA F-16 by Multiple Model Adaptive Estimation," *Proceedings of American Control Conference, San Francisco, June 1993* (1993).
18. MIL-STD-1797A *Flying Qualities of Piloted Aircraft*, January 1993.
19. Pogoda, Capt Donald L. *Multiple Model Adaptive Controller for the STOL F-15 with Sensor/Actuator Failures*. MS thesis, Air Force Institute of Technology, Wright-Patterson AFB, OH, December 1988.
20. Schaefer, Karl E. *Bioastronautics*. The MacMillan Company, New York, 1964.
21. Stevens, Capt Richard D. *Characterization of a Reconfigurable Multiple Model Adaptive Controller Using A STOL F-15 Model*. MS thesis, Air Force Institute of Technology, Wright-Patterson AFB, OH, December 1989.
22. Stratton, Capt Gregory L. *Actuator and Sensor Failure Identification using a Multiple Model Adaptive Technique for the VISTA F-16*. MS thesis, Air Force Institute of Technology, Wright-Patterson AFB, OH, December 1991.
23. Sun Microsystems, Inc. *Sun FORTRAN* (Sun release 4.1 Edition), December 1990.
24. Swift, Lt Gerald A. *Model Identification and Control System Design for the LAMBDA Unmanned Research Vehicle*. MS thesis, Air Force Institute of Technology, Wright-Patterson AFB, OH, September 1991.
25. Willsky, A. S. "A Survey of Design Methods for Failure Detection in Dynamic Systems," *Automatica*, 12:601-611 (December 1976).
26. Wright Laboratory Flight Controls Division, Flight Controls Techniques Branch, (WL/FIGS). Numerical data concerning the LAMBDA aircraft and its performance was obtained from Capt Stuart Sheldon and Capt Steve Rasmussen.

Vita

Captain David William Lane is a graduate of Wayne County High School in Waynesboro, Tennessee. He was awarded an Air Force Reserve Officers' Training Corps scholarship and attended Vanderbilt University in Nashville, Tennessee. He received his Bachelor of Engineering degree from Vanderbilt in May 1987. His first operational assignment was with the 28th Bombardment Wing, Ellsworth AFB, SD where he served as a B-1B maintenance officer for four years. Captain Lane was accepted into the Air Force Institute of Technology Electrical Engineering/Guidance and Control Program in 1992.

Captain Lane is married to the former Carolyn Kerr Hunt of Roswell, Georgia and has one son, Nicholas David, who was born in November 1993.

Permanent address: 27918 California Drive, N.E.
Lathrup Village, Michigan 48076

REPORT DOCUMENTATION PAGE			Form Approved OMB No. 0704-0188	
Public reporting burden for this collection of information is estimated to average 1 hour per response, including the time for reviewing instructions, searching existing data sources, gathering and maintaining the data needed, and completing and reviewing the collection of information. Send comments regarding this burden estimate or any other aspect of this collection of information, including suggestions for reducing this burden, to Washington Headquarters Services, Directorate for Information Operations and Reports, 1215 Jefferson Davis Highway, Suite 1204, Arlington, VA 22202-4302, and to the Office of Management and Budget, Paperwork Reduction Project (0704-0188), Washington, DC 20503.				
1. AGENCY USE ONLY (Leave blank)		2. REPORT DATE December 1993		3. REPORT TYPE AND DATES COVERED Master's Thesis
4. TITLE AND SUBTITLE Multiple Model Adaptive Estimation Applied to the LAMBDA URV for Failure Detection and Identification			5. FUNDING NUMBERS	
6. AUTHOR(S) David W. Lane, Captain, USAF				
7. PERFORMING ORGANIZATION NAME(S) AND ADDRESS(ES) Air Force Institute of Technology, WPAFB OH 45433-6583			8. PERFORMING ORGANIZATION REPORT NUMBER AFIT/GE/ENG/93D-23	
9. SPONSORING/MONITORING AGENCY NAME(S) AND ADDRESS(ES) Captain Stuart Sheldon Wright Laboratory Flight Controls Division, Flight Controls Techniques Branch, (WL/FIGS) Wright-Patterson AFB, OH 45433			10. SPONSORING/MONITORING AGENCY REPORT NUMBER	
11. SUPPLEMENTARY NOTES				
12a. DISTRIBUTION / AVAILABILITY STATEMENT Approved for public release; distribution unlimited			12b. DISTRIBUTION CODE	
13. ABSTRACT (Maximum 200 words) Multiple Model Adaptive Estimation (MMAE) is a method of estimating unknown system parameters by modeling all possible parameter configurations in several models. The parameters for this research are failure status conditions associated with flight control actuators and sensors on the LAMBDA Unmanned Research Vehicle, an experimental aircraft operated by Wright Laboratory Flight Controls Division at Wright-Patterson Air Force Base, Ohio. Six actuator failures and eight sensor failures are modeled, along with the fully functional aircraft, in fifteen elemental Kalman filters. These filters propagate and update their own aircraft state estimates in real time. A probability computation representing the likelihood of each elemental filter's match to the true condition of the aircraft is used to generate relative probabilities for each filter's hypothesis. In this research, the MMAE algorithm is extended for the identification of dual failures through the use of a hierarchical structure of filter banks. The ability of the MMAE to identify dual failures in the face of wind gust uncertainty and sensor noise is investigated. Aircraft state excitation is required for effective MMAE performance. Therefore, the form of an optimal input dither signal is derived through extensive experimentation. Dither signals are applied to the command inputs of a Quantitative Feedback Theory flight control system which controls pitch rate, roll rate, and sideslip angle. In particular, the MMAE performance is studied as sinusoidal dither inputs are varied in frequency and magnitude. An analysis of tuning techniques for the elemental filters within the MMAE is presented.				
14. SUBJECT TERMS Multiple Model Adaptive Estimation, Parameter Estimation, Kalman Filtering, Failure Identification			15. NUMBER OF PAGES 234	
			16. PRICE CODE	
17. SECURITY CLASSIFICATION OF REPORT Unclassified	18. SECURITY CLASSIFICATION OF THIS PAGE Unclassified	19. SECURITY CLASSIFICATION OF ABSTRACT Unclassified	20. LIMITATION OF ABSTRACT UL	